Acoustic and Visual Imaging

of Active Seafloor Seepage

in Various Deep-sea Environments

Dissertation

zur Erlangung des

Doktorgrades der Naturwissenschaften

(Dr. rer. nat.)

im Fachbereich Geowissenschaften

der Universität Bremen

vorgelegt von

Markus Brüning

Bremen, Januar 2012

Gutachter: Prof. Dr. G. Bohrmann
Prof. Dr. V. Spieß

Daten des Kolloquiums:
Cold seeps in the deep sea – Acoustical and visual imaging
reveals variations in sea floor features
29.06.2012, 15:00,
Hörsaal Raum 1550, Gebäude Geowissenschaften

Meinen Eltern

Abstract

Places where various fluids flow from the sedimentary seafloor into the ocean water are named cold seeps. They occur in all oceans in all water depth. Emanating fluids are frequently hydrocarbons, which also have the largest influences on the seafloor. Such sites in diverse surrounding conditions are the subject of this thesis. It aims at investigating several seep sites fed by end members of seeping hydrocarbon fluids. This work then allows deducting on seeps with intermediate conditions. The overall question is, how the different seep fluids influence and change the seafloor depending on the environmental conditions.

During three research cruises of RV METEOR between spring 2006 and autumn 2007 generally two-parted investigations were performed. The first component was a geophysical-hydroacoustic survey with long-range echo sounders. It aimed at the discovery and/or mapping of seep-related structures. It deployed multibeam echo sounders (KONGSBERG EM120 and EM710), a single beam parametric echo sounder (ATLAS PARASOUND), and two deep towed side scan sonars (EDGETECH DTS-1 and NOC's TOBI). The second phase was the ground truthing part with visual inspection and sampling. Here video sled and remotely operated vehicle dives were conducted at focuses of active fluid seeps. Samples were collected by gravity corer and other instruments. Based on those data, this dissertation comprises three manuscripts.

The first publication of the thesis focuses on the process of asphalt volcanism, the deposition and development of such lava-like deposits on the seafloor. The discovery of asphalt volcanism at Chapopote Knoll in the southern Gulf of Mexico offered the chance to research a unique heavy hydrocarbon deposit on the seafloor in 2900 m water depth. Observation results indicate the deposition of asphalt from the seepage of heavy petroleum liquids. Hence the Chapopote site can be classified as cold seep. In this thesis it possesses the role as heavy hydrocarbon end member. The asphalt was found to have characteristics (API gravity of 10-12°), which just allow it to migrate within the sediment, but it is on the other hand denser than water and flows over the seafloor after release. This is special among the seepage of hydrocarbons, which are generally buoyant in water. The encountered deposits show 'ropy' or 'rough' flow structures similar to magmatic lava flows. This direct observation points at an increase in viscosity at the contact with water and solidification soon after release due to the loss of volatiles. Asphalt deposits are then altered, volume reductions creates fissures, fractures, and finally the entire deposit breaks up into rubble. A succession of different alteration stages shows the periodic character of asphalt seepage. The most recent asphalt field covers an area of ~2000 m² where the flowing material had build up significant positive morphologies.

In the second part of the dissertation, at the other end of the spectrum, light molecular weight hydrocarbon gases erode the seafloor. There, the process is to be understood by mapping and observing the remaining morphologies to conclude on the interaction between rising seep fluids and sediment. Gas hydrate occurs frequently close to the seafloor at cold seeps, its influence on the interaction of seepage and sediment is therefore crucial to the development of seepage, which was also investigated within this project. The appropriate place is Batumi Seep in the eastern Black Sea, a purely gas driven cold seep system. It is located on a ridge of the continental slope offshore Georgia in water depth of 850 m. The seafloor shows irregular negative relief, which was caused by erosion of the seeping gas. Seafloor forms comprise structured, hummocky, and smooth morphologies. Roughness of the seafloor and authigenic carbonate presence correlates with high acoustic backscatter signals. A surrounding medium backscatter halo was found to be associated with gas hydrate within

the sediment. The distribution of individual gas emission points was governed by sealing gas hydrate layers. In the central part the seafloor becomes ruptured by buoyant gas and eventually gas hydrate. Following the outbreak and vigorous gas flow with possibly rafting of gas hydrate seafloor material is lifted and displaced. Models describing individual phases in the seepage process had been developed for both heavy and light end member scenarios.

Thirdly, the focus was on environmental conditions of the ocean water and quantification of the number of seeps. At the Makran continental slope offshore Pakistan a section of the subduction zone at 24°30'N 62°55'E was surveyed for cold seeps. The area of 90 by 50 km from the shelf break down to the abyssal plain contained at least 18 active seep sites in water depth between 500 and 2900 m. All seeps were located at ridges, more precisely, at anticlines. The seeps showed an exemplary succession from oxygen depleted conditions at the upper slope to oxygen rich deep water. A conservative estimate on the results yields an average of 0.3 seeps per kilometre of the offshore part of the Makran subduction zone.

Summarising all findings, a very general scheme to classify seep sites was developed. It involves five independent variables: fluid composition, flow volume, time, water depth, oxygen concentration, forming a five-dimensional cube. The first three are seep-intrinsic variables, the later two environmental variables. The appearance of the seep in the given conditions is determined. All possible seeps plot to a point within that cube.

Kurzfassung

Stellen an denen unterschiedliche Gase und Flüssigkeiten aus sedimentärem Meeresboden ins Meerwasser fließen, werden kalte Quellen genannt. Sie kommen in allen Ozeanen und in allen Tiefen vor. Bei den ausströmenden Fluiden handelt es sich oft um Kohlenwasserstoffe, welche den größten Einfluss auf die Entwicklung des Meeresbodens an kalten Quellen haben. Solche Orte, unter Berücksichtigung ihrer unterschiedlichen Umweltbedingungen, sind Gegenstand dieser Arbeit. Ziel ist es, mehrere Quellen mit größtmöglichen Unterschieden der austretenden Kohlenwasserstoffe zu untersuchen. Diese Arbeit erlaubt es dann, aus diesen Ergebnissen auf weitere Fälle mit durchschnittlicheren Bedingungen zu schließen. Die übergeordnete Frage ist, wie ausströmende Gase und Flüssigkeiten den Meeresboden beeinflussen und verändern, und wie dies von den jeweiligen Umweltbedingungen abhängt.

Während drei Forschungsexpeditionen des Forschungsschiffes FS METEOR, zwischen Frühjahr 2006 und Herbst 2007, wurden zweiteilige Erkundungen durchgeführt. Der erste Teil war dabei jeweils eine geophysikalisch-hydroakustische Vermessung mit Echoloten großer Reichweite. Sie zielte auf die Entdeckung und/oder Kartierung von quellenbezogenen Strukturen ab. Dazu wurden Fächerecholote (KONGSBERG EM120 und EM710), ein parametrisches Echolot (ATLAS PARASOUND) sowie tiefgeschleppte Seitensichtsonare (EDGETECH DTS-1 und NOCs TOBI) verwendet. Die zweite Phase umfasste die Beprobung und visuelle Beobachtungen. Weiterhin wurden Videoschlitten und Tauchroboter eingesetzt. Die Ergebnisse der ersten hydroakustischen Vermessungsphase dienten hierbei als Basiskartenmaterial zum Auffinden der kalten Quellen. Proben wurden per Schwerelot, aber auch mit weiteren Geräten, gewonnen. Basierend auf jenen Daten ist diese Dissertation kumulativ aus drei Manuskripten aufgebaut.

Der erste Teilbereich dieser Arbeit beinhaltet die Untersuchung eines Extremfalls des Kohlenwasserstoffspektrums, den Prozess des Asphaltvulkanismus und die Ablagerung und Entwicklung solcher lavaähnlicher Bildungen am Meeresboden. Die Entdeckung des Asphaltvulkanismus am Chapopote-Hügel im südlichen Golf von Mexiko bot die Gelegenheit, eine besondere Art schwerer Kohlenwasserstoffe auf dem Meeresboden in 2900 m Wassertiefe zu erforschen. Die Beobachtungen deuten auf die Ablagerung von Asphalt, ausgehend von schwerem, flüssigem Erdöl hin. Daher wurde Chapopote als kalte Quelle eingestuft. In dieser Dissertation spielt der Ort die Rolle zur Untersuchung von schweren Kohlenwasserstoffen. Der Asphalt hat Eigenschaften (API Schwere $10 - 12°$), welche gerade noch sein Fließen im Sediment erlauben, dagegen hat der Asphalt aber eine Dichte leicht über der von Seewasser. Folglich breitet sich die Masse nach dem Austreten ins Meerwasser auf dem Boden aus. Dies ist ein Spezialfall unter den Kohlenwasserstoffaustritten, da jene normalerweise im Seewasser auftreiben. Die angetroffenen Ablagerungen zeigen ‚faltige' oder ‚rauhe' Fließstrukturen ähnlich magmatischen Lavaflüssen. Dieses deutet auf eine Zunahme der Viskosität durch den Verlust von flüchtigen Bestandteilen beim Kontakt mit Wasser und eine Verfestigung bald nach dem Ausfließen hin. Die Asphaltablagerungen altern dann, eine Volumenabnahme lässt Risse entstehen, Brüche bilden sich, und schlussendlich zerfällt alles in Bruchstücke. Eine Abfolge von verschiedenen Alterungsstadien zeigt den periodischen Charakter von Asphaltausflüssen. Das jüngste Asphaltfeld bedeckt ~2000 m² und das geflossene Material hat eine Morphologie mit deutlichen Aufhöhungen erzeugt.

Im zweiten Teil der Dissertation, am anderen Ende des Spektrums, erodieren leichte Kohlenwasserstoffgase den Meeresboden. Hier gilt es, den Prozess mit Hilfe von Kartierung und Beobachtung der zurückbleibenden Morphologie zu verstehen und Rückschlüsse auf den

Einfluss des aufsteigenden Gases auf das Sediment zu ziehen. Gashydrat steht an kalten Quellen häufig dicht unter dem Meeresboden an, sein Einfluss auf den Aufstieg, das Ausströmen von Fluiden und der Effekt auf die Sedimente wirkt sich also entscheidend auf die Entwicklung der kalten Quellen aus. Der passende Ort für die Erforschung von kalten Quellen ist in diesem Zusammenhang Batumi Seep im östlichen Schwarzen Meer, eine reine Gasquelle. Sie liegt auf einem Rücken des Kontinentalhanges vor Georgien in einer Tiefe von 850 m. Der Meeresboden zeigt ungleichmäßige Vertiefungen, welche durch die Einwirkungen von erodierenden Gasströmen hervorgerufen werden. Meeresbodenformen beinhalten strukturierte, hügelige und glatte Morphologien. Die Rauhigkeit des Bodens und authigene Karbonate korrelieren mit hoher akustischer Rückstreuintensität. Ein umgebender Ring mit mittlerer akustischer Rückstreuintensität stimmt mit dem Vorkommen von Gashydrat im Sediment überein. Die Verteilung von einzelnen Gasaustrittspunkten wurde von der Abdichtung des Bodens durch Gashydrat bestimmt. Im Zentrum wird der Boden durch aufstrebendes Gas oder auch Gashydrat aufgebrochen. Anschließender kräftiger Gasfluss und möglicherweise das Auftreiben von Gashydrat trägt in der Folge das Sedimentmaterial ab. In der Dissertation wurden sowohl Modelle zu einzelnen (zeitlichen) Phasen des Austritts für den Fall des leichten als auch des schweren Extremfalls entwickelt.

Im dritten Teil liegt der Schwerpunkt auf der Betrachtung des Einflusses der Umweltbedingungen, zum Beispiel des Meereswassers, und der Quantifizierung der Anzahl kalter Quellen. Am Makran-Kontinentalhang vor Pakistan wurde ein Teil der Subduktionszone bei 24°30'N 62°55'O auf kalte Quellen hin erkundet. Das Gebiet von 90 mal 50 km Größe von der Schelfkante bis zur Tiefseeebene beherbergt mindestens 18 aktive kalte Quellen in Wassertiefen zwischen 500 und 2900 m. Alle Quellen befinden sich auf Rückenstrukturen, genauer, auf Antiklinalen. Die Quellen zeigten einen beispielhaften Verlauf von sauerstoffabgereicherten Bedingungen am oberen Hang, hin zu sauerstoffreichem Tiefenwasser. Eine zurückhaltende Einschätzung der Ergebnisse ergibt eine durchschnittliche Zahl von 0,3 Austrittsstellen pro Kilometer Unterwasserabschnitt der Makran-Subduktionszone.

Alle Erkenntnisse zusammenfassend wurde ein sehr allgemeines Schema zur Klassifizierung von kalten Quellen entwickelt. Es beinhaltet fünf unabhängige Variablen: Gas- bzw. Flüssigkeitszusammensetzung, Flussmenge, Zeit, Wassertiefe und Sauerstoff-konzentration, welche einen fünfdimensionalen Würfel aufspannen. Die ersten drei Variablen sind quellenabhängig, die beiden weiteren umweltabhängig. Basierend auf diesen Variablen kann das Aussehen einer kalten Quelle unter den gegebenen Bedingungen festgelegt werden. Alle möglichen Kombinationen der Variablen lassen sich auf einem Punkt im fünfdimensionalen Würfel abbilden.

Outline of the Dissertation

This thesis is divided into nine chapters. Chapter 1 introduces the field of cold seeps: their appearance on the seafloor, involved fluids, and consequences of the seep-process. Chapter 2 then highlights the lacks in current understanding of such systems and provides the motivation for this work. It also shortly outlines the research cruises during which required survey-data were acquired. Chapter 3 explains the methods used to collect those data. Subsequently the visited work areas are described in chapter 4. The next three chapters comprise research manuscripts, which are the main part of this thesis. The first publication, chapter 5, contains the mapping of a heavy hydrocarbon end-member seep, an asphalt deposits at Chapopote Knoll, Gulf of Mexico. The second manuscript, chapter 6, deals with seepage of the light end-member, methane, and the influence of free gas seepage on the seafloor at Batumi Seep, Black Sea. The third one, chapter 7, shows the survey of a segment of the Makran accretionary prism offshore Pakistan, where a systematic search for flares and backscatter anomalies proved to be a successful method. Short outlines of the manuscripts follow below. Chapter 8 then summarises the findings and provides an overall conclusion. Future demands are briefly listed in the final chapter 9. All references of the thesis are listed at the end after chapter 9.

Chapter 5 - Manuscript 1
Origin, Distribution, and Alteration of Asphalts at Chapopote Knoll, Southern Gulf of Mexico
Markus Brüning, Heiko Sahling, Ian R. MacDonald, Feng Ding, Gerhard Bohrmann
Published at MARINE AND PETROLEUM GEOLOGY

Special at the Chapopote Asphalt Volcano is the case that heavy hydrocarbon remained and flowed on the deep-sea floor, instead of floating up. Based on visual seafloor observations the asphalt deposit distribution was mapped. Additionally, work was focused on one area with apparent asphalt flow structures. Encountered flow morphologies lead to the conclusion that seepage of very heavy liquid and semi-solid petroleum, flowing on the seafloor, and rapid solidification formed ropy, and if vigorous degassing was involved, rough asphalt. Alteration processes then crack asphalts and finally the material disintegrates into fragments. A combination of heavy oil and temporary storage in a very shallow reservoir within the exposed knoll structure make this unique kind of seepage possible. Asphalt volcanism was found to be as significant by mass as other hydrocarbon seepage in the Gulf of Mexico.

Chapter 6 - Manuscript 2
Seafloor Development at Purely Gas Driven Batumi Seep, eastern Black Sea - Separation of Backscatter Signatures into their Origins
Markus Brüning, Gregor von Halem, Heiko Sahling, Ingo Klaucke, Thomas Pape, Gerhard Bohrmann
To be submitted to MARINE GEOLOGY

Batumi Seep is located in the eastern Black Sea at 850 m water depth. Due to the anoxic water conditions in the Black Sea and the seep's location within the gas hydrate stability zone, this vigorously bubbling system is an ideal end-member example to study interrelations between gas flow, sediment, and gas hydrate. We achieved to correlate backscatter intensity recorded in two frequencies by side scan sonar with seafloor morphology, free gas emission,

and gas hydrate occurrence in the shallow sub-seafloor. Additionally a relationship of seafloor morphologies to gas flow was defined.

Chapter 7 - Manuscript 3
Abundant Methane Seepage at the Continental Slope offshore Pakistan, Makran Accretionary Prism

Markus Brüning, Heiko Sahling, Tim Le Bas, Bramley Murton, Feng Ding, Volkhard Spiess, Gerhard Bohrmann
To be submitted to MARINE GEOLOGY

A section of the Makran accretionary subduction zone offshore Pakistan was searched for cold seepage. We ran acoustic and visual surveys to find and characterise seeps. First large range multibeam echo sounder and deep-towed side scan sonar, as well as sub-bottom profiler and water column information were used to identify potential seep areas. Consecutive water column scanning and then video observations on the seafloor located a number of seeps. It turned out that seep sites are confined to ridge crests, but spread over the full slope from 500 to 2900 m water depth. A conservative guess on the number of seeps along the margin was achieved.

Appendix - Manuscripts 4, 5, and 6

The appendix contains four further co-authored publications, which had been supported by my work within this PhD project. Throughout this text the first three are referenced as Ding et al. (2008a) (attached as A1), Ding et al. (2010b) (attached as A2), and Ding et al. (2010a) (attached as A3). Sahling et al. (2009) (attached as A4) investigated another area and seep class in the Black Sea, the Vodyanitskii mud volcano, and is therefore not as closely related to the research of this thesis as the former three.

Contents

List of Figures and Tables

List of Abbreviations

Units are generally abbreviated by SI units. Additional abbreviations used are listed below.

AOM	Anaerobic Oxidation of Methane
API	American Petroleum Institute
AUV	Autonomous Underwater Vehicle
BSR	Bottom Simulating Refelctor
CH4	Methane
CTD	Conductivity-Temperature-Density Sensors
DAPC	Dynamic Autoclave Piston Corer
DFG	Deutsche Forschungsgemeinschaft
(D)GPS	(Differential) Global Positioning System
DSDP	Deep Sea Drilling Program
GC	Gravity Corer
GEBCO	General Bathymetric Chart of the Oceans
GeoB	Geosciences University of Bremen, diverse sample or profile numbers
GHSZ	Gas Hydrate Stability Zone
GI-gun	Generator Injector gun
GIS	Geographic Information System
GLOMAR	Postgraduate School for Global Change in the Marine Realm
GMT	Generic Mapping Tool
M	METEOR
MAF	Main Asphalt Field
MARUM	Zentrum für MARine UMweltwissenschaften
MBES	MultiBeam Echo Sounder
m bsf	Metre Below SeaFloor
m bsl	Metre Below SeaLevel
MUC	Multi Corer
NOC	National Oceanography Centre
ODP	Ocean Drilling Program
OFOS	OceanFloor Obsevation System
OMZ	Oxygen Minimum Zone
P	POSEIDON
PC	push Core
PhD	Philosophiae Doctor
RCOM	Research Center Ocean Margins
ROV	Remotely Operated Vehicle
SAR	Synthetic Aperture Radar
SMI	Sulphate Methane Interface
SO	SONNE
SSS	Side Scan Sonar
TOBI	Towed Ocean Bottom Instrument
TOC	Total Organic Carbon
TTR	Training Through Research
TWT	Two Way Traveltime
USBL	Ultra Short Base Line
UTC	Universal Time

1

Introduction

1.1 Cold Seeps

Cold seeps are places of locally focused fluid leakage from the subsurface into the ocean. The fluids have no or only little increased temperatures compared to the environment (Paull et al., 1984), hence the prefix 'cold'. Seeping fluids are diverse in origin: groundwater, dewatering of sediment, material transformation and diagenesis. Fluids themselves are water or hydrocarbons, eventually with admixing of sediment particles. Driving forces are buoyancy and pressure gradients. Cold seeps are in opposition to hot vents. There, hydrothermally heated fluids escape where seawater percolates oceanic crust and heat causes advection (Corliss et al., 1979). Black smokers belong to such hot vents. At cold seeps, the terms 'seep' or 'vent' are used. The first refers to slow leakage, the second to more volumetric emission rates (Aharon, 1994; Campbell, 2006). Exact flow is, however, difficult to determine. Both expressions are employed exchangeable within this work as flow rates are not determined here.

The first discovery of a cold seep was published in 1984. Paull et al. found biological communities with great similarities to hot vent communities at the bottom of a carbonate wall on soft sediment at the base of the Florida Escarpment in the Gulf of Mexico. Examples for different cold seep communities are given in Fig. 1.1. Since their discovery cold seeps became an important topic in marine geological and biological research because they play a major role in geosphere and biosphere. Cold seeps had been found to be common on most continental margins around the world (Campbell, 2006; Kvenvolden and Cooper, 2003; Mazurenko and Soloviev, 2003). Fig. 1.2 gives an impression of the world-wide abundance of cold seeps. With ongoing research more locations can be added. Gaps without reported seepage are likely a sampling/survey bias.
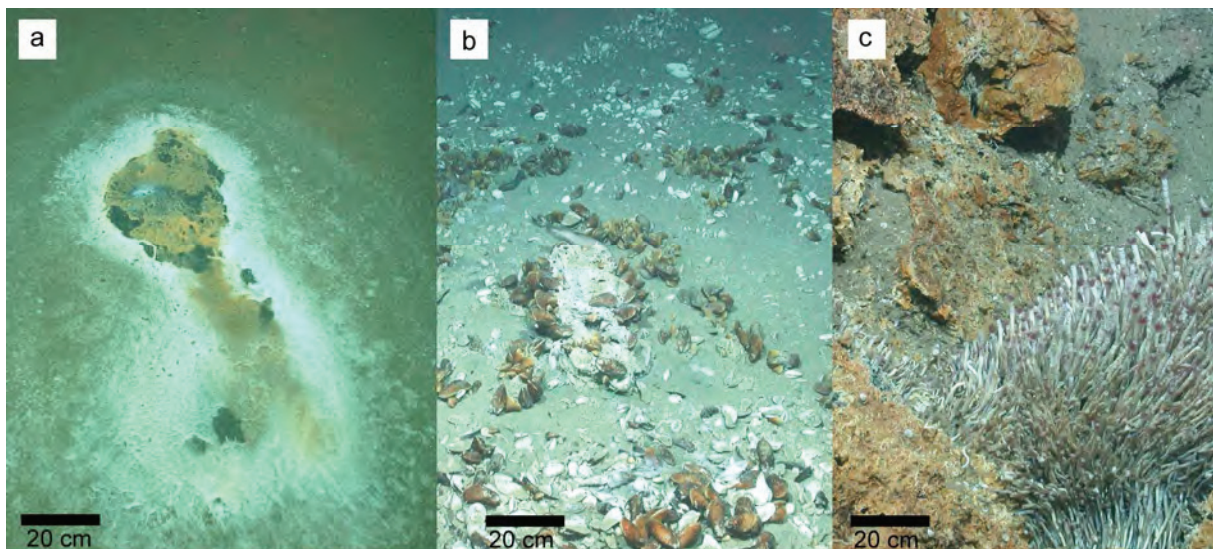
Fig.1.1: Examples of cold seeps: a) Bacterial mat around a bubble release site, oxygen depleted water, Makran, continental slope off Pakistan, 550 m water depth. b) Chemosynthetic clams and bathymodiolin mussels, white authigenic carbonate, continental slope off Pakistan, 1500 m water depth. c) Vestimentiferan tube worms and brownish authigenic carbonate, Athina mud volcano, Anaximander Mountains, eastern Mediterranean Sea, 1800 m water depth. Photos © MARUM.

Major research programs focused for example on Cascadia (TECFLUX 99, Bohrmann, 2000; ODP Leg 204, Tréhu et al., 2006; Bohrmann and Torres, 2006), northern Gulf of Mexico (e.g. Roberts and Aharon, 1994; MacDonald et al., 2003; Whelan et al., 2005), the Black Sea (GHOSTDABS, Michaelis et al., 2006; MUMM, e.g. Treude et al., 2006), Costa

Rica (DFG SFB574, Volatiles and Fluids in Subduction Zones, GEOMAR, Bohrmann et al., 2002), Makran (MAMUT project, von Rad et al., 2000; Kukowski et al., 2001; MARUM project Geo-Biosphere Interactions, Bohrmann et al., 2008a), Blake Ridge (Dickens et al., 1997; Holbrook et al., 2002; Hornbach et al., 2008).

Cold seepage is dominantly controlled by shallow sediments, i.e. the upper few hundred metres (Ding et al., 2008a; Ding et al., 2010a). However, fluids originate often from deeper layers. Examples are leaking oil and gas, and fluids expelled in subduction zones. In general, cold seepage is more continuous than hydrothermal venting (Paull et al., 1984; Campbell, 2006). However single sites within an area of cold seepage can be variable in emission as well in space as in time (Leifer et al., 2004; Linke et al., 1999; chapter 6). Fluid seepage shifts between various neighbouring vent sites or increases with periodically changing hydrostatic pressure like tides, on small time scales (Boles et al., 2001; Chanton et al., 2003), or changing eustatic sea level on glacial-interglacial (Teichert et al., 2003) and even longer time scales (Kiel, 2009).
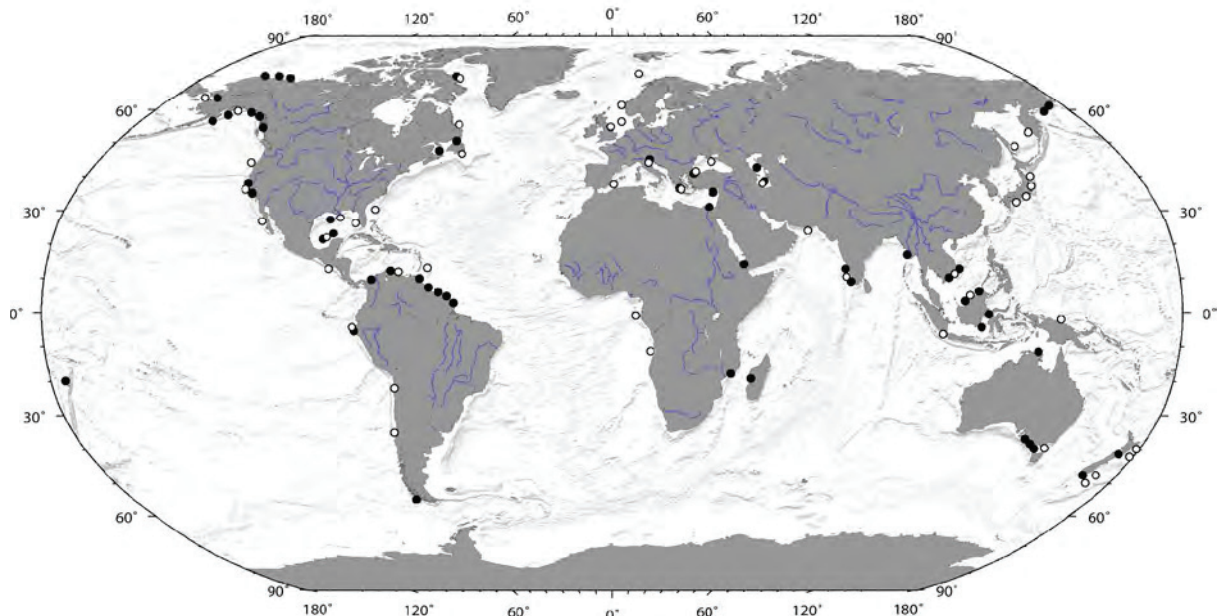
Fig. 1.2: World map of cold seepage: White dots: present hydrocarbon seeps (modified from compilation by Campbell, 2006), black dots: crude oil seeps into the marine environment (modified from Kvenvolden and Cooper, 2003).

1.2 Seafloor Manifestations of Seeps

1.2.1 Different Appearances of Seafloor Seepage

Seeps can have different appearances on the seafloor. Here four possible and frequent forms in which seepage can shape the seafloor are introduced.

Seep sites without own morphology did not develop an own significant morphology due to the seepage process. If there is an elevation or depression, it is below 5 m elevation, and hence not resolved with reconnaissance surface vessel based bathymetry surveys. These seeps

are often located on morphological highs or along faults. At these geological settings fluids become focussed during their ascent through the sediment spots. Areas influenced by the seepage then range from 10 - 1000 m in length or diameter. They are discernable by side scan sonar mapping as they usually generate increased backscatter. Another method to discover the sites are video observations, which reveal small scale morphology and biological communities caused by and based on the seepage. Seep sites without morphology are the most common form found in this work, and probably world wide. Due to the nature of the appearance, however, many more are still to be discovered. Examples can be found in the offshore Makran, with flare sites reported in chapter 7 belonging to this group, seeps in the eastern Black Sea (Klaucke et al., 2006), including Batumi Seep (chapter 6), and several seeps offshore Costa Rica (Sahling et al., 2008a) and California (Orange et al., 2002).

Mounds are hills on the seafloor, which originate from seepage and are up to 100 m high, diameters can reach several hundred metres. The mounds are made up of accumulations of methane derived autigenic carbonate and hemipelagic sediment. Pure seep-derived carbonate build-ups are named 'chemoherms' (Teichert et al., 2005). Therefore the hills show often a high backscatter signature. They are common on continental margins, e.g. Costa Rica (Sahling et al., 2008a), west of Ireland and northwest of Australia (Hovland et al., 1994), and offshore Brazil (Sumida et al., 2004), to give some examples. Small-scale morphology at many seeps without higher elevations is also described with the word 'mound' in the literature (Judd and Hovland, 2007), where the shape and not size applies. As said above, here the discrimination is based on swath bathymetry resolution, and those small mounds therefore fall in the first group.

Mud volcanoes are the most spectacular cold seep manifestation. Sizes span from one metre height and diameter to several hundred metres in elevation and tens of kilometres across (Kopf, 2002). The maximum dimension for an exemplar encountered offshore is 30 km diameter and 2 km height for serpentinite seamounts (Fryer et al., 1985; Kopf, 2002). Mud volcanoes are propelled by fluid overpressure in the subsurface. Expelled fluids carry mud breccia to the surface, where material flows on the ground and build up around the emersion point. The pile of mudflows radiating from a flat central mud-pool may have steep flanks or a flat appearance. A moat depression often surrounds mud volcanoes, indicating the mass deficiency of material removed at depth and build up to the new central elevation. Mud volcanism is generally accompanied by hydrocarbon seepage as mud feeder channels drain hydrocarbon source rocks, or mud-source is in itself a source rock (Kopf, 2002). Mud volcanoes may host cold seep communities (e.g. Jerosch et al., 2007), have a cover of carbonate crusts (Lykousis et al., 2004), and, furthermore, may contain gas hydrates (Bohrmann et al., 2003). Mud flows and cold seep communities cause increased backscatter compared to surrounding sediment (Lykousis et al., 2009). Mud volcanoes appear worldwide, on- and offshore. A summary is given by Kopf (2002). Examples are Haakon Mosby Mud Volcano offshore Norway (Jerosch et al., 2007), several mud volcanoes in the Anaximander Mountains, eastern Mediterranean (Lykousis et al., 2009), and on- and offshore Pakistan (Delisle et al., 2002), to list a few.

Pockmarks, circular or oval depressions of the seafloor interrupting sediment layers, are another frequent sign of fluid escape from the seafloor. They are generally 50 to 100 m wide and several metres deep, but can range from one metre to several hundred metres in diameter and tens of metres in depth (Judd and Hovland, 2007). Pockmarks result from the vigorous escape or outbreak of buoyant or overpressured fluid or gas hydrate from the seafloor, removing sediment and leaving a depression or crater, the pockmark, behind (Hovland and Judd, 1988). Pockmarks can remain active with continuous release of fluids, or be inactive

(Judd and Hovland, 2007). Depending on their size, pockmarks can be easily found by bathymetric surveys. Side scan sonar surveys reveal pockmarks by their characteristic shadows, and possibly added higher backscatter at the pockmark floor or side walls (Sahling et al., 2008b). Pockmarks appear worldwide in marine and lacustrine settings (Hovland and Judd, 1988). Pockmarks were, for instance, discovered in the North Sea, off Norway (Judd and Hovland, 2007), offshore west Africa (Gay et al., 2006; Sahling et al., 2008b), and in Makran (chapter 7).

Horizontal dimensions of cold seep's appearance on the seafloor vary largely, depending on the setting (see above) and method applied (Klaucke et al., 2008). Most sites are small and according search is necessary. "Accidental" discoveries are unlikely. Elevations or depressions are often neglectible in relation to their water depth; they range from tens of metres for carbonate chemoherms (Judd and Hovland, 2007), to hundreds of metres for mud volcanoes (Kopf, 2002). Horizontally seeps are as small as 1 m for bacterial mats (Fig. 1.1), to several hundred metres in Makran (chapter 7), or tens of kilometres in the case of mud volcanoes. The seafloor area which is actually seep-influenced in the example of the Makran continental slope is only 0.4 % (chapter 7, Fig.7.12).

1.2.2 Geological Settings of Cold Seeps

Cold seeps were found in many various offshore settings; however, not all geological settings favour their occurrence. Geological requirements for a seep to occur are: (1) The rise of fluids needs a driving force, pressure or buoyancy. Pressure can be increased by compaction or sediment loading. Buoyancy is present, if the density contrast between one fluid and the surrounding medium is such that one density is lower. Furthermore, (2) some permeability is necessary to allow migration and escape of fluids. It may be permeability of the entire rock, or pathways along faults. Finally, (3) the rising of fluids has to be faster than sedimentation rate, otherwise there is no net-ascent of fluid against the seafloor-level.

Seeps were discovered both at active and passive margins along continents, and in sedimentary basins. Active margins, in this case subduction zones, generate over-pressures within subducting sediment as well as extensive faulting in the prism above and by flexing of the subducting plate. If the subduction is erosive, all sediment on the oceanic plate is being subducted, and, additionally, the overriding plate is scraped off at the bottom (Vanucchi et al., 2001). In the accretionary case, sediment from the incoming oceanic plate is folded up in front of the overriding plate. The piled up sediment experiences compression, overpressuring, and dewatering.

At passive margins material eroded onshore piles up, e.g. in deltas. Gravity forces a downward compaction and expulsion of fluids upward. Independent of tectonic setting, ocean currents can force upwelling of nutrient loaded waters followed by high biological production and organic rich high sedimentation rates. Sedimentary basins are according to or even enclosed in passive margin.

Independent of the geological situation, fluid flow may happen pervasive or focussed. Pervasive flow certainly happens, when the sediment permeability is sufficient. However, it is more difficult to detect as the appearances described above (chapter 1.2.1) are unlikely to occur, additionally flow rates may be below measurement thresholds. Therefore work is concentrated on sites of focussed escape of larger volumes of fluids. Balances between pervasive and focussed flow are to be dealt with elsewhere beyond this thesis. Elements concentrating sub-surface fluid movement, like faults or anticlines, are favoured locations to encounter seeps. Fig. 1.3 provides a sketch of several possible sub-seafloor and seafloor settings of cold seeps.
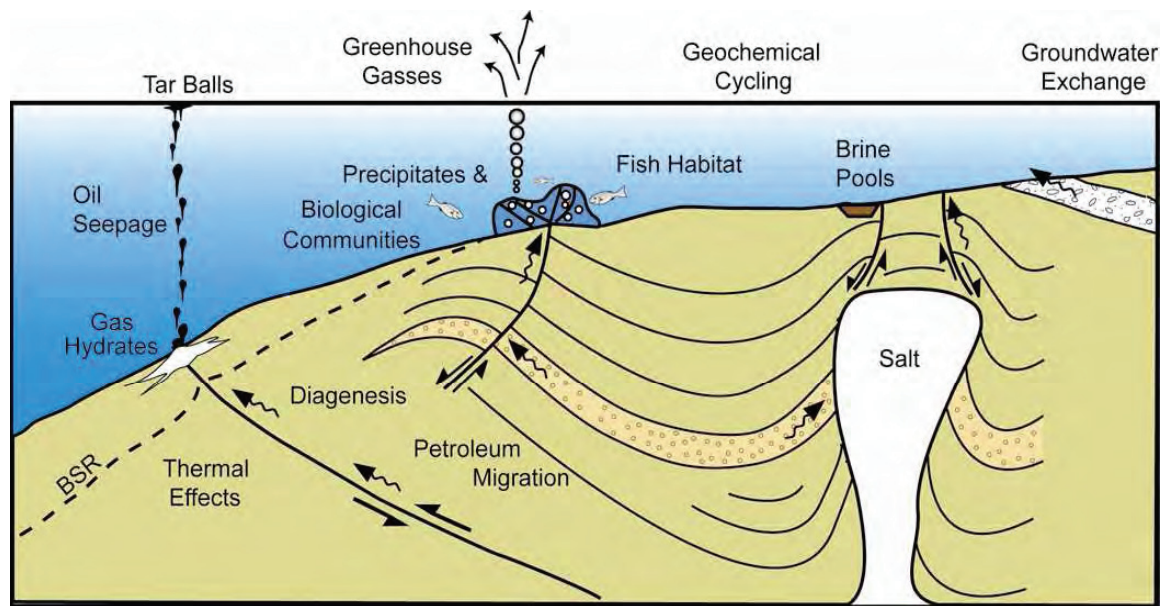
Fig. 1.3: MARUM / RCOM project E1 illustration of various possible seep settings (modified from Suess and Linke, 2006).

1.2.3 Fossil Seeps

Seep sites on the seafloor are not a recent phenomenon. They existed since Achaean times. Like in recent seeps, authigenic carbonate depleted in ^{13}C signatures as well as biomarker point to microbial utilisation of methane. At outcrops of fossil seeps typical indicators like chimneys, doughnut shaped carbonate, pipes, cemented or open conduits were found. The worldwide findings of such remains indicate a widespread occurrence in varying geological settings (Campbell, 2006). The oldest hydrocarbon seep documented is the Silurian El Borj site in Morocco (Barbieri et al., 2004).

Seep activity and the precipitation of carbonates were not constant with time but correlated proportional to sea level low stand and low deep water temperature (Kiel, 2009). A zonation according to flow-intensity and environmental conditions was reported for fossil and for present seeps alike. Chemosynthetic communities spread via step stones of hydrothermal vents, whale falls, and hydrocarbon seeps within the oceans (Campbell, 2006).

1.3 Fluids of Seepage

1.3.1 Definitions

Within this document fluids are defined as liquids and gases. Fluids need to fulfil the requirement to be viscous enough to move, liquids have a higher viscosity than gases. Examples for fluids are water, hydrocarbons ranging from C_1H_4, methane, to asphalt, a heavy petroleum complex mixture of hydrocarbons with a peak at n-C30 and a few resolved C29 to C32 hopanes (MacDonald et al., 2004; Schubotz et al., 2011). Sibuet and Olu (1998) give a more detailed review on fluid compositions found at cold seeps. Substances gaseous at surface pressure and temperature conditions are often dissolved in water in the deep marine environment. Nevertheless, if the concentration exceeds solubility, free gas appears even at 3000 metre below sea level (m bsl). Chapters 5 − 7 provide various examples with light hydrocarbon gases involved. Other solvents, e.g. salt, can be collected along the fluid's path.

On the other hand, fluids can transport solids as well. Where such a mud-slurry reaches the seafloor it can build a mud volcano. A speciality is the combination of water and light hydrocarbon gases, carbon dioxide, or noble gases forming clathrate ice under certain high pressure, low temperature, and gas-saturated conditions (Paull, 2001). The water molecules then form a cage around the guest molecule in the middle. Such gas hydrate fills pore space and hence hinders further fluid movement.

1.3.2 Sources of Fluids

This chapter describes the various possible fluids possibly involved in cold seepage, their release or generation from the sediment, and migration to seafloor seeps.

1.3.2.1 Submarine groundwater discharge

Meteoric groundwater is recharged by precipitation onshore. It eventually travels pressurised by gravity past the coastline in confined or un-confined aquifers and discharges from the seafloor. Such locations appear near-shore on the shelf (Glover, 1964; Domenico and Schwartz, 1998). Submarine groundwater discharge may leak freshwater or could be mixed with saltwater in the sub-seafloor. Tides and surges can have significant influence on the flow (Simmons, 1992).

1.3.2.2 Compaction and diagenetic de-watering

Compaction of sediment appears by continuous loading and pressure increase with burial depth. Pore water gets squeezed out, porosity is reduced. Sands are only little compacted with burial, but mud can contain 60% of water within pore space. Compaction dewatering occurs in any underwater sediment deposition environment, and especially in sedimentary basins and in accretionary prisms. (Fowler et al., 1985; Bekins and Dreiss, 1992). However, if pore water is blocked by a sealing layer, the sediment becomes over pressured. Consequently fracturing can occur. Eventually the pressure is released by eruptions of material and formation of a mud volcano (Kopf, 2002).

Diagenesis of minerals is another water source during burial, where water incorporated within the mineral lattice becomes released. The transformation of clays, e.g. from smectite to illite, occurs at temperatures starting from 90°C and results in a volume reduction proportional to smectite content (Chamley, 1994). The transformation of amorphous biogenic opal A silica via opal CT to quartz takes place at various temperature and pressure regimes. It results in a maximum volume reduction of 60 % (von Rad, 1979). Gypsum converts to anhydrite starting at about 40°C (Hill, 1937; Murray, 1964).

1.3.2.3 Hydrocarbon generation

Organic matter is omnipresent in marine sediments. Total organic carbon (TOC) usually amounts up to a few percent of the bulk material, but can reach, for example, up to 50% in sapropel of the Black Sea Unit II layer (Degens and Ross, 1974). The organic matter originates from land plants flushed by rivers into the sea, or from marine plankton and nekton. After dieing, the corpses are buried. Organic matter remains are soon recycled or later altered to kerogen, which is the source for hydrocarbon generation. The subsequent processes can be divided into shallow diagenesis, deep catagenesis and metamorphism. Fig. 1.4 shows an overview of the processes. The stage of maturity reflects the individual hydrocarbon stages and is used in petroleum exploration.
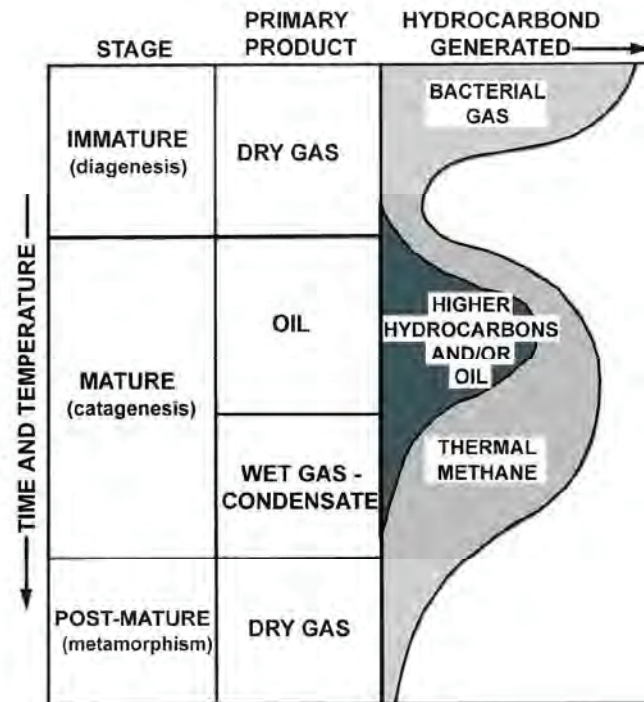
Fig. 1.4: Phases of hydrocarbon generation (modified from Rice, 1992).

Shallow organic matter degradation happens in a sequence:

Biogenic methane generation happens under anoxic conditions. The production of methane only stands at the end of organic matter decomposition, and several other oxidation processes happen before: oxidation by dissolved oxygen, by manganese oxides, by nitrate, by iron oxides, by sulfate. Each process yields less energy to the bacteria performing the reaction (Rice, 1992). Paull et al. (1994) give a condition for methanegeneration as diminishing of sulfate dissolved in the pore fluids by microbial sulfate reduction, because microbial methane production cannot start with sulfate present. Methanogenic archaea then break down organic matter to methane in a complex series of processes (Rice, 1992). Rice gives some additional conditions for biogenic methane generation: temperatures between 25 and 97°C, with optimum production from 35 to 45°C; abundant organic matter with TOC content above 0.5 %; sufficient pore space for the bacteria to flourish, i.e. > 1 μm, for fine grained material usually this translates to depth above 2 km; sedimentation rate between 200 and 1000 mm/a, if it is too low, conditions will be oxic and organic matter will be fully oxidised, if it is too high, organic matter is diluted and buried to too hot zones too quickly. The chemical reaction equations are given as follows:-

$$2\ CH_2O \rightarrow CH_4 + CO_2 \qquad \text{(fermentation of organic matter)}$$
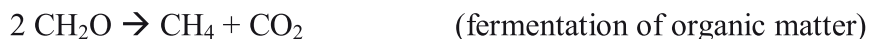
If hydrogen is available, CO_2 can be reduced to methane:

$$CO_2 + 4\ H_2 \rightarrow CH_4 + 2\ H_2O \qquad \text{(carbon dioxide reduction)}$$
(Paull et al., 1994)

Carbon dioxide reduction is the dominant reaction in marine sediments (Whiticar et al., 1986). Deeper burial favours the following process:

Rock buried deeply experiences high pressure and temperature conditions. The kerogene contained in such source rock is then cracked thermo-chemically into hydrocarbons, which are more mobile than the kerogene itself. Generally oil is produced earlier within a so called 'oil window', gas is formed later at even higher temperatures and pressures. The 'oil window' is covered by temperatures of about $100 - 150°C$, with a normal geothermal gradient of $30°C$ / 1000 m this translates to depth of 3000 to 4500 m. There are three types of kerogene with different hydrogen – carbon and oxygen – carbon ratios, producing different hydrocarbons. Type I has a high H:C and low O:C ratio, this kerogene is dominated by algae organic material and generates oil. Type II kerogene has intermediate H:C and O:C ratios, organic material comes from marine condition plants and animals. It produces oil, condensate and wet gas. Type III has low H:C and high O:C ratio, originating from land plants and generating dry gas. Another type (IV) is negligible for hydrocarbon generation. It contains organic matter, which is already thermally altered. Fig. 1.5 illustrates those conversion paths. This is only a short compressed summary of the entire field of Petroleum Geology. It is extracted from the books of Tissot and Welte (1984), North (1985), and Killops and Killops (2004). The entire suit of produced hydrocarbon fluids is buoyant and tends to rise from its source rock.
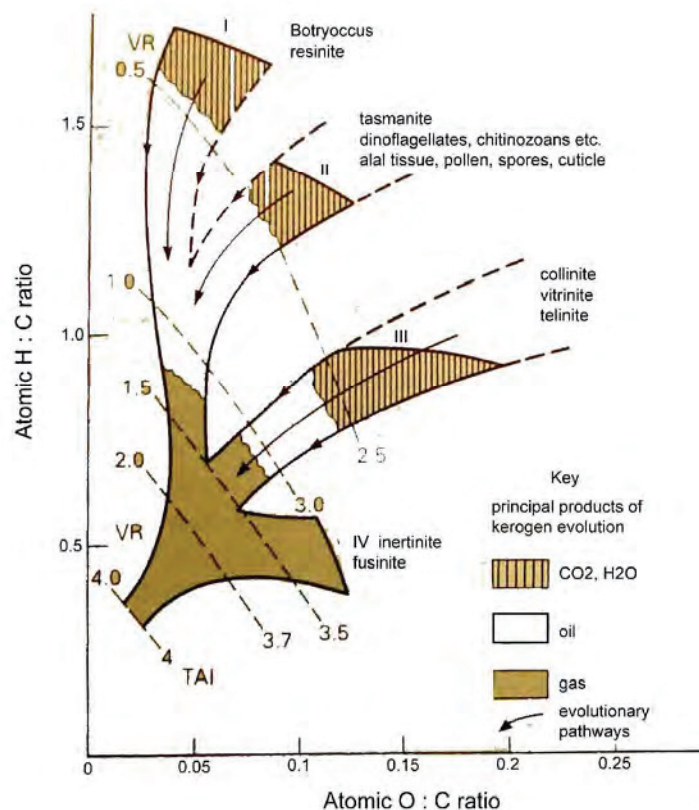
Fig. 1.5: Hydrocarbon generation from different kerogene types. Type I – algae, type II marine plankton and nekton, type III – land plants, type IV thermally altered kerogene (North, 1985).

At the surface it is possible to discriminate the origin (biogenic / thermogenic) of light hydrocarbon gases by their carbon and hydrogen isotope ratios (Bernard et al., 1976; Whiticar, 1999). This allows concluding about migration pathways from the different source areas.

1.3.3 Fluid Migration

Any fluid originating widespread within the sub-surface has to migrate to the seafloor if seepage shall occur. Migration can take place by different processes: advection, where the fluid itself moves; by diffusion, where individual dissolved molecules move within a host fluid along concentration gradients; or, in case of mud volcanoes an entire material column of fluid and mud breccia rises within a chimney.

The travelling fluid requires permeability within the bulk material, or voids along faults or along permeable sedimentary layers. Flow through porous media calculates by Darcy's law:

$$\frac{Q}{A} = -\frac{k\rho_w g}{\mu}\frac{\partial h}{\partial l}$$

(Eq. 1.3.1)

with Q – flow volume; A – cross area; k – permeability; ρ_w/μ – property of the fluid; g – gravity; $\delta h/\delta l$ – pressure gradient along flow path (Darcy, 1856; Domenico and Schwartz, 1998).

Hence, the flow depends not only on rock permeability, but also on fluid properties, and pressure gradient. Flow along channels or fault-planes may be estimated by the Bernoulli equation.

Diffusion in sediments is expressed by Fick's law:

$$J = -D^*_d \, n \, grad \, (C)$$

(Eq. 1.3.2)

with J – chemical mass flux; D^*_d – bulk diffusion coefficient, depending on ion and solvent; n – porosity; grad (C) – concentration gradient (Domenico and Schwartz, 1998). Diffusion is proportional to concentration gradient and porosity.

Flow is often focussed by geological structures. Faults gather pervasive flow, anticlines focus at their top. Fig. 1.3 showed some examples graphically. Rising fluids may reach the seafloor directly, or be retarded within traps. Such traps may be formed by sealing layers of anticlines, sealing fault planes, or on the sides of salt domes. The porous rock holding the fluid is called reservoir rock. Fluids, especially hydrocarbons, can change while stored in the reservoir. Gas and oil eventually separate with clear boundaries between each other and basal and surrounding water. Oil can become biodegraded by bacterial activity (Tissot and Welte, 1984; Head et al., 2006), or be washed by passing gas (Whelan et al., 2005). Traps are not entirely sealing or filled completely and overflowing so they buffer the flow from source rock to seepage. Gas hydrate may act both as seal and buffer. On the way to the surface or seafloor rising gases reach a zone of high pressure and low temperature. Fig. 1.6 shows the limits of the gas hydrate stability zone. Gas hydrate is stable within the gas hydrate stability zone (GHSZ). This zone is defined by pressure and temperature conditions with temperature line below the hydrate phase boundary line. The temperature is constant or rising from seafloor towards the water surface, increasing at geothermal gradient below the seafloor. The hydrate line is calculated, depending on gas composition and water salt content. If water is used up for hydrate formation, no new clathrate forms and free gas can exist. At the base of the GHSZ free gas is trapped and causes a bottom simulating reflector (BSR) in seismic reflection data (Delisle and Berner, 2002; Hyndman and Spence, 1992; Paull et al., 1994; Kvenvolden, 1998).
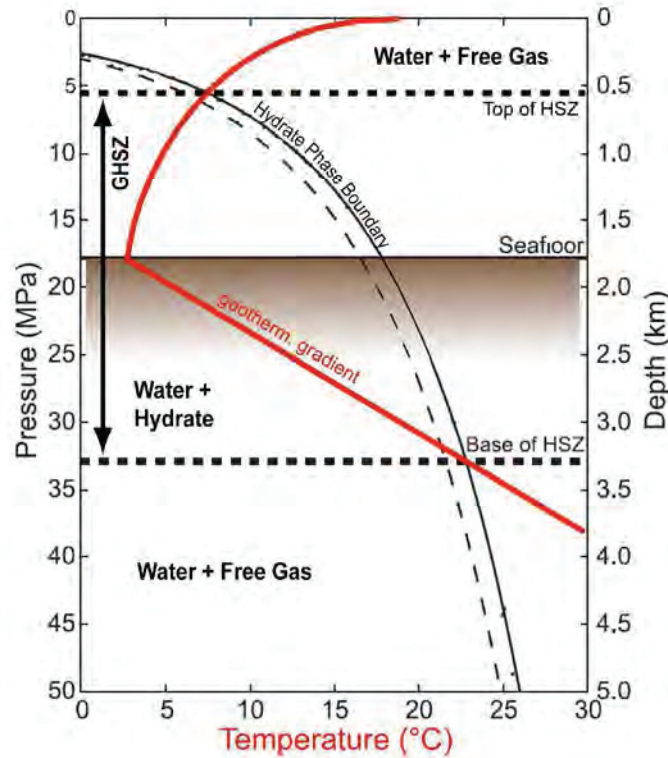
Fig. 1.6: Gas hydrate stability. Red: measured temperature, black solid line: calculated hydrate phase boundary, black dashed line: hydrate phase boundary position varies with gas composition and water salt content; and hence the limits of gas hydrate stability. (modified from Buffet and Archer, 2004).

If gas or oil bubbles reach the seafloor, they can continue to rise within the water column. Then free to move, they can rise quickly through the entire water column. At the sea surface oil eventually forms slicks by spreading to thin layers covering wide areas of the water surface. Fig. 1.7 shows a small slick from a droplet, which had just arrived at the Black Sea surface.

Fig. 1.7: Oil droplet forming a circular oil film (left), oil dispersed by waves (right). Above a seep in the Black Sea. Photo courtesy A. Bahr.

Combining, large persistent slicks can form above seeps (MacDonald et al., 1993). They can be tracked by satellite observation (see chapter 3.4) (MacDonald et al., 2000; Garcia and MacDonald, 2008). Gas bubbles travelling through the water long distances are dissolved. However, a skin of hydrate or oil can protect them from dissolution, so that they can rise thousands of metres. A plume of many bubbles can be observed by echo sounders (see chapter 3.1.2.2). Fig. 1.8 shows bubbles rising from a seep offshore Pakistan. According to their overall shape, these features are named bubble plumes or flares.
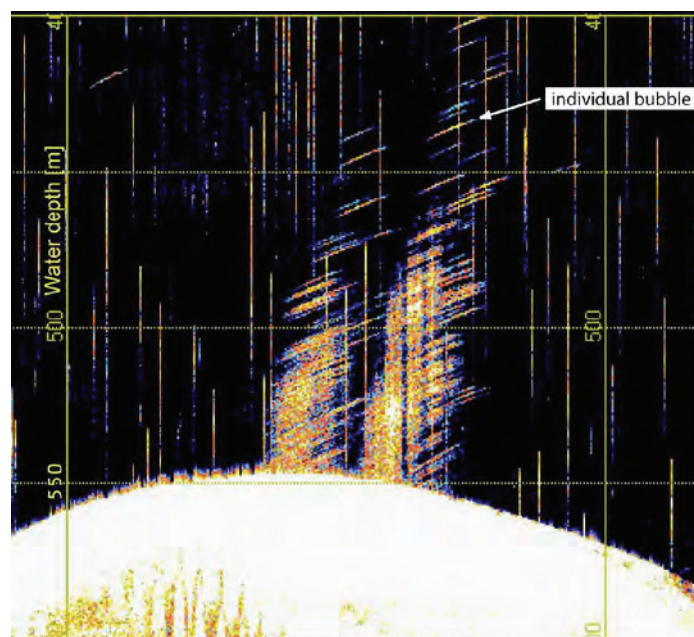
Fig. 1.8: Gas bubbles ascending through the water column. Individual bubbles create lines, many bubbles appear as blur. Flare 1 offshore Pakistan, Makran. ATLAS PARASOUND, 18 kHz echo sounder.

1.4 Geochemical Processes and Biological Communities

This chapter concentrates on a group of fluids, which allows to study and map fluid migration paths and history. Cold seeps emitting low molecular weight hydrocarbons are characterised by certain geochemical processes leaving material traces at the seafloor. Rising light hydrocarbons, especially methane, are an energy source for a row of microorganisms and higher fauna living in symbiosis. Via sulphate reduction methane becomes oxidised (Borowski et al., 1996). Hinrichs et al. (1999) and Boetius et al. (2000) found anaerobic oxidation of methane to be performed by a consortium of methanogenic archaea (operating in reverse) and sulphate reducing bacteria according to

$$SO_4^{2-} + CH_4 \rightarrow HCO_3^- + H_2O + HS^-$$

Sulphate originates from seawater, which acts as infinite source, methane rises from the sub-surface. The reaction itself occurs in a zone where both meet, called sulphate-methane interface (SMI). Its depth within the sediment is governed by the flux of methane, and to a minor extent of the sulphate's ability to enter the sediment. At very high methane fluxes the SMI may be at the seafloor. Fig. 1.9 shows schematic sulfate and methane profiles.
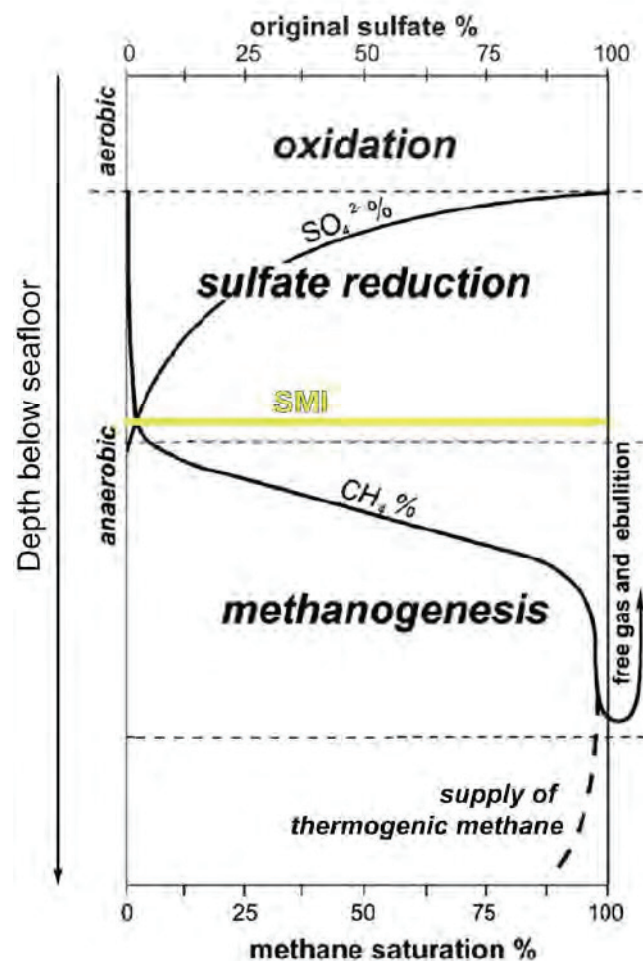
Fig. 1.9: Sulphate – methane interface (SMI): rising methane is oxidised by sulfate at the interface (modified from Campbell, 2006).

Carbonate builds up as waste product and may form irregular structures (Fig. 1.1c) or chimneys along pathways (Fig. 6.4.e). On the one hand side, this can be targeted in the search for seeps as it is distinctly different from non-seep sediment, see chapter 3. On the other hand, the carbonate remains unchanged at the seep, or extinguished seep, but still contains geochemical / isotope information records of the seeping fluids. The produced water dilutes the omnipresent salt composition of sea water. Therefore a chloride anomaly measured in pore water profiles can indicate the oxidation of methane.

Even though this work focuses on Geology and Geophysics, it is important to take a look on fauna on or close below the seafloor. Biological communities settle at cold seeps and make those places stand out against surrounding comparatively vast seafloor. The first reason to incorporate Biology is the dependence of several specialised species on fluid flow to nourish them. Flow rates are represented by species distribution and/or density of settlement (Sahling et al., 2002). Colonised patches therefore represent places fluid escapes on the seafloor, as biological production is related to fluid flow intensity (Sibuet and Olu, 1998). The second importance is the change of seafloor characteristics caused by the dwellers. By their sole presence on or close below the seafloor they increase roughness. Additionally, many of them precipitate authigenic carbonate as a residual product. Both roughness and carbonate as hard substrate are important factors to acoustical backscatter intensity.

The chemosynthetic life forms inhabiting seep sites exploit the chemical potential of rising fluids. The principle energy source is methane, and derived from its reduction by sulphate, sulphide (Sibuet and Olu, 1998). The sulphide in turn can be used by other macrofaunal species (Fisher, 1990). Bacteria alone, or higher life forms living in symbiosis with bacteria, feed on those methane and sulphide (e.g. Fiala-Médioni et al., 1993). Thereby they are independent of direct sunlight and photosynthesis for energy generation. They live on fossil fuels. The first to come into contact with locally present or rising fluids are microorganisms in pore space within the sediment. They might even trigger the ascent of fluids by their activity, e.g. by methanogenesis (Head et al., 2003). Fig. 1.10 shows an example of cold seep settlement according to fluid-feeding. Some characteristic communities are listed in order of increasing flow below. Sahling et al. (2002) reported them at Hydrate Ridge seeps in Cascadia. Jerosch et al. (2007) published a similar distribution for Hakon Mosby mud volcano.
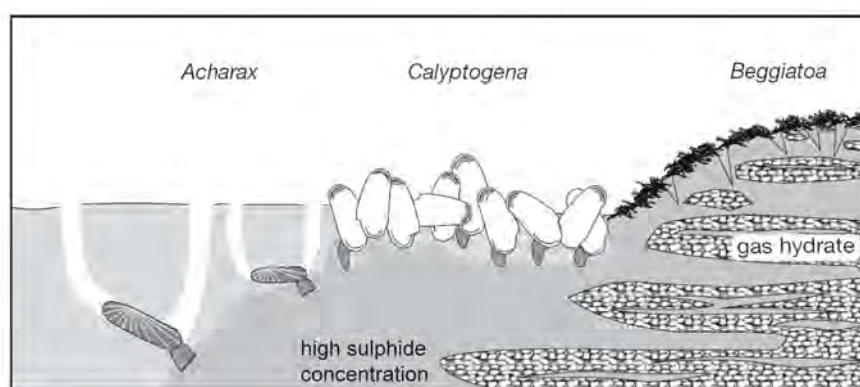
Fig. 1.10: Seep communities depend on fluid availability. Gas hydrate on the right hand side indicates the focus of seepage, to the left flow decreases and sulphide is only accessible with increasing depth (Sahling et al., 2002).

Lowest flow

- Solemyid clams (genus Acharax) (Carson et al., 1990; Sahling et al., 2002)

- Vesicomyid clams (genus Calyptogena) (Sahling et al., 2002)

- Mythilids mussels: (genus Bathymodiolus) (Sibuet and Olu, 1998)
   or thyasirid bivalves (Conchocele sp.) (Zonenshayn et al., 1987)
   or vestimentiferan tubeworms (siboglinidae) (Freytag et al., 2001)
   or pogonophoran tube worms (species Sclerolinum contortum and Oligobrachia
      haakonmosbiensis) (Jerosch et al., 2007)

- Bacteria (Beggiatoa) (Sahling et al., 2002; Jerosch et al., 2007)

Highest flow

Other non-seep related species are attracted by the seep community or the established hard grounds and add to the population.

1.5 Climate Impact

The frequent cold seep fluid methane has a large and persistent impact as greenhouse gas on temperatures of the atmosphere (Ramaswamy et al., 2001). For the past, during glacial and interglacials, a good correlation between temperature and atmospheric methane concentration was shown (Spahni et al., 2005). Influence of seepage on the atmospheric methane concentration cannot be certain for that period, but Hill et al. (2006) showed a good correlation of seep-activity (a tar-index) in the Santa Barbara Channel, California, with more seep-activity during warming periods. Sultan et al. (2004) and Mienert et al. (2005) show destabilisation of gas hydrate with warming bottom water at the Storrega Slide. Large amounts of gas hydrate must have been released during the slide.

However, the egg-hen problem applies for the gas hydrate and climate warming interconnection. Methane increases temperatures, but on the other hand, warmer temperatures trigger the release of methane from hydrates in melting permafrost (Walter et al., 2006; Walter et al., 2007) and destabilisation by the downward shift of the gas hydrate stability zone in the oceans (compare Fig. 1.6). Dickens et al. (1995) showed this case for the latest Palaeocene thermal maximum. In the present climate change, methane might be an element of a positive feedback (Houghton et al., 2001) and hence it is important to understand global methane fluxes. But does cold seep methane reach the atmosphere? Filtering by seep biology and water column oxidation reduce the amount (Boetius et al., 2000; Niemann et al., 2006). Various authors discuss on the transfer to the atmosphere and its significance (Kennett et al., 2003; Schmale et al., 2005; McGinnis et al., 2006; Artemov et al., 2007). Opposite to the problems caused in climate change, seeping hydrocarbon could be used beneficial.

1.6 Energy Resources

Surface seepage can indicate an active hydrocarbon system in the subsurface. Therefore, early oil-exploration techniques at the end of the 19th and early 20th century successfully located drill sites at known seeps. Those onshore activities proved to be profitable along the Gulf of Mexico coasts (Salvador, 1991). With continued development in exploration methods during the 20th century, the need to locate seep sites for successful reservoir discoveries ceased and hydrocarbon exploration became independent of the requirement to trace seeps. However, seeps continue to be geologically connected to deeper hydrocarbon generation. They may still be used as primary, comparable cheap, indicators in frontier oil provinces (Clark and Cleverly, 1991; Macgregor, 1993; Heggland, 1998; Abrams, 2005).

Apart from the hints surface manifestations give to hydrocarbon accumulations at depth, interest in shallow reservoirs, which are usually even closer related to seeps, grows in this time of peak-oil. Gas hydrate derived gas may replace conventional gas. Hydrate is widely dispersed within the seafloor (Boswell, 2009) on the one hand, but on the other hand there is a significant amount methane stored in shallow hydrate (Fig. 1.11) (Milkov, 2004). Whether it is economical to exploit those gas hydrates depends on their depositional and geological setting, the amount of hydrate in place, and distance to the market. Technological possibilities are already available, but the price on the market remains a key factor controlling production activities (Walsh et al., 2009). Test-drills are already completed, e.g., Mallik onshore in the Canadian Arctic (Dallimore et al., 2002; Weber et al., 2006) and offshore India by the Indian National Gas Hydrate Program (Collett et al., 2008).

The German research project 'SUGAR' (Submarine Gas hydrate Resources), started 2008, aims at the exploration, mining, and transport of natural gas from gas hydrates. It is a joint venture between academia and industry. Together, the possibility of replacing methane

by carbon dioxide within the clathrate cages without dissociating the hydrate, and therefore without destabilising the sediment, is tested (Geomar, 2010).
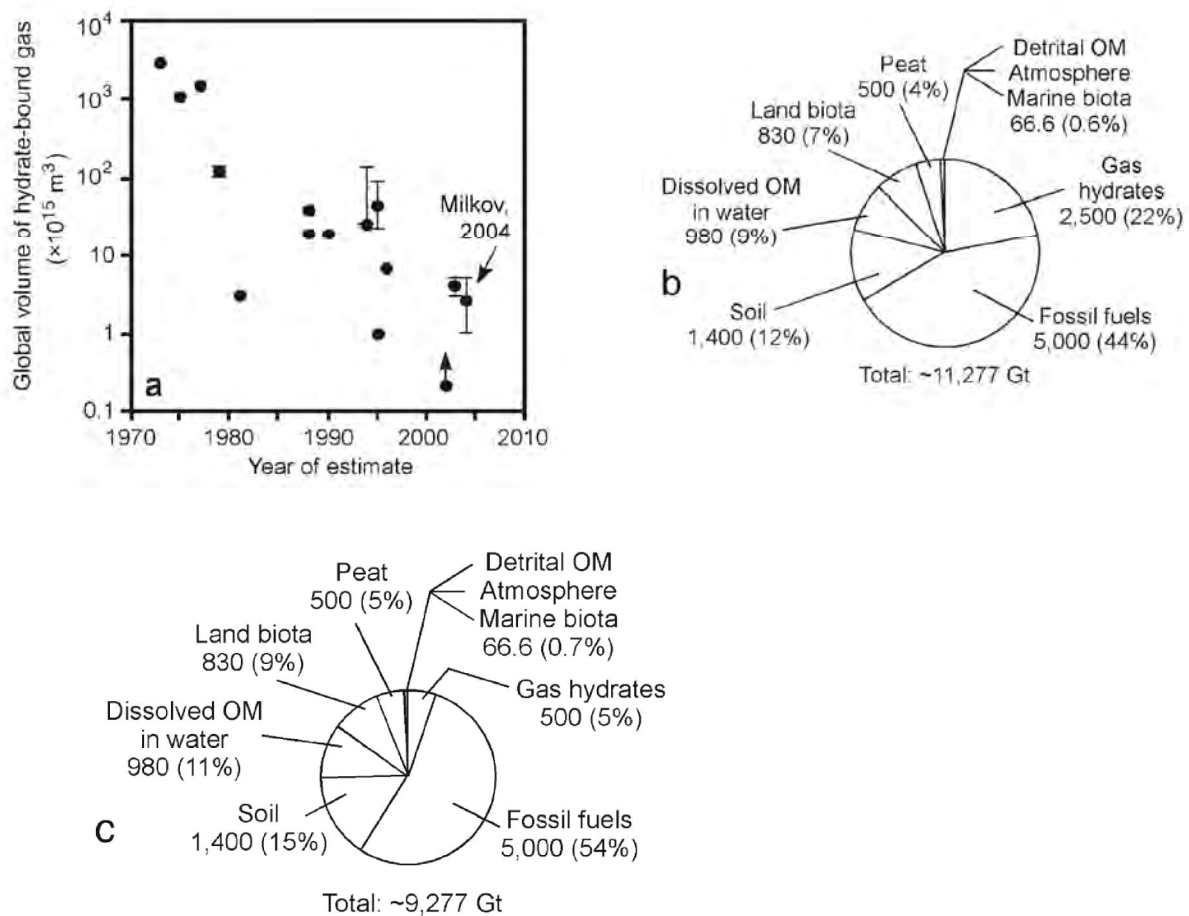
Fig. 1.11: Statistics of gas hydrate as energy resource. a) Estimate amount of stored gas was lowered with on-going research results. b) Organic carbon reservoirs on Earth (excluding dispersed kerogen and bitumen), plot with gas hydrate estimates at upper bound. c) Plot with gas hydrate estimate at lower bound (Milkov, 2004).

2

Motivation and Materials

2.1 Motivation

After cold seeps had been first discovered in 1984 they were found to be widespread at continental margins. Search for new seep sites keeps successful, now that the target characteristics are known and ever improving imaging techniques of reconnaissance are deployed. Cold seepage proved as pervasive and important feature in the cycling of carbon and other chemicals within the shallow sediment. With the emission of methane at many cold seeps they might play a role in climate changes. The relation to gas hydrate resources can be an important key to future natural gas exploitation. Cold seeps change the seafloor with a large variance in morphologic expressions. They are hotspots in deep-sea ecology with teeming life in an elsewhere vast desert. However, the research on cold seeps is still a young field and much more is to be understood. So far, many sites or regions had been covered by punctual observations or investigations on single topics. An overall understanding of the seep process requires still more research effort.

This work entitled "Acoustic and Visual Imaging of Active Seafloor Seepage in Various Deep-sea Environments" aims at the survey of seeps with end member fluids in different environmental settings. One fluid is highly viscous heavy petroleum, asphalt. Another is free gas, dominantly methane, escaping into anoxic waters. At those places it is to be understood, how these fluids shape the seep and influence the pristine seafloor. Other forms between the end members can then be interpreted aided by this work. Additionally, a section of a subduction zone is investigated to create a complete inventory of seep sites within the area.

This PhD project is focused on the mapping of the seafloor, but also the water column was scanned and sub-seafloor structures integrated to interpret seafloor features. Yet this is not sufficient to gain full understanding of seeps. Work areas were chosen world wide, in the southern Gulf of Mexico, the Black Sea, and the Makran offshore Pakistan to accomplish the tasks. Complementary work is done within other PhD projects as well as in the entire MARUM 'Seepage of Fluid and Gas' (E1), later restructured and renamed to 'Geo-Biosphere Interactions' (GB4). The PhD project of Feng Ding looking at the sub-surface structures in "Near-surface Sediment Structures at Cold Seeps and their Physical Control on Seepage: A Geophysical and Geological Study in the Southern Gulf of Mexico and at the frontal Makran Accretionary Prism/Pakistan" (Ding, 2008b) and this thesis complement each other. Three publications written by F. Ding and co-authored by M. Brüning are included in the appendix: Ding et al. (2008a) (attached as A1), Ding et al. (2010b) (attached as A2), and Ding et al. (2010a) (attached as A3).

This work was motivated by the following:

Upon the discovery in 2003 scientists in the Gulf of Mexico were surprised by the presence, appearance, and large extend of observed solidified asphalt material on the seafloor. Its surface morphologies indicate spreading into different directions. Away from flow morphologies other asphalts appeared weathered, with rough surface patterns. Morphologies remind the viewer of pahoehoe-type basaltic lava, extruded in a hot and molten state (Bohrmann and Schenk, 2004). The similarity between the asphalt flows and basaltic lava caused the scientists to speculate about a process during which hot or molten asphalt should extrude during several eruption-phases at the seafloor of the Gulf of Mexico which they termed asphalt volcanism (MacDonald et al., 2004). This new finding was commented in a short notice by other scientists who furthermore speculated about the potential involvement of supercritical water (Hovland et al., 2005). However, details of the asphalt were not known and there were many question marks. Major issues concern the characteristics of the asphalt discharge:

- In which state did the asphalt leak from the seafloor and how did it behave to attain its present appearance?
- Why settles asphalt on the seafloor, and is not floating off?
- What controls the flow direction? Is it topography / gravity?
- What is the extension of the asphalt occurrence and its link to general seepage of the knoll?

At Batumi Seep in the eastern Black Sea the other side end member is represented by release of light molecular weight gas. Sahling et al. (2004) found the vigorous gas emissions bubbling from an area of increased seafloor backscatter. The site is within the gas hydrate stability zone and due to anoxic conditions of the Black Sea lacks the biological settlement found elsewhere. Furthermore, there is no advection of liquids. Consequently, this is the ideal place to study the uncovered influence of gas seepage and gas hydrate presence on the pristine seafloor.

- What are the effects of a purely gas driven seep on the seafloor?
- How do the various seafloor morphologies evolve?
- Do they depend on different processes?
- Why do semi-circular structures evolve?
- Furthermore, is there an additional effect of shallow gas hydrate?
- Does the hydrate comprise a storage/retention system of the seepage?
- Does the seep change within a time-span of several years?
- Do backscatter pattern and gas hydrate content correlate?

The third research area offshore Pakistan, the Makran subduction zone, comprises the thickest accretionary wedge on Earth. Additionally, seasonal upwelling with high primary production results in the formation of an oxygen minimum zone within the water body. Both conditions in turn favour the accumulation of organic material rich sediments and hence production of hydrocarbons, which can seep off the seafloor. Research cruises in the 1970ies and 1980ies provided good seismic reflection survey-profiles of the sub-surface Geology. Both on- and offshore the Makran several cold seeps had been discovered. They include mud diapirs, mud volcanoes, seep molluscs, bacterial mats, authigenic carbonates, BSR, and increased methane concentrations of the sea water. However, so far no complete scan to create an inventory of all active seep sites exists. This thesis presents such a survey of a section of the continental margin to answer the following questions:

- What is the frequency of seeps along the margin?
- How are seeps distributed at the morphological features, canyons, ridges, and basins?
- Are there differences in the abundance of seeps at the upper slope, mid-slope terrace, lower slope, and on the oceanic plate?
- How does this accretionary case margin end member compare with the erosional case of Costa Rica and Nicaragua?

Is it possible to deduce a general classification scheme based on all the above tasks? Which is an appropriate structure? What are important variables governing seep patterns?

The following chapter provides details of the surveys undertaken to answer these questions.

2.2 Materials: Cruises

To face and fill the gaps explained above, this thesis integrates results from three marine research expeditions. Two, M67/2 and M74/2&3 were implemented in the RCOM/MARUM scheme, the third, M72/3 was part of the METRO project, which stands for 'Methane and methane hydrates within the Black Sea: Structural analyses, quantification, and impact of a dynamic methane reservoir'. The cruises abbreviations are formed by a letter for the deployed vessel: M – RV METEOR, and the consecutive cruise number and cruise leg letter.

M67/2a&b – Gulf of Mexico
The cruise was entitled 'Fluid seepage of Chile and in the Gulf of Mexico'. The Gulf part sailed from the port of Cristobal/Panama, paused once in Tampico/Mexico to exchange personnel and equipment, and ended on the island of Barbados (Fig. 2.1). The cruise lasted from 14 March 2006 to 25 April 2006. Objective of the cruise was to search the Campeche Knolls for (hydrocarbon) fluid seepage. It was the particular aim to investigate asphalt volcanism. During the first leg a multichannel seismic system was deployed and swath bathymetry surveys in combination with single beam echo sounding (as sub-bottom profiler and scanning the water column for gas bubbles) was carried out. The deep-towed side scan sonar failed for the most part of the cruise; it only provided data for six hours. The second leg was dominated by video observations and sampling by Remotely Operated Vehicle (MARUM's ROV QUEST 4000 m) at the Chapopote site. Besides that, geological sampling and TV-sled observations were conducted (Bohrmann et al., 2008b).
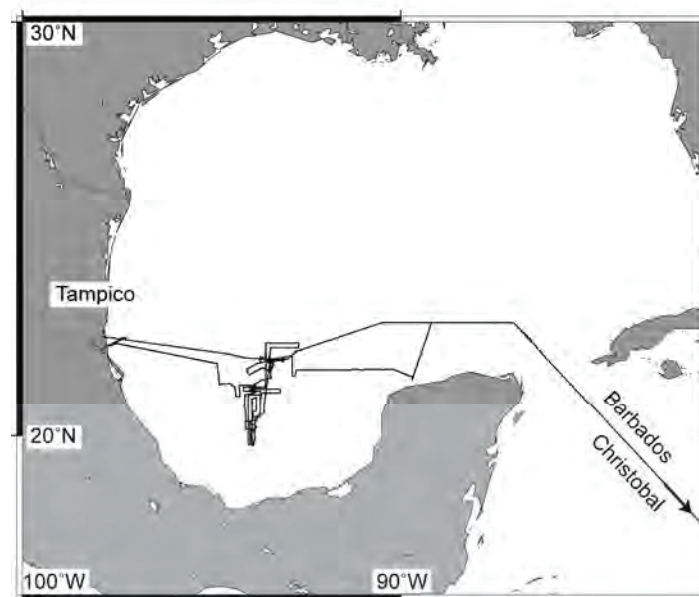
Fig. 2.1: M67/2 tracks in the southern Gulf of Mexico.

M72/3a&b – Black Sea
RV Meteor Cruise M72 addressed the 'Biogeochemistry, fluids, gas hydrates, and palaeo climate of the Black Sea'. Leg 3 (Fig. 2.2) commenced 16 March 2007 and ended 23 April 2007 in Istanbul/Turkey. There was one port call in Trabzon/Turkey for swapping scientists and instruments on 03 and 04 April 2007. The objectives of the cruise, besides others, were detailed investigations of the fluid seep sites offshore the town of Batumi in the eastern Black Sea. Target areas were Batumi Seep (gas quantification, sub-seafloor and seafloor mapping), as well as Colkheti Seep, and Pechori Mound. The applied methods were according to the M67/2 cruise. One difference was the reverse deployment of ROV and

acoustics: During the first leg seafloor observation and work was carried out with the ROV aided by mapping performed in earlier cruises (Sahling et al., 2004; Klaucke et al., 2006; Akhmetzhanov et al., 2007). While the second leg the GEOMAR's deep towed EDGETECH side scan sonar DTS was employed very successfully. Furthermore, a 3D seismic survey was run over Batumi Seep. Sediments and gas hydrates were sampled by the Dynamic Autoclave Piston Corer (DAPC) (Abegg et al., 2008). During both legs innumerable gas bubble streams escaping the seep were recorded in single and multibeam sonars (Bohrmann et al., 2007).
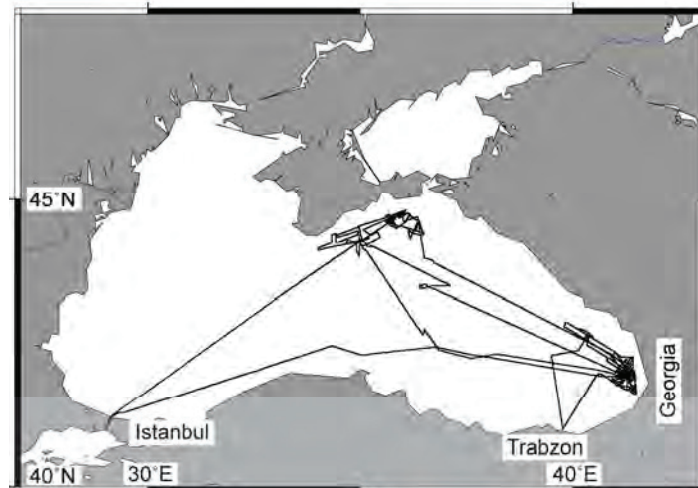
Fig. 2.2: M72/3 tracks in the Black Sea.

M74/ 2&3 – Makran

Leg 2 of Cruise M74 'Nitrogen cycle, cold seeps, carbonate platform development in the northwestern Indian Ocean' started and finished in Fujairah/UAE. It lasted from 07 October till 29 October 2007. The third leg ended in Male/Maldives on 27 November 2007 (Fig. 2.3). The cruise aimed at the continental slope of Pakistan as part of the Makran subduction zone. Objective was the characterisation of cold seepage in a section of the slope, from the shelf edge down to the oceanic plate. Swath mapping, deep towed side scan sonar (NOC's Towed Ocean Bottom Instrument, TOBI), multichannel seismics, single beam echo sounder, and TV sled surveys were applied during the first leg (Spiess et al., 2010). For the second leg side scan and seismics were exchanged by MARUM's ROV Quest. Acoustically discovered seeps in water depth between 550 and 2900 m were visited by TV sled and ROV dives (Bohrmann et al., 2008a).
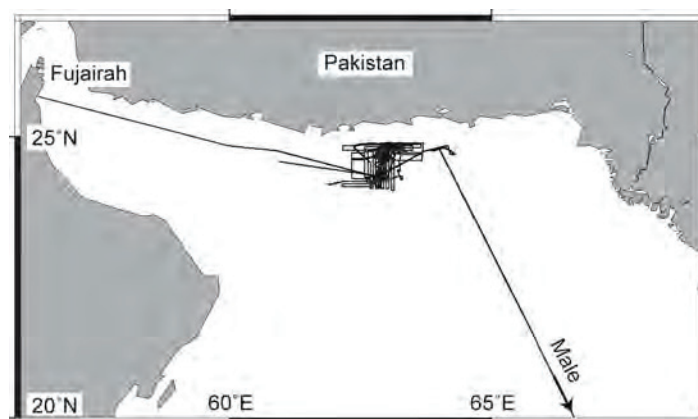
Fig. 2.3: M74/ 2&3 tracks in the Indian Ocean.

Various survey, observation, and sampling methods had been mentioned so far. There is a whole suit of them complementing each other. Partially they also rely on each other. Acoustic methods work generally on scales of kilometre to metre, whereas visual observations and sampling continue the imaging on metre to millimetre scale. The following chapter provides detailed explanations on the individual principles and instruments.

3

Methods

This chapter provides an overview of the various methods deployed to gather data for this thesis. Nevertheless, it does not claim to be as detailed as textbooks on the single topics (Telford et al., 1990; Kearey and Brooks, 1991; Urick, 1983; Blondel and Murton, 1997; Lurton, 2002) Chapters 5 − 7 contain some more specific descriptions of the instruments involved.

3.1 Desktop Study

Preceding to field surveys, investigations aiming at the collection of all available data of an area should be performed. Local institutes, geological surveys of the neighbouring nations, or internationally active research institutes could provide important and valuable data bases. In the Gulf of Mexico the regionally experienced researchers E. Escobar Briones and I.R. MacDonald were involved in the work. For the eastern Black Sea H. Sahling and I. Klaucke, who joined the earlier discovery cruise, took also part in the present one. Industry, here especially the energy sector, might be the best informed instance. However, their data is usually confidential and not available to public research. Apart from those regional studies, the utilisation of scientific publications is an inherent part of this research.

3.2 Positioning

All measurements and observations at sea need the information of their precise location to allow any further interpretation and judgement. Today the Global Positioning System (GPS) allows simple and reliable positioning with accuracies of several metres by calculating the receivers position relative to several satellites. Differential GPS (DGPS) yields even better accuracy of sub-metre accuracy for the deployed C-Nav (C & C Technologies, 2010) by applying a correction to the original GPS signal.

Because GPS only works above water, underwater a similar, but acoustic principle is applied. Travel times between a mobile pinger fixed to the submerged instrument and four receivers fixed to the vessel are calculated to position the pinger with direction and distance relative to the vessel. The system is named Ultra Short Base Line (USBL) due to the small offset between its receivers. An IXSEA POSIDONIA USBL system delivered positions during the cruises of this thesis. Limitations and errors are discussed below in chapter 3.4.2.1. At very large offsets of several kilometres the towed USBL does not work. Then the only way to determine instruments positions is a calculation of layback and position based on cable length to the instrument and vessel positions.

3.3 Satellite Based Radar

A relatively fast search for seeps with global coverage is the use of Satellite Synthetic Aperture Radar (SAR). It can detect oil slicks on the water surface due to the suppression of small scale surface ripples under the surfactant. Horizontal resolution is, e.g. for RADARSAT-1 8 to 100 m (Geo Community, 2010). Repeated observations of slicks are necessary to differentiate between anthropogenic pollution or seep sources. Slicks repeatedly occurring downwind from one point indicate seep sites. Application of SAR for this work belongs to desktop study and cooperation. Broad work had been done with SAR in the Gulf of Mexico (MacDonald et al., 1993; De Beukelaer et al, 2003; Garcia and MacDonald, 2008). Slicks had

also been observed in the eastern Black Sea and south of Pakistan (MacDonald and Garcia, pers.com, 2007).

3.4 Acoustical Surveys

3.4.1 Basics – Physics of Sound in Water

As we can all see – we cannot see deep into water. Shallow water is often too muddy, off-shelf water is pretty and clean to see 10s of metres deep. But there the seafloor of interest is far deeper. Light, electromagnetic waves, which human eyes recognise does not penetrate to the desired depth of interest. The attenuation of electromagnetic waves in water is too large. Therefore another kind of wave is utilised to research the deeper oceans, acoustics waves, compressive waves, travelling by the interaction between water molecules. The attenuation of water waves is negligible ~0.001 dB/km/Hz (Stoll, 1985), hence the full ocean depth can be investigated. However, there is still a drawback. The decrease in amplitude along a ray-path is proportional to the wave's frequency. And high frequencies with appropriate short wavelength are required to obtain a high resolution on the target. As a consequence, to achieve the desired detailed imaging on fluid seep sites (centimetre to millimetre resolution), an appropriate approach is required: long-range acoustic waves can detect areas of interest from surface vessels, but for their detailed studies it is necessary to reduce the source – target – detector distance and lower instrument platforms closer to the seafloor. There acoustical surveys of centimetre resolution and visual inspections yield observations to describe fluid seepage with the desired details. The following chapters give a brief overview of the methods important for this thesis.

3.4.2 Sonars

SONAR - SOund Navigation And Ranging was developed starting after the Titanic accident 1912 (Lurton, 2002). Transmitting and receiving acoustical waves using electronics was a revolution after thousands of years of depth measurements by lead line. But for a long time, depths were only measured below the sonar device with a single beam. A multitude of different sonar types, brands, and models emerged. Today transmitters are usually made of piezo-electric elements, which transform electrical voltages into mechanical waves transmitted into the water column. Tab. 3.1 provides an overview of sonars applied for this work. Transducers appear installed as flat dark, plastic sealed plates in vessel hulls or on tow-fishes. A second large development was the introduction of multibeam echo sounders in the 1970ies, which measure a swath of multiple soundings perpendicular to a vessels track. Opposite to those depth point measurement tools, sidescan sonars survey the seafloor-surface characteristics, and sub-bottom profilers and seismic systems the sub-seafloor as 2D slices.

3.4.2.1 Swath Bathymetry
The intention to do swath bathymetry is the survey of a wide fan, not only one track, as a survey vessel is under way. The wide swath yields an increased coverage per time, allowing surveying the seafloor's topography, the bathymetry, time efficient and with good resolution. The sonar swath is formed by multiple beams. Actually, the sonar transducer sends out a ping with wide opening angle across the vessel's track. Its returns from the seafloor are detected by a second transducer, which is installed perpendicular to the former. This setup is named 'mill cross' installation. The angle between both allows directed transmission with narrow beam

width along track, and for the following receiving specific detection of single sections of the returns. Consequently the measured returns are assigned to narrow fields of a few degrees opening angle as shown in Fig. 3.1. Received acoustic waves are transformed back to a voltage time series. A computer algorithm then automatically recognises the return from the seafloor by amplitude or phase information. The water depth is calculated applying a sound velocity profile. This profile has to be measured separately. Combining the measured distance between sonar and seafloor with the beam angle and GPS position, the shape of the seafloor can be imaged. Table 3.1 provides technical details of the KONGSBERG EM120 and EM710 multibeam sonars used to acquire data presented in this work. Data coverage depends on the performance and settings of the multibeam sonar, number of beams, swath width, survey speed, and water depth. Limitations in horizontal resolution are set by the beam angle which sets the footprint size. Vertical errors can originate from penetration of the sound waves into the seafloor and an incorrect sound velocity profile. The latter would in turn cause a horizontal deviation, if refraction of the sound waves occurs in water.

Raw data need to be processed for map presentation. Software employed for this was IFREMER's CARAIBES and MBARI's MB-SYSTEM. The processing consists of deleting bad data points, possibly by automatic algorithms. Cleaned data is assigned to grid cells, depth values therein averaged to obtain an more accurate depth per cell. The resulting grid of individual cell values can be plotted in different ways: colour coded, contoured, or in 3D. Generally the software GENERIC MAPPING TOOL (GMT) was used for this. Other possibilities are ESRI's ARCGIS for data integration, and IVS's FLEDERMAUS for 3D presentation. Table 3.1 shows small examples of swath bathymetry maps. Many more are included in chapters 5 - 7.
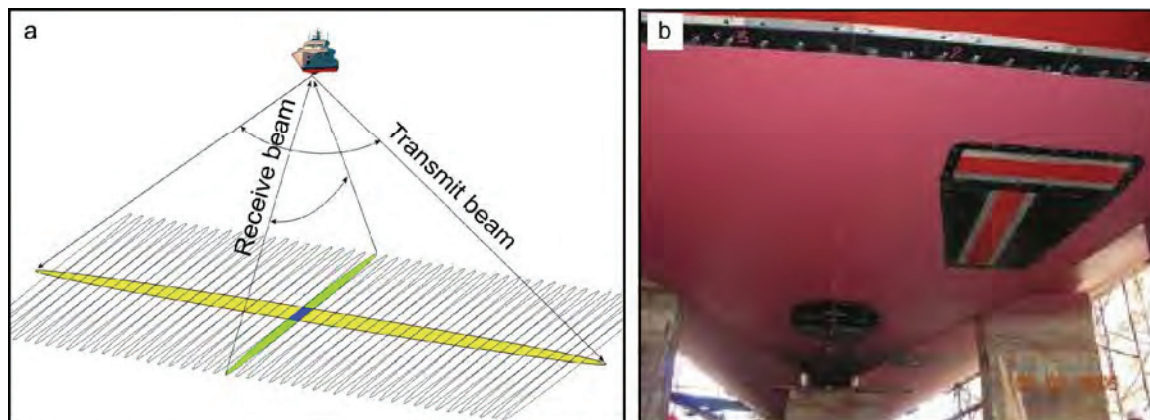
Fig. 3.1: Principle of multibeam sonar, transmission and reception with perpendicular orientation results in punctual depth measurements. a) Swaths in the water column (Applied Microsystems, 2009). b) T-shaped mill cross installation of EM710 tranducer and receiver in hull of RV Meteor (Leitstelle Meteor, ship yard report 8, 2006).

3.4.2.2 Single Beam Echo Sounder

Single beam echo sounders were deployed for certain applications. An ATLAS PARASOUND parametric echo sounders was used, first, as sediment echo sounder to scan the shallow subsurface, and, secondly, to detect gas bubbles within the water column. The system transmits two primary signals of 18 and 22 kHz. When employing it as sediment echo sounder, one makes use of the parametric effect of the two superimposed waves that result in an effective secondary signal of the difference frequency, 4 kHz, confined in the narrow transmission cone of the 18 kHz signal. A pure 4 kHz wave would have a larger opening angle and hence worse lateral resolution. The diameter of PARASOUND's footprint is about 7 % of the water depth. The wave penetrates up to 150 m into the seafloor and reflections

resolve sediment structures as a 2D slice along the vessel's track. The high primary frequency of 18 kHz was utilised for the bubble detection. The procedure was published by Nikolovska et al. (2008). Free gas reflects the incident acoustic energy and rising bubble streams show up as elongated, flare-shaped reflections in echograms. Table 3.1 contains more technical details on the PARASOUND system. PARASOUND data was plotted by H. v. Lom-Keil's SENT software. Table 3.1 presents examples of a seep recorded in both frequencies.

Another kind of sonar application is multichannel seismics. There, opposite to the hull mounted kinds above, the entire system is dragged behind the ship. A seismic source, often an air gun, generates high-energy un-directed acoustic waves, which reflections from the seafloor and sub-seafloor layers are recorded by a long chain of hydrophones inside a streamer pulled behind the vessel. During processing, echograms of the single channels are stacked to obtain a better signal to noise ratio and a clearer profile of sub-seafloor reflectors.

3.4.2.3 Side Scan Sonar

Side scan sonar records intrinsic characteristics of the seafloor surface, which the previously mentioned methods lack. The boundary between solid but permeable sediments and liquid water column is an important interface for geochemical processes and biological colonisation in this work. Hence, the precise knowledge of material properties and localities plays a major role. Side scan sonar devices emit an acoustic pulse of a certain length and then register a continuous record of the returning waves. The instrument is ideally towed 10 – 15 % of the horizontal range above the seafloor. Emitted waves can be reflected, but the method focuses on the backscattered part of the wave energy. Depending on the incident angle, different properties contribute in different proportions to the total backscatter intensity of an seafloor area: geometry, i.e. the angle of seafloor to the incident wave; material, i.e. hard or soft materials reflect or attenuate wave energy; roughness: rough surfaces reflect / scatter incident energy in many direction, whereas smooth surfaces reflect in only one direction according to Snell's law. Fig. 3.2 shows their relative importance in relation to seafloor characteristics and incident angles.

Data are presented as monochrome pixel lines across the sonar's track. Added up along track, they provide an imagery of the seafloor. Tab. 3.1, Fig. 6.2b,c and 7.3 show examples of side scan imagery. Side scan sonar models deployed in relation to this thesis cover reconnaissance as well as detail study tasks. The Towed Ocean Bottom Instrument (TOBI) (Fig. 3.3 a) was developed by the Southampton Oceanography Centre (SOC) and carried a long-range 30 kHz side scan sonar with 3 km range. It was hauled about 500 m above the seafloor. Processing was performed with the software PRISM (Le Bas, 1997) and LEICA ERDAS. It resulted in an imagery map with 3 m pixel size covering an entire continental slope. On an intermediate scale, the GEOMAR's EDGETECH DTS-1 (Fig. 3.3 b) was deployed. It had 750 m range, sounding at 75 kHz 100 m above the seafloor. The higher frequency of this model and decreased distance to the ground allowed production of 1 m pixel size imagery. Finally, for detail surveys the 410 kHz signal of the DTS-1 was used. Range was decreased to 100 m and altitude above ground to 10 m. This proximity and high frequency yielded imagery with 0.25 m pixel size. Processing of the DTS data was done with both IFREMER's CARAIBES and PRISM software. Limitations of side scan sonars occur due to the directional illumination the seafloor. Some geometrical structures aligned with incident rays may not be imaged. Bathymetrical highs can prevent sonar rays reaching the seafloor behind them. Due to the spreading of emitted signals, footprint sizes vary with distance to the fish: small in the vicinity, but large at far range. Processing then integrates measured data to fit into a raster. A major part is image enhancement by track-smoothing and filtering. The final image portraits the characteristics and shapes of the seafloor monochrome with illumination to both sides of the sonar track.
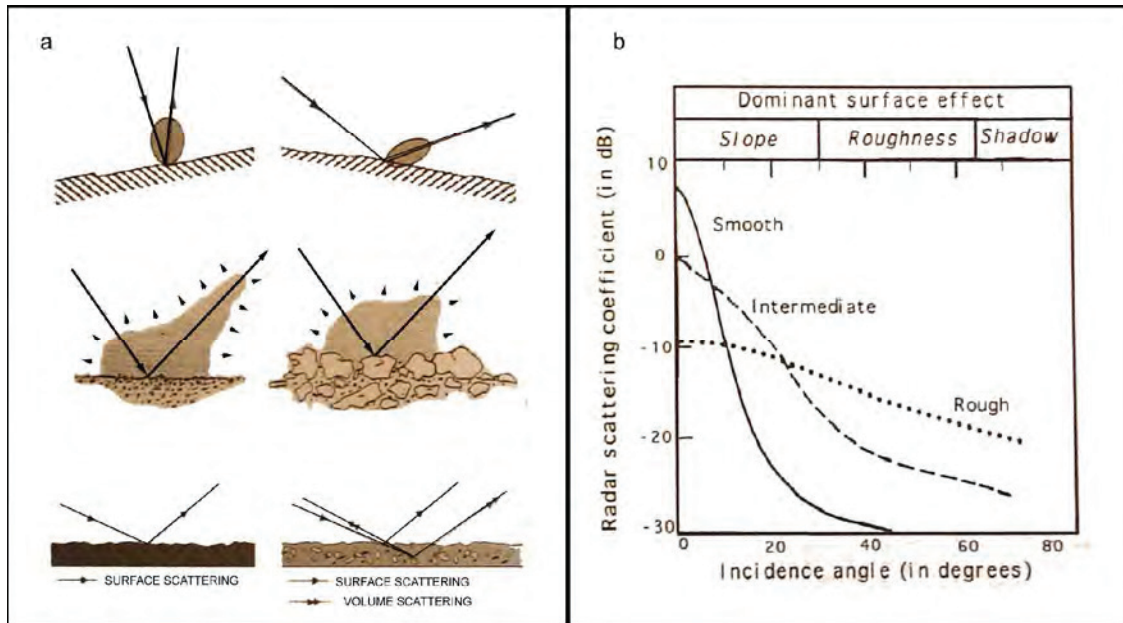
Fig. 3.2: Principle of acoustic backscatter. a) Black sound rays and brown backscatter 'clouds'. Top line: smooth seafloor, Snells' law. Middle line: fine and coarse grained seafloor. Bottom line: Surface and volume scattering. b) Relative importance of geometry, roughness, and material (Blondel and Murton, 1997).
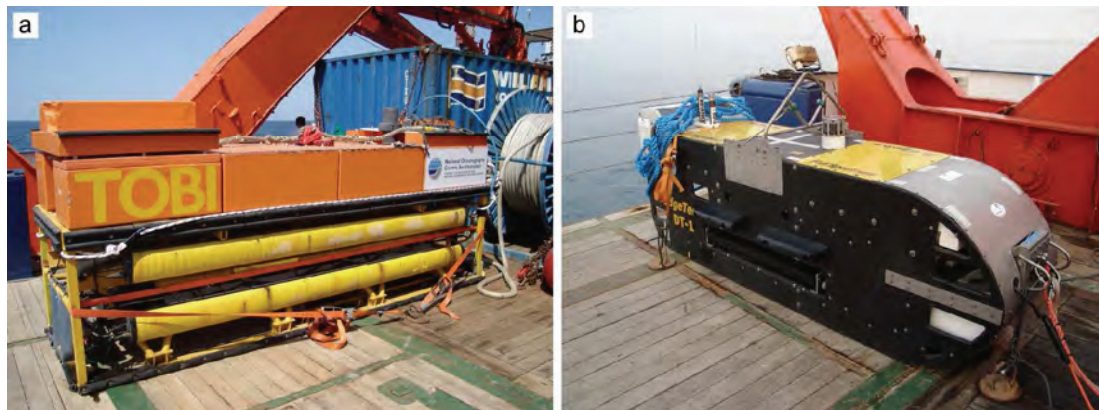
Fig. 3.3: a) TOBI 30 kHz side scan sonar. The vehicle weighs 2200 kg in air and is 4.5 m long. b) EdgeTech DTS-1 75 and 410 kHz side scan sonar. The fish weighs 910 kg in air and is 3.05 m long.

3.3.2.4 Forward looking sonar
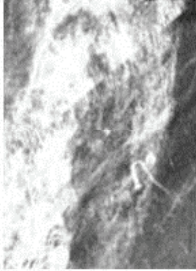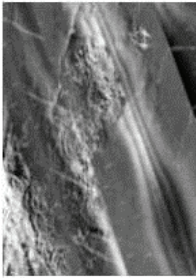
As a special deployment of sonar, the forward looking sonar was used to detect bubbles rising in the water column. The device is a KONGSBERG 625 kHz sonar with 50 m range installed in horizontal orientation. It was mounted on a Remotely Operated Vehicle, originally planned as obstacle avoidance aid. The large impedance contrast between water and gas produced very good reflections, allowing navigation to active seep sites solely by the search for those reflections in the water column (Nikolovska et al., 2008).

Summarising, Fig. 3.4 provides an overview of the various hull mounted and towed systems deployed from a research vessel.

Tab. 3.1: Sonars deployed during surveys for this thesis. (Le Bas, 2002; Atlas Hydrographic, 2004; Kongsberg, 2005a; Kongsberg, 2005b; EdgeTech, 2010).

		Multibeam		Singlebeam	
Manufacturer		Kongsberg	Kongsberg	Atlas Hydrographic	Atlas Hydrographic
Model		EM120	EM710	PARASOUND	PARASOUND
Installation		hull mounted	hull mounted	hull mounted	hull mounted
Frequency	[kHz]	12	70-100	4	18
Wave length	[m]	0.125	0.02-0.015	0.375	0.083
Range	[m]	12000	2000	10000	10000
Beam opening	[°]	1x2 per individual beam, 140° swath	1x1 per individual beam, 140° swath	4	4
No. of beams		191	400	1	1
Resolution	[m]			0.15	0.02
Processing cell / pixel size	[m]	20-100	5-100	0.1	0.02
Example		3 x 4 km, grid cell size 50 m, rainbow colour scheme, shading	1 x 1.4 km, grid cell size 8 m, rainbow colour scheme, shading	100 m	400 m

Images show same 2.2 km profile in 4 kHz and 18 kHz

Tab. 3.1 (cont.)

		Side scan		
Manufacturer		EdgeTech	EdgeTech	NOC
Model		DTS-1 75	DTS-1 410	TOBI
Installation		towfish	towfish	towfish
Frequency	[kHz]	75	410	30
Wave length	[m]	0.02	0.0037	0.05
Range	[m]	750	100	1500
Beam opening	[°]	1.3x75	0.75x75	0.8 x 45
No. of beams		2	2	2
Resolution	[m]	0.1x1.3	0.018x0.2	3x5
Processing cell / pixel size	[m]	1	0.25	3
Example		0.5 x 0.7 km	0.5 x 0.7 km	5 x 7 km

Fig. 3.4: Schematic sketch of different sonars deployed from a vessel: Single beach echo sounder, multibeam echo sounder, seismic reflection profiling, and side scan sonar (USGS, 2010).

3.5 Visual Observations

Only a visual observation of the seafloor provides highest resolution, best impression, and understanding of the seafloor environment (compare Fig. 1.1). However, visual inspections are far more time consuming than sonar surveys. Especially here, as said in the first paragraph of the chapter, the instrument has to be close to the target. Therefore visual observations should be used to ground-truth sonar data, at e.g. different appearances of side scan imagery maps. TV, or also called video, sled surveys are simple and require little personnel. On the other side, Remotely Operated Vehicle (ROV) dives yield the best state of the art examination in terms of observation, manoeuvrability, and according sampling. They are at the same time cost- and staff-intensive operations.

3.5.1 TV Sled

A TV sled is usually the first optical device deployed to inspect the seafloor. It is usually run along transects, where seepage is expected from other information sources. The sled contains a down-looking camera, lights, eventually scaling lasers and USBL transponder, all mounted in a robust frame and connected to a surface vessel by a data transmitting cable (Fig. 3.5). It follows the track run by the vessel. Contrary to the name, the system hovers about 2 m above the seafloor to collect its images. The deployed model was manufactured by OCTOPUS, Kiel. Onboard the TV stream is recorded, observed, and checked for consistencies with sonar data and cold seepage influence. It was possible to discriminate between seafloor with and without indications for seepage. Carbonate structures and chemosynthetic communities like bivalve beds, for example, appeared as a distinctive contrast to homogenous flat seafloor sediments (Fig. 3.6).
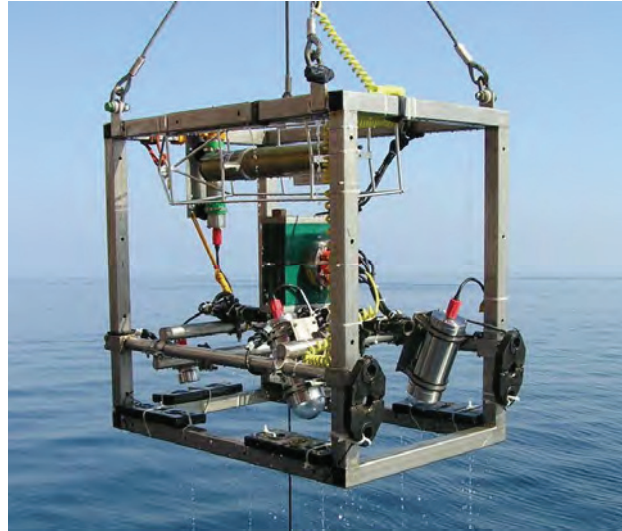
Fig. 3.5: Octopus TV sled. 1.2 x 0.8 m base area. Installed are (top to bottom) CTD, telemetry, lamps and camera.
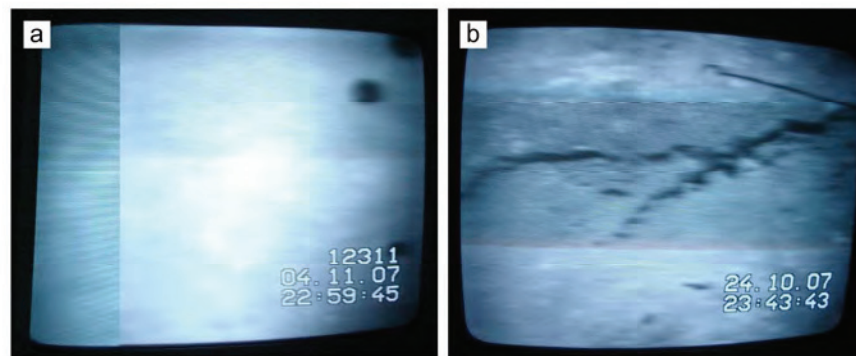
Fig. 3.6: Screenshots of TV sled images. a) hemipelagic, non-seep seafloor (with sea urchin). Image is about 1.5 m wide. b) Seep carbonates and clams. Image is about 2.5 m wide.

3.5.2 Remotely Operated Vehicle

Remotely Operated Vehicles (ROVs) offer the possibility to manoeuvre levitating self-propelled close to the seafloor. Besides necessary lights and camera, they can carry a variety of manipulators, instruments, and survey equipment. All those equipment can be deployed under visually controlled conditions. ROVs are connected to surface vessel via cable and remotely supervised from there. The ROV contributing to this thesis was MARUM's work-class ROV QUEST 4000 m, made by SCHILLING ROBOTICS. It carried 3 cameras, 2 manipulator arms, a forward looking sonar, an USBL pinger, and various exchangeable instruments. Even though ROVs offer an unique possibility to work in the deep sea, there are still limits: visibility is limited to around 20 m, but can be further reduced, if soft sediment becomes stirred into the water. As ROVs hover freely in the water, it stays a challenge to move precisely and quickly. Especially in large water depth (>2000 m) the error of USBL becomes important in relation to the achieved visual resolution. Navigation data sometimes do not fit to directions moved according to video sequences. ROVs provide detailed video coverage, high resolution photographs, and samples taken from hotspots of cold seepage. Chapters 5,6, and 7

contain a number of high resolution images: Fig. 5.5, 5.6, 6.4, 7.6, 7.7. Fig. 5.8 is a mosaic created from videostream. Fig. 3.7 shows ROV QUEST upon deployment.

Fig. 3.7: Work-class ROV QUEST 4000 m. 3.5 t weight in air, 3.3 m length
(Photo courtesy V. Diekamp)

3.6 Geological Sampling

The above mentioned methods yield results, which partially require further calibration or ground truthing to ascertain ambiguous geophysical methods. Several devices can recover samples from the seafloor. The following ones had been used to collect sediment cores in connection with work on this thesis: Gravity Corers (GC), MUlti Corers (MUC), Dynamic Autoclave Piston Corer (DAPC), and Push Cores (PC). Tab. 3.2 shows an overview of typical technical specifications and photographs. A GC consists of a core barrel, which is lowered to the seafloor on a wire and is pushed into the ground by the gravity of the attached weight. A solid plastic liner or foil inside the outer metal core barrel contains the sediment sample. The MUC targets on smaller, but undisturbed samples of the seafloor sediment and bottom water. It consists of several plastic tubes mounted in a stable frame. The frame lands on the seafloor and ensures stable conditions for sediment penetration. The DAPC is a special kind of piston corer. A piston corer freely falls the last metres until sediment penetration and then sucks material, assisted by the movement of a piston, into the core barrel. The DAPC then transfers the core into a pressure tight chamber to recover it under in situ pressure to the vessel (Abegg et al., 2008). PCs are plastic tubes with a handle at the closed end. They are operated by the ROV's manipulator arm to collect samples precisely from spots of interest.

Tab. 3.2: Sampling devices

	MUC	GC	DAPC	PC
	MUlti Corer	Gravity Corer	Dynamic Autoclave Piston Corer	Push Corer
	vessel based	vessel based	vessel based	ROV based
Core length	50 cm	3, 6, 9, or 12	2.5	31 cm
Core diameter	10 cm	14 cm	8.4 cm	8 cm
Target	Undisturbed surface sediment	Long sequences, stratigraphy, gas hydrates	In situ pressure samples, gas hydrate preservation	Precise location of cores
	Photo courtesy V. Diekamp	Photo courtesy V. Diekamp		

(Abegg et al., 2008; Bohrmann et al., 2008a)

3.7 Data Integration

All the previous methods yield differently scaled 3D to 1D results. They need to be combined and be presented appropriately to allow sophisticated interpretation. A Geo Information System (GIS) as special software, e.g. ESRI Arc GIS, is applied to integrate the various datasets by doing overlays, drawings, online, or printed. It is then the human, assisted by machines, to find an interpretation and story on the records.

4

Regional Settings

Three dissimilar locations have been selected as working areas to collect data for this thesis. First, resembling special end members of the seepage process, and, secondly to quantify the number of seeps occurring along a section of a continental margin. Very heavy, extremely viscous, almost solid and immobile hydrocarbons seeping from the seafloor can be found at one location in the deep sea. It is named Chapopote and located in the southern Gulf of Mexico. Such kind of deep-sea seep was only discovered a short time before the start of this project (MacDonald et al., 2004). On the other end of the spectrum, light, low viscous fluids are represented by one seep site, where almost only the gas methane (CH_4) bubbles from the seafloor. The site in the eastern Black Sea offshore Georgia, called Batumi Seep (Klaucke et al., 2006), was selected for this purpose. Finally, a section of the accretionary prism offshore Pakistan, named Makran, served as location to quantify a density of seeps per kilometre of slope. Seeps have been reported in the area before by several authors, but their distribution and number remained unclear.

4.1 Southern Gulf of Mexico

The Chapopote asphalt site is located on a knoll rising 400 m above the abyssal plain. The Chapopote Knoll is one of the Campeche Knolls stretching in the Campeche Bay (Fig. 4.1). The Campeche Knolls are bordered to the north by the Sigsbee Abyssal plain, to the west by a flatter and deeper seafloor section, the Veracruz Tongue, to the south by the shallow shelf and Mexican coast, and to the east by the Banco de Campeche, as part of the carbonate platform of Yucatan (Bryant et al., 1991). The hummocky surface of the Campeche region was created by salt diapir activity (Bryant, 1991). The salt is present in the entire slope area of the Bay of Campeche. In the south and central part of the Campeche Knolls the salt formed many diapiric ridges with around 1 km of heavily deformed sediments remaining on top. To the north salt domes are more separated and pierce the seafloor. Numerous isolated hills or knolls were formed (Bryant, 1991). The evaporate deposits date back to late Triassic time, when opening coincided with temporarily flooding of the basin creating those deposits widespread (Salvador, 1991). The main opening of the gulf happened after the salt-formation. Therefore, today two separated salt tectonic influenced regions exist in the northern and southern Gulf (Bryant et al., 1991). Since Late Jurassic the basin was geologically stable, besides continuous subsidence. An up to 15 km thick sequence of, mostly marine, sediments accumulated (Salvador, 1991). It provides good petroleum source rocks, especially those sediments of latest Jurassic and Cretaceous age (Magoon et al., 2001). Following the deformation, migration of hydrocarbons from source rocks to local highs occurred. Accordingly, several oil fields are producing. They are located close to the shore and are related to salt tectonic features. (Meiburg, 1995; Guzmán-Vega et al., 2001). Leakages of oil from the seafloor were proven by MacDonald et al. (2004) by the repeated detection of localised oil slicks in SAR satellite data. They coincide with elevations of the Campeche Knolls. At one of those sea surface slick locations the Chapopote asphalt site was discovered during RV SONNE expedition 174 (Bohrmann and Schenk, 2004). Even though, the discovery of asphalt deposits at Chapopote made this kind of seep popular and the term 'asphalt volcanism' was created (MacDonald et al., 2004), other knolls accommodate the same material. Seafloor asphalt was first reported by Pequegnat and Jeffrey (1979) at the Sigsbee Knolls. Side scan sonar and TV sled profiles proved occurrence of asphalt at the knoll 30 km south of Chapopote Knoll (Fig. 4.2). Following the work at Chapopote in 2006 a cruise of RV JUSTO SIERRA found asphalts at several knolls and ridges in the area (MacDonald, 2007). Therefore, it can be concluded that asphalt volcanism is a frequent process of seepage in the southern Gulf of Mexico.
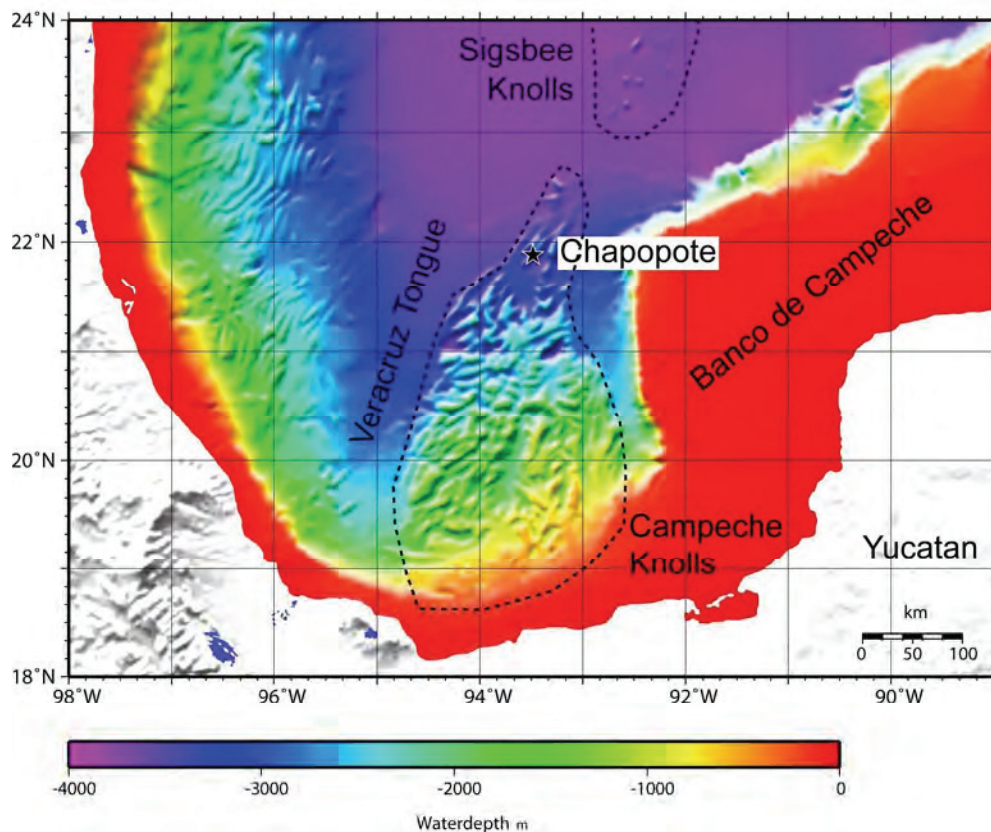
Fig. 4.1: Regional setting southern Gulf of Mexico. Chapopote is one of the Campeche Knolls. Data source: GEBCO, Digital Atlas, 2003.
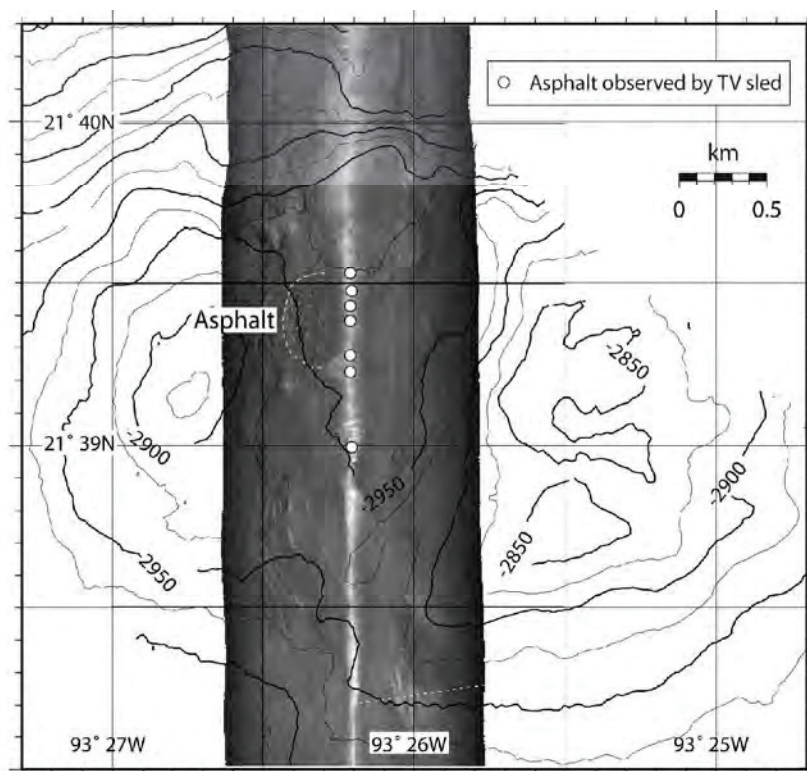
Fig. 4.2: Asphalt at Knoll 2139 30 km south of Chapopote. DTS side scan sonar profile crossing a central depression at the top of the knoll. High backscatter is white. Asphalt signatures are located within the half circle. White dots mark asphalt observed by TV sled.

37

4.2 Eastern Black Sea

The Black Sea is known for its many cold seeps (Egorov et al., 2003; Klaucke et al., 2006; Naudts et al., 2006; Artemov et al., 2007). There are mud volcanoes (Krastel et al., 2003; Wagner-Friedrichs et al., 2008) as well as pure gas seeps (Artemov et al., 2007; Naudts et al, 2008). The abundance of seeps is triggered by the favoured preservation of organic matter due to anoxic conditions in the water mass below 100 – 200 m (Deuser, 1974). Buried carbon is eventually converted to methane (compare chapter 1.3.2.3 and 1.4). In the eastern Black Sea, sediments accumulate in the Rioni Basin, which is enclosed by the Greater Causacus and the Achara-Trialet Thrust Belt mountain chains as shown in Fig 4.3 (Robinson et al., 1997). Several seeps without sediment material transport had been found in the marine part of the Rioni Basin (Klaucke et al., 2006). Batumi Seep is one of those seeps offshore Georgia.
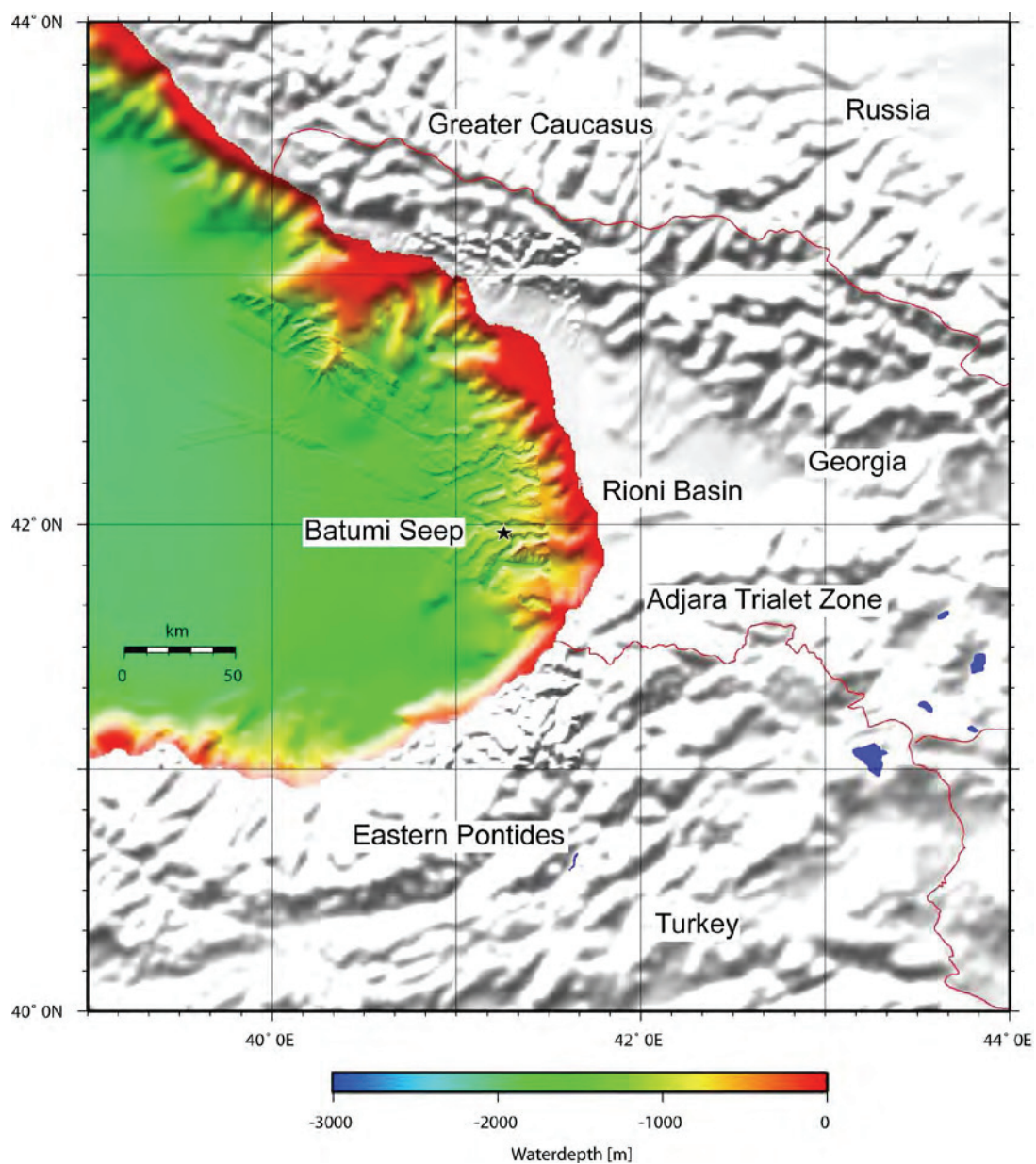
Fig. 4.3: Regional setting eastern Black Sea. Batumi Seep is located on a ridge between erosional canyons. Data from M72/3 survey (KONGSBERG EM120, 60 m grid) and GEBCO, Digital Atlas, 2003.

It was named after the nearby town Batumi and was already investigated during previous cruises (PO 317/4: Sahling et al., 2004; Klaucke et al., 2005; Klaucke et al., 2006; TTR15: Akhmetzhanov et al., 2007). The seep sites on a local high of Kobuleti Ridge. The ridge stretches in east-west direction and is bordered by erosional canyons shaping the continental slope.They are named Supsa Canyon, to the north, and Central Canyon to the south (Klaucke et al., 2006). This ridge and canyon pattern is present at the entire continental slope of Georgia (Fig. 4.3). Kobuleti Ridge, and other ridges as well, are underlain by diapiric structures (Tugolesov et al. 1985; Wagner-Friederichs, 2007). Diapirs formed under the compressional influence from the Greater Caucasus and the Achara-Trialet Thrust Belt (Banks et al., 1997). Several of the transformed sediment layers could act as source rocks (Robinson et al., 1997). One of them is the Maikopian Formation of late Oligocene to Miocene, which is rich in organic material and a good source rock known to be present in the entire Black Sea (Tugolesov et al, 1985).

4.3 Makran

The Makran accretionary system can be seen as end member of convergent plate boundaries with the largest accretionary wedge on Earth. Today, the subducting plate transports 7 km thick layers of sediment into the subduction zone. The upper 4 km are frontally accreted, whereas the lower 3 km are underthrust and later partially underplated leading to uplift and extension (Kopp et al., 2000; Platt et al., 1985; White and Louden, 1983). Such large accumulations are superior locations for the occurrence of seepage in conjunction with compaction-driven dewatering (Bekins and Dreiss, 1992). Transformation of deeply buried organic matter by thermal cracking (North, 1985) or by biological activities (Paull et al., 1994; Wiese and Kvenvolden, 1993) favour the rise of light hydrocarbons.

The Makran subduction zone is located at the north-western part of the Indian Ocean. It stretches over about 1000 km length from the Arabian Sea in the west to the onset of the Indian continent in the east (White, 1982). Those boundaries are defined by the Minab and Ornach-Nal Faults, respectively. Convergence is almost perpendicular and at a rate of about 4 cm/a (De Mets et al., 1990) and takes place at least since Cretaceous time (DeJong, 1982). Starting at the deformation front, east-west trending accretionary ridges spread northwards, about 150 kilometres offshore, and up to 300 kilometres onshore (White and Klitgord, 1976). Fig. 4.4 shows a map of the region. The marine part is characterised by relative high sedimentation rates, so that no distinct trench develops, and basins between accretionary ridges become filled up (White, 1982). Kukowski et al. (2001) describe the morphotectonics of ridges, basins, and intersecting canyons of the area between 62°10'E and 63°40' E in detail. Starting from a flat and shallow shelf, the upper slope down to a depth of 1000 m is cut by numerous deep canyons and has an overall steep gradient of ~8°. The slope continues with a smooth morphology as flat mid-slope terrace at 1°. The lower slope further down is built up by a sequence of accretionary ridges, which are especially steep at their ocean-facing flanks. Individual canyons, joining each other and gaining size on the way down-slope cut through these large ridges. The last large, fully developed ridge, named First Ridge, borders to the flat abyssal plain. The overall angle from mid-slope terrace to First Ridge is 2°. Farther offshore a shallow ridge bulges the seafloor (White et al., 1982; White and Louden, 1983; von Rad et al., 2000). This new accretionary ridge is called Nascent Ridge.

During monsoon season offshore Makran nutrient rich water rises to the ocean surface and fuels a high production zone. High organic matter concentration of 1-5% TOC reflecting the deposition of the large biological activity in the surface water were proved farther east (Schulz et al., 1998). Accordingly, the water column in Makran was found to be depleted in oxygen at depth between 100 and 1100 m (von Rad et al., 1995; von Rad et al., 2000). The

presence of large amounts of buried organic matter favours the generation of seep fluids and so add to seepage. Indeed, cold seepage was reported for the Makran region on- and off-shore. It may express in mud volcanism (Snead, 1964; Wiedecke et al., 2001; Delisle et al., 2002; Delisle, 2004), or be indicated by benthic life (von Rad et al., 1996; von Rad et al, 2000; Schmaljohann et al., 2001). A widespread bottom simulating reflector (BSR) suggests the presence of gas hydrate and free gas below it (White and Klitgord, 1976; White, 1977; Minshull and White, 1989; von Rad et al., 2000).
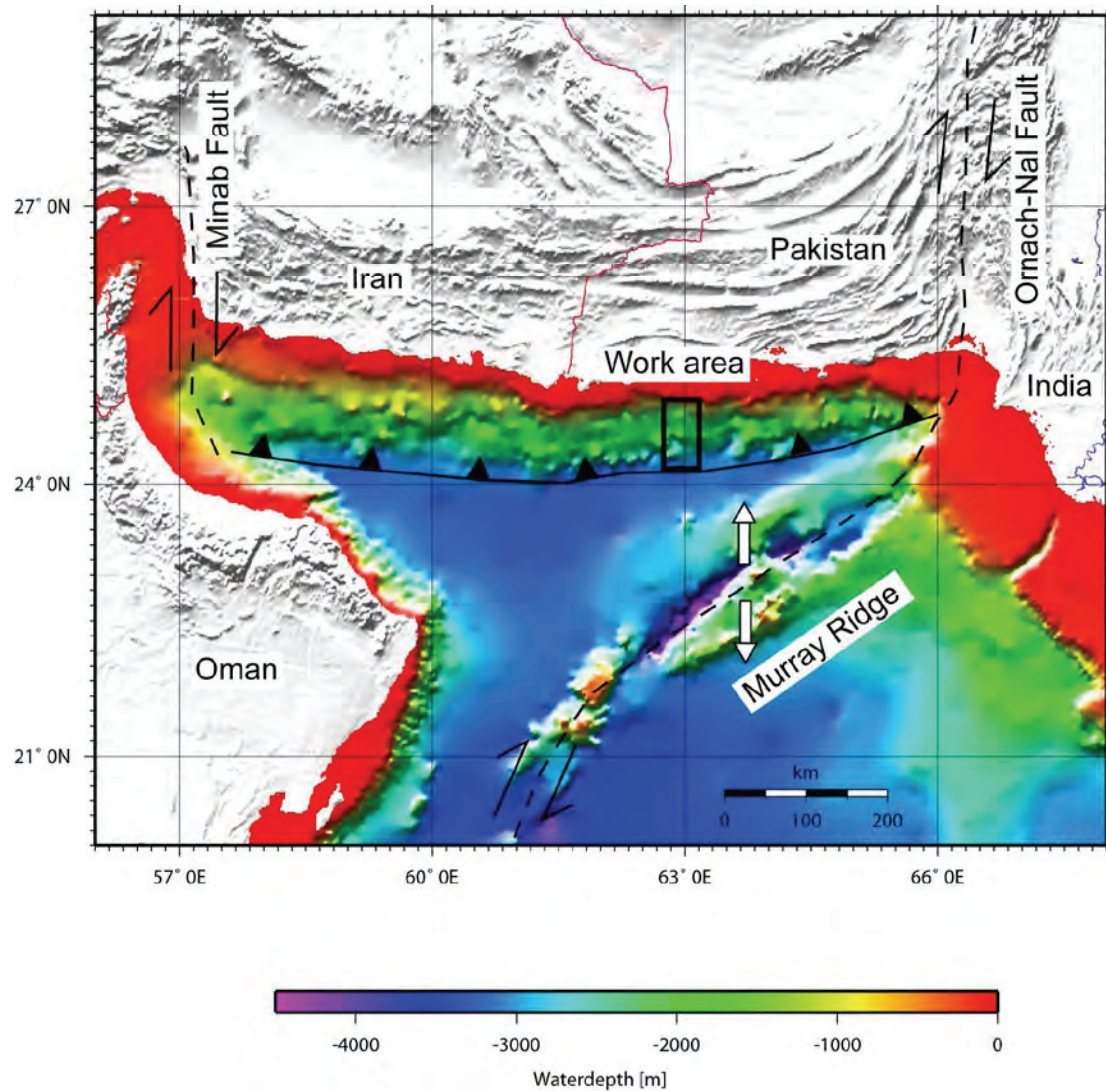
Fig. 4.4: Regional setting Makran subduction zone in the north western Indian Ocean. Accretionary ridges characterise off- and onshore areas. Data from GEBCO, Digital Atlas, 2003.

5

Origin, Distribution, and Alteration of Asphalts at Chapopote Knoll, Southern Gulf of Mexico

Markus Brüning [a], Heiko Sahling [a], Ian R. MacDonald [b], Feng Ding [a], Gerhard Bohrmann [a]

[a] MARUM, Center for Marine Environmental Sciences and Department of Geosciences, University of Bremen, GEO Building, PO 330440, 28334 Bremen, Germany
[b] Texas A&M University, 6300 Ocean Drive, HRI-121, Corpus Christi, TX 78412-5869, USA

Abstract

Following the discovery of asphalt volcanism in the Campeche Knolls a research cruise was carried out in 2006 to unravel the nature of the asphalt deposits at Chapopote. The novel results support the concept that the asphalt deposits at the seafloor in 3000 m of water depth originate from the seepage of heavy petroleum with a density slightly greater than water. The released petroleum forms characteristic flow structures at the seafloor with surfaces that are 'ropy' or 'rough' similar to magmatic lava flows. The surface structures indicate that the viscosity of the heavy petroleum rapidly increases after extrusion due to loss of volatiles. Consequently, the heavy petroleum forms the observed asphalt deposit and solidifies. Detailed survey with a remotely operated vehicle revealed that the asphalts are subject to sequential alterations: e.g. volume reduction leading to the formation of visible cracks in the asphalt surface, followed by fragmentation of the entire deposit. While relatively fresh asphalt samples were gooey and sticky, older, fragmented pieces were found to be brittle without residual stickiness. Furthermore, there is evidence for petroleum seepage from below the asphalt deposits, leading to local up-doming and, sometimes, to whip-shaped extrusions. Extensive mapping by TV-guided tools of Chapopote Asphalt Volcano indicates that the main asphalt deposits occur at the south-western rim that borders a central, crater-like depression. The most recent asphalt deposit at Chapopote is the main asphalt field covering an area of ~2000 m². Asphalt volcanism is distinct from oil and gas seepage previously described in the Gulf of Mexico and elsewhere because it is characterized by episodic intrusions of semi-solid hydrocarbons that spread laterally over a substantial area and produce structures with significant vertical relief. As Chapopote occurs at the crest of a salt structure it is inferred that asphalt volcanism is a secondary result of salt tectonism.

5.1   Introduction

Asphalt volcanism has been introduced as a novel type of hydrocarbon seepage by MacDonald et al. (2004). The authors found asphalt deposits with lava-like appearance at the seafloor in more than 3000 m of water depth in the southern Gulf of Mexico. The term asphalt was used to signify the solid state of the petroleum deposit that was composed of a degraded, unresolved complex mixture of hydrocarbons with a peak at n-C30 and a few resolved C29–C32 hopanes. The asphalts occurred in an area of approximately one square kilometer on one of the Campeche Knolls that was subsequently named Chapopote, the Aztec word for tar. Satellite data guided MacDonald et al. (2004) to the hydrocarbon seep sites where rising oil bubbles formed persistent oil slicks on the sea surface. TV-guided grab sampling revealed the presence of oil and gas hydrates in close neighborhood to asphalts in the sediments. Chemosynthetic fauna was observed, namely vestimentiferan tubeworms that implant into fissures in or below asphalts, and vesicomyid as well as mytilid bivalves in close proximity to asphalts. The recovered asphalt pieces were brittle and had no residual stickiness, they showed columnar joining and chilled margins. Lava-like flow structures and properties of the asphalt hand specimens lead MacDonald et al. (2004) to speculate that the asphalts may have been warm and molten at the time they have been extruded followed by rapid cooling at contact with the cold bottom water. The term asphalt volcanism was used by MacDonald et al. (2004) because of the crater-like morphology of Chapopote (Fig. 5.1) and the other knolls and elongated hills in the surrounding, which resembled volcanoes. Swath mapping revealed that the elevations are 5–10 km in diameter rising 350–800 m above the surrounding abyssal plain. The main asphalt deposits at Chapopote were observed at the southern rim of a crater-like depression as well as in the depression itself. Furthermore, several of the mapped knolls and elongated hills are characterized by linear and crescent-shaped faults and slump scars. In

many cases, the slumps are associated with down-slope sediment lobes that extend far out over the adjacent sea floor. MacDonald et al. (2004) suggested that repeated, extensive eruptions of molten (possibly warm) asphalt may lead to hydrate destabilization and that both, mechanical energy as well as decomposing hydrates, causes faulting, slope failures, and masswasting mapped at Chapopote and other salt domes in the Campeche Knolls. Hovland et al. (2005) took up the assumption that the asphalt erupted in a hot state and proposed that asphalts volcanism might be generated by supercritical water. In summary, this provocative concept invokes hot hydrothermal fluids originating at the crust/ sediment interface at about 13 km sediment depth that are able to transport asphalt dissolved with the supercritical water inside the piercement salt structures that occurs at Chapopote, which may act as vertical thermally insulated conduits. The supercritical water concept is mainly based on the fact that the asphalts resemble lavalike, hot flows and the finding of authigenic precipitates in the pores of the asphalts, which might have been deposited during cooling and solidification of the flows. Motivated by the initial publications by MacDonald et al. (2004) and Hovland et al. (2005) a research expedition was conducted in order to find out how asphalts are deposited on the seafloor. The multi-disciplinary studies included high-resolution seismic reflection studies, seafloor observation by TV-sled and remotely operated vehicle (ROV), and sample collection. While we still do not have unambiguous evidence against the supposition that asphalts erupt in a hot state, several lines of evidence exist that the flowstructures are created by emanating heavy petroleum without any significant thermal anomaly. Upon release at the seafloor, the heavy and already very viscous petroleum further increases its viscosity, becoming immobile, and leaving behind the observed asphalt deposits. We adopt the term 'flow' to denote the continuous, spreading nature of asphalt deposits characteristic of Chapopote. In this study we continue using 'asphalt' as a term for the solidified and, thus, very - heavy petroleum following the publications by MacDonald et al. (2004), Hovland et al. (2005), and Ding et al. (2008a) although we do not know the chemical composition of the deposits. Organochemical characterization of the oil is underway (Schubotz et al., 2007). One key evidence for the concept of seeping heavy petroleum comes from high-resolution seismic reflection studies indicating a shallow hydrocarbon reservoir (Ding et al., 2008a). The work could show that hydrocarbons are trapped in a shallow reservoir that is overlain by an only 100–200 m thin seal interval in the area of the crest at Chapopote Knoll (Fig. 5.2). It is very likely that hydrocarbons in such a shallow reservoir are subject to intensive biodegradation, as reviewed by Head et al. (2003), producing an even heavier petroleum from crude oil, which is already heavy in the deep offshore area in the Gulf of Campeche (Magoon et al., 2001). Ding et al. (2008a) hypothesize that such heavy hydrocarbons may still be mobile enough to break through some 100–200 m of seal sediments above the reservoir to reach the seafloor where they flow out, loose their volatile components and get further altered. As a consequence, asphalts with characteristic flow structures are left at the seafloor. Additional evidence that seeping heavy petroleum has produced the asphalt deposits are provided in this study, which concentrates on the detailed description of flow structures at Chapopote based on ROV observations. As a first step, observations by TV-guided tools and ROV are used to systematically map the distribution of asphalts in relation to morphological features of Chapopote. The detailed mapping shows a clear succession pattern of asphalt occurrences that we interpret as evolutionary stages of relatively fresh to heavily altered deposits. Mapping of the main asphalt fields provides quantitative data on the thickness and the extent of the most recent asphalt deposits. Furthermore, we propose a model that explains how the flow structures are formed that combines all the detailed ROV observations. This study is accompanied by detailed studies on authigenic carbonates (Naehr et al., 2009) and gas hydrates (Klapp et al., 2010).
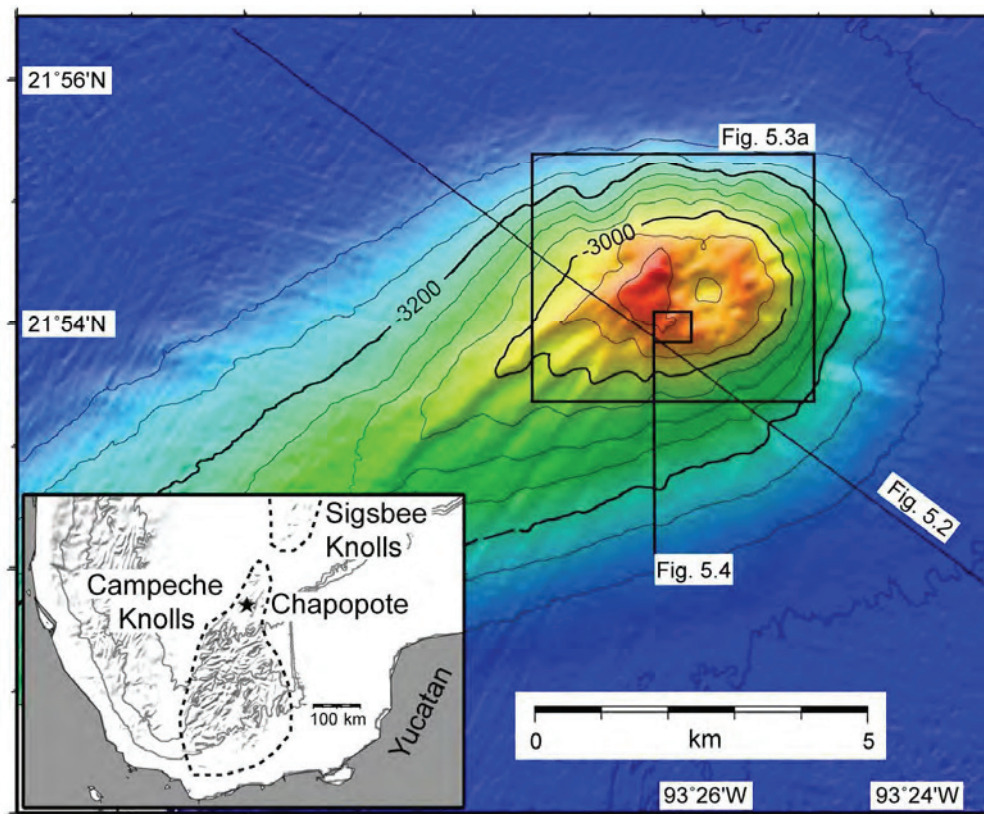
Fig. 5.1: Swath bathymetry of Chapopote Knoll. The line indicates the seismic profile closest to the asphalt site shown in Fig. 5.2. Inset: Bathymetric map of the Campeche Bay, southern Gulf of Mexico. The star indicates the location of Chapopote. The overview map is based on the GEBCO 1 min data set (GEBCO, Digital Atlas, 2003).

5.2   Regional Setting

Campeche Knolls and Sigsbee Knolls are two, active salt provinces in the southern Gulf of Mexico (Fig. 5.1, inset; Bryant et al., 1991). Most of the salt has probably been deposited during the opening of the gulf in Late Jurassic (Salvador, 1991). In the area of the Campeche Knolls 5–10 km thick sediments occur above the salt unit of which most of the sediments have been deposited in Cenozoic times (Magoon et al., 2001). The thick sediments provide prolific petroleum source rocks with the most productive ones of latest Jurassic and Cretaceous age (Magoon et al., 2001). Salt activity has formed the knolls and elongated hills in the Campeche area, which favours trapping as well as leakage of oil and gas. Ding et al. (2010b) summarized swath bathymetry and satellite data of oil slicks showing more than 40 knolls and local summits with evidence for oil seepage in a depth range of 1000–3300 m. So far, asphalts have been found at Chapopote and very likely also at Challenger Knoll in the Sigsbee Knolls area which was photographed by Pequegnat and Jeffrey (1979). However, based on the abundant evidence for widespread oil seepage in the area, it is likely that many more asphalt deposits exist at other knolls and elongated hills. A comprehensive seismostratigraphic study has been carried out at Chapopote (Ding et al., 2008a) revealing that a coarse-grained sediment unit of Miocene age very likely acts as shallow hydrocarbon reservoir (Fig. 5.2). Local salt tectonism since the late Miocene has lead to up-doming of this sediment unit that is only covered by a thin (100–200 m), fine-grained sediment layer on the crest of the knoll that acts as seal. However, hydrocarbons apparently invade the seal sediments in the wider vicinity around the crest of the knoll, where they can be seen as high-

amplitude reflector packages. Acoustic transparent zones indicative of fluid pathways occur below the crest (Ding et al., 2008a).
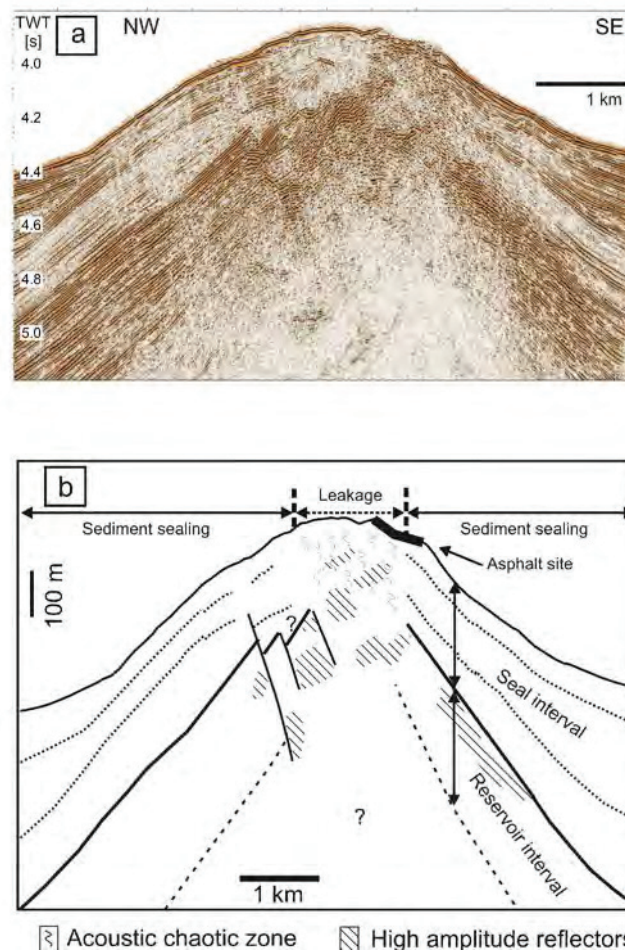
Fig. 5.2: a) High-resolution seismic profile across Chapopote Asphalt Volcano. Seismic source was a 4.1 + 1.7 L GI-gun generating a 30–300 Hz signal. Data are processed wtih 5 m bin spacing. b) Interpretation. Hydrocarbon accumulations are indicated by hatchings. Acoustically chaotic reflections indicate hydrocarbon migration. Modified from Ding et al. (2008a).

5.3 Methods

5.3.1. Bathymetry

Bathymetric data from Chapopote were collected during the RV Meteor Cruise M67/2, legs A and B in March and April 2006 with the Kongsberg Simrad EM120 multibeam echo sounder (Bohrmann et al., 2008b). Soundings were combined with the dataset surveyed during the SO174 cruise measured with the same echosounder system onboard RV Sonne (Bohrmann et al., 2004). At Chapopote Knoll, coverage was sufficient to calculate maps with a grid-spacing of 20 m. Data were processed with IFREMER's Caraibes software applying automatic filters and manual editing. The Generic Mapping Tool (GMT) software was used to produce topographic maps.

5.3.2. Visual Surveys, Sample Collection, and Asphalt Mapping

Two towed TV-tools were used in order to image asphalt deposits at the seafloor, a TV-sled and a TV-guided multicorer (TVMUC) for targeted sample collection. They transmitted real-time monochrome video data, so that the seafloor images were continuously displayed on the vessel. The field of view of the downward looking camera was about 4 m². The altitude of 2–3 m above the seafloor was manually adjusted by the winch operator. Tow speed was about 0.5 knots. An IXSEA POSIDONIA ultra-short baseline (USBL) navigation system provided real-time positions for the towed platforms. Detailed observation, mapping, and sampling were conducted with the work-class remotely operated vehicle (ROV) QUEST 4000 m operated by MARUM. ROV QUEST is equipped with two manipulators, a 3 MPixel still camera, three video cameras, and a suite of lamps. ROV positions were obtained by using the IXSEA POSIDONIA USBL system and a Doppler velocity log. Exploratory tracks were planned to extend survey data over the largest asphalt extent of the Chapopote Knoll. During surveys, the ROV was piloted along these lines while recording video from a forward-looking camera and taking opportunistic photographs of subjects of interest (Bohrmann et al., 2008b). The distribution of asphalts at Chapopote Knoll was mapped using the video records and the time-indexed positions of the ROV QUEST. Along the exploratory tracks, we mapped the points in which asphalts were observed. A similar approach was used to integrate the TV-sled results. On a more detailed scale we evaluated images of the downward looking camera of the ROV on the south-western part of the summit. Again symbols were placed along the navigation-tracks at appropriate positions. This smaller scale mapping required accurate navigation for the location of visual images. Raw USBL navigation was too noisy and required processing, i.e. calculation of a smooth line from scattered raw data points. The main asphalt field (MAF) was included in the area of detailed mapping. Here asphalts completely paved the seafloor and exact positioning of features was required. After despiking and filtering, remaining errors in the navigation were still up to 5 m, as judged by re-occupying marked sites on successive dives. Discrepancies were especially large between dives separated by time spans of days. As a consequence, we took the navigation of a single dive (no. 83) as reference for positioning, and shifted data from other dives so that bench-mark features were aligned with no. 83. Although the resulting navigation was not precise enough to geo-position images, symbols representing asphalt features were drawn after inspection of mosaics, video clips, and high-resolution photo images at their best-estimated positions. Mosaics of videos recorded by downward looking camera were processed with IFREMER's ADELIE software. However, they were only used as one component of the mapping dataset because the mosaics tended to be distorted due to irregular ROV movement, and hence could not be used as a visual map. Despite all the effort of mapping features at the position given by navigation data, and fitting visual observations at the same time, the resulting map of the MAF retains distortions and displacement errors, but accurately depicts the relative locations and extents of asphalt flows and other features. Symbols used to classify for the different asphalt characteristics into three categories attempt to mimic the observed patterns, e.g. parallel lines to represent ropy asphalt and irregularly curved closed symbols represent fresh-rough asphalt.

5.4. Results

5.4.1. Distribution of Asphalt Deposits

The close-up swath map of Chapopote shows that the knoll comprises a central crater-like depression surrounded by an asymmetrical rim, with prominent faults south-west of the summit area, and a slump scar at its north-western flank (Fig. 5.3a). The occurrence of asphalts was studied in relation to these morphological features using TV-guided tools (Table 5.1). The extensive mapping revealed that the main asphalt presence was located at the south-western rim. This area with asphalts was by far the most extensive deposit, consisting of apparently different generations of asphalt flows, which had undergone varying stages of alterations. It was situated on the foot of more than 10-m high morphological offset (Fig. 5.3b). While the present study concentrates on these asphalts on the south-western rim of Chapopote, additional asphalt deposits were observed in other localities (Fig. 5.3a). The most altered asphalts, consisting of broken-apart, decimeter-sized pieces in soft
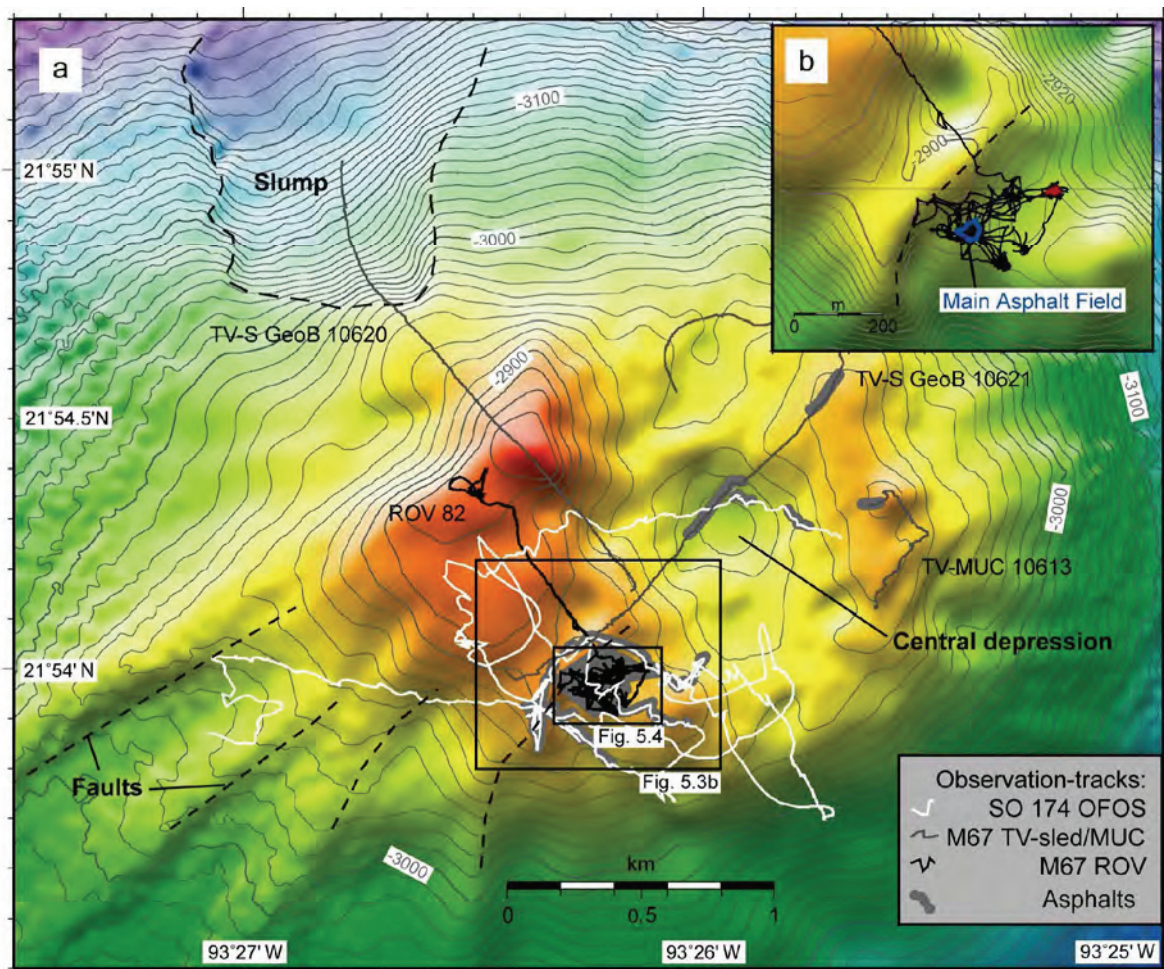
Fig. 5.3: a) Bathymetric map showing the summit of Chapopote Knoll with tracks of video equipped devices. Grid cell size for the map is 20 m. Bold grey lines signify asphalts. b) Detailed view of the main asphalt deposit showing the small-scale bathymetry.

47

Tab. 5.1: Data of visual surveys at Chapopote during Cruise M67/2.

Device	GeoB No.	Start		End		Area	Duration
		Latitude N	Longitude W	Latitude N	Longitude W		[hh:mm]
TV-MUC	10612-2	21°54.230'	93°25.927'	---	---	central depression	01:05
TV-MUC	10613	21°54.12'	93°25.65'	21°54.322'	93°25.644'	E ring	02:15
TV-MUC	10614	21°53.978'	93°26.190'	21°53.980'	93°26.223'	SW ring	00:58
TV-MUC	10616	21°53.92'	93°26.17'	21°54.10'	93°26.27'	SW ring	02:27
TV-sled	10620	21°54.15'	93°26.153'	21°55.024'	93°26.783'	W depression, highest peak, slump	02:37
TV-sled	10621	21°54.12'	93°26.14'	21°54.545'	93°26.058'	SW ring, central depression, NE ring	02:44
ROV	10615 / Dive 80	21°53.920'	93°26.152'	21°53.917'	93°26.146'	SW rim	01:04
ROV	10617 / Dive 81	21°53.942'	93°26.131'	21°53.949'	93°26.238'	SW rim, asphalts	10:56
ROV	10619 / Dive 82	21°54.333'	93°26.497'	21°53.926'	93°26.049'	SW rim, asphalts	16:06
ROV	10622 / Dive 83	21°53.949'	93°26.249'	21°53.927'	93°26.147'	SW rim, asphalts	11:21
ROV	10625 / Dive 84	21°53.380'	93°26.131'	21°53.690'	93°26.131'	SW rim, asphalts	18:05

GeoB and the dive numbers are MARUM station numbers.

sediments, occurred in two areas on the north-eastern rim close to local summits. These deposits were partly covered by sediments and probably represent the oldest deposits that we found at Chapopote. In addition, asphalts occurred in the central depression, but the extent of the individual flows in this area was generally much smaller than those at the south-western rim. However, the presence of mytilid mussels and vestimentiferan tubeworms at one of the asphalt deposits in the central depression indicated recent hydrocarbon seepage.

5.4.2. Flow Structures of Asphalt Deposits, Alteration, and Oil and Gas Seeps

The area with the most extensive asphalt deposits on the southwestern rim of Chapopote was mapped in detail during four ROV QUEST dives (Fig. 5.4). Within the area shown in Fig. 5.4 we observed four sites with evidence for recent asphalt deposits, i.e. 'main asphalt field' (MAF), 'west field', 'SO174 field', and 'asphalt edifice'. While the MAF is the largest deposit of recent asphalts and presented in detail below, the 'asphalt edifice' illustrates the dynamics of asphalt discharge (Fig. 5.5a). Petroleum was released from the seafloor forming whip-like extrusions that floated in the water column. The oil was positively buoyant but viscous enough to remain attached to the seafloor. The extrusions eventually sink down and lead to the stacked pattern of flows, which had built an edifice about 2 m long and 1 m high. We believe that the 'asphalt edifice' is an example in miniature of the process of heavy petroleum seepage that leads to the observed asphalt deposits throughout the area. However, individual flows were generally much larger in size and apparently spread over the seafloor. Many flows have a 'ropy' appearance (Fig. 5.5b–f and 5.6b). Ropes were curving, tubular structures that had diameters from 1 cm to a few decimeters. Smaller-diameter ropes often occurred in parallel arrays (Fig. 5.5c–e); thicker ropes occurred as solitary features or as bulging edges of a flow (Fig. 5.5b,h). In addition to flows with a ropy surface we designate a second 'rough' surface texture as illustrated in Fig. 5.6a,b. Rough structures were found in combination with, and in close proximity to, surfaces with a ropy appearance. The rough surface was generally anisotropic and chaotic. Surfaces appeared irregular with numerous edges or inflated swells in the size range of 1–10 cm. In general, deposits with a rough surface were thicker than those with a ropy surface. Both surface types (ropy and rough) were devoid of any sediments or detritus, which suggested a relatively recent deposition. The distribution of microbial mats and vestimentiferan tubeworms at recent asphalt deposits was sporadic and patchy. Bacterial mats generally occurred on concave surfaces on the asphalts, e.g. in the

cavities between ropes (Fig. 5.5c,e,h), as small patches on rough asphalts (Fig. 5.6a), or as meter-wide patches draped over ropy surfaces (Fig. 5.5d). Although the mats are currently under investigation by microbiologists, their dependence on the asphalts is unclear (A. Boetius, pers. comm.). Vestimentiferan tubeworms occurred as individual specimens or in a few instances as clusters in connection to the recent asphalt flows (Fig. 5.5b,h and 5.6a,b). The tubeworms always implanted below the edges of individual flows with ropy surfaces or lived scattered on asphalt with rough surfaces. After deposition at the seafloor, asphalt is apparently subject to alteration. Loss of volatile compounds probably leads to shrinkage, forming fissures (Fig. 5.5f), and cracks (Fig. 5.6d) in the surfaces. Continued alteration probably leads to fragmentation of the contiguous asphalt deposits, which eventually form breccia of mixed sizes (Fig. 5.6e,h). At the oldest stages, the darker colored asphalts were visible under a thin layer of sediments. In general, fragmented asphalt was widespread in the area on the southwestern rim of Chapopote (Fig. 5.4). Different symbol sizes for the fragmented asphalts illustrated the different stages of alteration and their extent on the seafloor, from continuous asphalts that are just fragmented (e.g. around the 'bubble site', Fig. 5.4) to those asphalts that only consists of cobble- to pebble-size pieces in soft sediments. The map shows that fields with continuous asphalt deposits existed mainly east of the nowadays fresh asphalts.
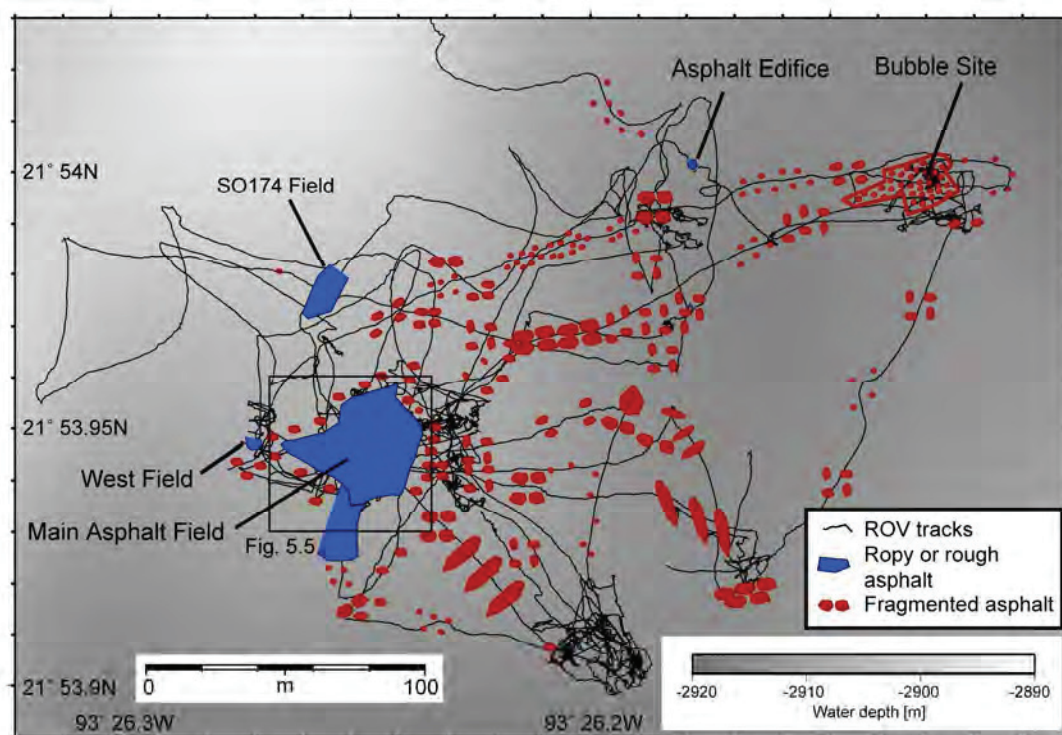
Fig. 5.4: Detailed track-chart of four M67/2 ROV dives in the area with highest asphalt density on the south-western rim of Chapopote's summit. Observed asphalt patterns are indicated by symbols according to the appearance of asphalt. Symbol sizes refer to relative size of asphalt pieces and coverage observed at the seafloor, from centimeter to meter size; symbols are larger than asphalt pieces in nature.

Heavily altered asphalt breccia was generally devoid of chemosynthesis-based communities; however, a few exceptions were noted, e.g. the lush communities of vestimentiferans and mytilids close to an active gas vent (Fig. 5.6f). Here, we observed a train of gas bubbles escaping through a mixture of asphalt and layers of white gas hydrate. The mytilid assemblage was restricted to a radius of about 10 m surrounding the vent site. We

therefore attribute their occurrence to gas release and/or hydrocarbon seepage and not asphalt presence. Further evidence for hydrocarbon seepage are based on the observation that vesicomyid clams and (in a few instances) bacterial mats were observed in sediments in close vicinity to the asphalt deposits. Sampling by push corer next to fragmented asphalts revealed that the sediments were permeated by petroleum (Fig. 5.6g), indicating hydrocarbon seepage that occurs independently of the asphalt deposits. The petroleum formed long, sticky filaments during the withdrawal of the push core that drifted in the water until becoming attached to the ROV. A further example for petroleum seepage is shown in Fig. 5.5g. A whip-shaped blackish extrusion 20 cm in length that we assume to be heavy petroleum rose from up-domed asphalts with irregular surface structures.

5.4.3. Main Asphalt Field

The main asphalt field (MAF) is the largest deposit of fresh asphalt found to date on Chapopote, followed in size by 'SO174 field' and 'west field' (Fig. 5.4). The MAF was mapped in detail with the ROV QUEST in order to investigate the temporal sequence of asphalt deposition and the distribution of extrusion sites. The MAF was a semi-circular asphalt deposit 40 m across located on a gently inclined slope that was a few meters higher in the northwest (Fig. 5.4). It consisted exclusively of recent asphalt with ropy or rough surface textures (Fig. 5.7a). Based on this small-scale mapping we infer a relative sequence of flow events and directions (Fig. 5.7b). Most importantly, no asphalt structures in the MAF could be unambiguously interpreted as discrete 'exit points' from which heavy petroleum has flowed in the past. Instead, mapping was based on the supposition that flows accumulate on top of each other (Units 1–5) and that the topmost one was the youngest (Unit 5). A video mosaic from the center to the northern edge of the MAF illustrates this sequence (Fig. 5.8). The track covered a flow with microbial mats (Unit 4), crossed over two stages of flows of intermediate age (Units 2–3), and terminated at the limit between the asphalt deposit and the regular deep-sea hemipelagic sediments. The flow at the edge of the main asphalt field was characterized by fissures in the ropy surface. Apparently, the oldest deposit in Fig. 5.7b was the fragmented asphalt buried in the sediments. Vestimentiferan tubeworms were mainly associated with the flows of intermediate age, but sparse or absent at the youngest and the oldest deposits. The sizes of the exposed tubes were generally ~20 cm and apparently never exceeded 50 cm. The MAF had a complex small-scale relief that was decoupled from the primary direction of its flow structures. For example, the asphalts in the north-eastern area (Fig. 5.7b) were elevated by 1 or 2 m over distances of 2 m and more but did not show any corresponding surface structure, i.e. downward flow patterns (Fig. 5.7a). In total, there were more than 20 small-scale up-domed areas. The distribution of young (Unit 5) to old (Unit 1) asphalt deposits at the MAF follows a concentric pattern (Fig. 5.7), suggesting that the main source region was in the northern part of the field and that the heavy petroleum flew preferentially down the gentle slope.
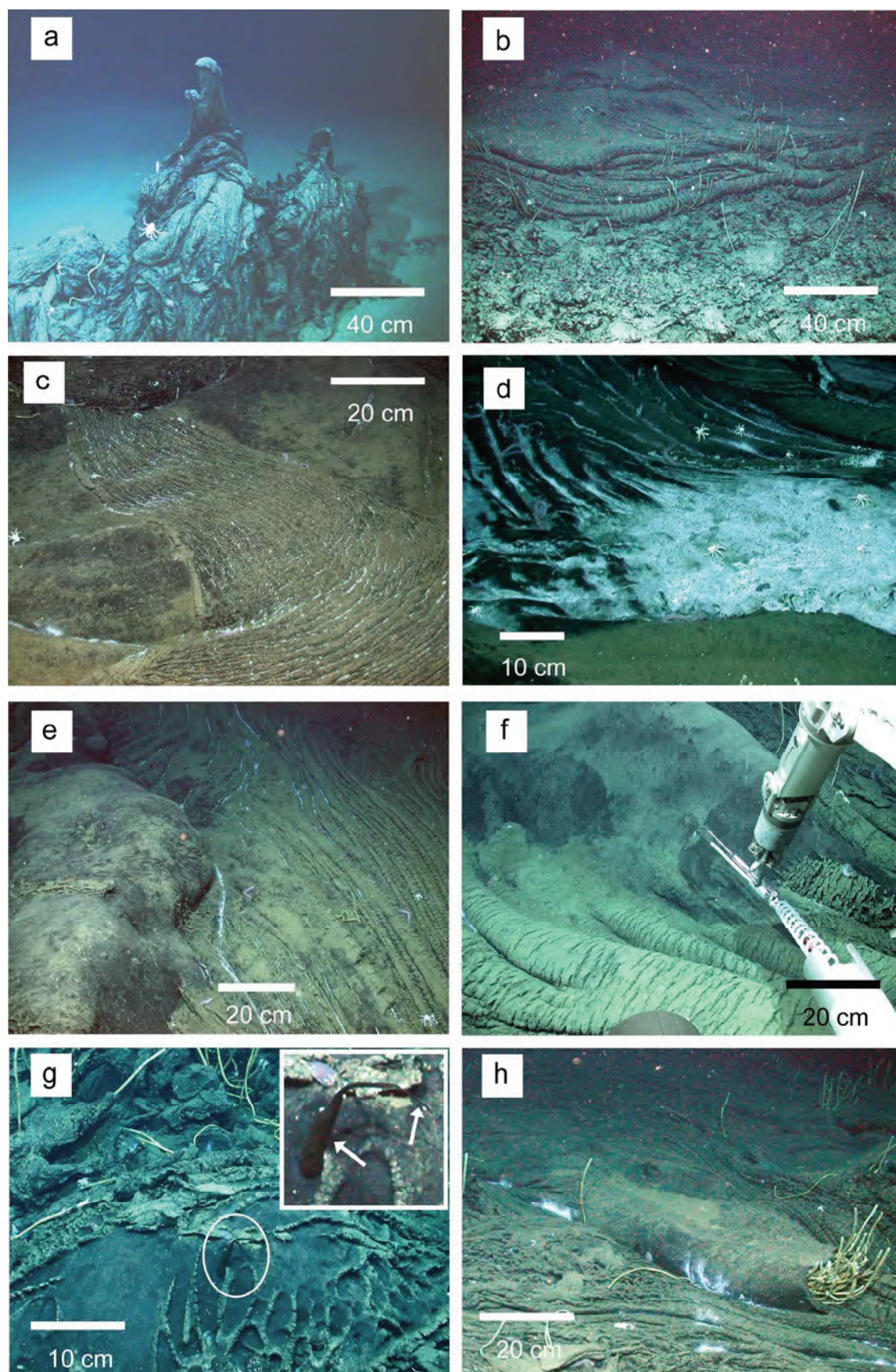
Fig. 5.5: ROV QUEST images taken at Chapopote Knoll. a) Whip-shaped extrusions forming the 'asphalt edifice'. b) Flow with ropy surface overlays deposit with rough surface. c) Flow structure with longitudinal and transversal surface ropes. d) Microbial mats on ropy asphalts.

Fig. 5.5 (cont.) e) Up-domed asphalt deposits in between ropy asphalts. f) Fissures in the foreground in ropy asphalts indicate volume shrinkage. The background shows up-domed asphalt. g) Up-domed asphalts with a characteristic polygonal surface structure and a whip-shaped extrusion of most likely heavy petroleum. h) A coiled-up asphalt layer forming an individual, thick rope. Vestimentiferan tube worms grow out of the opening. All photos © MARUM.

Furthermore, younger deposits were generally smaller in extent than older indicating that the volume of the extruded material may have decreased with time. Alternatively, the area of extruded material may have decreased as the total volume of asphalts increases and extrusions had to 'fill' a larger volume before meeting the water. During the cruise, there was no evidence for the flow of heavy petroleum that was as large in size as the observed asphalt deposits. However, there were at least two sites with small whipshaped blackish extrusions (Fig. 5.5g) that we interpret as petroleum seepage, but at a smaller scale.

5.4.4. Extent and Thickness of Asphalt Deposits

To estimate the amount of asphalt found at Chapopote, we assume that the main asphalt field (MAF) is representative of a recent asphalt deposit. The area that was covered by asphalts in the MAF is about 2000 m² (Fig. 5.7). However, the area of the single flow that extended further to the south is not included in this total because its dimensions are not well constrained. A first-order approximation is used to estimate the thickness of the asphalt deposit. The edges of the MAF were typically formed by one layer of asphalt deposit that was about 0.4 m thick at the northern limit and appeared to be somehow thicker at the southern borders of the field (up to 1 m). The central areas were typically formed by two to four generations of asphalts (Fig. 5.7b). Assuming an average thickness of flow of 0.7 m, this would result in a total thickness of about 1.4–2.8 m. Due to the fact that the thickness of the asphalt deposit is crucial for the volume estimation, we assume a thickness of about 2 m and allow a large range of uncertainty of ±1m. As a result, we obtain an estimated volume of 4 (±2) x 10^3 m³ asphalt at the MAF. The asphalts at the south-western rim of Chapopote consisted of both fresh and altered asphalt deposits. The area covered by asphalts was about 28,000 m² when drawing a simple polygon around the mapped occurrences shown in Fig. 5.4. The extent of asphalts outside of this well-charted area is difficult to estimate. Based on the extensive surveys that covered many of the morphological structures in the summit area of Chapopote (Fig. 5.3) we are confident that we could delimit the major fields of asphalt, with those at the south-western rim comprising the most extensive field. Based on the TV-surveys it appeared that all asphalt deposits in the central depression and on the north-eastern rim were in total much smaller than those at the south-western rim.

5.4.5 Asphalt Samples

Asphalts samples were taken by ROV QUEST and by gravity corer (Table 5.2). They range from recent asphalt deposits with ropy surface to altered, fragmented asphalt pieces (Fig. 5.9). Two samples from freshly-deposited asphalts with a ropy surface texture were taken by the manipulator of ROV QUEST. These samples were negatively buoyant, whereas a further sample taken at one of the up-domed asphalt deposits was, unexpectedly positively buoyant (Fig. 5.6c). The recovered pieces of ropy asphalts were sticky and cohesive when examined on deck. The positively buoyant piece was recovered in a pressure-tight chamber

and released considerable amounts of gas after recovery during depressurization. The piece reverted to a highly viscous liquid phase after degassing and temperature equilibration at about 25°C. A fragmented asphalt piece was taken from the seafloor in the area of the gas bubble stream (Fig. 5.9b). It was brittle and stiff without stickiness. Attached to the asphalts were bathymodiolid mussels and sponges. Two gravity cores were taken at the MAF each recovering about 100 cm of pure asphalts (Fig. 5.9a). The freshly-recovered asphalts released bubbles from less than millimeter-sized vesicles indicating the release of gas with a strong odor of hydrogen sulphide. Under atmospheric conditions the sampled asphalt was pliant, but stiff enough to avoid collapse. In addition, a thick intrusion of gas hydrate was found at the base of one gravity core.

Fig. 5.6 (next page): ROV QUEST images taken at the seafloor of Chapopote Knoll. a) Asphalt with rough surface structure. Arrow indicates a microbial mat. b) Asphalt with rough surface structure below a ropy flow. c) Asphalt sample wrenched from an up-domed deposit. The sample was positively buoyant, GeoB 10622-1. d) Fractures on an asphalt deposit. e) Highly altered asphalt fragments, partly sediment covered with vestimentiferan tube worms. f) Luxurious chemosynthetic communities (vestimentiferan tubeworms, bathymodiolin mussels) as well as sponges and galatheid crabs colonising fragmented asphalt close to the gas bubble site. g) Push core taken in soft sediments close to asphalt deposits containing heavy petroleum forming filaments (arrows), GeoB10619-13. h) Fragmented asphalts. All photos © MARUM.
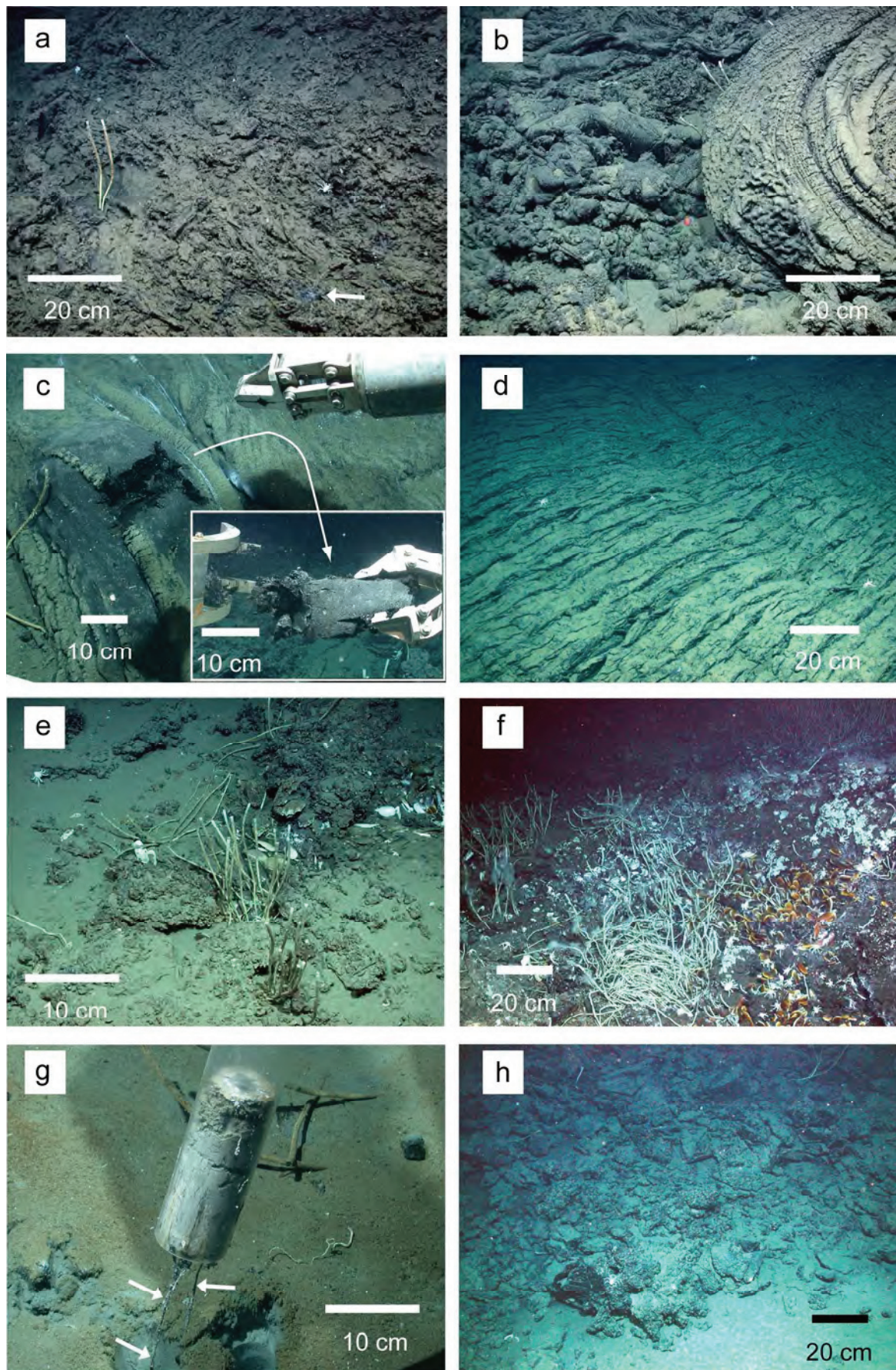
Fig. 5.7 (previous page): Maps of the main asphalt field (MAF). a) Facies map illustrating the distribution of ropy flows and deposits with a rough surface as well as the small-scale relief as observed by the ROV. b) Interpretation of the facies map illustrating at least five generations of asphalt deposits. Each generation was characterized by the asphalt appearance and the observation which flow rested on top of the other.
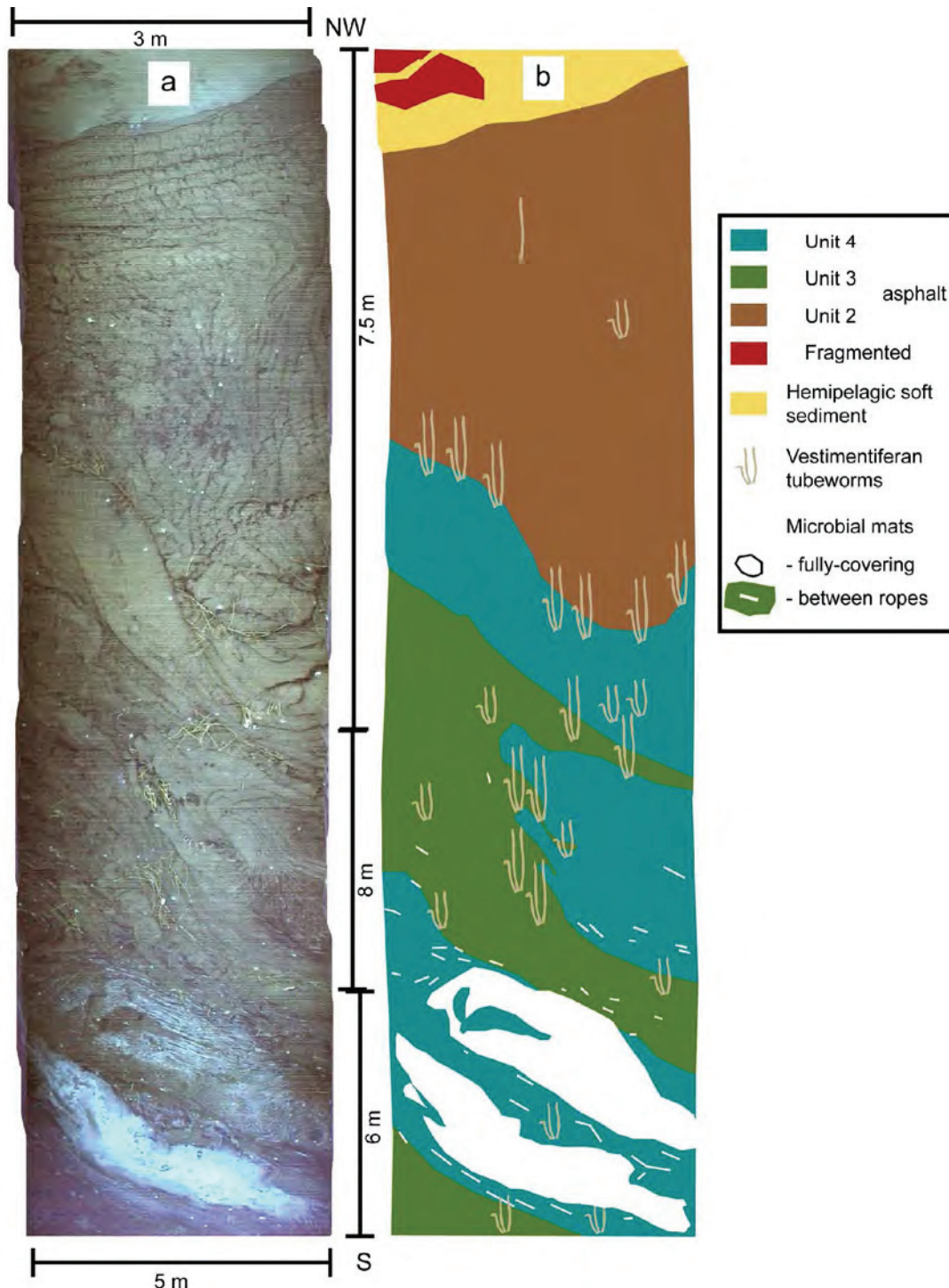
Fig. 5.8: a) Video mosaic along a transect through the main asphalt field originating at the northern edge (top of frame) and proceeding to near the center (bottom of frame). The location is indicated in Fig. 5.7a. The image illustrates that different generations of asphalt accumulate one on top of another. The mosaic is somewhat distorted due to increasing ROV altitude from NW to S and changing viewing angle. Mosaic produced by ADELIE software © IFREMER including MOTION-2D © INRIA. b) Mapping and interpretation of the video mosaic shown in a). Different asphalt flow generations are marked by different colors.
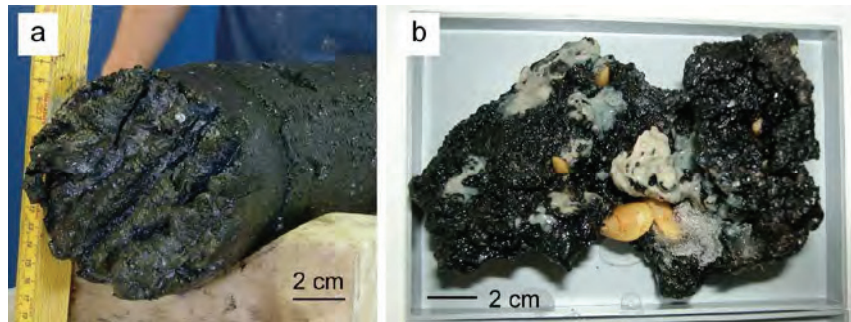
Fig. 5.9: Asphalt samples recovered from Chapopote Asphalt Volcano. a) A recent asphalt deposit with ropy surface texture sampled by gravity corer. The asphalts were gooey and slightly sticky, GeoB10623-2. b) A piece of fragmented asphalt with bathymodiolin mussels and porifera attached to it. The piece was brittle and without stickiness, GeoB 10622-3.

5.5. Discussion

5.5.1. Asphalt Distribution at Chapopote

The finding that the main asphalt deposits occur at the southwestern rim at Chapopote (Fig. 5.3a) confirms the earlier observations by MacDonald et al. (2004). The most extensive asphalt deposits were situated on the foot of a morphological offset (Fig. 5.3b), which is very likely the surface expression of a fault related to the set of faults farther to the southwest. The main asphalt deposit was thus located directly above the hydrocarbon reservoir imaged by high-resolution seismics (Fig. 2; Ding et al., 2008a), with faults providing the pathways for heavy petroleum seepage. The presence of asphalts at the south-western rim, in the central depression, and on the north-eastern rim followed generally the same southwest–northeast trend as the fault planes imaged by Ding et al. (2008a). This may suggest that faults intersecting the hydrocarbon reservoir determines asphalt distribution. TV-sled surveying of morphologically distinct features such as the slump on the north-western flank or the central crater-like depression did not result in any evidence for a relation of these features to hydrocarbon seepage (MacDonald et al., 2004). Therefore, these features might be interpreted as a result of the interplay between salt movement and sedimentation as discussed by Ding et al. (2008a).

GeoB No.	Device	Location	Latitude N	Longitude W	Corrected Position on Fig. 5.7	Properties
10618	GC	ropy surface indicates MAF	21°53.95'	93°26.21'		pure asphalt, ropy surface, large piece of gas hydrate at bottom
10623-2	GC	ropy surface indicates MAF	21°53.959'	93°26.223'		pure asphalt, ropy surface, cf. Fig. 9a
10617-5	ROV-Suction	MAF	21°53.940'	93°26.226'	21°53.948' / 93°26.241'	brittle centimeter sized asphalt pieces, drilled from smooth/ropy surface
10617-6	ROV-Manipulator	MAF	21°53.945'	93°26.229'	21°53.944' / 93°26.239'	~40 cm piece of soft sticky asphalt
10617-7	ROV-Suction	MAF	21°53.953'	93°26.226'	21°53.952' / 93°26.238'	brittle centimeter sized asphalt pieces
10617-8	ROV-Suction	MAF	21°53.951'	93°26.224'	21°53.953' / 93°26.239'	brittle centimeter sized asphalt pieces
10619-13	ROV-PC	between SO174 Field and Bubble Site	21°54.035'	93°26.184'	21°54.035' / 93°26.184'	oily sediment, cf. Fig. 6g
10619-15	ROV-Suction	between MAF and Bubble Site	21°53.969'	93°26.184'	21°53.969' / 93°26.184'	fragmented asphalt
10619-17	ROV-Suction	E of MAF	21°53.970'	93°26.185'	21°53.959' / 93°26.222'	brittle asphalt, not buoyant
10622-1	ROV-Pressure	MAF	21°53.956'	93°26.227'	21°53.954' / 93°26.245'	up-domed asphalt, cf. Fig. 6c
10622-3	ROV-Net	Bubble Site	21°53.990'	93°26.124'	21°53.990' / 93°26.124'	fragmented, brittle asphalt, cf. Fig. 9b
10625-16	ROV-Suction	MAF	21°53.953'	93°26.250'	21°53.943' / 93°26.245'	sticky asphalt, microbial mat-covered

GC – gravity core, ROV – suction is a suction sampler, PC – push core. Corrected position provides sample location in Fig. 5.7, cf. navigation error in Methods chapter.

Tab. 5.2:
Asphalt samples taken in the surveyed area. GeoB no. are MARUM station numbers.

5.5.2. Asphalt Formation and Post-depositional Alteration

The results of this study revealed additional support for the idea that heavy petroleum seepage leads to the asphalt deposits observed at Chapopote Knoll. We developed a simple but comprehensive model that integrates our observations during seafloor mapping as well as sampling (Fig. 5.10). To start with, the observations of whip-shaped extrusions (Fig. 5.5a,g) clearly indicate seepage of heavy petroleum, which has slight positive buoyancy, but is viscous enough to remain attached to the point or extrusion. Similar processes have been long noted at shallow-water tar seeps (Vernon and Slater, 1963). Oil with a specific density close to water has an API gravity of just above ~10°. This places it at the boundary between heavy oil (10°–12° to 20° API) that is still mobile at reservoir conditions and very-heavy oils (<10°–12° API) that has no mobility at reservoir conditions (Tissot and Welte,1984). In contrast to the small, whip-like, and floating extrusions, extensive asphalt deposits were negatively buoyant (<10° API) because they clearly flowed at the seafloor (e.g. Fig. 5.5c). Formation of asphalt deposits thus depends on viscosity of heavy to very-heavy petroleum (~10° API) that is at a tipping point: i.e. the viscosity is low enough to allow the ascent through the sediment, but after emission at the seafloor, it rapidly becomes immobile, probably due to the loss of volatile compounds. The supposition that the viscosity of heavy petroleum rapidly increases during spreading at the seafloor is substantiated by the observed flow structures. For example, the ropy surface texture of the flow shown in Fig. 5.5c seems to be a result of extension and compression. The gravity-driven downward flow was characterized by extensional forces and 'ropes' that were parallel to the flow direction whereas compressional forces seemed to occur at the 'lobe' with 'ropes' that were orientated perpendicular to the direction of movement. In general, the ropy surface structure (Fig. 5.5b–f) is largely comparable to the folds of pahoehoe magmatic lava that forms due to compression of material that is more viscous at the surface and less viscous in its interior (Fink and Fletcher, 1978; Gregg et al., 1998). Compressional forces might be exerted on the flow due to friction at the base or at retention against an obstacle (Fig. 5.10a). In a similar way, the levee-like deposits at the edges of flows (Fig. 5.5b) have been observed in lava flows that are characterized by viscosity gradients (Hulme, 1974). In contrast, the rough surface structure of the asphalt (Fig. 5.6a,b) is not directly comparable to any lava surface pattern. However, we speculate that the rough surface is the result of heavy petroleum that is too viscous to form any flow structures compared to oil that has formed ropy surfaces. Furthermore, escaping gas might have contributed to the surface roughness. Several observations point to the fact that methane as well as other volatile hydrocarbons exsolut from the heavy hydrocarbons upon deposition (Fig. 5.10b). The gas forms pores in the inner parts of the deposits, which are sealed by the relatively harder and more impermeable exterior asphalt layer. The first evidence for gas filled pores is the observation of free gas that escaped from freshly recovered asphalt samples. However, this is an equivocal finding as gas might have formed only due to the pressure relieve during sample recovery. A further evidence for gas filled pores that have developed in the asphalts after deposition comes from the experience that one asphalt sample was positively buoyant despite the fact that the hydrocarbons clearly flew at the seafloor. Exsolution of gas may lead to inhomogeneities and locally decreased density that accounts for the positive buoyancy of some pieces. Direct evidence for pores in asphalts comes from scanning electron microscopy images showing non-connected, isolated pores of varying sizes between 0.1 and 0.5 mm (Hovland et al., 2005). However, these pores were found in altered, brittle asphalt and not in recent, pliant asphalt, thus, it can not be ruled out that the pores have developed during the alteration process.
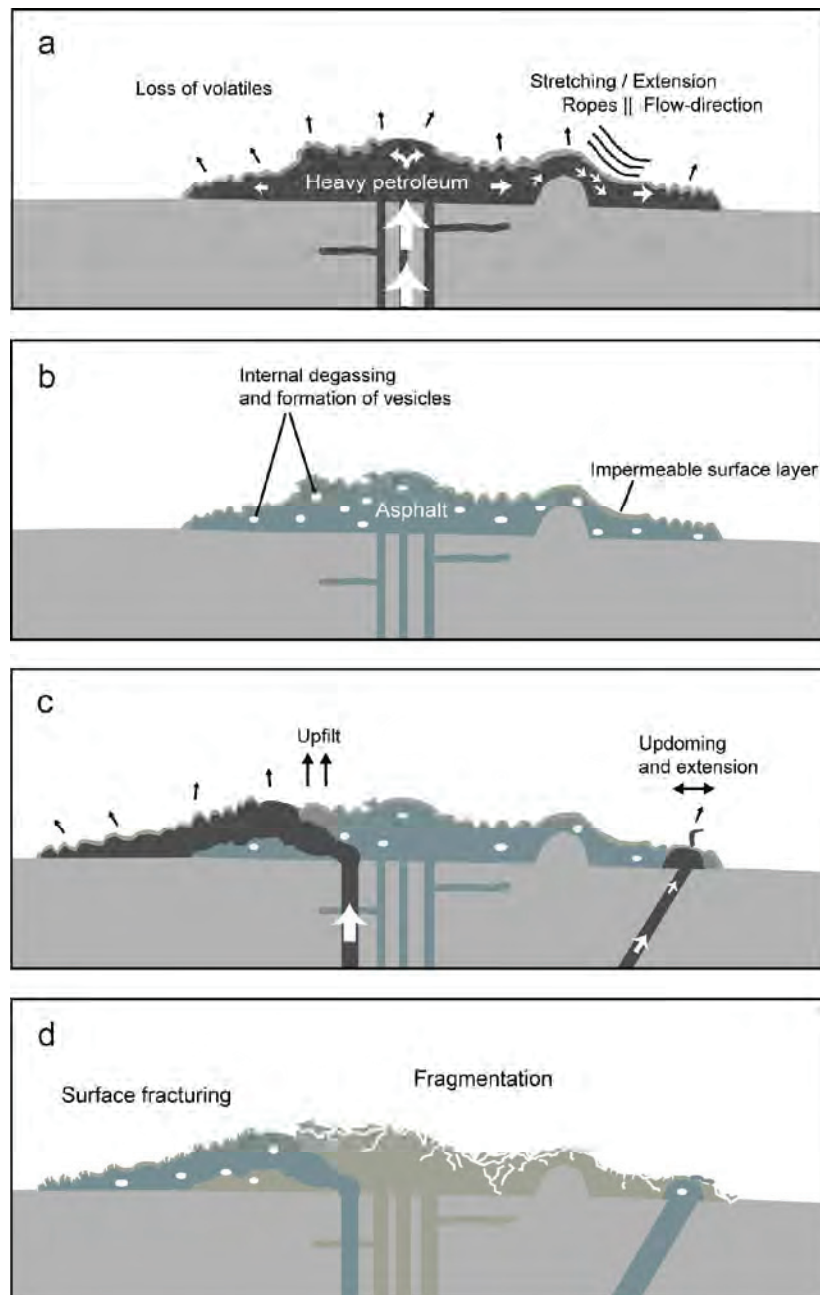
Fig. 5.10: Model of the formation of asphalt deposits at Chapopote Knoll. a) Expulsion of heavy petroleum forms characteristic flow structures due to a higher viscosity at the surface of the flow compared to the interior During deposition, the asphalts lose volatile compounds into the water column. b) The impermeable surface layer prevents further degassing into the water. Internal exsolution creates vesicles. c) Further heavy petroleum emission leads to local up-doming of and piercing through the older deposit. d) The asphalts are further altered due to biodegradation, oxidation, and further loss of volatiles, which causes shrinkage and the formation of fissures, cracks, and, finally, the fragmentation of the asphalt deposit.

Methane (and other volatile hydrocarbons) that are sealed by the impermeably exterior asphalt layer may migrate toward the base of the deposit where it eventually forms gas hydrate. Such a hydrate layer was observed at the base of the asphalt deposit sampled by gravity corer. High concentration of volatile hydrocarbons at the base of the asphalt is also indicated by the presence of vestimentiferan tubeworms that commonly root with their posterior parts below individual flows (e.g. Fig. 5.5h and Fig. 2A,D in MacDonald et al.,

60

2004). As it is known that these tubeworms generally live on hydrogen sulphide that is taken up through the posterior part of the tube (Freytag et al., 2001) it is feasible to assume that the microbial-mediated processes connected to hydrocarbon degradation primarily occur on the base of the asphalt deposit that is in contact with sediments. As illustrated in the model, different generations of flows occur and overlap each other (Fig. 5.10c). Because we did not identify discrete exit points at the seafloor, we assume that a new flow pierces through older deposits. Alternatively, rising petroleum inflated existing asphalts, leading to local up-doming and stretching of the surfaces, which produced either characteristic polygonal patterns (Fig. 5.5g) or, if the up-doming was very intensive, smooth surfaces (Fig. 5.5e,f). As the examples from the main asphalt field illustrate, more than 20 small-scale up-domed areas of asphalts exist and at least two petroleum whips were observed, which suggests continued flow of heavy petroleum below and through existing asphalt deposits. Recently deposited heavy petroleum flows are subject to alteration (Fig. 5.10d), which is probably caused by a combination of various processes, including continuing loss of volatile compounds, chemical oxidation, and biodegradation. These processes convert the originally sticky and cohesive freshly-deposited heavy-to-extra heavy petroleum to the brittle asphalt pieces without residual stickiness as described in MacDonald et al. (2004) and shown in Fig. 5.9b. The change in the consistency of the asphalts goes along with a change in the geochemical composition as shown by preliminary geochemical investigations (Schubotz et al., 2007) indicating that the brittle (most altered) asphalt pieces contained the least amount of methane and other gaseous hydrocarbons. The alteration is further accompanied by a change in the surface texture of the deposits as observed by ROV QUEST: shrinkage leads to progressive formation of fissures (Fig. 5.5f), fractures (Fig. 5.6d and Fig. 2A,B in MacDonald et al., 2004), and fragmentation of the deposits (Fig. 5.6e,h).

5.5.3. Age Constraints

All deposits that we have observed and sampled were stiff and apparently immobile. The time it takes a recently deposited asphalt to show signs of alteration such as fissures (Fig. 5.5f) might be estimated based on the tube length of vestimentiferan tubeworms. Studies of two different vestimentiferan species from sites at 550 m water depth the northern Gulf of Mexico found growth rates of about 3 cm/yr up to a length of 50 cm (Bergquist et al., 2002). This suggests a slow growth rate for cold seep vestimentiferans. Assuming that the taxonomically distinct species at Chapopote do not grow at a different rate, the average size of tubeworms provides a basis for constraining the minimum age of deposits colonized by these animals. Most of the tubes in the area of the main asphalt field (MAF) were about 20 cm long (Unit 4) but never exceeded 50 cm in length. Hence, it corresponds to an age of about 7–17 years. This age estimation may be used to obtain insight into the process of asphalt alteration after deposition. Due to the fact that fissures only occurred at some of the oldest deposits in the MAF (Fig. 5.7) we may state that it takes about a decade or longer that these signs of alteration appear on the surface of the deposit. The further process of alteration that leads to fracturing and fragmentation probably takes hundreds to thousand years, given that some of the most fragmented asphalts are sediment covered, and that the deep southern Gulf of Mexico experiences a Pleistocene sedimentation rate of about 7.5 cm/kyr (Worzel et al., 1973).

5.5.4. Significance of Heavy Petroleum Seepage

At Chapopote hydrocarbon seepage is not restricted to the extrusion of heavy to very-heavy petroleum which leads to the asphalt deposits but is accompanied by less viscous petroleum seepage, the escape of gas bubbles, as well as oil-coated gas bubbles, that lead to the formation of oil slicks on the sea surface (MacDonald et al., 2004). While the latter sources are unconstrained, we roughly calculated the volume of asphalts at the main asphalt field (MAF) at the south-western rim of Chapopote in the order of 4 ($\pm$2) x 10^3 m³. In order to set this value in relation to published hydrocarbon seeping rates we may assume that the MAF is at least about 20 years old, as indicated by the maximum length of the vestimentiferan tubeworms. If we further consider that the seepage is continuous over time, we may estimate a seeping rate that is 200 ($\pm$100) m³/year or less. We believe that this estimated value is high and that the actual average seeping rate is somehow lower. At first, the deposit is likely to be older than 20 years as tubeworm settlement may have started several years after deposition of the heavy hydrocarbon at the seafloor. Furthermore, the process of seepage of high-viscosity oil is likely to be very slow itself. In addition, hydrocarbon seepage that leads to asphalt deposition is probably a discontinuous process that occurs in pulses. Despite these considerations, we may compare the heavy hydrocarbon seepage rate of less than 200 ($\pm$100) m³/year for the MAF at Chapopote Knoll in the southern Gulf of Mexico with values from the hydrocarbon seepage province in the northern gulf. MacDonald et al. (1993, 2005) estimated the amount of oil that rises up to the sea surface from natural oil seeps using satellite data. This oil is probably transported as coating around gas bubbles (De Beukelaer et al., 2003). About 20,000–86,000 m³/year hydrocarbons are released along this pathway in the area offshore Louisiana, which is at least a factor of 100 more than the average annual seeping rate at Chapopote. However, at more than 40 knolls and local summits of ridges in the Bay of Campeche oil slicks have been identified in satellite data suggesting that hydrocarbon seepage is in general an abundant phenomenon in the southern Gulf of Mexico (Ding et al., 2010b). Assuming that at least some of these knolls and ridges are comparable to Chapopote with asphalt deposits of similar extent, we propose that heavy petroleum seepage in the southern Gulf of Mexico is a significant process that is comparable to the much better documented hydrocarbon seepage without asphalt deposits in the northern part of the Gulf.

5.6. Conclusion

The present ROV-based study confirms the concept that asphalt deposits at Chapopote originate from the seepage of heavy to very heavy petroleum at the seafloor. The viscosity of the seeping oil with an API gravity close to 10° is high due to the combined effect of, firstly, a crude oil that is anyway heavy in the Bay of Campeche (~22° API; Magoon et al., 2001) and, secondly, a shallow hydrocarbon reservoir that is only 100–200 m below the summit area at Chapopote (Ding et al., 2008a). The shallow reservoir makes the oil susceptible to biodegradation mainly due to the low temperature and an extensive oil–water contact zone (Head et al., 2003). Asphalt volcanism is distinct from oil and gas seepage previously described in the Gulf of Mexico and elsewhere because it is characterized by episodic intrusions of semi-solid hydrocarbon that spread laterally over substantial area and produce structures with significant vertical relief. Although the process implies a pressure release cycle in which material accumulates in shallow reservoirs before breaking through, we find no evidence that this is an exothermal process. At Chapopote, asphalt volcanism occurs at the crest of a large salt structure. Other examples in the southern Gulf of Mexico show similar localization. It is inferred therefore that, like mud volcanism, asphalt volcanism is a secondary

result of salt tectonism. Faulting and mass-wasting in evidence at the Chapopote salt dome is probably attributed to salt movement and over-steepening at the flanks of the knoll.

Acknowledgements

6

Seafloor Development at Purely Gas Driven Batumi Seep, eastern Black Sea - Separation of Backscatter Signatures into their Origins

Markus Brüning [a], Gregor von Halem [a], Heiko Sahling [a], Ingo Klaucke [b], Thomas Pape [a], Gerhard Bohrmann [a]

[a] MARUM, Center for Marine Environmental Sciences and Department of Geosciences, University of Bremen, GEO Building, PO 330440, 28334 Bremen, Germany
[b] IfM – GEOMAR, Wischhofstrasse 1-3, 24148 Kiel, Germany

Abstract

Batumi Seep is a purely gas driven cold seep system in the eastern Black Sea on the continental slope offshore Georgia. It is located on Kobuleti Ridge in water depth between 840 and 860 m inside the gas hydrate stability zone. The site was surveyed acoustically by vessel-mounted multibeam echo sounder, 75 and 410 kHz deep-towed side scan sonar, and 4 kHz sub-bottom profiler. Mapping was ground-truthed by visual observations of the seafloor, conventional and pressure core sampling. We found a structured high backscatter zone, surrounded by a medium backscatter halo. The high backscatter matches backscatter signatures in the higher side scan frequency and seafloor positions of gas vents. Seafloor morphologies like structured, hummocky, and smooth, observed visually fit 410 kHz side scan imagery. Authigenic carbonates were found in high backscatter areas, whereas gas hydrates were found ubiquitous in medium and high backscatter of 75 kHz. We explain the origin of backscatter pattern of the 75 kHz frequency to be morphology, carbonate, gas in the water column, gas hydrate for high intensity, but solely gas hydrate for the surrounding medium backscatter halo. We suggest a succession of processes responsible for the observations: formation of a sealing gas hydrate cap after gas invasion, thereby diversion and spreading of gas, rupture of the seafloor in central parts, resulting in eroded rough morphology and accompanied by vigorous gas flow. The seep was found to be stable within years. The amount of gas hydrate stored within the top 20 m below seafloor is 1700 kt. A content of at least 75 % massive gas hydrate was calculated to provide sufficient buoyancy for rafting of sediment.

6.1 Introduction

At cold seeps fluids, liquids and gases, escape from the sediment into the ocean. Depending on local settings, fluid composition, and flow rates different seeps develop. Examples are mud volcanoes, e.g. Dvurechenski mud volcano (Bohrmann et al., 2003), mounds offshore Costa Rica (Sahling et al., 2008a), mud volcanoes in the Anaximander Mountains, eastern Mediterranean Sea (Lykousis et al., 2004), and Håkon Mosby mud volcano (Ginsburg et al., 1999). In almost all cases both gas and liquid occur combined, and the individual effects of the components on the characteristics of the seep remain unclear. Batumi Seep offshore Georgia is different as it is solely based on advection of gas and is an ideal example for a purely gas-driven cold seep system (Klaucke et al., 2006; Haeckel et al., 2008). Below the seafloor gas forms hydrate (Klaucke et al., 2006; Klapp et al., 2010), but gas also escapes as free bubbles into the water column (Klaucke et al., 2005; Nikolovska et al., 2008). There are no fauna and no higher organisms present due to the anoxic conditions of the Black Sea (Deuser, 1974). Hence, biota does not obscure processes of interaction between sediment and gas flow with, e.g. accumulation of shell beds. However, Anaerobic Oxidation of Methane (AOM) (Boetius et al., 2000) is performed by microorganisms below the seafloor at the sulfate methane interface and precipitates of carbonate as residuum accumulated (Klaucke et al., 2006).

Batumi can serve as a model for other gas-influenced seeps, where deep-sourced gas rises into the gas hydrate stability zone, transits it (Flemings et al., 2003), then forms shallow gas hydrates close to the seafloor, or gas escapes into the water column. Similar systems are Blake Ridge (Gorman et al., 2002) and Hydrate Ridge (Tréhu et al., 2004) on the east and west coast of North America, respectively, the Kouilou pockmarks in West Africa (Sahling et al., 2008b), and seeps in the Sea of Okhotsk (Luan et al., 2008). A complete understanding of

Batumi Seep would lead to more insights at other locations with mixed fluid sources and biological communities, too.

We aim to evaluate the relationship between the backscatter halo already presented by Klaucke et al. (2006) and the stored gas hydrate. To achieve understanding we apply different complementing methods: multibeam echo sounder, side scan sonars, sub-bottom profiler, video observations, and coring A 75 kHz side scan sonar was the main tool and others guided the interpretation of the backscatter imagery. Generally, backscatter strength is influenced by local geometry / slope, roughness of seafloor, and intrinsic material properties (Blondel and Murton, 1997). Gas in the ray path of the sonar in the water column also strongly affects the acoustic signal (Klaucke et al., 2005; Nikolovska et al., 2008).

This study is based on data of RV METEOR Cruise M72/3 in March and April 2007. We are in the rare, and privileged, situation to have a full coverage of the seep with two side scan frequencies. Visual observations by Remotely Operated Vehicle (ROV) allow for good interpretation of side scan imagery. Questions about causes of particular backscatter anomalies, development of encountered seafloor morphologies, and the content of gas hydrate are to be answered. As Batumi Seep was seen to be a very dynamic system in terms of gas emissions (Sahling et al., 2004; Akhmetzhanov et al., 2007), the question is how influenced morphologies and how stable gas hydrate below the seafloor are, if it changes within a time span of years. To complete the picture of the area, other studies on Batumi Seep are submitted or already published: seismic investigations (Wagner-Friedrichs, 2007), on the gas seepage from a chemical point of view (Pape et al., 2010; Pape et al., 2011), and on the quantification of gas released into the water (Nikolovska et al., 2008).

6.2 Regional Setting

The work area is located in the easternmost part of the Black Sea on the Georgian continental slope. The seafloor there is made up of several east-west trending canyons and ridges. The latter are underlain by diapiric structures (Klaucke et al., 2006; Wagner-Friederichs, 2007). They originate from compressional conditions starting in Eocene time due to the northward move of the Arabian Plate into Eurasia (Spadini et al., 1996; Nikishin et al., 2003). Consequently, the eastern Black Sea is bound by mountain chains, the Greater Caucasus to the north and the Eastern Pontides to the south (Robinson et al., 1996).

The water-body of the Black Sea was and is crucially controlled by the limited exchange to world oceans through the Bosporus Strait (Scholten, 1974). Subsequently, a characteristic sequence of sediment was deposited, and is pervasive in the entire basin. During the Pleistocene and until 9000 years BP the Black Sea was an aerated fresh water lake. Then, caused by rising sea level after deglaciation, heavier salt water spilled from the Mediterranean through the Bosporus. The denser water sank to the bottom and led to density stratification of the Black Sea (Deuser, 1974), which limited downward mixing of oxygen. Therefore anoxic conditions developed and spread upwards to a recent level of $100 - 200$ m below sea level.

Conditions in the water column are recorded by sediments. Ross and Degens (1974) defined three distinct units pervasively found in the Black Sea: Unit 1 is the most recent, deposited during conditions like at present, usually 30 cm thick. It consists of light and dark micro-laminae of coccolith ooze with >40 % calcium carbonate. Dark layers contain more organic matter. The base of the Unit 1 is dated to be 3000 years BP. Following below is Unit 2 with 40 cm thickness and composed of sapropel containing up to 50 % organic matter. The base of Unit 2 is dated as the onset of anoxic conditions in the specific water depth, which is 6200 years BP for 500 m below sea level. The deepest, Unit 3, consists of alternating light and dark lutite layers deposited during lacustrine conditions. Unit 3 extends to larger depths.

Deeper sediments are prone to produce oil and gas. Oil source rocks were described onshore in Georgia (Robinson et al., 1997). Even though their extend is unknown offshore, Klaucke et al. (2006) and Akhmetzhanov et al. (2007) showed several seep sites on the continental slope where hydrocarbons reach the seafloor (Fig. 6.1). Wagner-Friedrichs (2007) showed a Bottom Simulating Reflector (BSR) beneath the 850 m deep part of the Kobuleti Ridge, where Batumi Seep is located.
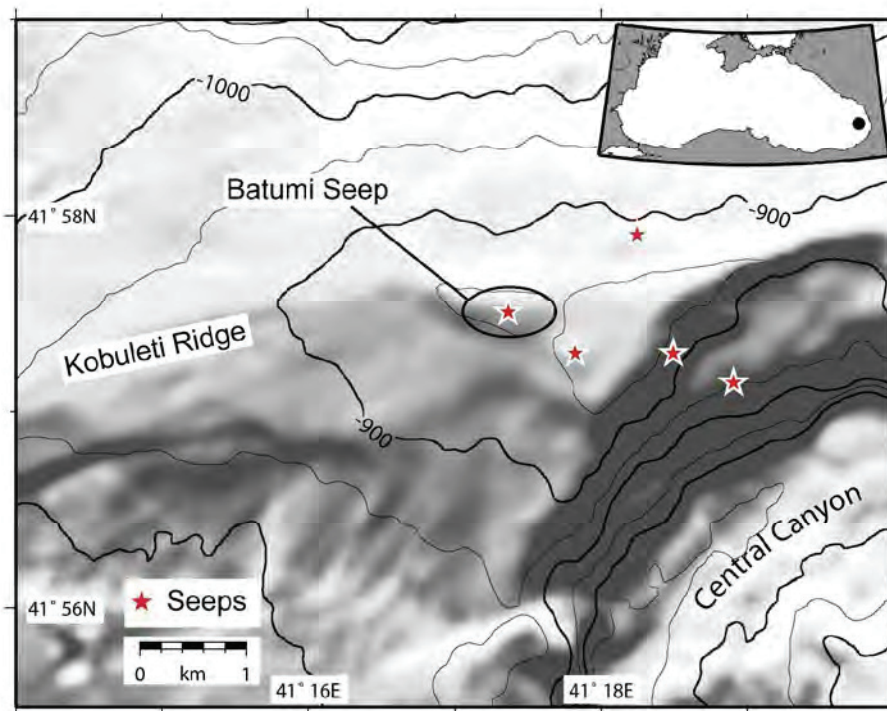
Fig. 6.1: Bathymetric map of the Batumi Seep area. M72/3 KONGSBERG EM120 data. Batumi Seep is situated on Kobuleti Ridge running from east to west. In the south-eastern part of the figure runs "Central Canyon". Small map: Location of Batumi Seep in the eastern Black Sea.

6.3 Methods

The RV METEOR Cruise M72/3 was divided into two legs. During leg A a Remotely Operated Vehicle (ROV) was available for dive work. Data published by Klaucke et al. (2006) served as navigation base for dives at Batumi Seep as the more detailed surveys presented here were not yet available then. For leg B equipment onboard was exchanged to perform acoustical surveys: multi-channel seismics and side scan sonar.

6.3.1 Multibeam Echo Sounder

Bathymetric data of the Georgian continental slope was collected during legs M72/3 A and B. A KONGSBERG EM120 12 kHz multibeam echo sounder was run for surveys of the entire slope. A more detailed mapping of the Kobuleti Ridge, especially Batumi Seep, was done with a higher resolution KONGSBERG EM710 70-100 kHz swath system (Bohrmann et al., 2007). Seven manually edited profiles recorded during a seismic 3 D survey yielded a sufficient coverage to produce a bathymetric grid with 8 m cell spacing at 30 to 70 soundings per cell. We used IFREMER's CARAIBES software to process data, followed by the Generic Mapping Tool (GMT) and ESRI ARCGIS softwares to produce maps.

6.3.2 Side Scan Sonar

The seafloor of Batumi Seep was mapped by an EDGE TECH DTS-1 deep-towed side scan sonar, which is operated by IfM-GEOMAR. The DTS is a dual-frequency sonar utilising a 75 and/or 410 kHz chirp signal. The across-track-ranges are 750 m and 100 m, respectively. To obtain an optimal ensonification of the seafloor, altitudes above the ground were kept to 100-150 m and around 15 m, respectively. This was achieved by adjusting the tow-cable length. Across-track resolutions are 1.8 cm for the high frequency, and 10 cm for the low frequency, whereas the along-track resolution is 1.3 m at 750 m range and 0.2 m at 100 m rage at the applied speed over ground of 2.5 to 3 kn (1.3 to 1.5 m/s). As the Batumi Seep was discovered with the DTS system in 2004, profiles were placed to extend on that known basis. A first single 75 kHz survey was located along the identical line as reported in Klaucke et al. (2006). It was followed by 10 parallel 410 kHz profiles across the 75 kHz profile. According to the geometrical constraints pixel sizes of 1 m and 25 cm were selected in the processing. It was performed with IFREMER's CARAIBES software, and, mainly, NOC's PRISM (Le Bas et al., 1995; Le Bas, 1997). Due to overlapping of the high frequency profiles a stencilling (cutting) was necessary and done with an extension of PRISM for LEICA ERDAS. Finally, maps were imported to ESRI ARCGIS.

6.3.3 Visual Observations

On leg M72/3 A MARUM's work-class Remotely Operated Vehicle (ROV) "QUEST 4000 m" was deployed at Batumi Seep in four dives (Table 6.1). For visual control QUEST was equipped with three video cameras and a suit of lamps. Videos of two cameras were stored on miniDV tape and as digital frame grabs recorded every 5 seconds. Additionally, high resolution still images were taken at features of interest manually with a 3 MPix camera. An IXSEA POSIDONIA USBL system provided data for navigation. Post-dive processing utilising ARCGIS and IFREMER's ADELIE software extension on the GIS yielded precise position data to locate videos and images on the seafloor. Tracks of the 4 dives add up to a distance of 2000 metres travelled with seafloor observations. ROV work was concentrated at and around gas emission sites, partially within the water column above the seafloor without visual contact to the ground, nevertheless there were profiles of observations between the gas seeps.

Tab. 6.1: ROV dives at Batumi Seep during M72/3 A.

GeoB No.	Start		End		Duration
	Latitude N	Longitude W	Latitude N	Longitude W	[hh:mm]
11904 / Dive 156	41°57.945'	41°17.108'	41°57.565'	41°17.507'	09:55
11907 / Dive 157	41°57.520'	41°17.100'	41°57.542'	41°17.412'	08:45
11919 / Dive 162	41°57.531'	41°17.342'	41°57.401'	41°17.273'	06:30
11921 / Dive 163	41°57.400'	41°17.267'	41°57.542'	41°17.840'	13:36

6.3.4 Adjustment of Side Scan Sonar and Video Surveys

We were able to perform a correction-shift to align side scan sonar data and video observations to make more accurate comparison at the metre-scale possible. As the ROV almost vertically below the stern, we judge the ROV-POSIDONIA positions as most accurate of the different systems. Because the deep-towed side scan sonar fish was dragged up to 1500 m behind the vessel, we aimed to adjust its positions by the more precise ROV navigation.

Therefore we looked for features to use as fix-points, which are clearly identifiable in all surveys. A scarp at 41°57.46N, 41°17.49E is an ideal feature (Fig. 6.2 and 6.3). It was visually observed by ROV. It unequivocally appears in the 410 kHz sonar imagery. Hence, we shifted the whole 410 kHz imagery 25 m to the north-west. We assume a remaining uncertainty of +/-2 m for these both systems. The 75 kHz imagery was compared with the shifted 410 kHz map. Expressions of faults on the seafloor visible in both frequencies served as fix-points for adjustment. With a shift of 35 m SW faults as well as high backscatter in 75 kHz imagery align with irregular backscatter in 410 kHz imagery. The shifting process was concentrated on the central and eastern part of Batumi Seep, because the 75 kHz imagery seems to have geometric distortions in the fault expression in the west. We presume positioning errors of +/-5 m for the part east of the nadir / tow-fish track, and +/- 50 m for the western part.

6.3.5 Sub-bottom Profiler

An ATLAS PARASOUND echo sounder provided information on sediment structures (Bohrmann et al., 2007). The system generates a 4 kHz signal restricted to a 4° cone due to a parametric superposition of two higher primary frequencies. Maximum penetration was around 200 m at a vertical resolution of 10 cm. The horizontal resolution was 15 pings/100 m.

6.3.6 Sediment and Gas Sampling

Sediments were cored with two devices, a gravity corer (GC) and a Dynamic Autoclave Piston Corer (DAPC). The GC consisted of a 14 cm diameter core barrel of 3.5 or 6.0 m length with a weight of 800 kg. It was lowered into the seafloor at rope speed of 1.0 to 1.5 m/s. The GCs were positioned precisely by USBL (IXSEA POSIDONIA) (Bohrmann et al., 2007). The DAPC is a piston corer that recovers samples under in situ pressures to ensure gas hydrates do not disintegrate during recovery. The core barrel is 2.5 m long and has a diameter of 8.4 cm (Abegg et al., 2008). Back on the vessel the core can be degassed in controlled manner with gas being sampled (Pape et al., 2011).

6.3.7 Calculations of Hydrate and Methane

Hydrate in place was calculated with the following equation

$$V_{GH} = A * z * \phi * P \qquad\qquad\qquad \text{(Eq. 6.3.1)}$$

V_{GH} − volume of gas hydrate within the seafloor, A − surface area, i.e. medium backscatter zone, z − layer thickness, ϕ − pore volume = porosity, P − percentage of hydrate in pore space

Conditions for buoyancy are reached at a minimum gas hydrate layer thickness of:-

$$d_2 = \frac{\rho_{sedi}(1-\phi)d_1}{\rho_{GH}} \qquad\qquad\qquad \text{(Eq. 6.3.2)}$$

d_2 − minimum layer thickness necessary for buoyancy, ρ_{sedi} − sediment density, (1-ϕ) − sediment volume, i.e. (1 − porosity), d_1 − layer thickness of sediment to be lifted, ρ_{GH} − density of gas hydrate layer

Constants and variables are collected in Table 6.2.

Tab. 6.2: Figures used in rafting-calculation.

Variable / Constant	Value	Units	Source
Density Sea Water, Black Sea	1021	kg/m³	Pape et al., subm.
Bottom Water Temperature at Batumi Seep	9	°C	Bohrmann et al., 2007
Density Gas Hydrate	910	kg/m³	Haeckel et al., 2008
Density Methane Gas, 84 bar, 9°C	68.86	kg/m³	peacesoftware.de/eigenwerte
Density of bubble fabric hydrate, 80/20%	237	kg/m³	calculated from above
Porosity Unit 1	85	%	Haeckel et al., 2008
Porosity Unit 2	72	%	Haeckel et al., 2008
Porosity Unit 3	61	%	Haeckel et al., 2008
Density Unit 1 (dry)	2529	kg/m³	Pape, T., pers. Comm., 2009
Density Unit 2 (dry)	2500	kg/m³	Pape, T., pers. Comm., 2009
Density Unit 3 (dry)	2631	kg/m³	Pape, T., pers. Comm., 2009

6.4 Results

6.4.1 Overview

The Batumi Seep is located on a local high of Kobuleti Ridge in water depth between 840 and 860 m. The rather flat summit of the ridge was surrounded by a zone of seafloor undulations where depth varies by $1 - 4$ m on the west, south and east. The flanks of the ridge farther down were smooth and homogenous without topographic features. The northern slope was steeper than that to the south (Fig. 6.2a). An east-west (105°) trending fault cut through the top of the ridge. It was discernable in bathymetry, but much clearer in side scan sonar imagery figures (Fig. 6.2a,b,c). Many gas vents were observed in the flat ridge-top and undulating areas south of the fault.

Roughly in the same area 410 kHz side scan imagery indicated a structured seafloor, bound to the north by the clearly visible fault. It was broken up into 11 segments of about 200 m length and incised the seafloor. Lateral displacement was not observed. Other structures consisted of high and low linear or semi-circular backscatter oriented in an E-W direction. Lengths of these structures were in the order of several tens of metres. They covered an area of 900 by 300 m or ~0.2 km² on the seafloor (Fig. 6.2b). A detailed description will follow later in chapter 6.4.2.

The backscatter anomaly of 75 kHz side scan sonar had a larger extent; it enclosed the area the 410 kHz anomaly and extended down the ridge. The elliptical anomaly was about 1500 by 500 m or 0.6 km² large. In contrast to the low-homogenous backscatter seafloor surrounding, it consisted of medium and high backscatter zones. Again, the segmented fault was clearly visible. In the western part it showed an incision on the seafloor, to the east it comprised high backscatter only. The high backscatter zone (0.22 km²) was almost identical with the extent of structured seafloor in 410 kHz imagery. In the eastern part it was rather homogenous, but interconnected by medium backscatter zones, whereas in the west it showed structures with semi-circular nature (Fig. 6.2c). A medium backscatter zone surrounded high backscatter. In the east there was a round sharp borderline to low backscatter. We will therefore refer to this as a "halo". To the west medium backscatter weakened and had a frayed boundary to low backscatter. High backscatter indicated bubble flares on the rim of the halo in the north-east and south. The instantaneously changing backscatter across nadir on outer limits of the anomaly originates due to the side scan vehicle track diagonal across the ridge.

On one side there was illumination against slope on the other side parallel or down slope. Backscatter returns became accordingly increased and decreased.

Several sediment cores were taken by GC and DAPC to correlate backscatter intensity to samples. At several sites of high backscatter, carbonates occurred at the seafloor or in shallow sediments above 40 cm depth (Fig. 6.2d). Gas hydrates and signs of hydrate dissociation in cores (moussy and soupy texture) were found pervasive at Batumi Seep. Hydrates appeared at high as well as at medium backscatter locations, in shallow sediments and down to maximum penetration depth of 4.13 m. GCs GeoB 11946 and 11975 from the eastern medium backscatter area revealed hydrates. Massive pieces were present in the first core in the interval minimum from1.52, likely higher, down to at least 3.04 m bsf, but moussy sediment structures indicated former hydrate presence in Units 1 and 2, too. In the other core hydrates started at 1.23 down to at least 3.04 m bsf. Besides these vent-specific materials we recovered the usual Black Sea sequence of Unit 1 to 3 (Degens and Ross, 1974). However, the units occurred in largely varying and locally changing thicknesses. Even below identical ship's positions un-equal sequence thicknesses had been found.

4 kHz sediment echo sounding profiles showed three different sub-surface signatures on Kobuleti Ridge across Batumi Seep. Off the seep sediments were well stratified and acoustical penetration reached 60 m below seafloor (Fig. 6.3). At the seep, exactly corresponding to the halo on the seafloor we observed a zone of blanking in the sediments, indicating free gas, which prevents further passing of seismic energy causing transparency (Anderson and Hampton, 1980). Blanking started at 20 m bsf on average, around 15 m bsf to the east of the 75 kHz backscatter anomaly, with the resolved sediment body above the transparent zone becoming thicker towards the west. Towards the west the blanking also turned narrower laterally. At the southern side of the seep, overburden above the transparent zone was in many places ~10 m thick. Sediments above blanking comprised irregularly strong reflectors. Several strong reflectors extended for about 100 m laterally in varying depths and positions (Fig. 6.3). Due to the limited penetration of coring we cannot correlate them to samples. These large scale observations were supported on a smaller scale to complete understanding of the total system.

Fig. 6.2 (next page): Maps comparing sonar data. a) Bathymetric map of the Batumi Seep area compiled from EM710 soundings. Grid spacing is 8 metre. Dots mark individual gas flares identified from EM710 water column displays. b) DTS 410 kHz side scan sonar imagery. Light colours represent high backscatter. Processed at a pixel size of 0.25 m. Strong bright and dark grey-levels around nadir are caused by varying altitudes above seafloor, target altitude was 15 m. c) DTS 75 kHz side scan sonar imagery. Light colours represent high backscatter. Processed at a pixel size of 1 m. Straight dark lines on the eastern side of the map are artefacts. d) Interpretation of both side scan sonar frequencies, flare locations as determined from EM710 soundings, and shallow occurrence of carbonates.
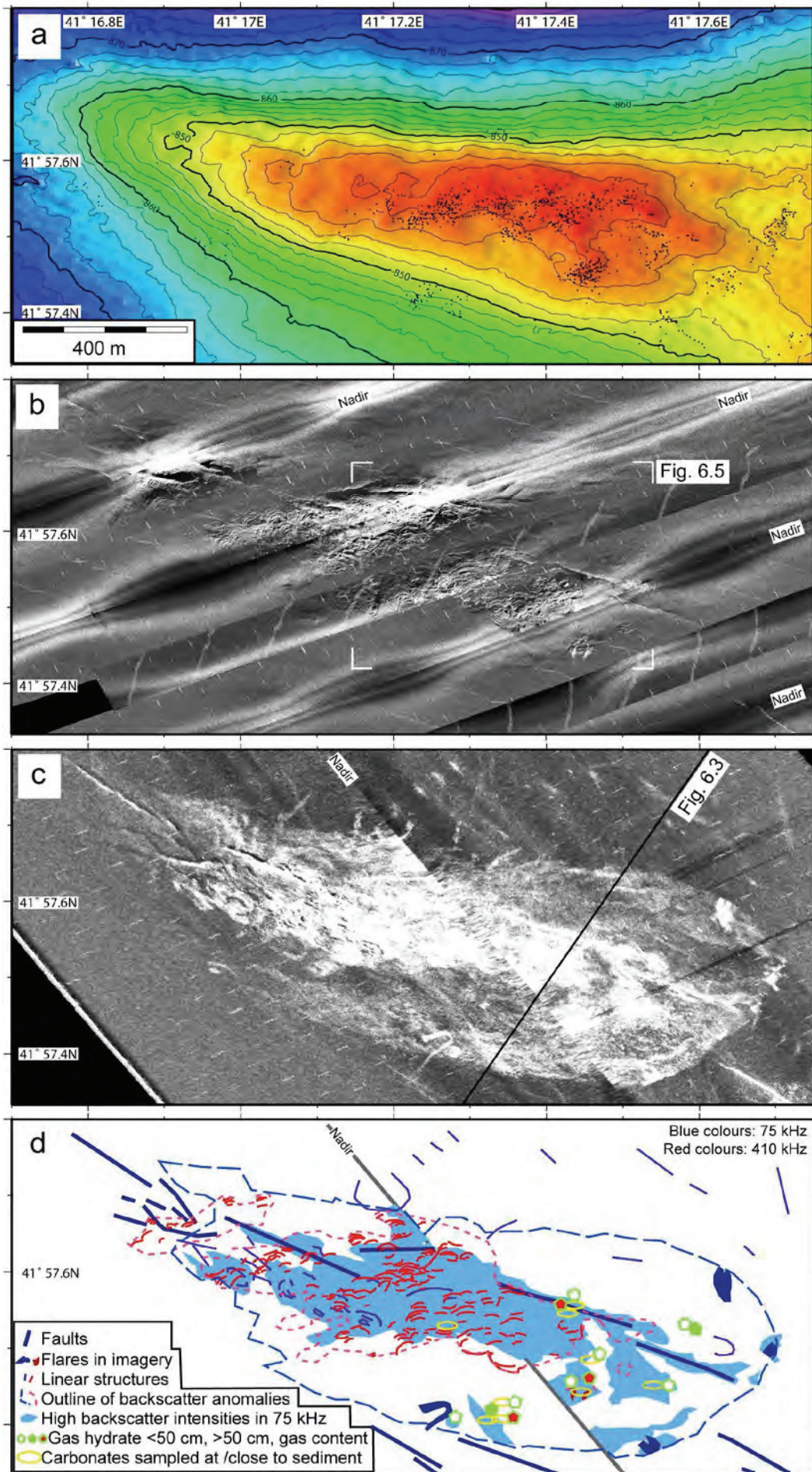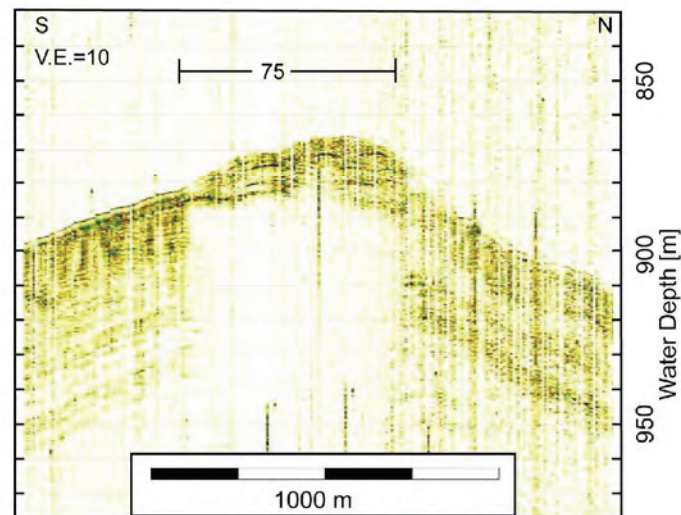
Fig. 6.3: 4 kHz ATLAS PARASOUND profile across Batumi Seep. Bar indicates extent of backscatter anomaly (halo) in side scan imagery. Note irregularly distributed strong reflectors in sediment above acoustical blanking. Intense vertical lines are due to interference with another echo sounder.

6.4.2 Small Scale Morphology

Visual observation of the seafloor showed strongly varying morphologies, from smooth flat sediment to rough blocks, steep walls and vertical chimneys (Fig. 6.4). We later discuss interpretation of the 410 kHz side scan with imagery optical surveillance. The observation made by ROV QUEST focused on the inspection on actively bubbling gas vents. The vent sites themselves, as well as in the parts in-between them, a series of morphology zones was discovered: structured, chimney-covered, smooth-structured, hummocky, smooth, and perforated seafloors.

Structured seafloor comprised a rough and irregular morphology. The ground was formed by asymmetrically shaped pieces of sediment. Nearly vertical scarps did often expose lighter coloured sediments. Steep walls had heights up to one metre (Fig. 6.4d).

Smooth structured seafloor was similar to the former, but had a cover of recent soft sediment, 10 and more centimetre thick, concealing sharp edges (Fig. 6.4c).

Chimney-like structures were superimposed on structured or smooth structured seafloor. The chimneys were up to 40 cm high and 3 to 10 cm thick vertical pinnacles rising up into the water. The diameter of individual chimneys changed along their length which appears like a spiral-like shape in some cases. They were based on local highs of rounded shape and up to one metre diameter.

A *hummocky seafloor* had a smooth surface of soft sediments, but undulations of 10 to 40 cm height with wavelengths of several metres. Isolated mounds of several decimetres height and with diameters of up to one metre were seen, too (Fig.6.4b).

A *smooth seafloor* showed no morphology or elevations like undisturbed usual non-seep deep sea areas.

Perforation of the seafloor occurred superimposed on the previous forms. Dense clusters of partially interconnected, holes covered the ground. Diameter and width of the cone shaped depressions was around 5 cm. The inner walls uncovered fine horizontal laminations of light and dark grey sediment layers of 1 to 3 mm thickness each (Fig.6.4a, e).
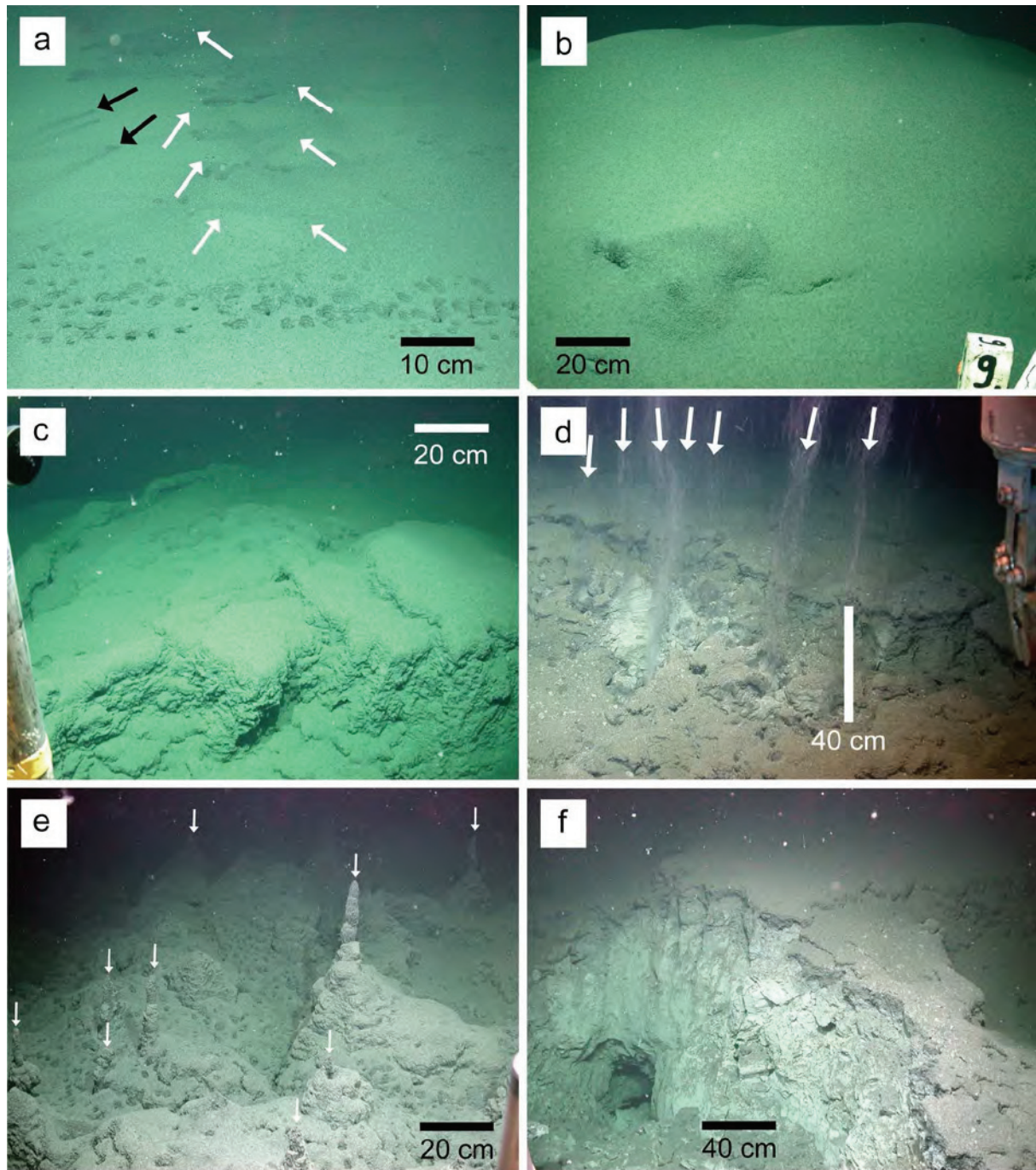
Fig. 6.4: Photos taken by ROV.
a) Smooth seafloor, perforated in the foreground. Some of the holes release rising gas bubbles, indicated by white arrows, into the water. Three holes in the background have a spur of darker sediment blow-out (black arrows). b) Hummocky seafloor. Undulations are decimetres high and have a wavelength in the order of metres. c) Smooth-structured seafloor. A layer of recent sediment masks rough structures below. d) Scarp and structured seafloor. In-between seafloor covered by soft sediment, several bubble streams rise from rough seafloor. Light horizontally layered sediment indicates a fresh outcrop on the left hand side. e) Chimney-like structures. Long narrow poles, up to 40 cm long, stand upright based on carbonate concretions. Soft sediment on the seafloor is perforated by holes. f) Structured seafloor with steep scarp, fresh outcrop of formerly buried sediment beneath smooth flat seafloor. There is a ~30 cm diameter hole at the base of scarp.

Seepage of free gas bubbles emanated from these holes, often from holes aligned on a straight line (Fig. 6.4d). However, only a small fraction of holes was active at a time (Fig. 6.4a). Some very intense gas flows discharged from larger holes of 15 to 20 cm diameter. Seepage varied in intensity. During one dive it was encountered to increase from quiescence to several L/min within several minutes (Sahling, pers. com., 2009). No gas was seen to escape from the chimneys.

Visual observations correlate with the 410 kHz side scan sonar imagery. Figure 6.5 presents an overlay of both. First, outside of the feature-rich central part smooth feature-less seafloor was visible in both acoustical and optical systems. Secondly, the outline of side scan structures accompanied with scarps or smaller and smooth slopes (downward to the centre) in the video observations. All the area containing structures in the side scan imagery represented a depression. The drop into the depression followed rather high backscatter and very small scale structures representing a hummocky seafloor. The very central part of observations was made up of structured and smooth structured, partly with chimney-like features, and many scarps. The imagery provided a very similar impression with several east-west oriented bright and dark areas indicating ridges and valleys. Smooth structured seafloor was found in an area with relatively lower backscatter intensity, which correlated well with the visually observed soft sediment cover of the seafloor attenuating acoustic energy.
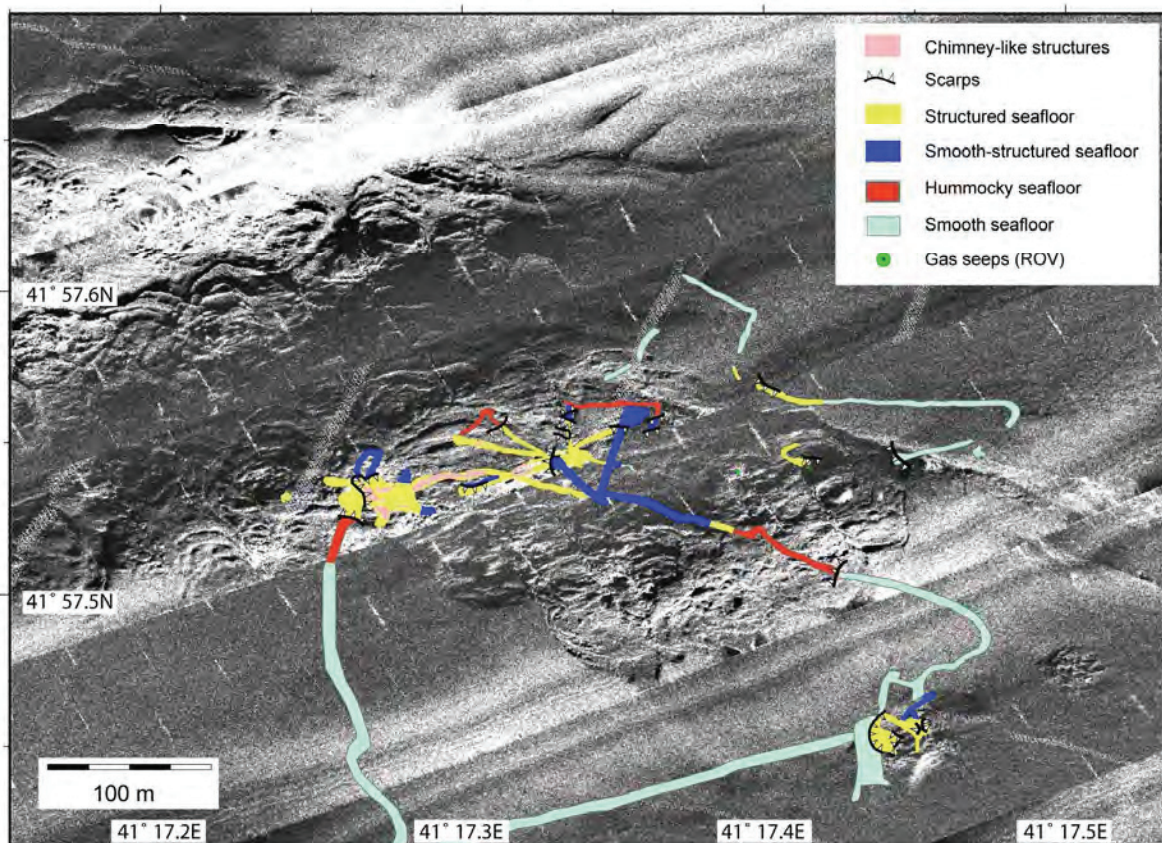
Fig. 6.5: Enlargement of 410 kHz side scan sonar imagery and ROV seafloor observations. Light colours represent high backscatter. Processed at a pixel size of 0.25 m. Strong bright and dark grey-levels around nadir are artefacts.

6.5 Discussion

6.5.1 Origin of 75 kHz Backscatter Anomaly

Observations made so far allow us to define causes for the features on 75 kHz side scan imagery. We assume a maximum penetration of 2 m in soft sediments (Mitchell, 1993; Klaucke et al., 2008; Sahling et al., 2008b). Hard substrates, however, decrease the value instantaneously. Rough seafloor encountered in 410 kHz side scan sonar imagery, and identified by video observations, correlates with high backscatter in 75 kHz side scan sonar. Two isolated high backscatter areas in the south eastern part are larger (~100 m diameter) than the encountered structures in 410 kHz (75 and 40 m). In the western part of Batumi Seep both outlines fit approximately, the 75 kHz high backscatter is by trend not as large in extent (Fig.6.6a). Firstly, the high backscatter of the lower frequency can be attributed to the roughness of the local slope. Where the high frequency resolves and images the slopes, the larger footprint and pixel size of the low frequency only delivers high backscatter intensity (Blondel and Murton, 1997). Secondly, these results fit well to findings of Klaucke et al. (2008) who found a good agreement of 410 kHz and video observations. 75 kHz high backscatter returned generally a larger high backscatter area than the visible features on the seafloor at seep sites due to deeper penetration into the seafloor.

Gas bubbles in the water above the seafloor appear as high, characteristically curved backscatter in side scan imagery (Klaucke et al., 2005). Many bubble flares were recorded by vessel-based multibeam echo sounder EM710 (Nikolovska et al., 2008; more positions added, Sahling, pers. comm., 2009). Their seafloor positions are marked in Figures 6.2a and 6.6b. These flare positions were found within both cruises, M72/3 A and B, but were not active continuously. Most were located in high backscatter areas mentioned before, where they are not discernable as there is no additional contribution to the backscatter strength. Many flare positions are to be found on an isolated high backscatter spot, which overlays a much smaller rough morphology seafloor in the south eastern part of Batumi Seep. Here free gas in the water column can explain the high backscatter. Several flares were situated along the halo rim. At three locations this fits to flare-shaped high backscatter caused by rising gas bubbles. Widespread distribution of gas in the sediments can be excluded from PARASOUND data. The gas front found was much too deep at 20 m bsf and was beyond the penetration of DTS side scan sonar. We assume very shallow gas only to be present related to active gas seepage sites in the feeder-channels.

Authigenic carbonates as hard reflector on the seafloor or in the shallow sub-surface would increase backscatter. They were only recovered in cores from high backscatter areas, where they certainly contribute to the backscatter intensity.

Summing up, high backscatter in 75 kHz imagery can be explained by the presence of a (1) rough seafloor morphology, (2) rising gas bubbles, (3) authigenic carbonates. This, however, still leaves half of the backscatter anomaly, the medium backscatter intensity, unexplained. There is only one candidate remaining, which can create the measured data. It is gas hydrate, which was discovered as hard substrate in a medium backscatter zone in the eastern part of Batumi Seep. Pape et al. (2010 and 2011) found gas hydrate to occur most concentrated just below Unit 2 in the top of Unit 3. This interval was found at a depth of ~1.2 m bsf in the eastern medium backscatter area of the halo.
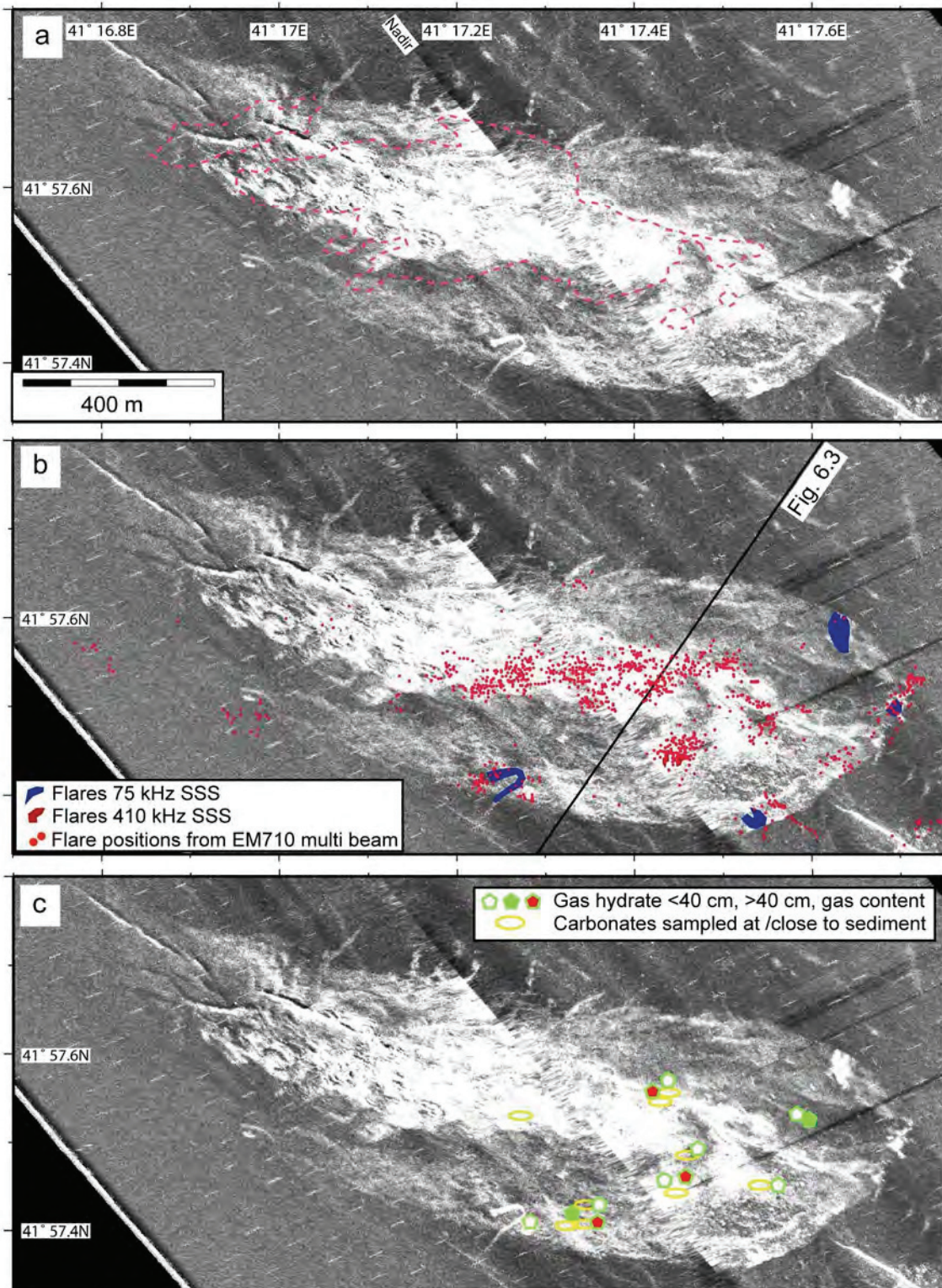
Fig. 6.6: Causes of 75 kHz backscatter anomaly.
a) Extend of rough seafloor in 410 kHz (dashed line).b) Flares in 75 (blue) and 410 (red) kHz side scan sonar, and KONGSBERG EM710 multi-beam echo sounder (dots). c) Gas hydrate and authigenic carbonates recovered from cores during M72/3. Pentagon symbols refer to gas hydrate, or indicators like soupy moussy sediment texture, in shallow sediments below and above 0.4 m bsf, or to gas recoveries from DAPC cores >10 L gas / L sediment (Pape et al., 2011). Occurrence of carbonate is marked, where they were found above 0.4 m bsf.

6.5.2 Temporal Changes in 75 kHz Imagery

We evaluate the development of Batumi Seep within 2.5 years between October 2004 (published in Klaucke et al., 2006) and April 2007 in terms of changes in imagery in 75 kHz side scan sonar. Temporal changes of the seep will emerge first in gas flares, secondly in gas hydrate content, and thirdly in morphology and carbonate content. Flares were seen in seafloor observations to change intensity on the scale of hours. Therefore two observations years apart are not suitable to evaluate those changes in gas release. Generally both images show the same features, fault, high backscatter areas, and halo. A close comparison reveals differences between both, which do not only originate from changes in Geology, but rather from a different ensonification geometry. Even though the track of both surveys is identical, the altitudes of the tow-fish above the seafloor varied. This results in unfortunate distortions especially west of the nadir. It can be found in, e.g., unequal angles of the fault segments in the west. Therefore it is not possible to calculate a mathematical difference between both images pixel-wise. However, qualitative evaluations of changes are possible for some features. Differences are shifted locations of flares, intensification from low to medium backscatter in the northern part ($\sim$0.03 km³), slight extension of the halo towards the north-east, giving a more rounded halo-shape. Figure 6.7 presents old and new imagery next to each other. But, both are close to the limit of uncertainty. No changes were found in high backscatter areas like the structured features in the west, the central part, and two isolated high backscatter areas towards the south-east. Fault expressions, and the overall appearance of the backscatter anomaly kept also unchanged. Shape and patterns are consistent with time. To allow for an evaluation the temporal development, we suggest extending the time between surveys to at least a decade. Additionally, the full geometry, horizontally and vertically, of the tow-fish has to be taken into account for side scan data acquisition.
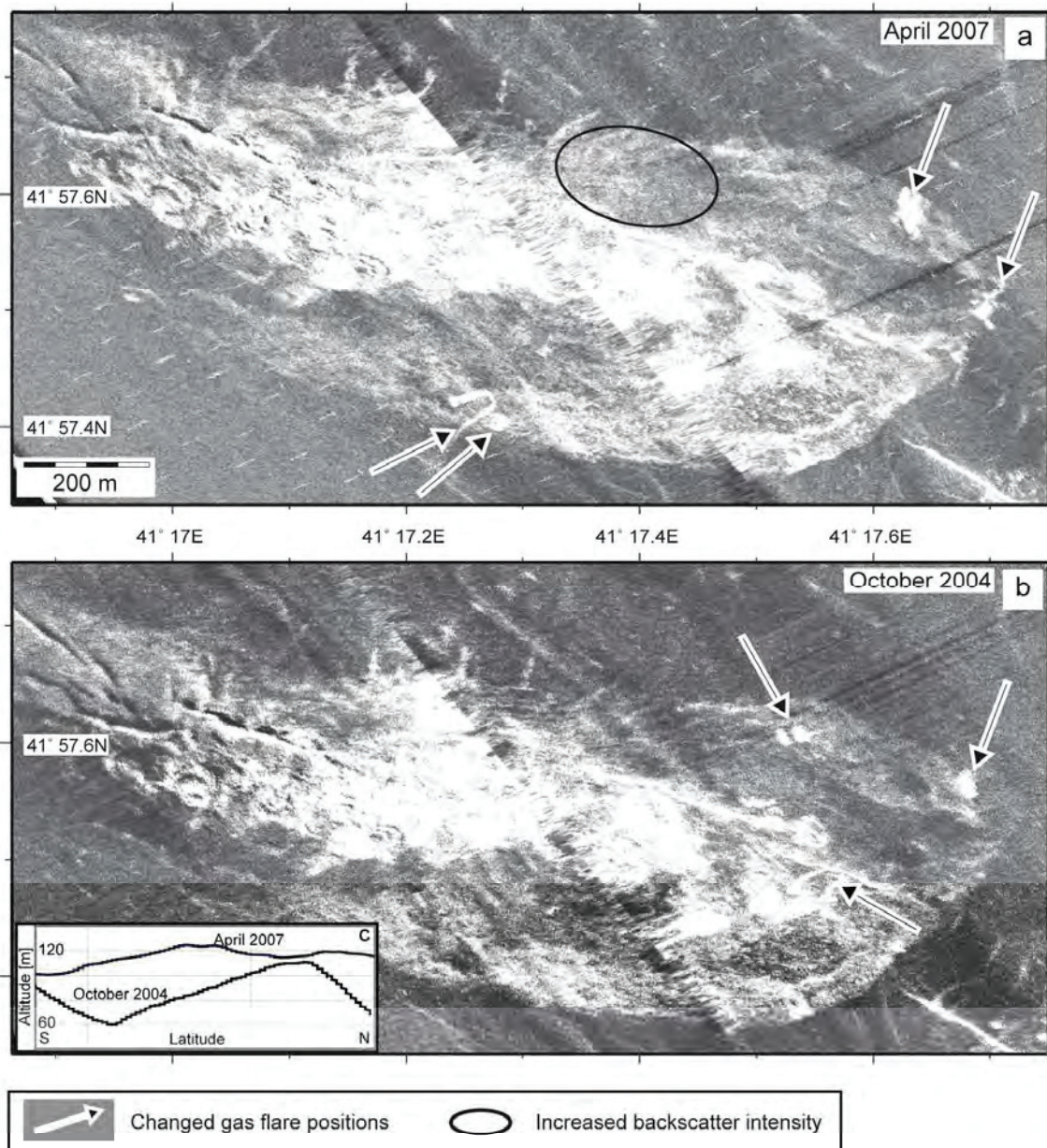
Fig. 6.7: Comparison of DTS 75 kHz side scan sonar imagery of Batumi recorded 2.5 years apart. Tracks and processing are identical, only altitudes of the tow-fish varied. Differences in the images are due to changes in Geology as well as Geometry. a) Recorded on 07 April 2007 during M72/3 B.b) Recorded on 23 October 2004 during RV Poseidon 317/4.

6.5.3 Conceptual Model of Seafloor Development

We present a principle model of the development of Batumi Seep with its different morphological features and backscatter patterns. Fife phases in time, corresponding in space from east to west, can describe the seep development.

Phase1: Initial pre-seep setting
The fault cuts the seafloor, there is no gas migration at the seafloor and no signs in backscatter indicate seepage (Fig. 6.8a). In the following part we suggest a migration of the seep phases with time. At Batumi Seep the phases were found in different locations, Phase 1 in the east and on the rims of the seep. Further phases westwards and closer to the centre.

Phase 2: Gas ascent and accumulation

Gas rises along the fault and gathers close to the seafloor. Wagner-Friedrichs (2007) found vertically offset faults cutting the seafloor as well as the BSR on a seismic profile through the main body of Batumi Seep. Whether only the faults or the entire sediment serves as pathway for rising gas from below the BSR is uncertain (Wagner-Friedrichs, 2007). Flemings et al. (2003) recommend balancing lithostatic and fluid pressures as mechanism to allow the passage of gas through the GHSZ in a gas column even though it should form solid hydrate at local conditions. In shallow sediments close to the seafloor lithostatic pressure turns small, and hence hydrates form in the ridge-crest. Pape et al. (2010) concluded from gas analysis the present formation of new gas hydrates. They seal off the seafloor and force free gas to pool underneath and escape along the rims (Fig. 6.8b). The cap appears as medium backscatter halo in 75 kHz side scan imagery. Pape et al. (2011) found hydrate concentrated at the boundary between Units 2 and 3. This would be beyond the penetration depth of the 75 kHz sonar (2 m). However, the process of cap growth described above additionally accumulates fine grained pore space blocking gas hydrates in shallower sediments. Heeschen et al. (2011) found gas hydrate concentrations of > 15 % pore volume in several Batumi cores. The maximum of 24 % pore volume was derived in a core close to the central fault. The gas pool below the hydrate cap was seen as blanking in the sediment echo sounder profile (Anderson and Hampton, 1980; Zühlsdorff and Spiess, 2005), hydrate layers as strong reflectors (Fig. 6.3). Consequently, the hydrate layer protrudes outward (i.e. downward the ridge flanks) and builds a cap. Gas bubble streams occur on the cap's edges. The cap's elevation level on its sides keeps balanced as gas escapes at the shallowest points. The cap grows deeper down along the ridge flanks as passing gas solidifies with water to hydrate. In this context individual release-points change positions between north and south slope according to the cap's build-up. Upon escape into the water column gas bubbles drag along small particles of soft sediment and form the observed perforations of the seafloor (Fig. 6.4a). Gas flow is relatively low compared to other vents (see below). Gas pressure and lithostatic pressure are in balance. Bubble release shifts location to holes of least resistance. Such jumping activity was explained by an electrical analogue model by Leifer et al. (2004).

Phase 3: Breaching of the gas hydrate cap

Processes change with more and more hydrocarbons accumulating. Hydrates form concentrated accretions just below the seafloor, in approximately 0.5 to 2 m bsf. They bulge up the sediment into mounds creating a hummocky surface (Fig. 6.4b) (Hovland et al., 2006) as it was observed next to smooth seafloor. Eventually the gas pressure becomes large enough to exceed sediment strength and gas breaks through the seal and flows long-lasting into the water column (Fig. 6.8c). At those locations carbonates produced by AOM cement the substrate around the pathways (Peckmann et al., 2001). Pape et al. (2010) expect the active AOM-zone within the upper tens of centimetre, whereas the sub-recent AOM zone extended to 0.9 m bsf. Gas escaping the seafloor can form the numerous small holes in the seafloor. Repeated release of gas causes a volume deficiency and subsidence. Subsidence is increased by sediment consolidation due to shaking of particles when gas moves along its way.

Phase 4: Peak seepage and erosion

More and more gas accumulates as hydrate, even though gas seeps through the cap. At some point pressure and buoyancy of gas and hydrate layers exceeds the sediment stability and breaks it, preferentially parallel to the pre-defined weakness of the visible fault. Semi-circular breaks point to previously round hydrocarbon accumulations. Rigid hydrate slabs lift sediment on top up (Fig. 6.8d). After light hydrocarbons escaped the cavern collapses, the escape pathway suffers erosion. Suess et al. (2001) propose a rafting scenario for Hydrate Ridge (see chapter 6.5.6). This solid combination of gas and hydrate is ideally buoyant.

MacDonald et al. (1994) describe disappearing, i.e. floating, of a semi-circular hydrate piece in the Gulf of Mexico. Semi-circular structures observed in side scan data presented in this study support upward rotation of buoyant lenses with the lighter end, leaving round shapes on the seafloor. Similar appearances were often observed for gas hydrate outcrops, e.g. Bush Hill (MacDonald et al., 1994) and Hydrate Ridge (Chapman et al., 2004). Drift direction of eroded sediment was often observed in small scale around holes (Fig. 6.4a); hence the location of re-deposition of the sediment varies, but it happens likely in the vicinity. As large blow-outs occur seldom, it is difficult to confirm the re-deposition zones. After initial removal of sediment, a gap with rough seafloor remains where continued gas venting has less resistance. Rising bubble streams prevent settlement of sinking sediment at those spots. Because earlier pathways of gas streams were stabilised by carbonate, they remain as upright chimneys (Fig. 6.4e) in the erosion process, where surrounding sediment is removed (Paull et al., 2005). Even though these were tubes of gas transport in earlier times (compare Díaz-del-Río et al., 2003), the chimneys appear to be clogged by carbonate precipitates today. Such plugging was reported at other locations (Hovland et al., 2002; Mazzini et al., 2004). With extensive gas flow, AOM continues to produce extensive and clogging carbonate precipitates. Mazzini et al. (2004) describe horizontal carbonate formation preferentially below clayey layers in coccolith rich layers of Unit 1. Gas is then diverted horizontally and the zone of hummocky morphology migrates away from the fault down slope.

Phase 5: End of active phase

Sealing of the seafloor by pervasive carbonate precipitates outranks gas ascent and no more gas breaches through the seafloor (Fig. 6.8e). Due to the reduced supply of hydrocarbon from below gas hydrate equilibrate to the new situation and decay slowly without formation of bubbles. Released gas dissolves into the water. As a result the shape of the halo is frayed. This last stage starts 900 m distance along the fault from the rim of the halo observed on 75 kHz side scan imagery. Sediments cover morphologies of earlier seepage. Ross and Degens (1974) give a sedimentation rate of 10 cm/ka, however, we expect higher values in this location, because sediments eroded from the active part of the seep partially settle in this area.

Kobuleti Seep south-east of Batumi Seep (Klaucke et al., 2006) is excluded from these considerations. A close inspection, however, provides several similarities on the smaller scale.
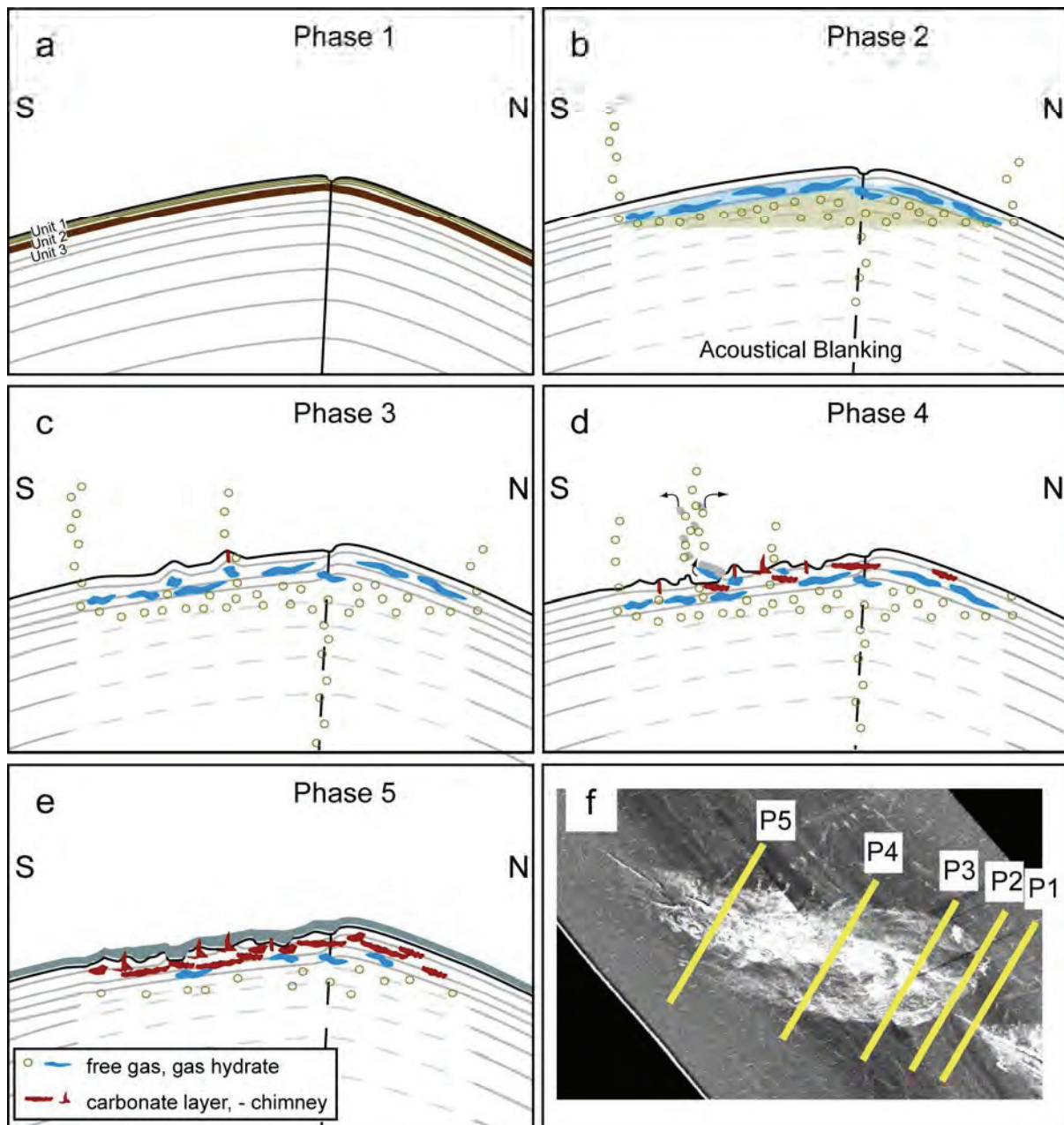
Fig. 6.8: Model of 5 development stages of Batumi Seep. a) Extensional (normal ?) fault is present, no seepage yet. b) Supply of gas along fault, formation of gas hydrate cap in shallow sediments, gas pools below and escapes on the sides. c) Seafloor south of the fault subsides, but local accumulations of gas hydrate and / or gas cause localised uplift producing a hummocky seafloor. Gas seepage into the water continues. Carbonates precipitate along gas pathways by AOM. d) Gas hydrates float up and erode sediment, intensive gas seepage follows. It removes further soft sediment. AOM continues to produces extensive carbonate precipitates. e) Gas supply ceases, gas hydrates partially decompose to equilibrate to the new conditions, and pervasive carbonates limit flow into the water column. Soft sediment obscures structures of the seafloor. f) Map indicating location of phases 1 – 5.

6.5.4 Gas Hydrate Stored at Batumi Seep

We calculate the content of gas hydrate to 1700 kt, and the amount of methane stored in the seep area as $13.8*10^9$ mol or 220 kt. The volume containing hydrate was determined from the extent of the backscatter-halo as outlined in Fig. 6.2d (0.6 km²) and the thickness of the hydrate zone (20 m) approximated from sub-bottom profiler data. Below there is free gas, which would add up to the methane budget, but cannot be evaluated so far. Pape et al. (2011) evaluated five Dynamic Autoclave Piston Corer (DAPC) cores from the area by gas analysis. Although the number of samples is small, the cores were taken at different backscatter intensities and are therefore assumed to be representative of the entire seep. Pape et al. (2011) limit their calculations of methane contained at the maximum core length recovered by DAPC, 2.65 m. Their gas sampling procedure averaged over possible layers of massive hydrates as well as free gas or methane free sediment. We extend our calculation deeper incorporating their gas hydrate content by volume. They found 4.3 core-vol.% gas hydrate in Unit 2 (0.3 − 1 m bsf) and 16.3 core-vol.% in Unit 3 (1 − 2.65 m bsf). Unit 1 contained no hydrates. We assume the hydrate content of Unit3 to continue down to the top of the gas pool at 20 m bsf. Then there are 18 060 m³ gas hydrate in Unit 2 and 1 858 200 m³ in Unit 3 for the Batumi Seep area. With a density of 910 kg/m³ for hydrate (Haeckel et al., 2008), the total mass is 1 707 kt. Assuming the gas to be >99% methane (Pape et al., 2011) and a hydration number of 6 (Hester and Brewer, 2009), there are $13.8*10^9$ mol or 220 kt of methane present in the upper 20 m of the backscatter halo.

Comparing these values to other locations, we compare to Torres et al. (2004) and Tréhu et al. (2004) reporting on high gas hydrate contents in Southern Hydrate Ridge, Cascadia. They found massive hydrates in the sediment as well as gas bubble streams in the water column. Pore water chemistry indicated rise of methane as gas bubbles already below the seafloor (Torres et al., 2004). A 300 x 500 m large high backscatter patch was mapped, but not as detailed as in this study. Drilling during ODP Leg 204 revealed gas hydrate contents of 20-26 % in the upper 30 m below the summit of southern Hydrate Ridge. Horizontal and vertical extent and methane in place (Table 6.3) are in the same range as at Batumi Seep for the summit area. However, Tréhu et al. (2004) show that gas hydrates are spread over a larger area and deeper as well, but not as concentrated. Blake Ridge is another area where gas hydrates were estimated. Reflection-seismic profiles and drilling (ODP Leg 164) constrain the estimates (Holbrook et al., 1996; Dickens et al., 1997). Both authors provide gas hydrate contents, but based on a much larger area (100 000 km² and 26 000 km², respectively) and greater depth, down to the BSR, 450 m bsf. Therefore the values are several orders of magnitude larger than our estimate for Batumi Seep. Calculated for the layer thickness and horizontal extent of Batumi, Blake Ridge contains only 40% of gas hydrate. This is reasonable as the setting at Blake Ridge lacks the focussing into a narrow ridge-crest. .

Location	Area of backscatter patch [km²]	Hydrate content [vol.% of sediment]	Layer thickness [m]	Hydrate in place [kt]	Methane in place [kt]	Methane in place [mol]	Source
Batumi Seep	0.6	16	20	1,707	220	$1.38*10^{10}$	this study
Batumi, upper 2.65 m	0.5	16	2.65	133	17	$1.07*10^{9}$	Pape et al., 2011
Blake Ridge	100000 (BSR)	1-4	250	$3*10^{10}$	nn	nn	Holbrook et al., 1996
Blake Ridge	26000 (BSR)	0-9	260 (190 - 450 mbsf)	$3.64*10^{8}$	$4.7*10^{7}$	$2.94*10^{15}$	Dickens et al., 1997
Blake Ridge, 0.6 km², 20 m	0.6	0-9	20	646	83	$5.2*10^{9}$	Dickens et al., 1997, modified
Southern Hydrate Ridge (Summit)	0.15	20-26	30	930	122	$7.5*10^{9}$	Tréhu et al., 2004
Sea of Okhotsk	average 0.11 km²	10-40	nn	nn	nn	nn	Shoji et al., 2005
Kouilou Pockmarks, Congo	0.45+0.09+0.17=0.71	nn	23	nn	nn	nn	Sahling et al., 2008

Tab. 6.3:
Comparison of gas hydrate and methane content of several cold seep areas.

85

6.5.5 Testing a Rafting-Process

As proposed above, rafting of hydrate has eroded and shaped the rough seafloor of Batumi Seep. First, we assume a "best case" for the rafting with a bubble fabric gas hydrate (Suess et al., 2001). A bubble fabric would have larger buoyancy than massive hydrate as it contains free gas. Haeckel et al. (2008) showed that the majority (93 %) of methane in surface sediments of Batumi Seep rise in form of bubbles. We optimistically calculate a case of bubble fabric consisting of 80% gas and 20% hydrate. Heeschen et al.'s results (2011) support such a supposition with their finding of an average of 14 %, and 24 % maximum, pore volume filled by gas hydrate. Furthermore their results indicate the active formation of hydrate and non-steady state conditions. The mixture of gas and hydrate shall accumulate below a rigid slab of sediment. As soon as buoyancy of hydrocarbon exceeds gravity of sediment, the slap can raft if cohesive forces are broken. Following Pape et al. (2011) we first test a case where gas gathers at the boundary between Unit 2 and 3. A gravity core (GeoB 9922-1, 1 km WSW of Batumi Seep) served as reference station without seep-influence to obtain data for the calculation (Table 6.2). The overlaying, undisturbed, sediment thickness would be 1.5 m in this case. To lift it, a bubble fabric layer of at least 0.65 m is necessary. In a second case, a shallower layer of only 0.3 m thickness requires a bubble fabric layer of 0.09 m to be raised. In both cases about one third of the sediment thickness in gas-hydrate-mix is required for rafting. Alternatively, if massive hydrate has to provide the buoyancy forces, layers of 4.58 m and 0.61 m would be necessary, respectively.

For a different scenario of slumping seafloor Paull et al. (2003) estimated a hydrate content as large as >83 % for sediment-hydrate-mixed chunks required for floating. Such thick layers of massive gas hydrate or bubble fabric have not been observed at Batumi Seep. Hydrates occurred rather spread over the core volume, especially Unit 3 (Pape et al., 2011). Locally, however, morphology suggests up-doming with gas accumulation underneath. Sampling of such places would be necessary to prove assumptions. We consider floating of slabs with an size of several square meters to be unlikely. Based on our observations, we support a small-scale (tens of centimetre) detachment of sediment, followed by focussed and vigorous flow of gas bubbles as major erosion process. After expulsion the bulged sediment above former gas caverns collapses. As a result the observed morphologies with first small and large holes, hummocky seafloor, and finally scarps form. Up-blown material settles in the vicinity obscuring structures forming smooth-structures seafloor.

6.5.6 Implications on Other Seep Sites

Acoustic backscatter signatures similar to those encountered at Batumi Seep had been observed at other seeps, too. A rough morphology analogue to the semi-circular and linear features observed both in 410 and 75 kHz imagery were reported by Zitter et al. (2005). They found such ridges on Amsterdam Mud Volcano in the Anaximander Mountains area, eastern Mediterranean. They used lower frequency sonar (30 kHz), having lower resolution; and visual inspection by submersible proved the presence of ridges and valleys. Those structures originate from vertical mud movement in expansion and collapse cycles (Zitter et al., 2005). Examples with many analogues to the Batumi case are the Kouilou Pockmarks in West Africa in 3000 m water depth within the hydrate stability field (Sahling et al., 2008b). Similar to Batumi sized patches of high and structured backscatter were associated to the pockmarks. Below the pockmarks and backscatter patches a ~25 m thick layer of high reflectivity was observed in sub-bottom profiler, followed by an acoustic blanking. Coring of sediments revealed up to 2 cm thick horizontal layers or sub-vertical veins of gas hydrate like in Batumi, but in depth between 0.5 and down to 12 m bsf. The last value is the maximum penetration

achieved by the gravity corer used. Carbonates occurred only close to the sediment surface. Additionally the seafloor is colonised by seep fauna (Sahling et al., 2008b).

6.6 Conclusions

The ridge top of Kobuleti Ridge at Batumi Seep is shaped by fluid flow. We infer the occurrence of gas hydrate and carbonate from side scan imagery by integrating other acoustic, visual, and geological data. In detail, we found the following reasons responsible for the acoustic backscatter anomaly in 75 kHz side scan imagery of Batumi Seep.

Medium backscatter of the halo originates from gas hydrate present finely dispersed in Units 1 and 2 (upper up to 1.5 m) or in more massive pieces at the top of Unit 3 (~1.5 m bsf). High backscatter inside the medium backscatter area is caused by rough seafloor morphology and authigenic carbonate which add up there to the effects of ubiquitous gas hydrate.

Considering relatively short time scales, i.e. years, we suggest Batumi Seep to be a stable system. Gas hydrate content and morphology remained constant over a time span of 2.5 years. Individual gas flares, however, varied within days. Additionally, we assume the seep to evolve on geological timescales. The seep development began with a nascent fault in the ridge. Gas rises along it through the gas hydrate stability zone (GHSZ). Close to the seafloor gas hydrate forms impermeable and sealing layers within the sediments (the halo) which divert the gas flow to its edges, but also cause local uplift. Eventually gas hydrate and gas become more buoyant than overlaying sediment and rupture the seafloor. Gas flow then erodes seafloor sediment and formerly up-domed seafloor collapses. At the contact between rising gas and seawater in the sulfate-methane-interface, microbial Anaerobic Oxidation of Methane (AOM) (Boetius et al., 2000) triggers precipitation of authigenic carbonate. This in turn seals and stabilises pathways and hinders gas release. In non-active areas sedimentation obscures signs of seepage at the seafloor again.

We calculated the amount of gas hydrate stored within the top 20 m of the sediment inside the halo area as 220 kt, or $1.38 * 10^{10}$ mol methane. Rafting of sediment by buoyant gas hydrate requires the following conditions: Minimum requirement to lift a plate of thickness "1" is a bubble-fabric hydrate of thickness "1/3". For massive hydrate a layer thickness of "3" would be necessary. More likely are small-scale ruptures of the seafloor induced by buoyant forces of gas and hydrate and vigorous outbursts of free gas blowing off soft sediment.

Rough morphology of up to a few metres height at other seep sites can be attributed to gas seepage. Features align with pre-existing weaknesses, but tend to have a semi-circular shape. Hummocky, but in the surface smooth seafloor is an early or low gas flow stage, scarps, ridges and incisions mark higher gas flow rates and a longer period of activity. Overall large similarities in backscatter patterns exist between different seeps which appear to be independent of tectonic or geological setting. Seepage is the most important factor in shaping the local seafloor.

Acknowledgements

7

Widespread Methane Seepage at the Continental Slope offshore Pakistan, Makran Accretionary Prism

Markus Brüning [a], Heiko Sahling [a], Tim Le Bas [b], Bramley J. Murton [b], Feng Ding [a], Volkhard Spiess [a], Gerhard Bohrmann [a]

[a] MARUM, Center for Marine Environmental Sciences and Department of Geosciences, University of Bremen, GEO Building, PO 330440, 28334 Bremen, Germany
[b] National Oceanography Centre (NOC) Southampton, University of Southampton, Waterfront Campus, European Way, Southampton, SO14 3ZH, United Kingdom

Abstract

The continental slope of the Makran subduction zone offshore Pakistan was surveyed for cold seeps during RV METEOR Cruise M74/2&3 in October and November 2007. The investigated section of the slope stretched from the shelf break down to the abyssal plain within a rectangular work area of 90 by 50 km, centred at 24°30'N 62°55'E. We ran a systematic search sequence of acoustic and visual methods confined to that box. First, reconnaissance surveys with multibeam echo sounder, deep-towed 30 kHz side scan sonar, and single beam echo sounder were performed. The single beam would register gas plumes in the water column as well as indicate gas and gas hydrate within the sediment. In a second phase the identified potential seep targets were checked and documented by TV sled and remotely operated vehicle ground truthing.

We discovered in total 23 active seep sites, 16 of them with bubble flares. 18 were contained within the 50 km segment. Seeps are spread over the entire slope from 500 to 2900 m water depth; however, their locations are restricted to crests of accretionary ridges. Detailed studies of two flare sites in 1650 and 2900 m water depth showed very good correlation of high backscatter signatures and sub-bottom acoustic blanking with the occurrence of carbonate and/or chemosynthetic communities on the seafloor. Conversely, no correlation between high backscatter signals and seep areas was found at the upper slope, where side scan imagery only images the steep slope topography and sedimentary processes.

Summarising, we found on average 0.3 methane seeps per kilometre of continental slope, which is a conservative estimate of the widespread cold seepage process. A comparable number of seeps can be expected along the entire 800 kilometre offshore length of the Makran margin.

7.1 Introduction

Seepage of methane-rich fluids is a well-known phenomenon at convergent continental margins yet the frequency of seeps is largely unexplored. For example, cold seeps have been found at convergent margins characterised by accretion, such as the Mediterranean Ridge (Cita et al., 1995), Makran (von Rad et al., 1996; von Rad et al., 2000), Sunda (Wiedicke et al., 2002), Barbardos (Henry et al., 1996), Nankai (Henry et al., 2002), Cascadia (Kulm et al., 1986; Suess et al., 1999), and Aleuten (Suess et al., 1998). Despite the fact that seeps have been discovered at these accretionary prisms, there is a lack of knowledge how numerous the phenomenon actually is as a result of shortage of systematic surveys. As a consequence, the frequency of seeps along a continental margin segment on the scale of tens of kilometres is unexplored. Therefore, it is difficult to estimate the significance of seepage in general, its impact on geochemical cycles as well as its role as habitat for unique biological communities.

In contrast to accretionary systems, seeps have been systematically found along a continental margin characterised by subduction erosion. More than 100 seeps occur along the ~ 460 km margin segment offshore Costa Rica and southern Nicaragua (Ranero et al., 2008; Sahling et al., 2008b). In this systematic survey seeps were identified using a combination of bathymetry, side-scan sonar imagery, TV-sled observations, and sampling. This was possible due to the fact that seepage of methane-rich fluids (1) is often related to geological features with a more or less pronounced morphology, (2) often leads to precipitation of authigenic carbonates that causes high backscatter in side scan sonar images, and (3) often leads to the presence of chemosynthetic communities that are readily identified using TV-guided tools. One of the great potentials of the result that seeps occur approximately every 4 km along this Middle American continental slope is, that geochemical turnover rates and fluxes estimated

for one seep, e.g., the flux of methane (Mau et al., 2006), might be extrapolated to the scale of an entire margin segment. Considering that about 43500 km convergent ocean margins exist on earth and that these margins might be classified either as erosive or accretionary or a mixture of both (von Huene and Scholl, 1991), it is of great interest to study the frequency of seeps at an accretionary system and how it compares to an erosive margin setting.

The Makran accretionary wedge may be considered as an end member of convergent plate boundaries due to the record 7-km thick sediment pile that enters the subduction zone (White and Louden, 1983; Platt et al., 1985; Kopp et al., 2000). The upper 4 km of the incoming sediments are offscraped and frontally accreted sediments form a sequence of long, narrow, sub-parallel accretionary ridges. The lower 3 km sequence is underthrust and later underplated further to the hinterland leading to uplift and extension. The tectonic processes have formed one of the most extensive accretionary complexes on earth. At present, it has an extent of about 1000 km along strike, bound by the Minab and Ornach-Nal Faults, and about 450 km cross strike with about 300 km on-shore and 150 km off-shore.

The continental margin of the Makran region is well known for its evidence for methane seepage as well as the intersection of the continental slope with the oxygen minimum zone (OMZ) in the water column located at a depth of about 100 to 1100 m (von Rad et al., 1996; von Rad et al., 2000). Both processes may produce sub-oxic methane or sulphide-rich sediments that are inhabited by filamentous sulphur oxidizing bacteria such as *Thioploca* or *Beggiatoa* (Schmaljohann et al., 2001). In addition, seepage of methane-rich fluids outside of the OMZ may provide the nutritional source for other chemosynthetic communities such as vesicomyid clams (Krylova and Sahling, 2006; von Rad et al., 2000). Furthermore, active mud volcanism was documented on shore as well as at shallow water depth on the continental shelf close to the coastline (Delisle et al., 2002; Delisle, 2004; Snead, 1964; Sondhi, 1947). In addition, there has been evidence for mud volcanism on the abyssal plain just seaward of the first accretionary ridge although without any evidence for methane seepage at present (von Rad et al., 2000; Wiedicke et al., 2001).

In this study we present the results of a systematic search for methane-rich fluid seeps at the seafloor at the continental slope offshore Pakistan. The results were obtained during a very successful expedition campaign on RV METEOR (M 74/2 & 3) in October-November 2007; one leg focused on the geophysical exploration using swath mapping, high-resolution seismics, TOBI side scan sonar, 18-kHz PARASOUND water column surveys and TV-sled surveys, the other leg concentrated on remotely operated vehicle (ROV) QUEST dive surveying and sampling of the seep sites (Bohrmann et al, 2008a). A major finding of the cruises was that gas emissions are very common at the continental slope from the deepest depth of 2870 m to the shallowest depth that we were allowed to work at of about 500 m (Bohrmann et al., 2008a). In total, we found 16 sites with gas emissions in the entire study area and 12 sites with gas emissions within the area systematically surveyed by side scan sonar, which we concentrate on in this study. ROV-based observations have shown that at all the studied gas emission sites chemosynthetic communities occur and that their composition varies along an intrinsically linked oxygen/depth gradient (Bohrmann et al., 2008a).

The objective of this study is to present the results of the systematic search for methane seeps in this multi-scale approach combining swath mapping, side scan sonar imagery, PARASOUND echo sounder as well as seafloor observations by TV-sled and ROV QUEST. We show that seeps can be systematically found by this approach by showing four regional examples. By extrapolating the results of the regional studies to the entire area mapped by side scan sonar we can take an inventory of all methane seeps at the 50 km wide continental slope segment. Ground truthing by seafloor observations in combination with direct evidences for bubble emission from 18 kHz echo sounder suggest that at all of the listed sites methane is actively seeping at present. The geological setting of the seeps is discussed on the basis of

published high-resolution multichannel seismic data that were acquired during the same expedition (Ding et al., 2010a).

7.2 Study Area

The study area is located at the continental margin offshore Pakistan, which is part of the Makran accretionary wedge (Fig. 7.1). The M74-based bathymetry of the investigated area is shown in Figure 7.2. It is part of the already studied margin segment and its morphotectonics has comprehensively been described by Kukowski et al. (2001) and is briefly summarised here. The continental slope can be divided into three distinct zones: The upper slope from the shelf (water depth less than 100 m) to a depth of about 1000 m is characterised by a steep slope of ~8° and many narrow and deeply cut gullies and canyons. The mid-slope terrace with a slope of only 1.1° has a very smooth morphology and separates the lower from the upper slope. A sequence of accretionary ridges with remarkably steep seaward flanks can be observed at the lower slope. The general sloping angle from the First Ridge to the mid-slope terrace is about 1.9°. A new accretionary ridge called Nascent Ridge (Kukowski et al., 2001), protodeformational zone or frontal fold (White, 1982; White and Louden, 1983; von Rad et al., 2000) develops seaward of the First Ridge. There is no morphologically distinct trench probably due to the high sedimentation rates. The abyssal plain at a water depth of about 3000 m displays an undulating topography. These features have been interpreted as near vertical thrusts by Kukowski et al. (2001) but have been later discussed convincingly by Uchupi et al. (2002) and Ding et al. (2010a) as a result of bottom or turbidity current action, a supposition that we follow in this study. The otherwise relatively uniform continental slope in our study area is dissected by the Save canyon as well as by the deep incision that is discussed as the surface trace of the Sonne strike-slip fault (Kukowski et al., 2000; Kukowski et al., 2001).

A pronounced bottom simulating reflector (BSR), which is usually attributed to the presence of gas hydrates above and free gas below, has been found throughout the study area at sediment depths of about 600 to 800 m. It laterally extends from water depth deeper than about 1350 m to the deformational front (Minshull and White, 1989; von Rad et al., 2000; White and Klitgord, 1976; White, 1977). Computing of compressional wave velocities using inversion techniques of reflection (Sain et al., 2000) and refraction (Grevemeyer et al., 2000) data yield an unusually thick (~200 − 350 m) low-velocity zone at BSR depth indicative for large quantities of free gas.

Fig. 7.1: Map of the Makran accretionary prism with the main tectonic features and the location of the work area.
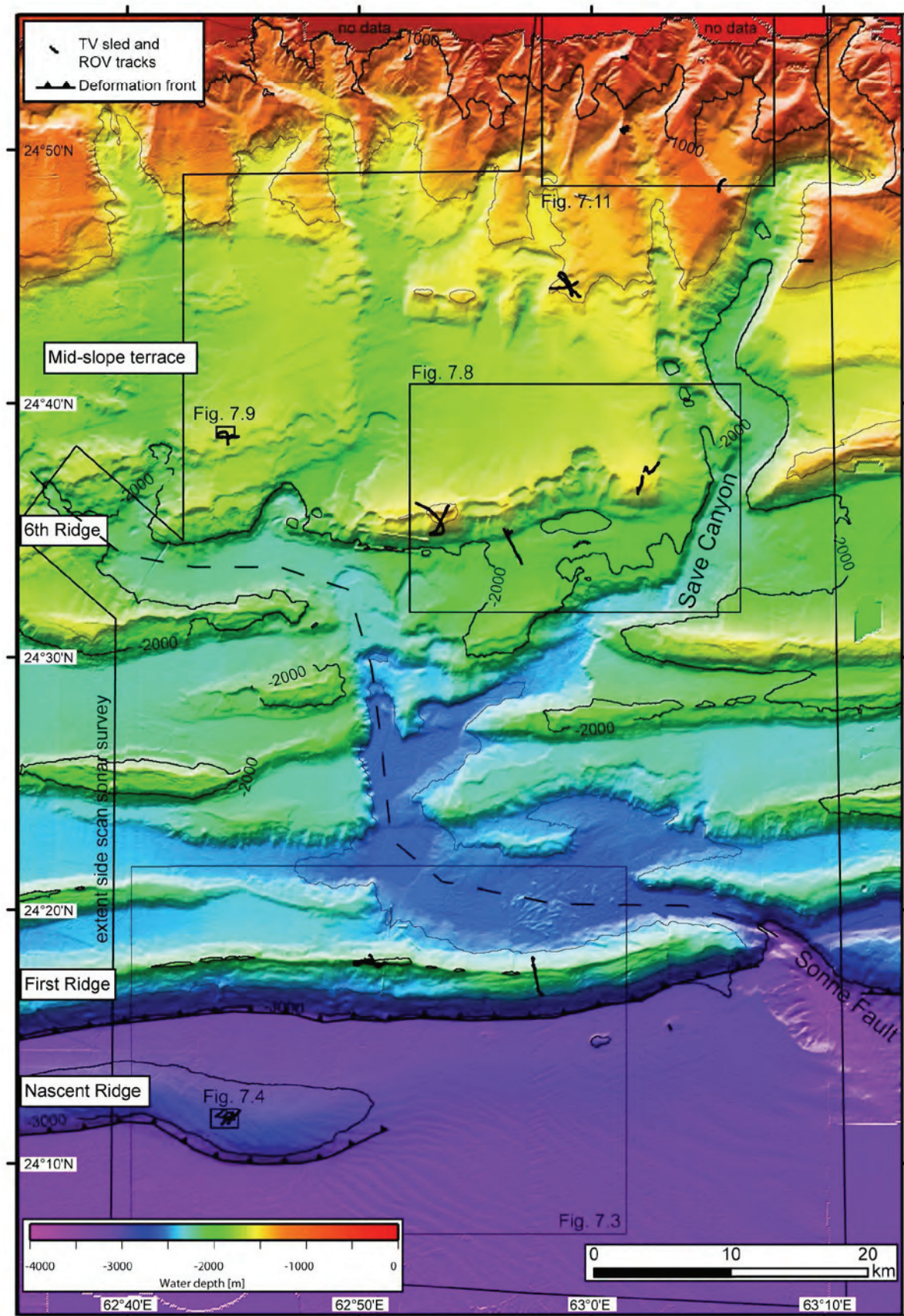
Fig. 7.2: Swath bathymetry map of the study area showing the area covered by TOBI side scan sonar, the track lines of TV-sled tows and ROV QUEST dives as well as major structural elements. Boxes indicate the outlines of figures that are shown in the result section.

7.3 Methods

A KONGSBERG EM120 multibeam echo sounder was employed for swath mapping. The EM120 has a frequency of 12 kHz and can cover full ocean depth with 191 beams at a maximum opening angle of 140°. Raw data were processed using a sound velocity profile that was obtained during the first CTD station at Nascent Ridge (M74/2, GeoB 12302). Swath data were processed with the program MB-SYSTEM 5.0.9 using a median spike filter, outer beams were removed according to the profile's overlap and data quality, and remaining pings manually edited. Grids were then calculated by omitting data where ships velocity was less then 2 km/h. Grid cell size was 50 m. MB-SYSTEM produced a netCDF grid, which was then visualised in GENERIC MAPPING TOOL (GMT) or further exported to ESRI ARCGIS. The bathymetry obtained during M74 was then superimposed on earlier surveys of the area obtained during RV SONNE expeditions 90, 122, 123, and 124 as well as the global GEBCO 1 min data set (GEBCO Digital Atlas, 2003) to obtain full coverage.

The Towed Ocean Bottom Instrument (TOBI) of the National Oceanography Centre (NOC), Southampton, UK, was deployed during M74/2. TOBI is 4.5m x 1.5m x 1.1m large, it carries side scan sonar transducers, 3 m long with 2 x 600 W output. A 750 kg depressor weight between the ship's cable and an umbilical sank the vehicle to the desired depth. The depth was adjusted by the cable-length. The frequencies of the sonar are 30.37 kHz (starboard) 32.15 kHz (port), send with one ping of 2.8 msec duration every 4 seconds. The resulting beams are 0.8° wide horizontally and spread 45° vertically. A swath width of 6000 m can be obtained from the 4 seconds recurrence rate. The vehicle hosted a CTD to record accurate depth values. During M74/2 TOBI was successfully deployed twice. The first four profiles were 90 km long, stretching from the limit of the 12 nm zone around 700 m water depth, down onto the oceanic plate with more than 3000 m water depth. For the second deployment profiles were cut by 15 km to 75 km length as the imagery did not provide the desired cognition in the steep shallow region. In total 10 profiles 5.5 km apart cover the Makran continental slope between 62°40'E and 63°10'E (Fig. 7.2). A total of 950 km side scan profiles were run at 2 kn tow speed, with parallel acquisition of multichannel seismics. The altitude above the seafloor was kept at $300 - 400$ m, and at 600 m close to ridges. TOBI data were processed with the Linux-based PRISM software (Le Bas et al., 1995; Le Bas, 1997). Prior to the main processing, the vehicle positions were calculated from ship's positions, cable length, and vehicle depth. Complementary data for tow-cable length, pressure, altitude, and gyro compass were manually edited. The chosen resolution of pixels was 3 m, which corresponds to an averaging of 4 samples across track and 3 samples along track.

Main processing comprised removal of the water surface reflection, removal of high intensity noise and speckle, a median filter of 3x3 pixels, an interpolation to fill gaps of up to 7 pixels, and a ping-wise illumination correction. Side scan data were slant range corrected using the bathymetry from RV METEOR'S EM120 multibeam echo sounder. The accuracy of positioning along track from the cable length is good, but not well constrained across track. A comparison of seafloor features in bathymetry and backscatter imagery allowed a correction the TOBI navigation. A recalculation became then necessary due to the processing involving slant range correction with relief. Gaps originating from the yaw movement of the vehicle were filled by adding a background layer processed with the real beamspreading of 0.8°, which had been set to 0° in the standard processing.

The single beam sounder ATLAS PARASOUND was employed as sediment echo sounder as well as to search for evidence of gas bubbles in the water column. The system transmits two frequencies of 18 and 22 kHz, respectively. When employing it as sediment echo sounder, one makes use of the parametric effect of the two superimposed waves that result in an effective signal of 4 kHz and a narrow transmission cone. The diameter of the footprint is

about 7 % of the water depth. For the use as bubble detection echo sounder the high primary frequency18 kHz was utilised following the procedure outline in (Nikolovska et al., 2008).

A TV-sled was used to conduct reconnaissance surveys in order to find indications for seepage at the seafloor. The vehicle was connected to the ship via cable and towed at a speed of ~ 1 kn along predefined tracks. An online transmission provided monochrome video images via coaxial cable, so that the seafloor was continuously displayed on the vessel. Image quality was sufficient to recognise clams, mussels, and rocks. The sled's altitude of 2-3 m above the seafloor was manually adjusted by the cable length following visual control. The range of view of the downward looking camera was limited to a few meters. Videos were stored on VHS tape. IXSEA POSIDONIA USBL yielded positions to plot the track lines.

Detailed surveys and sampling was carried out with the ROV QUEST 4000 m during the M74/3 cruise. It is equipped with a 3 MPixels photo camera, two video cameras, one of them HD quality, and several light sources. It was possible to see up to 12 m with the available amount of illumination. IXSEA POSIDONIA USBL in combination with a Doppler-log provided positions. A forward looking 625 kHz sonar was used to detect bubble streams according to the method described in (Nikolovska et al., 2008).

The general approach to identify seep sites was to carefully compare the side scan sonar images with the swath maps in order to classify backscatter anomalies that might be related to methane seepage. These potential features were then observed by TV-sled. In addition, the presence of hydroacoustic anomalies in the water column was used to conduct detailed ROV QUEST studies (Bohrmann et al., 2008a). Surveys by ROV QUEST were carried out at those sites that revealed evidence for methane seepage such as chemosynthetic communities or seep-related carbonates discovered by TV-sled.

7.4 Results

During the cruises M74 Leg 2 and 3 a 50 km wide continental slope segment was swath mapped and almost entirely imaged by TOBI side scan sonar from the abyssal plain at ~3200 m to the upper slope at ~400 m water depth (Fig. 7.2). In addition, specific sites at the seafloor were studied by 14 TV-sled tows and 18 ROV QUEST dives (Table 7.1). Within the side scan covered area a systematic search for methane seepage was carried out. In summary, the results show that (1) methane seepage and gas emissions are often related to backscatter anomalies at ridge crests and that these sites can systematically be detected in the backscatter map, (2) several backscatter anomalies are not related to seepage, and (3) at the upper slope methane emission occurs at sites without backscatter anomalies. The results are presented in two sections, in the first part, the findings in selected regions from the abyssal plain to upper slope depths are presented; in the second part a complete inventory of all seep-related sites is given.

Tab. 7.1a: TV-sled deployments ROV QUEST dives performed during cruises M 74 leg 2 and 3 at the continental margin offshore Pakistan.

TV-sled	GeoB	Area	Start Latitude N	Start Longitude E	End Latitude N	End Longitude E	Water depth [m]	Duration [hh:mm]	Track length [m]
1	12205	Flare 1 upper slope	24°53.606'	63°01.330'	24°53.623'	63°01.301'	604-626	01:17	600
2	12206	Flare 2 upper slope	24°50.83'	63°01.4'	24°50.874'	63°01.408'	1037-1042	02:01	1600
3	12207	upper slope	24°48.323'	63°05.5'	24°48.705'	63°05.755'	1005-1181	01:11	1200
4	12209	Flare 3 6th ridge	24°37.462'	63°02.788'	24°36.380'	63°02.017'	1590-1622	04:31	4200
5	12217	6th ridge	24°35.939'	62°53.856'	24°36.329'	62°51.527'	1472-1688	05:22	6800
6	12218	Flare 5 Nascent Ridge	24°12.055'	62°44.847'	24°11.013'	62°44.528'	2882-2909	02:21	2100
7	12219	Slump First Ridge	24°17.817'	62°57.513'	24°16.602'	62°57.922'	2213-2375	03:25	2500
8	12220	Flare 4 First Ridge	24°18.007'	62°50.562'	24°17.919'	62°51.092'	1986-1948	01:46	1300
9	12310	Flare 7	24°38.613'	62°44.803'	24°38.366'	62°44.334'	1669-1664	03:14	3200
10	12311	Flare 6, Pockmark, 6th ridge	24°35.015'	62°56.272'	24°33.492'	62°56.273'	1770-1935	02:01	3000
11	12323	7th ridge, northern end of mid-slope terrace	24°44.180'	62°59.432'	24°44.30'	62°59.071'	1484-1478	03:35	4800
12	12325	Flare 4 First Ridge	24°17.832'	62°50.341'	24°17.983'	62°49.669'	1951-2186	05:10	5500
13	12345	7th ridge, northern end of mid-slope terrace	24°44.619'	62°59.150'	24°44.499'	62°58.231'	1477-1514	01:12	2100
14	12346	slump at canyonwall upper slope	24°45.610'	63°09.309'	24°45.601'	63°08.800'	1236-1527	00:56	1000
							Total:	38 hours	40 km

Tab. 7.1b: ROV QUEST dives during M 74 leg 3 at the continental margin offshore Pakistan.

ROV	GeoB	Area	Start		End		Water depth	Duration
			Latitude N	Longitude E	Latitude N	Longitude E	[m]	[hh:mm]
179	12301	Flare 5 Nascent Ridge	24°11.750'	62°44.308'	24°11.741'	62°44.258'	2800-2900	04:09
180	12313	Flare 2	24°50.787'	63°01.483'	24°50.829'	63°01.419'	1000-1100	05:37
181	12315	Flare 2	24°50.796'	63°01.440'	24°50.786'	62°01.424'	1000-1100	09:48
182	12317	Flare 7	24°38.624'	62°44.660'	24°38.633'	62°44.644'	1640-1660	06:52
183	12319	Flare 1	24°53.619'	63°01.410'	24°53.631'	63°01.422'	550-600	03:01
184	12320	Flare 1	24°53.491'	63°01.469'	24°53.630'	63°01.425'	550-600	10:20
185	12322	Flare 7	24°38.638'	62°44.262'	24°38.565'	62°44.398'	1640-1660	09:24
186	12324	Flare 6	24°34.97'	62°56.30'	24°34.85'	62°56.30'	1600-1800	10:05
187	12326	Flare 5 Nascent Ridge	24°11.771'	62°44.324'	24°11.744'	62°44.308'	2800-2900	10:10
188	12328	Flare 2	24°50.796'	63°01.447'	24°50.754'	62°01.436'	1000-1100	09:29
189	12333	Flare 2	24°50.745'	63°01.448'	24°50.800'	63°01.421'	1000-1100	02:33
190	12334	Flare 3	24°37.267'	63°02.617'	24°37.219'	63°02.530'	1550-1600	01:32
191	12338	Flare 7	24°38.504'	62°44.205'	24°38.649'	62°44.253'	1640-1660	09:30
192	12339	Flare 5 Nascent Ridge	24°11.746'	62°44.307'	24°11.740'	62°44.301'	2800-2900	07:55
193	12343	Flare 2	24°50.705'	63°01.453'	24°50.692'	63°01.450'	1000-1100	08:25
194	12348	Flare 11	24°44.515'	62°58.639'	24°44.548'	62°58.914'	1450	05:00
195	12352	Flare 4 First ridge	24°17.909'	62°50.412'	24°17.929'	62°50.098'	1950-2050	07:48
							Total:	121 hours

7.4.1 Regional Examples

7.4.1.1 Nascent Ridge and First Ridge

The morphology and the backscatter characteristics of the lower slope and the abyssal plain are shown in figures 7.3a and 7.3b, respectively. Key morphological features in this area are Nascent Ridge, First Ridge, an additional less pronounced ridge, and part of the Save canyon / Sonne fault system. The abyssal plain at ~3100 m water depth is relatively smooth but shows in some areas NW-SE trending sediment waves with a wavelength of ~2 km and a height of 5-20 m. Nascent Ridge is a sinoidal elevation rising up to 400 m above the abyssal plain. The backscatter of Nascent Ridge is generally low but at the local summit linear high backscatter anomalies exist in relation to gas emissions that we termed "Flare 5". Slumping is suggested by heterogeneous backscatter down slope of a pronounced headwall at the southern flank of Nascent Ridge.
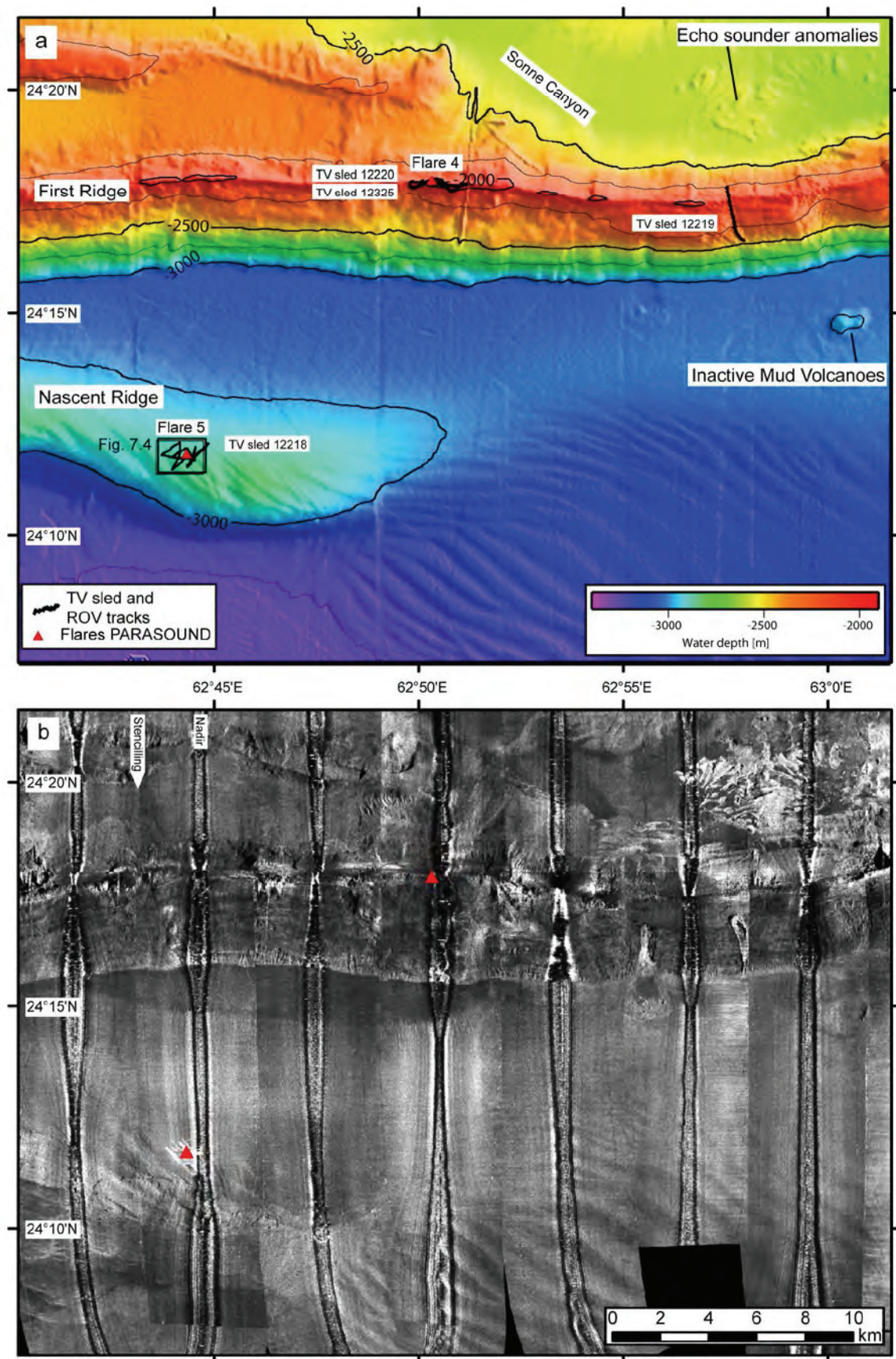
Fig. 7.3: Maps of the area with First Ridge and Nascent Ridge at the lower slope. a) Swath bathymetry. Inactive mud volcanoes were described by Wiedecke et al. (2001), echo sounder anomalies were reported by Kukowski et al. (2001). b) TOBI side scan sonar. High backscatter is white.

The backscatter anomalies at Flare 5 at Nascent Ridge are generally elongated and NW-SE trending, which is parallel to the widespread occurring sediment waves at the abyssal plain and parts of Nascent Ridge (Fig. 7.2). However, the width of each of the ~5 elongated backscatter anomalies is about 100 m whereas the width of the sediment waves is about 1km. The overall extent of the linear backscatter anomalies is about 800 m as shown in Figure 7.4. Unfortunately, parts of the area of interest were below the side scan sonar tow fish blind zone, also called nadir, and are thus not imaged. The subsurface structure in the area of the backscatter anomalies were studied using PARASOUND echo sounder and illustrated for two profiles in Figure 7.5. Well stratified sediment layers become invisible in some parts of the profile due to acoustic blanking below sediment depth of about 10 m. The position of the blanking zones as indicated in Figure 7.5 were mapped and plotted on the composite map (Fig. 7.4). Overall, there is a good congruence between the occurrence of blanking zones in sediment echo sounder and the occurrence of high backscatter in the side scan image. However, on a small scale, the position of the two features does not match in detail.
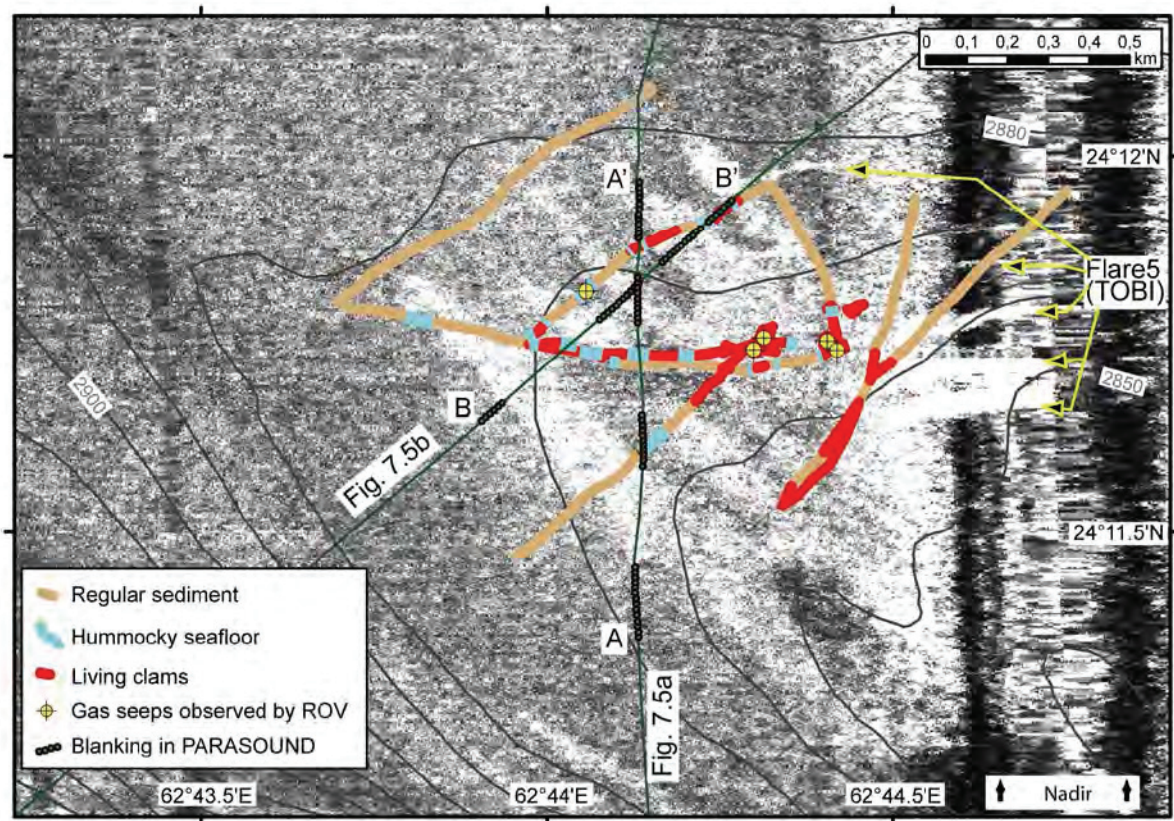
Fig. 7.4: Composite map of Flare 5 at Nascent Ridge showing bathymetric contours (5 m interval) draped over the side scan sonar image. High backscatter is white. Seep-related features are indicated by colour coding along the track lines of TV-sled and ROV QUEST. Dotted lines indicate the location of blanking zones along PARASOUND echo sounder profiles shown in Fig. 7.5.
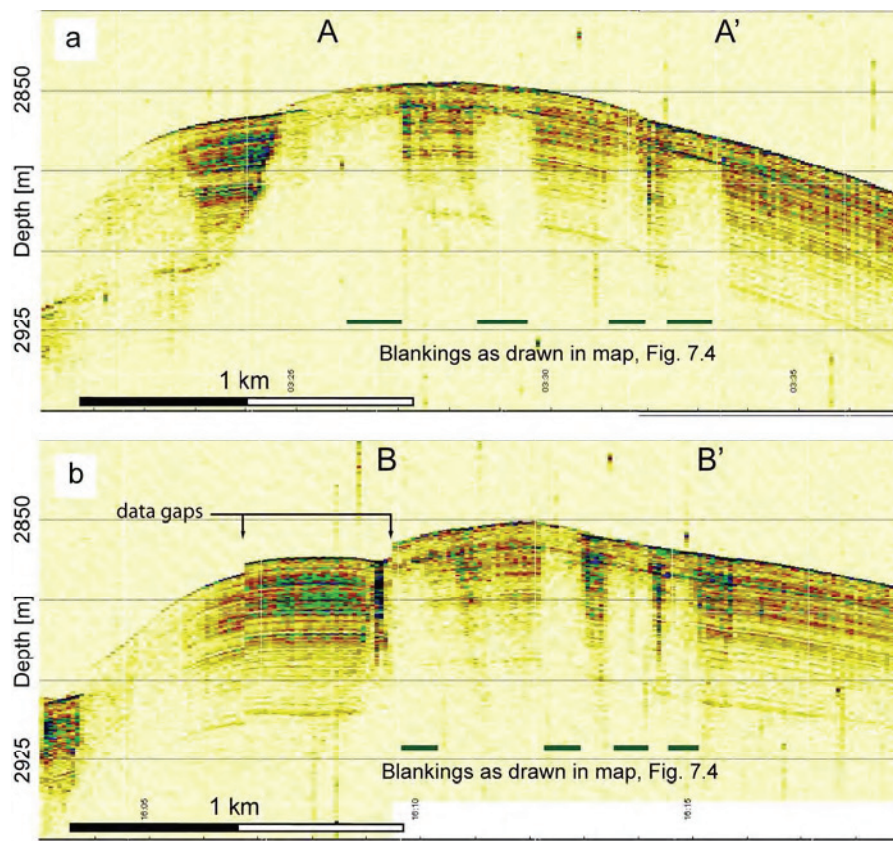
Fig. 7.5: PARASOUND echo sounder profiles in the area of Flare 5 at Nascent Ridge (location see Fig. 7.4).

Seafloor observations using TV-sled (GeoB12218) and ROV QUEST (dive 179, 187, 192) revealed the existence of five sites with bubble emissions (Fig. 7.6a), the presence of vesicomyid clams and pogonophoran tube worms. In addition, the seafloor was hummocky in some areas with elevations of ~0.5 m and a diameter at the base of about 2 m (Fig. 7.6b). The small mounds are often brighter in colour compared to the surrounding sediments and vesicomyid clams were observed in the valleys between them. In general, the extent of the chemosynthetic communities and the hummocky area corresponds well with the overall extent of the backscatter anomalies (Fig. 7.4). Beside the NW-SE trending linear high backscatter patches that indeed reflect the seafloor properties, bubble plumes that rise from the seafloor in the water column have caused high backscatter. This phenomenon was already noticed in the unprocessed side scan data that detected hydroacoustic anomalies in the water column. These anomalies stretch out over seafloor imagery as EW running high backscatter patterns (Fig. 7.4). There is generally a good match between the location of the bubble emission sites observed by ROV QUEST and the high backscatter seen in the side scan data.

The First Ridge is an E-W running ridge that abruptly rises about 1000 m above the abyssal plain. The backscatter of the ridge is generally low but shows some areas with high backscatter near the crest and at the steep (20°) southward facing flank. The nature of one backscatter anomaly at the flank of the First Ridge was explored by a TV-sled tow (GeoB 12219) that revealed a continuously soft sediment covered seafloor. The ridge crest was further explored by two TV-sleds (GeoB 12220 & 12325) and ROV QUEST dive 195 in an area with evidence for weak gas emission (Flare 4) and small-scale high backscatter at the seafloor. The observations revealed the occurrence of spatially very limited vesicomyid clam clusters in some areas that are indicative for methane seepage (Fig. 7.6c). In addition, steep flanks of exposed bedded sediments were observed (Fig. 7.6d) but most of the observed area

was covered with soft sediments. Although not shown in detail here, the occurrence of high backscatter generally matches with the occurrence of vesicomyid clams.
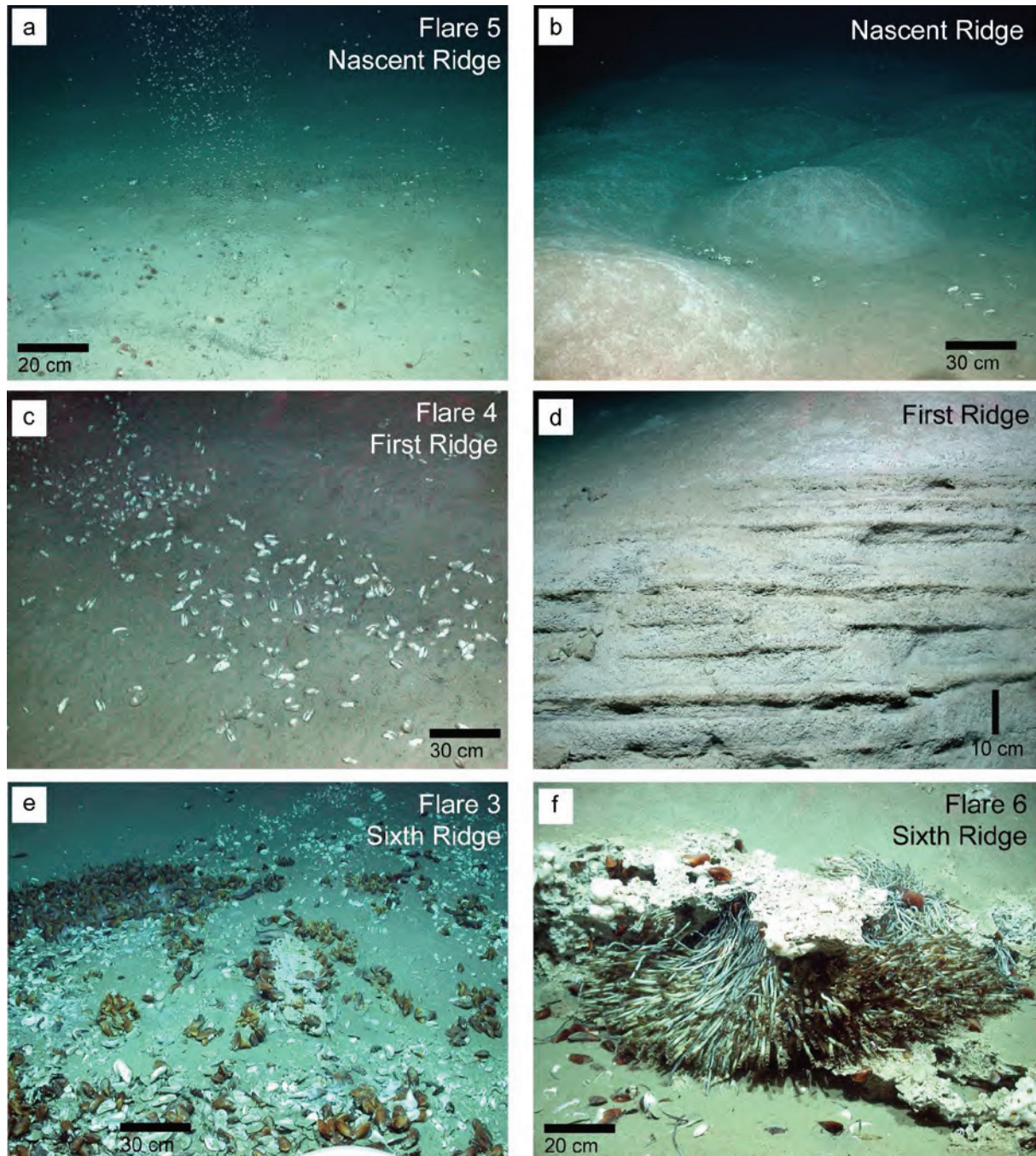
Fig. 7.6: Images taken by ROV QUEST during RV METEOR cruise 74/3. a) Gas emission at Flare 5, 2870 m depth, Nascent Ridge. b) Hummocky seafloor structures about 50 cm high and 2 m wide at Flare 5. c) A scattered cluster of vesicomyid clams at Flare 4, 2000 m depth, First Ridge. d) Outcroping bedded sediments close to the crest at First Ridge. e) Mytilid and vesicomyid bivalves, seep-related carbonates at Flare 3, 1500 m depth, Sixth Ridge. f) Vestimentiferan tube worms, bivalves, and seep-related carbonate at Flare 6, 1820 m, Sixth Ridge. Photos © MARUM.
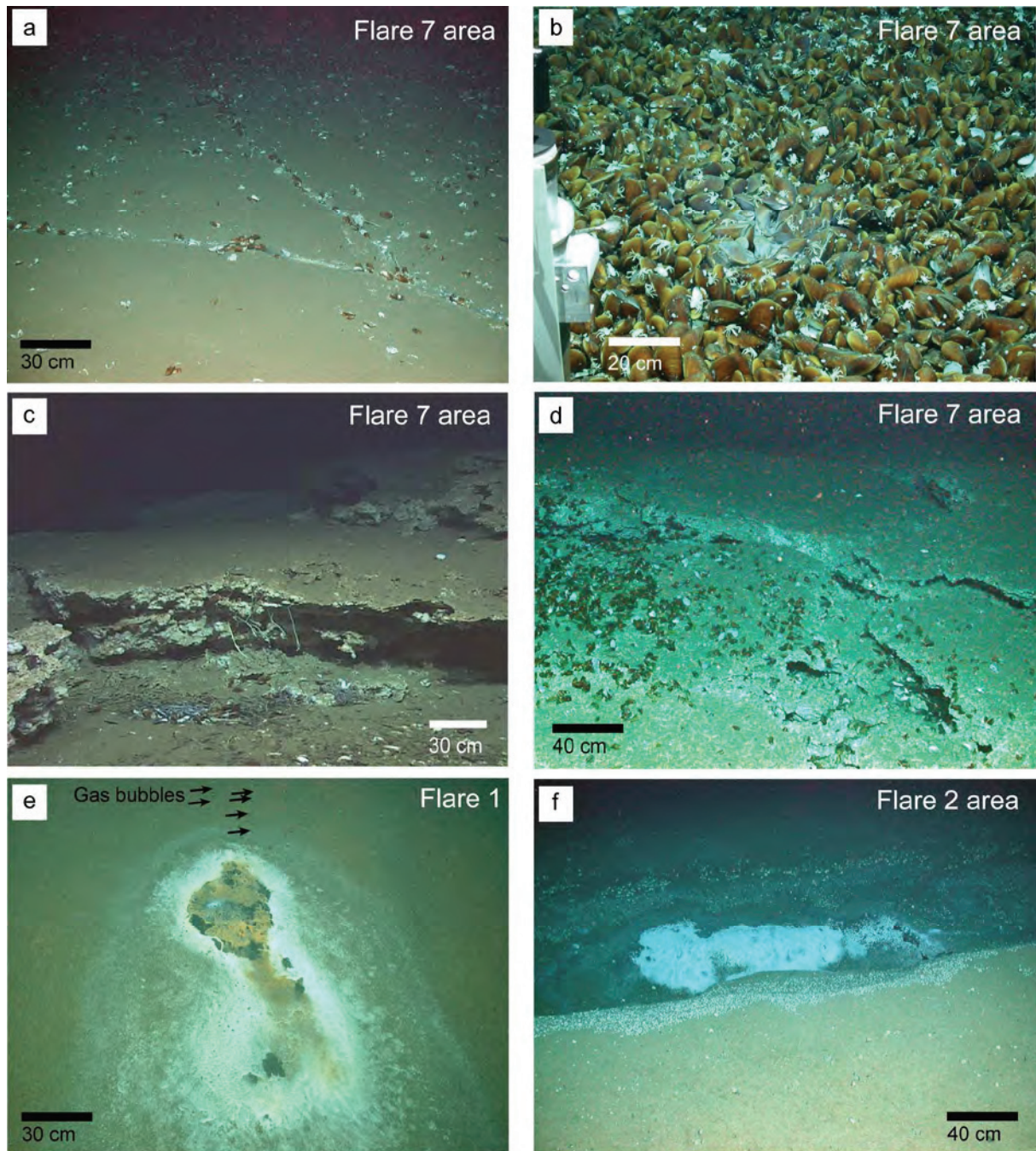
Fig. 7.7: Images taken by ROV QUEST during RV METEOR cruise 74/3. a) Mytilid and vesicomyid bivalves, partially lined up, on soft sediment at Flare 7. 1640 m depth. b) Dense bed of bathymodiolin mussels and wandering galatheid lobsters. Some mussels have a white stain. c) Carbonate platform at Flare 7. A variety of fauna settles especially at the lower level in the foreground: vestimentiferan tubeworms, crabs, clams, barnacles. d) Gaps within the carbonate platform at Flare 7. e) Bacterial mat at Flare 1, 575 m depth. Bubbles escape from the centre of the mat. f) Chemosynthetic community settlement in a graben structure at Flare 2, 1020 m depth. Bacterial mats are located in the centre, bordered by polychaetes and mussels. Photos © MARUM.

7.4.1.2 Sixth Ridge and Flare 7 at the mid-slope terrace

The Sixth Ridge forms the southern boundary of the mid-slope terrace at a water depth of about 1500 m (Fig. 7.2 and 7.8a). The ridge is bordered to the east by the Save canyon system. Its southern flank is about 400 to 600 m high and indented due to mass wasting

processes. South of the ridge the seafloor is considerable plain at water depth of ~2000 m. The side scan image shows the relatively uniform low backscatter of the mid-slope terrace and the plain at the foot of the Sixth Ridge (Fig. 7.8b). High backscatter occurs in some areas of the Save canyon floor and its walls as well as at the branch of the canyon that borders Sixth Ridge.

High backscatter is also associated with the Sixth Ridge connected to three different morphologies, (1) on top of the local summits, (2) in the area of the headwalls of slump scarps, and (3) within the slope. The backscatter anomalies at two local summits are elongated in E-W direction ~200 m long and just 50 m wide, namely at Flare 3 and Seep I. The high backscatter is patchily distributed. Two TV sled tows (GeoB 12217, 12209) and one ROV QUEST dive (190) confirmed the presence of patchily distributed seep-related carbonates, mytilid and vesicomyid bivalves at these sites as illustrated in Fig. 7.6e. In addition, evidence for gas emission was revealed by a weak hydroacoustic anomaly in the side scan sonar at the local summit at Flare 3. As we did not map Flare 3 and Seep I in detail, the relation between high backscatter and the occurrence of carbonates and chemosynthetic communities is presented for another location, Flare 7, located further to the west (see below).

High backscatter is generally associated with the steep headwalls of the slump scarps that form the southern flank of the ridge. Unfortunately, these features have not been observed by TV-sled. The high backscatter in the south flank below the headwalls was surveyed with TV-sled (GeoB 12217, Fig. 7.8b) showing solidified sediments that crop out at these sites but no sign for methane seepage. An active bubble emission site at the lower slope of the southern flank (Flare 6) was associated with the occurrence of chaotic seep-related carbonates, vesicomyid clams, and vestimentifieran tube worms (Fig. 7.6f) as well as a strong hydroacoustic anomaly in the water column recorded by 18 kHz echo sounder. Flare 6 is located just below the side scan sonar tow fish and, thus, was not imaged (Fig. 7.8b). Its extent, however, must be limited as no backscatter anomaly was recorded next to the known methane seep site. Finally, a circular morphological depression of a pockmark, about 500 m in diameter, was detected in the bathymetry (Fig. 7.8a). The walls of the ~20 m deep depression show high backscatter but not the central depression (Fig. 7.8b). Visual observation of the pockmark by TV-sled showed only soft sediment covered seafloor (GeoB 12311).
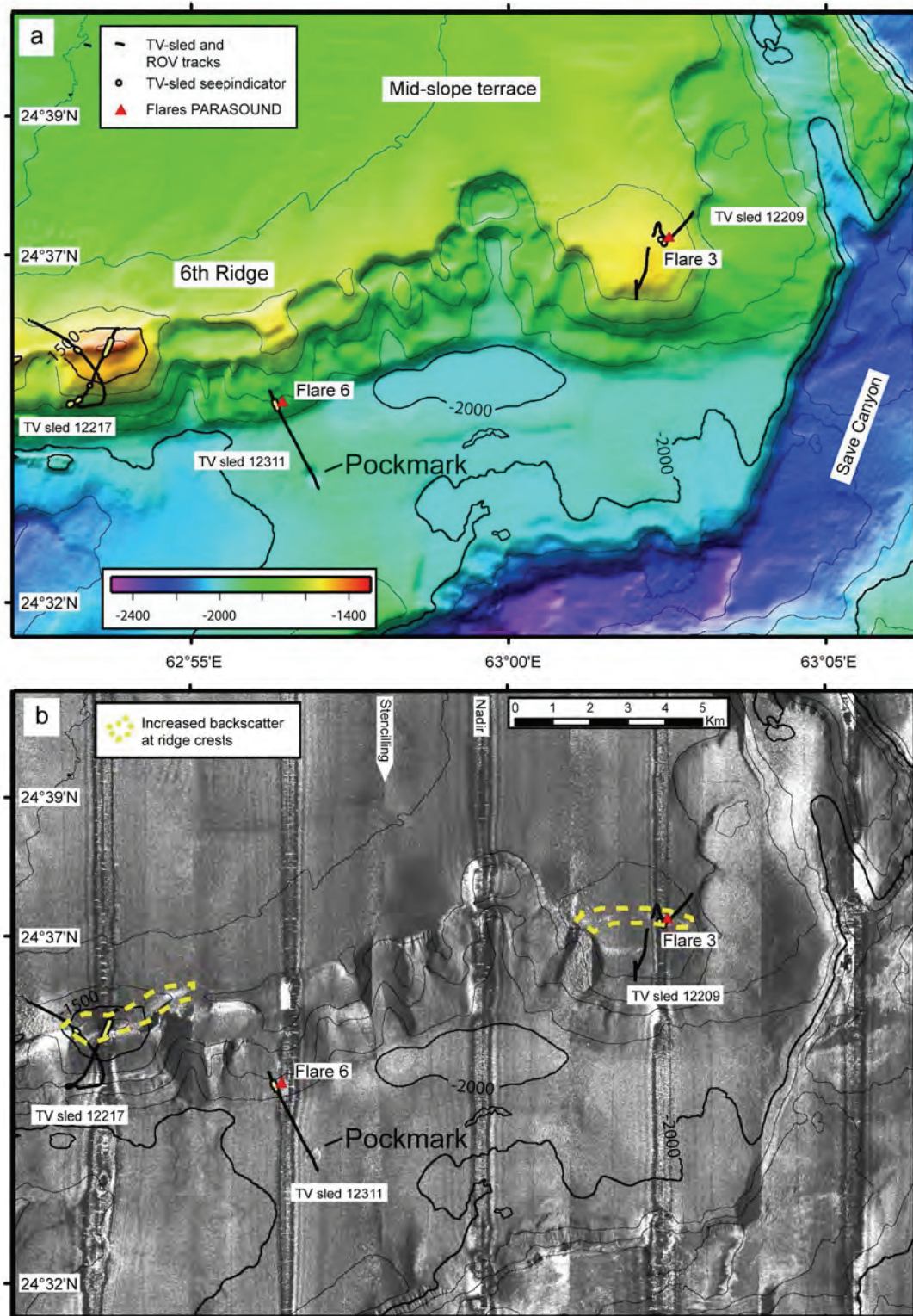
Fig. 7.8: Maps of Sixth Ridge and adjacent areas, the track lines of TV-sled and ROV QUEST deployments, and main morphological features. a) Swath bathymetry. b) TOBI side scan sonar image. High backscatter is white.

Flare 7 is located north of Sixth Ridge at the lower part of the mid-slope terrace (Fig. 7.2). The seafloor manifestation of seepage at Flare 7 is comparable to those seeps discovered at Sixth Ridge, e.g. Flare 3, yet better mapped by TV-sled and thus presented here. The seeps at the Sixth Ridge and Flare 7 have in common that a linear high backscatter anomaly is

associated with a local summit next to or just above a slide complex. In case of Flare 7 the elevation is about 30 m high. The backscatter anomaly is elongated in EW direction about 800 m long and 300 m wide (Fig. 7.9). Its eastern boundary is not imaged as it is located below the side scan tow fish. PARASOUND shows a hard, unstructured reflector of ~15 m thickness at the elevation. No structures are visible underneath, layered sediments, which occur on the sides of the elevation, appear to be interrupted in that blanking zone (Fig.7.10).
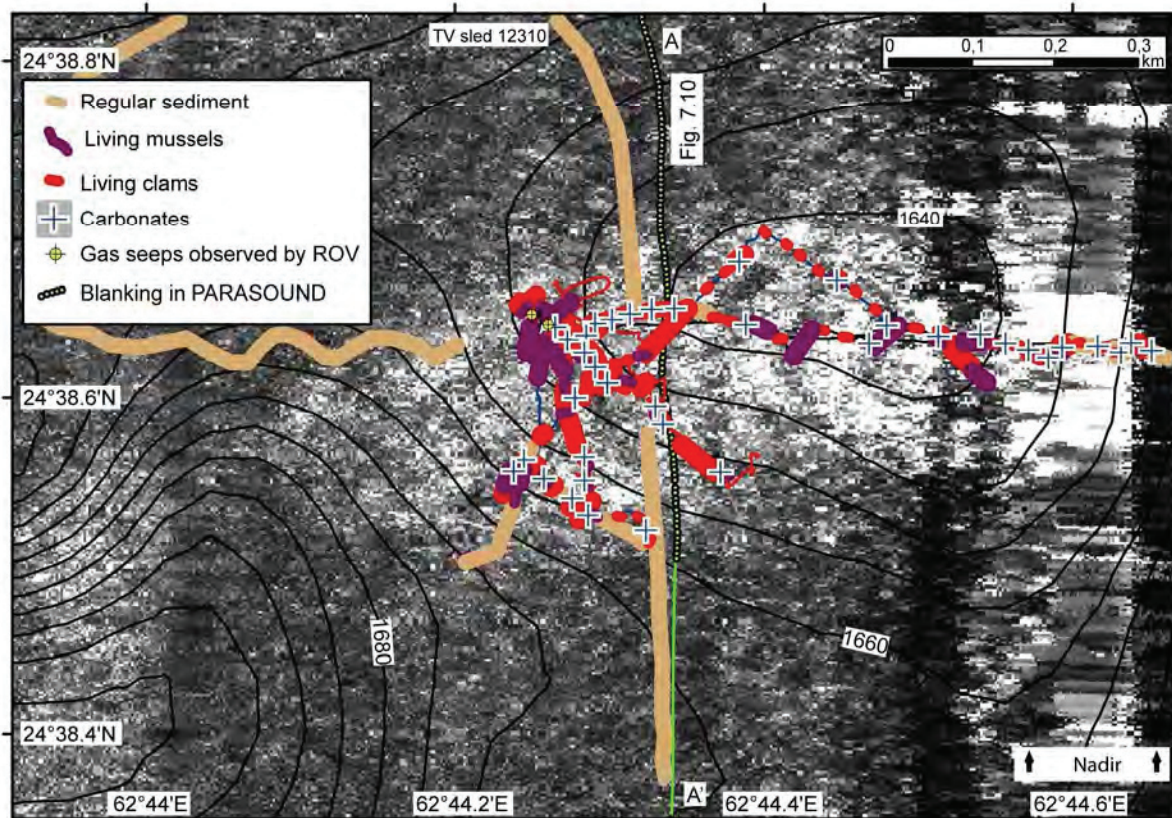
Fig. 7.9: Composite image of Flare 7 showing swath bathymetry contours (5 m interval) draped over side scan sonar image. Seafloor observations are indicated by colour coding of the TV-sled and ROV QUEST track lines.
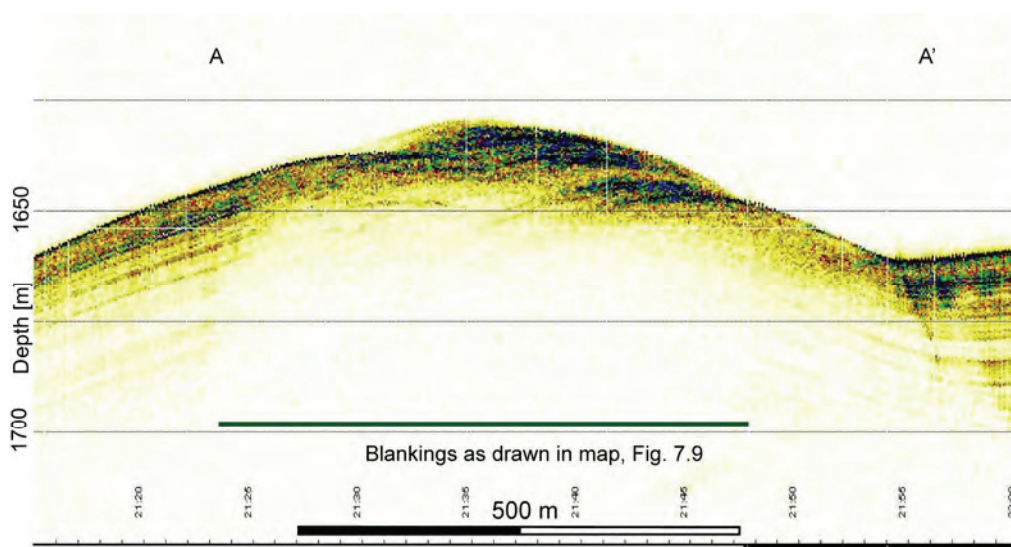
Fig. 7.10: PARASOUND echo sounder profile crossing Flare 7 (location see Fig. 7.9).

A TV-sled (GeoB 12310) and three ROV QUEST dives (182, 185, 191) were conducted to confirm the presence of chemosynthetic communities, such as dense mytilid bivalve fields (Fig. 7.7a,b), vesicomyid clam cluster, and vestimentiferan tube worms. In addition, carbonates occur either as slabs or as widespread crusts draped by a thin sediment veneer (Fig. 7.7c). The latter type can be detected due to the linear settlement of bivalves possibly occurring along cracks in the crusts. In general, there is a good correspondence between the occurrence of chemosynthetic communities and carbonates and the presence of high backscatter (Fig. 7.9). However, the high backscatter area appears somehow larger. In addition, the small scale heterogeneous distribution of seep-related features within this area does not find any correspondence in the backscatter image, which is rather uniform throughout the area.

7.4.1.3 Upper slope
The upper slope at depth between ~500 m and 1500 m is steep and has a ragged topography due to erosive gullies, which causes a complex side scan sonar pattern (Fig. 7.11a,b). High backscatter is mainly associated with the eroded flanks of the ridges and the central axes of the channels, whereas low backscatter can be found at small areas at the crests of some ridges. In addition data gaps occur and appear as black areas (low backscatter, i.e. shadows) at the crest of other ridges as these were not imaged by side scan due to the tow fish flying too deep (Fig. 7.11b). In the area of the upper slope at least five hydroacoustic anomalies were detected using the 18 kHz echo sounder as indicated in Figure 7.11. Some of these bubble emissions occur at ridge crests that are well imaged showing low backscatter (Flare 1, Flare 13), while others occur at the erosive flanks which show high backscatter (Flare 14, Flare 16). Seafloor observations at Flare 1 revealed that bubbles emanate from soft sediments that are typically inhabited by filamentous mat-forming bacteria in a concentric pattern two to four meter in diameter (Fig. 7.7d,e).
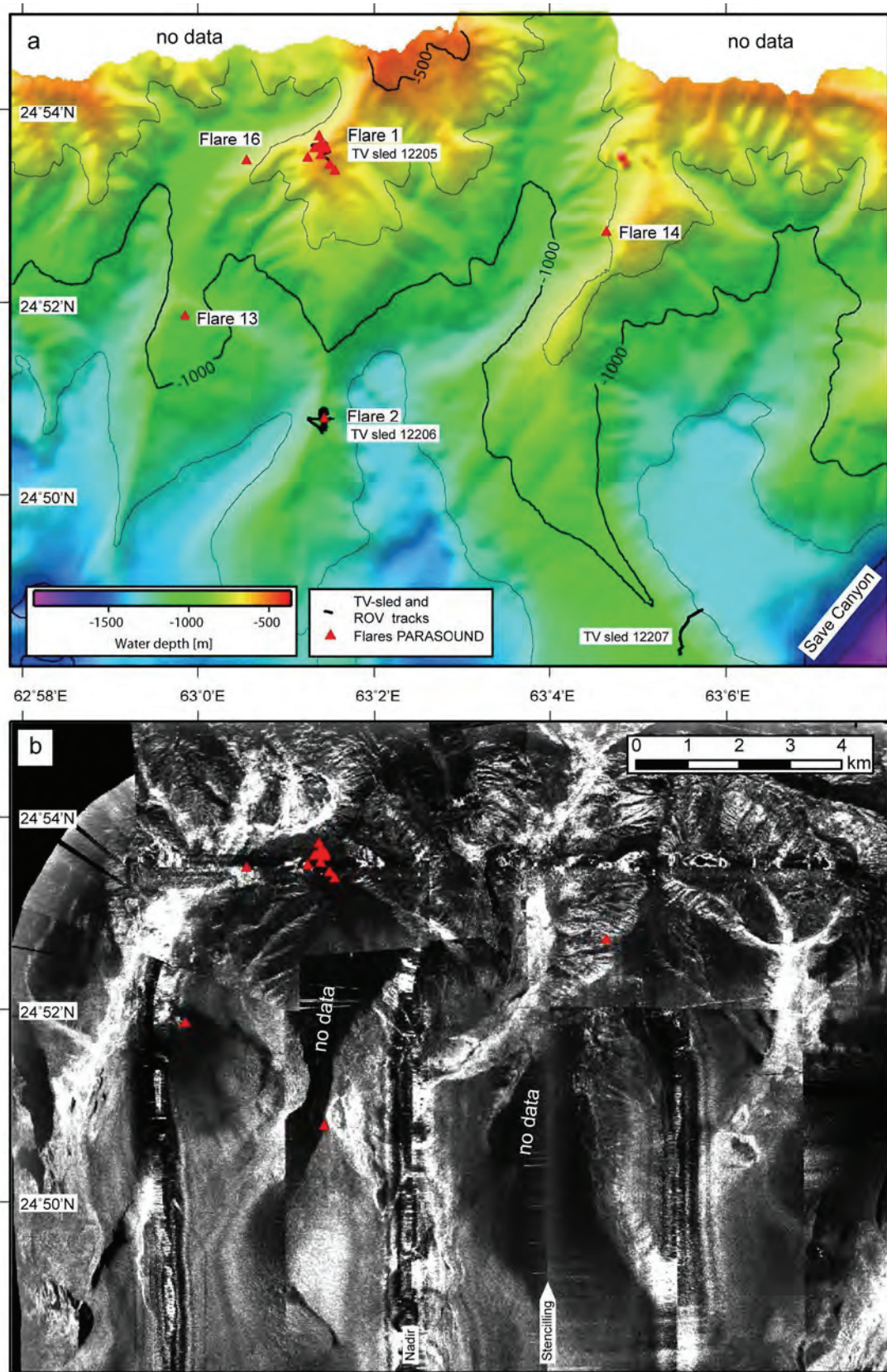
Fig. 7.11: Maps of the upper continental slope, location of gas emission sites "Flares", the track lines of TV-sled and ROV QUEST deployments, and main morphological features. a) Swath bathymetry. b) TOBI side scan sonar image. High backscatter is white.

7.4.2 Seeps Inventory

The regional examples showed that methane seeps typically occur at the crests of the accretionary ridges and are associated with elongated backscatter anomalies. Based on this finding, we identified additional backscatter anomalies in the TOBI side scan sonar data outside of the areas shown in the regional examples (Figure 7.2, 7.3, 7.8, 7.9, and 7.11). In total, 11 seeps with backscatter anomalies occur in the study area as summarised in Figure 7.12 and Table 7.2. At five of these 11 sites hydroacoustic anomalies indicating gas emissions were detected, six sites were surveyed by TV-sled or ROV QUEST and all revealed evidence for active methane seepage at present by the occurrence of living chemosynthetic communities. The inventory also lists the finding of gas emission sites without backscatter anomalies (four sites) and those seeps that have not been imaged (three sites). In total, 18 sites with evidence for active methane seepage or bubble emission have been found in the study area.

7.5 Discussion

7.5.1 Seafloor Mapping at Flare 5 and 7

The two methane seeps that have been studied in detail by PARASOUND echo sounder and TV-sled as well as ROV QUEST differ in the composition of chemosynthetic communities and the extent of seep-related carbonates at the seafloor, yet both sites are characterised by pronounced higher backscatter (Fig. 7.4 and 7.9). At both sites high resolution sediment echo sounder profiles indicate blanking of the seismic energy that we interpret as evidence for free gas (Fig. 7.5 and 7.10), which has also been confirmed by the observation of gas emissions at the seafloor. The extent of blanking seen in the echo sounder is broadly similar to the extent of high backscatter seen in the side scan images suggesting a causal connection. However, the connection must be indirect as it is very unlikely that the ~30 kHz side scan signal penetrates up to a sediment depth of ~10 m, which is the upper limit for the blanking zones in the echo sounder records. We suggest that the shallow existence of gas in the sediments induces widespread microbial-mediated anaerobic oxidation of methane (AOM) to take place, which then causes precipitation of authigenic carbonates in the sediments (Ritger et al., 1987). As we did not systematically sample the sediments in this study, we can not validate this suggestion by own data. However, the fact that seep-related carbonates in the sediments causes high backscatter in side scan sonar has been documented and discussed in many other seep areas (Johnson et al., 2003; Klaucke et al., 2006; Klaucke et al., 2008; Sahling et al., 2008a; Sahling et al., 2008b).

In addition to the proposed pervasive authigenic carbonate precipitation in the sediments other seep manifestations may contribute to the high backscatter such as gas hydrate deposits, exposed carbonates or chemosynthetic communities. Evidence for shallow gas hydrate deposits exists at Flare 5, where hummocky seafloor has been observed in some areas, with individual mounds being ~50 cm high and 2 m wide at the base (Fig. 7.6b). These mounds resemble those bacterial-mat covered mounds at Hydrate Ridge that contain shallow gas hydrates deposits (Suess et al., 2001; Sahling et al., 2002). The mounds at Flare 5 are not covered as densely by whitish bacterial mats as their counterparts at Hydrate Ridge, but, speculatively, may also be inhabited by bacteria that cause the sediments to appear brighter than those in the vicinity. The existence of chemosynthetic communities as well as carbonates have been documented at both sites by ROV QUEST, although detailed studies on the faunal

composition as well as isotopic and petrographic investigations of the carbonates are pending, their general appearance at the seafloor is typical and similar to many other methane seeps (Suess et al., 1985; Suess and Whiticar, 1989; Sibuet and Olu, 1998; Sahling et al., 2003; Han et al., 2004; Teichert et al., 2005; Sahling et al., 2008a; Sahling et al., 2008b). The contribution of the visible fauna, carbonates, and hydrates close to or at the seafloor to the elevated backscatter appears to be obvious but the distribution map of these components in relation to the backscatter anomaly suggests, that the contribution is only small. While the fauna, carbonates, and hydrates occur within the area of high backscatter there are considerably large areas that are devoid of these components that are still characterised by high backscatter. Therefore, we suggest that widespread carbonate precipitation as a result of anaerobic oxidation of methane is the key process leading to high backscatter, and call upon further studies to prove this.

The shape of the high backscatter at Flare 5 and Flare 7 (Fig.7. 4 and 7.9) is very likely the result of the geometry of the pathways the methane-rich fluids take during their ascent integrated over time. While these pathways are probably largely controlled by shallow sub-surface faults or other weakness zones within the sediments, the formation and self-sealing by carbonate precipitation may lead to horizontal spreading of the seep-influenced area (Hovland, 2002). The elongated, EW orientated high backscatter patch at Flare 7 is thus likely the result of an EW trending fault system as discussed below in combination with horizontal dispersion due to carbonate formation (Fig. 7.9). The NW-SE trending of the backscatter anomalies at Flare 5 coincides with the general NW-SE trend of the sedimentary waves in the area (Fig. 7.2, 7.3) and suggests a linkage between theses processes. However, the wavelength of the sedimentary waves (~2 km) is much larger than the distance between two neighbouring linear backscatter anomalies at Flare 5 (~100 m). Unfortunately, the resolution of the PARASOUND echo sounder is insufficient (Fig. 7.5) and, thus, we have no conclusive explanation for the parallel elongated backscatter anomalies.

7.5.2 Sub-seafloor Structures at Nacent Ridge, First Ridge, and Sixth Ridge

The sub-seafloor structures in the area of several seeps have been studied using high-resolution multi-channel seismics (Fig. 7.13). Three seismic images have been selected in order to illustrate a common feature underlying methane seepage occurring at ridges, which is the existence of anticlines that act as hydrocarbon reservoirs (Ding et al., 2010a). Seismic profile GeoB07-364 crossed Nascent Ridge some kilometres east of Flare 5 and First Ridge some kilometres west of Flare 4, respectively (Fig 7.12).

Nascent Ridge is the youngest anticline mainly composed of sediments of the incoming oceanic plate, which are characterised by lower reflection amplitudes compared to the slope sediments. Considerable amounts of slope sediments (200 ms TWT) have accumulated between Nascent Ridge and First Ridge with typical onlap structures at the landward side of Nascent Ridge. Below Nascent Ridge high reflector amplitudes with typical bottom simulating reflector (BSR) characters exist, i.e. it occurs at a constant depth below the seafloor intersecting otherwise continuous sedimentary reflectors. This reflector has been previously discovered and described as a result of free gas that has accumulated below the gas hydrate stability zone (Grevemeyer et al., 2000; White, 1979; White, 1982). The gas eventually rises through the sediments within the gas hydrate stability zone causing blanking zones observed in PARASOUND profiles, and emits at the seafloor at Flare 5 (Bohrmann et al., 2008a).

In the area of Flare 4 First Ridge is underlain by an anticline. The frontal side of the ridge seems to be piecewise normal-faulted or slided. Reflections in these slided sediments are very chaotic. High reflection amplitudes below the central part of the ridge indicate the presence of gas analogous to the observations at Nascent Ridge but less pronounced and less extensive. The observation that bubble emissions and chemosynthetic communities exist near the crest of First Ridge suggest that the vertical upward movement through the sediments is the preferential pathway for the gas. Another possibility would be that hydrocarbons migrate through the flank of the ridge; however, the slide complex seems to hinder fluid flow.

The internal structure of Sixth Ridge varies considerably along strike, as shown in Figure 7.13 b and c. Profile GeoB07-413 crossed the Sixth Ridge just east of Seep I while profile GeoB07-354 crossed Flare 3. As discussed in detail by (Ding et al., 2010a), there is considerable variation in the depth of Unit V along the Sixth Ridge despite the fact that the bathymetric height of the ridge does not change much. While Unit V is exposed in the western profile GeoB07-413 close to Seep I it is covered by a thick (0.6 s TWT) thick sediment package at the eastern profile GeoB-354 directly crossing Flare 3. Unit V represents the uppermost layer of imbricate sediments from the former oceanic plate whereas the sediments above have its source from the slope, as reasoned by Ding et al. (2010a). Flare 3 overlays sediments that are also characterised by high amplitude reflectors and, in addition, by vertically chaotic zones identified as chimneys transporting gas-rich sediments to the surface.

In the area of Seep I strong reflectors indicate accumulation of hydrocarbons below Unit V. Normal faulting provides a suitable pathway for these fluids that are then released from the seafloor close to or at the local crest of the ridge. The profile crosses the Sixth Ridge just east of Seep I were one of several slump scarps can be seen in the bathymetry (Fig. 7.8a). There is, thus, evidence that methane-rich fluids may seep out close to the slump scarps, as these are characterised by high backscatter, too. Unfortunately, we have not surveyed these by TV-sled and can therefore only speculate if methane seepage indeed occurs at these sites. We restrain from considering these high backscatter slump scarps as seepage sites for three reasons: (1) we have no direct evidence for seepage at any of the features (including the lack of hydroacoustic anomalies), (2) the intention of this study is to produce a reliable minimum estimate of seepage phenomena in the study area and, thus, we included into the inventory (see below) only those sites with convincing evidence of seepage, and (3) high backscatter is associated with erosion and slumping at many sites e.g. at many ridges, along the canyon walls, and at the upper slope just because of steep flanks or exposed hard ground.

7.5.3 Inventory of Seep Sites

The almost complete coverage of the continental margin segment shown in Figure 7.2 and 7.12 by TOBI side scan sonar allowed a systematically search for backscatter anomalies that are potentially related to methane seepage. As discussed above (chapter 7.5.1), active methane seepage like indicated by living chemosynthetic communities as well as seep-related carbonates occur at backscatter anomalies at Flare 5 and Flare 7 (Fig. 7.4 and 7.9) but also at Flare 3, Flare 4, and Flare 11 (Table 7.2). As also discussed above (chapter 7.5.2), the location of several methane seeps is above anticlines that have trapped hydrocarbons like exemplified for Flare 5, Flare 4, Flare 3, and Seep I. Morphologically, these seeps are located at ridge crests. Following these observations, we systematically searched in the side scan sonar data and found five additional sites (Seep II − VI) that are characterised by elongated high backscatter anomalies at ridge crests. Although we lack seafloor observations at these sites we deduce that these are methane seep sites. In addition, there is evidence that Flare 7

and Flare 11 situated at the mid-slope terrace are also located above anticlines, although we lack detailed information of the subsurface structure. In general, sediment-covered accretionary ridges exist at the mid-slope terrace as shown by seismic and morphotectonic studies (White and Louden, 1983; Platt et al., 1985; Minshull et al., 1992; Kukowski et al., 2001). Furthermore, Flare 7 and Flare 11 are located at roughly EW trending local summits as exemplified for Flare 7 (Fig. 7.9) that could be the morphological expression of the former ridge crest. Moreover, about 10 km east of Flare 7 an anticline has been mapped by Ding et al. (2010a) (anticline IV), thus, Flare 7 is probably located above a continuation of this anticline. In conclusion, apart from the upper slope, discussed below, almost all of the identified methane seep sites at the mid-slope terrace and the lower slope are located at local summits and ridge crests and are associated with linear EW-trending high backscatter anomalies.
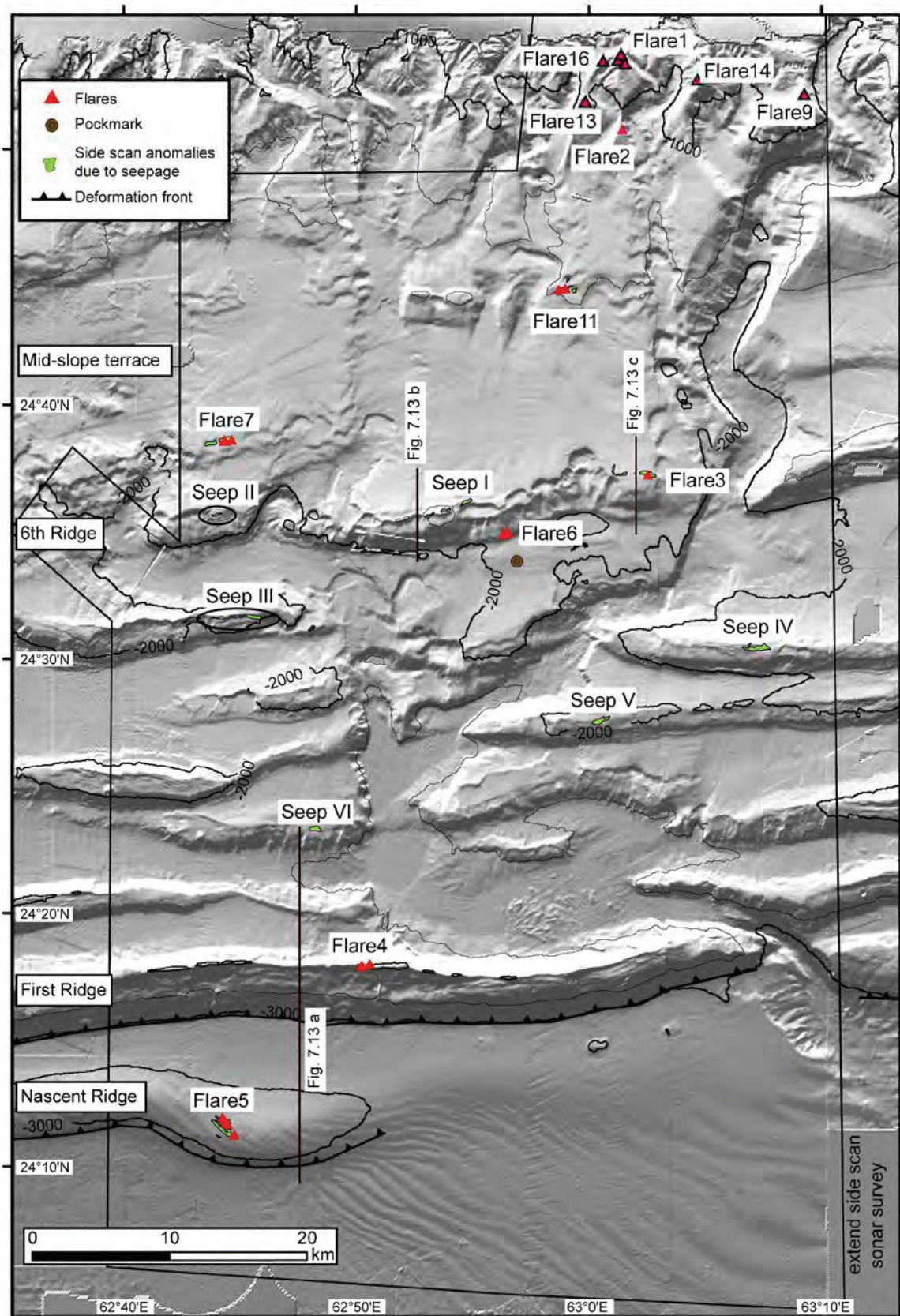
Fig. 7.12: Summary of evidence for methane seepage drawn on shaded bathymetry. Indicated are the locations of gas emission sites "flares" as indicated by hydroacoustic anomalies in echo sounder, the outline of seep-related high backscatter anomalies, and the major seafloor observations. The lines indicate the location of seismic profiles shown in Fig. 7.13.
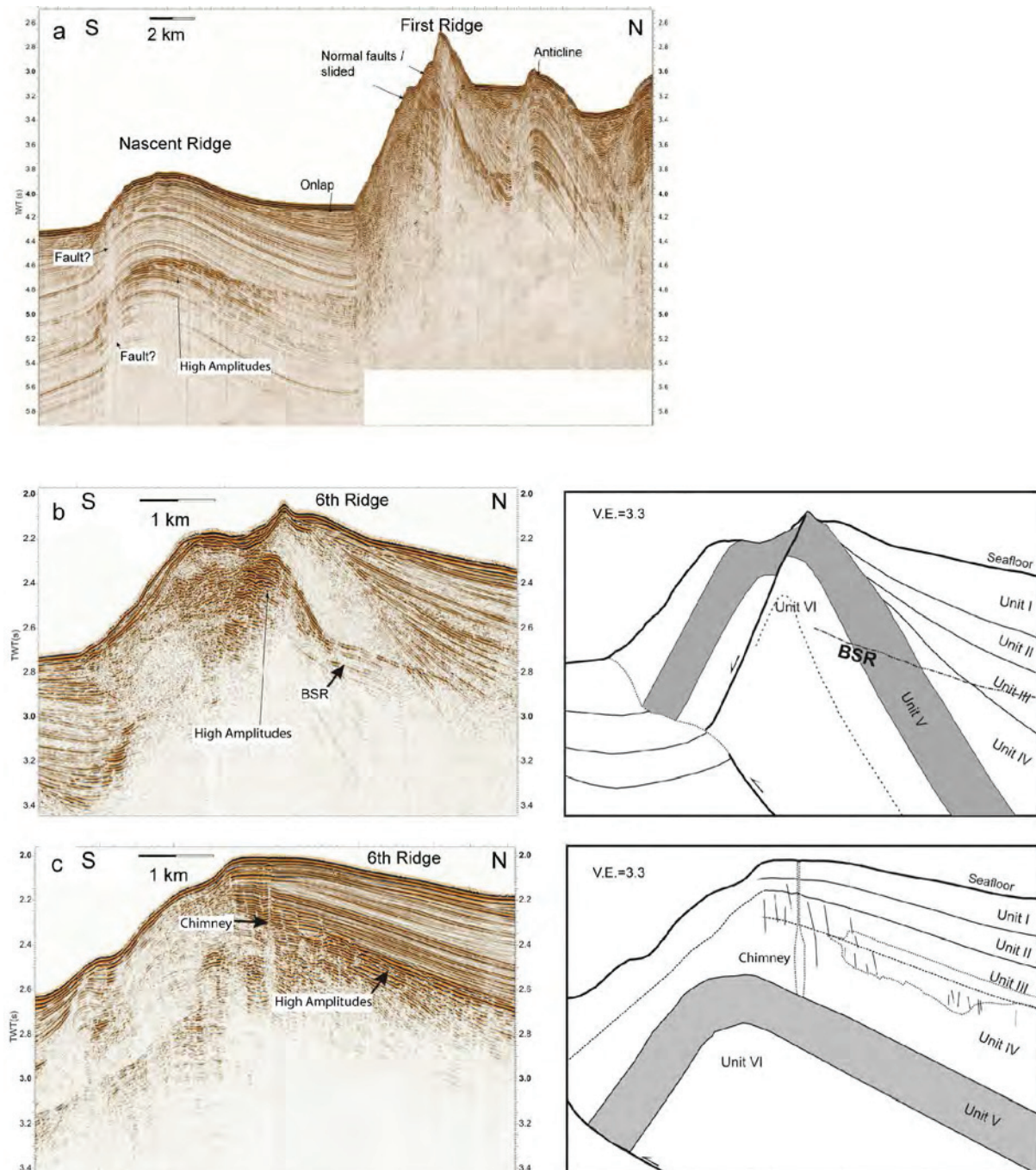
Fig. 7.13: High-resolution seismic profiles. a) Profile crossing Nascent Ridge and First Ridge. High amplitude reflectors underneath Nascent Ridge indicate accumulated free gas. Profile GeoB 07-364. b) Western seismic profile crossing Sixth Ridge, Unit V is exposed. Profile GeoB 07-413. c) Eastern seismic profile crossing Sixth Ridge, Unit V is buried. Profile GeoB 07-354. (Ding et al., 2010a)

Tab. 7.2 (next page): Summary of methane seeps within the side scan sonar survey area as shown in Figure 2 and 8. The seeps are characterised by the presence (+) or absence (-) of hydroacoustic anomalies indicative for bubble emission and backscatter anomalies in the side scan sonar data as well as a short description based on TV-sled and ROV Quest observations.

Number	TV-sled (GeoB no) ROV (dive no)	Name / Area	Position Latitude N	Longitude E	Hydroacoustic anomaly	Backscatter anomaly	Depth [m]	Seafloor observation
1	TV-sled 12205, ROV 183, 184	Flare 1 upper slope	24°53.6'	63°01.4'	+ (several weak)	-	575	Several patches with bacterial mats (Beggiatoa)
2	-	Flare 16 upper slope	24°53.5'	63°0.5'	+ (several weak)	-	ca. 800	No observation
3	-	Flare 9 upper slope	24°52.2'	63°09.3'	+ (weak)	-	670	No observation
4	-	Flare 14 upper slope	24°52.7'	63°04.7'	+ (strong)	-	754	No observation
5	-	Flare 13 upper slope	24°51.9'	62°59.9'	+ (2 weak)	No data	910	No observation
6	TV-sled 12206, ROV 180, 181, 188	Flare 2 upper slope	24°50.8'	63°01.4'	+ (2 strong)	No data	1020	Several bacterial mats (Beggiatoa, Thioploca), vesicomyid clams, ampharetid polychaets, carbonates
7	TV-sled 12323, 12345, ROV 194	Flare 11 mid-slope terrace	24°44,5'	62°59'	+ (2 weak)	+	1460	Extensive fields with mytilid mussels, vesicomyid clams, widespread carbonates
8	TV-sled 12310, ROV 182, 185, 191	Flare 7 mid-slope terrace	24°38.6'	62°44.5'	+ (4 weak)	+	1650	Extensive carbonates, vestimentifera, mytilids, vesicomyid clam
9	TV-sled 12209, ROV 190	Flare 3 sixth ridge	24°37.25'	63°02.5'	+ (very faint)	+	1500	Mytilid mussels, vesicomyid clams, vestimentifera, some carbonates
10	TV-sled 12311, ROV 186	Flare 6 sixth ridge	24°34.9'	62°56.5'	+ (2 strong)	No data	1820	Extensive mytilid mussel fields, exposed carbonates, vestimentifera/vesicomyid clams
11	TV-sled 12217	Seep I sixth ridge	24°36'	62°53'	-	+	1500	Bivalves, carbonates
12	-	Seep II sixth ridge	24°35.7'	62°44'	-	+	ca. 1700	No observation
13	-	Seep III sixth ridge	24°31.5'	62°44.5'	-	+	ca. 1900	No observation
14	-	Seep IV lower slope	24°30.5'	63°07'	-	+	ca. 1600	No observation
15	-	Seep V lower slope	24°27.5'	63°00.5'	-	+	ca. 2000	No observation
16	-	Seep VI lower slope	24°23.2'	62°48.3'	-	+	ca. 2300	No observation
17	TV-sled 12220, 12325, ROV 195	Flare 4 First Ridge	24°17.9'	62°50.25'	+ (very faint)	+	2000	Vesicomyid clams
18	TV-sled 12218, ROV 179, 187, 192	Flare 5 Nascent Ridge	24°11.5'	62°44.5'	+ (very strong)	+	2870	Vesicomyid clams, pogonophoran tube-worms, "mounded" topography

The only exception to this general pattern is Flare 6, located at the base of the Sixth Ridge. It is a considerably active methane seep with active gas emission, flourishing chemosynthetic communities and seep-related carbonates observed by ROV QUEST. Despite the fact that this seep was not imaged by side scan sonar, as it was unfortunately located just below the tow fish (Fig. 7.8b), its extent must have been small. This is in contrast to the other backscatter anomalies that are elongated and regularly large enough to be seen in the side scan sonar image. A seismic profile crossing this seep site indicates an active thrust between the south-flank of the anticline underlying Sixth Ridge and the piggy-bag basin (Fig. 6.5b in Ding et al., 2010a). This fault may give way to hydrocarbons that have accumulated below the well-visible BSR in the sediment-filled basin.

The inventory of methane seeps would not have been complete without the information on the location of hydroacoustic anomalies indicating gas emission from echo sounder systems (Bohrmann et al., 2008a). Especially at the upper slope the side scan information was limited due to the rough terrain causing data gaps as well as high backscatter due to slope erosion. Any potential seep-related backscatter would have been overlooked due to the high background backscatter. In addition, visual seafloor observations at Flare 1 indicate that the extent of individual seep sites of only a few meters in diameter (Fig. 7.7d) might be too small to be seen in the backscatter image that has nominal pixel sizes of about 3 m (Blondel and Murton, 1997).

In summary, a total of 18 methane seeps were found within the study area shown in Figure 7.2 and 7.12 using TOBI side scan sonar and 18 kHz echo sounder data. Without doubt, all twelve sites with bubble emissions as indicated by hydroacoustic anomalies in the water column are methane seeps that had been active, at least during our visit in 2007. However, the finding of extant chemosynthetic communities at each of the nine sites that have been observed by either TV-sled or ROV QUEST indicate that these seeps have been active at least for several years but likely for decades or longer. Although five sites with backscatter anomalies exist that have neither been observed visually nor have there been any bubble emissions been detected, we propose that these sites are also active methane seeps, due to the finding that all other better studied seeps have been active as well.

Within the study area, there have been additional reports of potential seep sites besides those bubble sites and bacterial mats at the upper slope, that we re-discovered and already listed in Table 7.2 (von Rad et al., 2000; Schmaljohann et al., 2001). A mud volcano field south of First Ridge (Wiedicke et al., 2001) was already suggested to be presently inactive with respect to methane seepage. Based on our data, we confirm the supposition that the mud volcano field on the abyssal plain is dormant, as no backscatter anomaly was associated with these mounds (Fig. 7.3b). Anomalies in the water column registered by sediment echo sounder have been interpreted as the active eruptions of a mud diapir (Kukowski et al., 2001). The acoustic anomalies are located at the floor of the Save canyon / Sonne fault system landward of the First Ridge (Fig. 7.3a). This area is characterised by small scale morphology with horizontal dimensions of 100-1000 m and some 30 m height that caused high backscatter. Although the origin of these features is unknown we speculate that this is solidified material that is exposed at the seafloor due to erosive activity along the canyon floor. We therefore propose that the up to about 50 m high and 1 km wide acoustic anomalies shown in Kukowski et al. (2001) are side echoes caused by the features and not active eruptions as the geological setting at the canyon floor differs greatly from all other known methane seep sites summarised in this study. In addition, the height and width of the acoustic anomaly in Kukowski et al. (2001) is very different from all other 12 hydroacoustic anomalies caused by gas emission (Bohrmann et al., 2008a). The diatreme above Anticline I (Ding et al., 2010a) convincingly shows seismic characters such as acoustic turbidity and regional updoming of the BSR that identifies it as fluid seepage related. In our study the "diatreme" is signified as pockmark and shown in Fig. 7.8. It is a morphological depression about ~500 m

wide and ~20 m deep. High backscatter is associated with the rim of the pockmark, which could be a result of the small scale morphology, whereas the central part was characterised by low backscatter. This is in agreement with a TV-sled survey that did not show any evidence for recent methane seepage.

The inventory of 18 methane seeps in the study area is a minimum estimate about the frequency of this phenomenon at this margin segment. It is likely that additional seep sites have been overlooked by side scan sonar, for example, in the steep terrain at erosional slopes such as the canyon walls or the upper slope, where high background backscatter does not allow to detect any seep-related backscatter anomalies. In addition, several gas emissions especially at the upper slope have probably been missed due to the narrow beam width of the 18 kHz echo sounder to detect these as hydroacoustic anomalies in the water column (Bohrmann et al., 2008a). However, this is intended as first minimum inventory of a ~50 km wide continental margin segment from the abyssal plain to the upper slope indicating that, on average, every ~3 km along the slope one methane seep exist.

Based on data from the same RV METEOR cruise M74 Römer et al. (subm.) deduced gas flow rates from ROV video data and gas sampling. They also related results from seafloor observations to hydroacoustic flare intensity. Investigating flares 1, 2, and 5, they found a flow of $0.8 \pm 0.5 \times 10^{6}$ mol yr^{-1} km^{-1} for the 50 km section surveyed. Continuing on the paragraph above, the one seep every ~3 km would emit about 2.4×10^{6} mol yr^{-1} of methane.

7.5.4 Distribution of Methane Seeps

Methane seeps have been found throughout the continental slope offshore Pakistan at water depths between 575 m and 2870 m (Fig. 7.12, Table 7.2). Those seeps at the lower slope and the mid-slope terrace are generally located in a section of the continental margin where a pronounced bottom simulating reflector was described at water depth between ~1350 m and ~3000 m (White and Klitgord, 1976; White, 1977; Minshull and White, 1989; von Rad et al., 2000). Geophysical modelling suggests a thick zone of free gas below the BSR (Grevemeyer et al., 2000; Sain et al., 2000). As discussed above, almost all seeps at these depths are related to hydrocarbon reservoirs that exist within anticlines. The map illustrates that the distribution of these seeps at the accretionary ridges is rather uniform (Fig. 7.12). If seepage has been discovered at a ridge it is only one site that has been discovered, the Sixth Ridge is an exception. Here several seeps have been identified that conspicuously co-occur with abundant slump scarps, therefore, it might be speculated that there is a profound relationship between seepage and slumping. For example, it is straightforward to imagine that the fault underlying the linear backscatter at Flare 3 or Seep I acts as weakening zone that facilitate the seaward side of the ridge flank to collapse (Fig. 7.8). Speculatively, this may have happened frequently along Sixth Ridge as many slump scarps are visible in the bathymetric map as well as the side scan image. We further speculate that slumping opens additional pathways, which may lead to an abrupt release of the hydrocarbon reservoir. Such a scenario would explain why we have only found evidence for seepage at those segments of Sixth Ridge between slump scarps but not in the slump scarps itself. Further seismic studies may help elucidating the relationship between seepage and slumping. Active slumping as well as methane seepage at Sixth Ridge is probably a result of intensified thrusting related to underplating of material from the subducting plate in this area. In a wide-angle seismic study Kopp et al. (2000) showed evidence that a basely accreted block exist below the mid-slope terrace, its seaward limit coincides with the location of Sixth Ridge.

In contrast to the seeps discussed above, the geological setting of those seeps at the upper slope is largely unknown. In general, the upper slope is part of the accretionary wedge that experiences uplift and probably extension due to continued underplating of sediments

from the subducting oceanic plate (Platt et al., 1985). At the same time, it is subject to erosion leading to the formation of a rough topography with gullies and ridges (Kukowski et al., 2001). The discovered methane seeps are either located at the crests of ridges or in the upper parts of the erosional slopes. The geological control of methane seepage is speculative, as the subsurface architecture of the sediments has not been studied so far. It could be that deep hydrocarbon-rich fluids ascent due to the supposed extensional stress regime. Alternatively, the occurrence of methane seepage could be a result of strong biogenic methane production at shallow sediment depth due to high rates of organic-rich sediment accumulation in combination with reduced oxygen availability in the stable OMZ. Further studies are needed to elucidate the origin of methane seepage at the upper slope.

It is interesting to notice that methane seeps have not been detected directly at or close to the prominent Sonne fault or Save canyon system in the study area (Fig. 7.12). We actually have chosen the area such that both settings are included; the continuous accretionary ridges as well as more dynamic fault and canyon systems. We speculated that tectonic activity or sediment erosion and transportation may somehow increases the likelihood that fluids are released. One reason for not finding seeps is certainly a bias in our method, as methane seeps may not be detectable in side scan sonar data at these erosive features. However, if gas emission would be significant at these fault and canyon system, we should have detected it by 18 kHz echo sounder, which we have not. This is in contrast to the finding by of vesicomyid clam clusters in a canyon at the continental slope east of our study area (von Rad et al., 2000). In conclusion, we disregard the fault and canyon system as mayor area for fluid seepage due to the lack of evidence for gas emission but admit that additional seep sites may be found by, e.g., additional TV-sled surveys.

7.6 Conclusion

The systematic search for methane seeps combining 18 kHz echo sounder (Bohrmann et al., 2008a) and side scan sonar (this study) as well as swath bathymetry, sediment echo sounder, TV-sled, and ROV QUEST observations has resulted in an inventory of methane seeps. A total of 18 methane seeps have been discovered at the ~50 km wide continental slope segment offshore Pakistan at water depth between 575 and 2870 m. It can be expected that all of these 18 sites are presently active due to the finding that gas emissions have been found at 12 of the 18 sites and because at all of the nine sites studied in detail by TV-sled or ROV QUEST chemosynthetic communities were found (Table 7.2). It is likely that additional seep sites exist, especially additional gas emission sites at the upper slope, which have not been discovered so far due to limited 18 kHz echo sounder coverage (Bohrmann et al., 2008a). In addition, backscatter anomalies related to methane seepage may be obscured in erosive areas with high background backscatter such as canyon sidewalls or within slump scarps. The inventory is therefore a minimum estimate of seeps with, on average, about one seep occurring every ~3 km along the margin.

This systematic survey is thought as a first step towards quantitative estimates of seep-related processes such as budgeting of methane emission for an entire 50 km margin segment. The study area might be considered as representative for the entire ~800 km wide continental slope of Makran as it is characterised by remarkably uniform accretionary ridges that can be traced over hundreds of kilometres (White and Louden, 1983; Minshull and White, 1989; Kopp et al., 2000). Thus, the study contributes to the general understanding of methane seepage related to accretion of a thick sediment pile that is transported with the incoming oceanic plate. Within the study area we found no evidence for mud volcanism, which is in agreement with geophysical studies indicating that the main sediment dewatering takes place

close to the deformation front (Fruehn et al., 1997). As a result, the subducting and accreted sediments are well consolidated and mud volcanism may not be expected. Alternatively, anticlines trap hydrocarbons that eventually rise towards the seafloor (Ding et al., 2010a). The occurrence of free gas below the BSR as proposed based on seismic studies and the observed gas bubble emissions from the seafloor indicate that free gas is a major component of fluid seepage at the slope of the Makran continental margin.

The sediment-rich Makran accretionary wedge may be considered as one end-member of convergent continental margin. On the other side, the erosive continental margin offshore Costa Rica and southern Nicaragua may be considered as another end-member. At this margin characterised by subduction erosion, almost all of the ~400 m of sediments on the subducting plate is subducted (Kimura et al., 1997). In addition, the overriding plate is eroded at its base due to abrasion by the bended downgoing oceanic plate or seamount and ridge subduction (Ranero and Huene, 2000; von Huene et al., 2004). Subduction erosion leads to normal faulting of the overriding plate and seepage of fluids that are release as a result of mineral dewatering at the plate boundary (Ranero et al., 2008). The frequency of fluid seepage has been estimated in a systematic search similar to the approach followed in this study and revealed that, on average, one seep exist every 4 km along the studied margin segment (Sahling et al., 2008a). Methane seepage occurs mainly as seepage of methane-rich liquids, i.e. advection of pore water; no evidence for gas bubble emission was found so far (Mau et al., 2006). Despite the complete different geological setting and manifestation of methane seepage it is interesting to notice that in both areas offshore Pakistan and offshore Costa Rica/Nicaragua the frequency of seep sites along the margin is comparable with one seep occurring every 3 and 4 km along the margin, respectively. It demonstrates that seepage at convergent margin settings is in general a frequent phenomenon that warrants further studies.

Acknowledgement

8

Summary and Conclusion

Compiling data for this thesis I have seen a large variety of seep structures on the seafloor. There are many varying forms of carbonates, biota, gas hydrates, backscatter patterns, and morphologies in the very various environments. Several factors exist, which control the cold seeps appearance, so that the seep can take a completely different look.

The combination of acoustic and visual survey methods proved an efficient and successful tool to (1) locate seeps on the seafloor, (2) measure their extent, (3) describe internal structures, (4) identify fine detailed features, and deduce processes important for the development of the seep. All different scales complemented each other: from hundreds of metres surveyed by vessel based acoustic instruments to millimetre small details of exposed asphalt and carbonate or gas bubbles observed by ROV-based cameras at the very centres of seeps. Depending on the state of knowledge of the seep, range and necessary resolution for the next step of investigation were adjusted, always becoming finer to gain more facets with increasing resolution. Acoustic and visual mapping was used to cross-calibrate the different findings, assuming visually observed features to be present at acoustically mapped regions with identical backscatter signatures.

Excellent experiences were made with the mapping requirements to pinpoint new seeps in an area. The application of single beam echo sounder to spot bubble flares rising in the water column, for example, was advanced to almost guarantee findings in a prospective area during a survey of several hours duration. The available suite of instruments was deployed to achieve the potential maximum. The possibilities to explore and map seeps are critically influenced by the slope gradient, if it is too steep, side scan sonar fails to image seep sites, and it is an advantage to concentrate on water column flare imaging to trace gas releasing seeps. However, the state of the art changes. New technical inventions and developments improve the survey capabilities. The next chapter elaborates further on that subject.

The majority of questions listed in the motivation chapter had already been answered successfully within the individual chapters on the special topics of asphalt volcanism (chapter 5), gas seepage (chapter 6), and the quantification of seeps at the Makran margin (chapter 7). Therefore, this conclusion focuses on a broader range. It provides a frame for development of an overall scheme to characterise and classify, or, possibly, predict, cold seeps from the given intrinsic and environmental conditions.

There are several independent variables, which govern the active seep in the deep-sea. These have been investigated within the different natural environments and dealt with in the three manuscripts above. Here I would like to summarise that work in form of a new presentation form. It follows as a concept of vector mathematics. The selected variables for the presentation are independent of each other. Hence, they can be visualised as perpendicular vectors within a multidimensional space. The rule of independence states that a new independent vector has to be perpendicular on all others, which is achieved by the product of all existing vectors with the new one to be equal zero.

$$\vec{v}_1 \perp \vec{v}_i \Leftrightarrow \prod_1^n \vec{v}_n = 0 \qquad \text{(Eq. 8.1)}$$

Using this way it is possible to construct and think n dimensions of variables, but it is not printable as a 2D paper figure. Multivariate analysis often restricts and plots two variables at a time in a two axis graph to simplify the figure. Applying the concept on cold seeps, any seep appearance could be predicted by a five-dimensional plot or cube. The first three axes are intrinsic to the seeping fluid, the other two belong to environmental conditions:

One axis represents the ***fluid composition***, hydrocarbons ranging from light methane gas to extra heavy petroleum and asphalt. Water certainly seeps as well, but throughout the thesis it became clear, that mostly hydrocarbons make the contribution to the seeps studied. Water might and does play a more pronounced role at other seeps, like mud volcanoes. Here we focussed on hydrocarbon fluids. This axis represents only the physical properties and effects on the sedimentary seafloor. Asphalt solidifies, the high-viscosity oil is still sticky, stabilising and gluing surrounding material, the lighter gas then has more buoyancy force and works contrarily against the existing sedimentary structure. Heavy petroleum and oil can assist to build seafloor morphology, at least on small scales. Opposing, light components erode the seafloor forming holes, rough structures, or entire pockmarks. Gas hydrate can both accumulate and raise the seafloor in half-circles, or float up and carry away material. Rising water has an effect similar to gas, but the driving forces are usually much weaker.

A second axis represents the ***flow rate***. It can range from non-existing, pervasive and less than the sedimentation rate (i.e. no or dormant seep) to vigorous with severely eroding effect on surrounding sediment. A weak flow will only attract little seep fauna and leave little and difficult to observe traces on or only below the seafloor. A vigorous flow has the potential to attract the entire suite of fauna, and change the seafloor morphology by erosion, deposition of asphalt, accumulation of gas hydrate, or as a mud volcano. The flow rate also governs the depth of the SMI, a focus of carbonate precipitation. Fauna can also indicate the flow rate as different species utilise different concentrations of seep fluid or its derivatives. At Makran Flare 7 porous carbonate plates appear with a storey pattern outcropping and overhanging at some sides. The top of the plate is densely settled by mussels at places, whereas other areas show only hemipelagic sediment cover. Openings in the interior of plates had been observed as well. The supposition is that the carbonates have grown within the sediment. The outcrops require then a sediment removal. These results point at more vigorous flow seasons or periods alternating with low continuous flow rate to build up the carbonate storeys.

The third variable defines the ***time*** axis. Seeps develop with time, for example by building of authigenic carbonate deposits, expansion on large terrains, and increasing fauna settlement. This axis could also be named age axis. The Makran seeps at Nascent Ridge (Flare 5) and at mid-slope (Flare 7) are good examples. The emission rate of gas appeared to be similar at both sides. The time, the seeps had existed for can be very roughly estimated just by the position within the accretionary prism: Nascent Ridge is very young, whereas the mid-slope ridge at Flare 7 is significantly older. All mid-slope seeps in the Makran appear very developed with large areas covered by thick carbonates and well settled by organisms. At Nascent Ridge all these features appear like the ridge itself very nascent. See Fig. 8.1 below for a visual example plot.

The fourth axis holds ***water depth***. The depth controls the pressure, which is a major element for different physical and chemical processes. The second major element is the temperature. In the deep ocean it changes constantly with water depth, though there are changes from area to area due to regional oceanography. Hydrate stability and solubility of gases are a function of pressure and temperature. The upper boundary of the GHSZ is located around 800 m bsl and does vary within different ocean water masses. If gas hydrate can form, it plays a major role as new phase, for instance by cementing the sediment, blocking pathways, or temporarily stores rising gas as buffer medium. Especially the Batumi manuscript (chapter 6) shows the influence of gas hydrate and free gas on the formation of seep morphology. Gas dissolved in water increases the water's buoyancy, but free gas can create much larger force while migrating. The solubility increases with pressure. The number of moles of a substance necessary to form free bubbles also increases with depth due to the increasing compression with depth.

The fifth axis is the ***oxygen concentration***. It allows or limits the population of seeps by fauna. A teeming fauna precipitates more carbonates, builds up more and widespread

structures. Consequently, high oxygen concentration favours formation of chemoherm carbonates, which makes seeps in oxygen rich water easier to be imaged by backscatter surveys. The Makran flares are ideal examples: The shallow seeps within the oxygen minimum zone were only a bubble emission point surrounded by a bacterial mat. In combination with the steep slopes they were not detectable in side scan sonar data. Contrary, with more oxygen available large amounts of mussels and crabs can settle at, for example Flare 11, which was clearly visible in backscatter imagery.

A seep can be characterised by these five variables and be plotted within the 5D-cube. However, individual seeps may eject different fluids at different flow rates at different times and therefore plot as a cluster and not as single points. This behaviour was observed for most seeps within this project. It reflects a certain natural variation with most systems not exactly defined. Other factors hindering a clear classification are sedimentation and bioturbation burying seep indicators. Fig. 8.1 illustrates two relationships as examples. The first case (Fig. 8.1a) shows the influence of flow rate and time on the Makran seeps. Flare 1 at the upper slope and Flare 5 at Nascent Ridge are grouped at a comparable age. The upper slope seeps are relatively often affected and destroyed by slope instabilities.
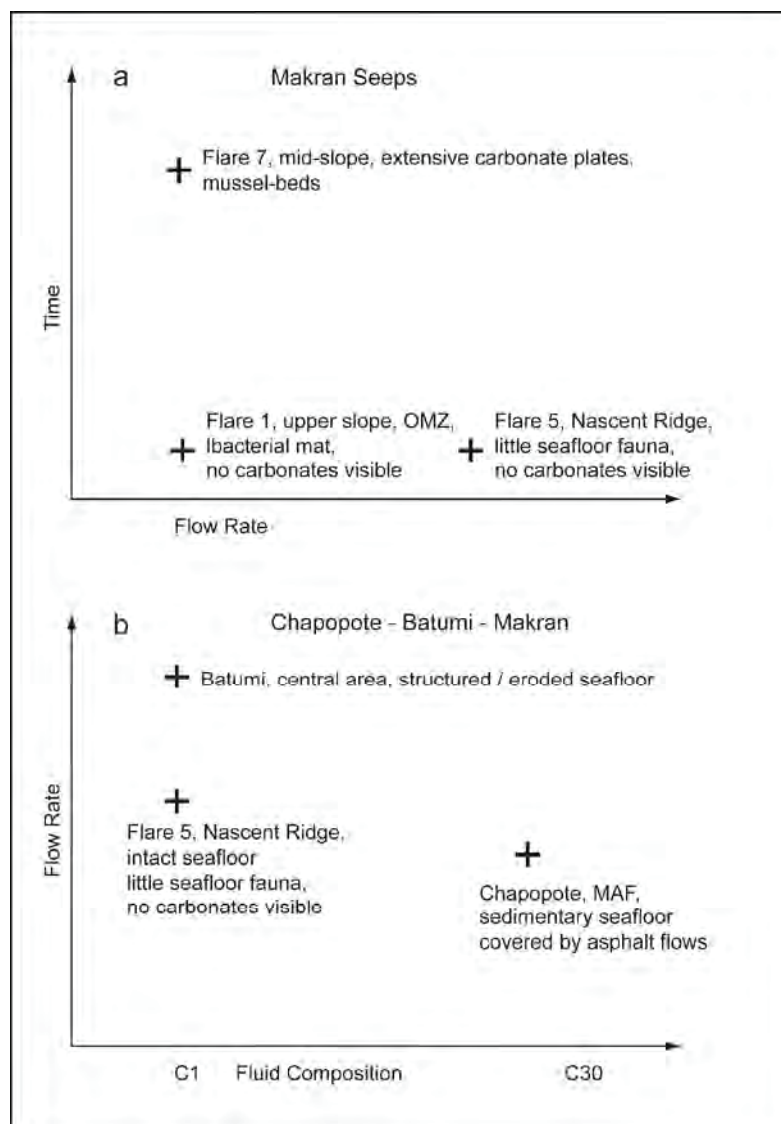
Fig. 8.1: 2D-plot examples. a) Time vs. Flow Rate for Makran Seeps. b) Flow rate vs. Fluid Composition

Contrary, the mid-slope ridges are more stable and seeps can develop rather undisturbed during the accretion process from the deformation front to the mid-slope, even though they are up-lifted by several hundreds of metres.

The second case (Fig. 8.1b) compares fluid composition and flow rate. Both Makran Flare 5 and the Chapopote Main Asphalt Field are assumed to have a similar flow rate. However, the fluid composition is very dissimilar. In these both cases the flow's energy is not sufficient to erode the seafloor. At Chapopote the seafloor is even stabilised by the outflow of heavy oil and deposition of asphalts.

This thesis contributes to the creation of the 5D-cube introduced above by setting especially the fluid viscosity axis. Thanks to research of the past decades enough observations had been made to fill the cube. However, it assumes similar environmental conditions to be settled by similar communities world-wide, which is supported by observations. Alike species of shells and vestiminfera, for instance, had been found at seeps world wide. Hot vents, cold seeps, and whale falls supply enough step stones for biological life to spread with ocean currents. The ocean water mass can be taken to be well mixed with the same concentrations of elements present globally. Local conditions like in the enclosed Black Sea with the shallow Bosporus Strait or high production zones like Makran can deviate from the general pattern. This was taken as advantage and exploited for this thesis.

9

Outlook

Still many questions remain beyond those solved in this work. Some could have been investigated with more available time to work at the single sites, others require new technological developments. There is a long list of individual questions on the three work areas, which will be dealt with below. More general research questions are beyond the scope of this work: exploitation of hydrocarbons at cold seeps; increased seafloor stability vs. geohazards by seafloor destabilisation at seeps; final judgement on significance of seepage on geochemical cycles and biological communities on ocean scales.

Mapping of new seep sites can fill the cube of different variables controlling seep appearance developed in the previous chapter. Future research could investigate for instance the validity or dependency on additional factors. This might be developed into new end-member studies. More new end-members may also be suggested. Further research is necessary on other combinations of end-members than dealt with here. However, seeps need to be found according to the theoretical desired conditions, e.g. extremely deep water combined with maximum volume flow. A filled 5D-cube providing key seeps for the five variables could one day find its place in Geology text books compared to Bowen's reaction series for magmas. New technical developments of autonomous vehicles reduce the time spent at sea, hence the cost, but still provide more detailed mapping due to the proximity of the object of interest. Such Autonomous Underwater Vehicles (AUVs) had been on the market during the research expeditions of this thesis, but not yet fully implemented in the institute's regular cruise equipment.

The characterisation of seeps was based on acoustical mapping and observation by TV sled or ROV. This equals only one observation at one spot per time. It was found, however, that conditions of seepage quickly change from exit points to another. Individual releases start and fall dormant again. Observations should ideally happen over an entire seep area at the same time. Long time observations are necessary. Additionally, the quantification to measure flow volumes as pervasive, dissolved flow (geochemically) or in bubble streams (by volume measure, optically, or acoustically) is very important to characterise seeps. The PhD thesis by M. Römer (2011) contributes already well to the latter method. Moreover, the amount of seep fluids retained in the seafloor (gas, liquid, or gas hydrate) should be measured aided by drilling. New devices built at MARUM allow such investigations by recovering pressurised samples under in-situ conditions. New technical developments will be implemented in long term seafloor-observation-networks focussing on various topics, one should be cold seeps.

Chapopote Knoll still needs to be covered with a deep-towed side-scan sonar survey to map all exposed asphalts. Furthermore it would be sensible to drill through the known asphalt sites to, first, identify, if there is a layer of hemipelagic sediment buried underneath, which might be dated then. Secondly, deep coring should resolve the total thickness and, possibly, ancient flow-surface layers, which might be coated by ropy or rough surfaces. What is more, drilling could uncover buried asphalts off the asphalt fields buried by hemipelagic sediment presently.

At Batumi Seep it is still questionable, if the proposed migration of the seep along the fault actually happens. A re-survey after 2.5 years did not clarify this. Repeated side scan sonar deployments on decadal scale are more promising. In any case, it has to be ensured to move the sonar fish on exactly the same paths as during previous surveys as this limited the comparison presented in this work by slightly varying geometries. Recovery of pressurised drill-samples could back up the model of different phases of seep development with the recovery of gas hydrates.

Makran work would benefit from an improved mapping of the upper slope. Based on the well-known bathymetry, side scan surveys might be adjusted to local slope conditions to image seeps on those flanks. Water column scanning has proved successful and could be extended to identify new seep sites. Leaving the principle of a conservative estimate, the number of seeps found within the narrow footprint of the PARASOUND single beam could be

extrapolated to the not-surveyed upper slope proportions. At Nascent Ridge a coring transect with gravity corer or DAPC could further clarify the origin causing the backscatter fingers due to carbonate and / or gas hydrate. Now that a comparable number of seeps was found at erosive as well as at accretionary subduction zones, it is an important step further forward to compare the overall flow volumes in both cases.

It is to be found out how much time and continuity it takes to obtain fully developed seeps at equilibrium with given conditions. This is necessary to classify seeps at the correct and fixed position within the 5D-cube.

References

Abegg, F., Hohnberg, H.-J., Pape, T., Bohrmann, G. and Freitag, J., 2008. Development and application of pressure-core-sampling systems for the investigation of gas- and gas-hydrate-bearing sediments. Deep-Sea Research Part 1, 55: 1590-1599.

Abrams, M.A., 2005. Significance of hydrocarbon seepage relative to petroleum generation and entrapment. Marine and Petroleum Geology, 22: 457-477.

Aharon, P., 1994. Geology and biology of modern and ancient submarine hydrocarbon seeps and vents: an intruduction. Geo-Marine Letters, 14: 69-73.

Akhmetzhanov, A.M., Ivanov, M.K., Kenyon, N.H. and Mazzini, A., 2007. Deep-water cold seeps, sedimentary environments and ecosystems of the Black and Tyrrhenian Seas and the Gulf of Cadiz, Preliminary results of investigations during TTR-15 cruise of RV Professor Logachev, June-August 2005, UNESCO, Paris.

Anderson, A.L. and Hampton, L.D., 1980. Acoustics of gas-bearing sediments I. Background. The Journal of the Acoustical Society of America, 67(6): 1865-1889.

Applied Microsystems, 2009. www.appliedmicrosystems.com_Applications_By_Technology_Multi-Beam_System.aspxMultibeam.jpg

Artemov, Y.G., Egorov, V.N., Polikarpov, G.G. and Gulin, S.B., 2007. Methane emission to the hydro-and atmosphere by gas bubble streams in the Dnieper Paleo-delta, the Black Sea Marine. Ecol J, 6: 5-26.

Atlas Hydrographic, 2004. Atlas Parasound, Bremen, pp. 4.

Banks, C.J., Robinson, A.G. and Williams, M.P., 1997. Structure and regional tectonic of the Achara-Trialet Fold Belt and the adjacent Rioni and Kartli Foreland Basins, Republic of Georgia. In: A.G. Robinson (Editor), Regional and Petroleum Geology of the Black Sea and Surrounding Region. AAPG Memoir. AAPG, Tulsa, pp. 331-345.

Barbieri, R., Ori, G.G. and Cavalazzi, B., 2004. A Silurian cold-seep ecosystem from the Middle Atlas, Morocco. Palaios, 19: 527-542.

Bekins, B.A. and Dreiss, S.J., 1992. A simplified analysis of parameters controlling dewatering in accretionary prisms. Earth and Planetary Science Letters, 109: 275-287.

Bergquist, D.C., Urcuyo, I.A. and Fisher, C.R., 2002. Establishment and persistence of seep vestimentiferan aggregations on the upper Louisiana slope of the Gulf of Mexico. Marine Ecology Progress Series, 241: 89-98.

Bernard, B.B., Brooks, J.M. and Sackett, W.M., 1976. Natural gas seepage in the Gulf of Mexico. Earth and Planetary Science Letters, 31(1): 48-54.

Blondel, P. and Murton, B.J., 1997. Handbook of Seafloor Sonar Imagery. Wiley-Praxis Series in Remote Sensing. Wiley, Chichester, 314 pp.

Boetius, A., Ravenschlag, K., Schubert, C.J., Rickert, D., Widdel, F., Gieseke, A., Amann, R., Jørgensen, B.B., Witte, U. and Pfannkuche, O., 2000. A marine microbial consortium apparently mediating anaerobic oxidation of methane. Nature, 407.

Bohrmann, G., Linke, P., Suess, E. and Pfannkuche, O., 2000. Cruise report SO 143, TECFLUX. GEOMAR, Kiel.

Bohrmann, G., Heeschen, K., Jung, C., Weinrebe, W., Baranov, B., Cailleau, B., Heath, R., Hühnerbach, V., Hort, m., Masson, D.M. and Trummer, I., 2002. Widespread fluid expulsion along the seafloor of the Costa Rica convergent margin. Terra Nova, 14: 69-79.

Bohrmann, G., Ivanov, M., Foucher, J.P., Spiess, V., Bialas, J., Greinert, J., Weinrebe, W., Abegg, F., Aloisi, G., Artemov, Y., Blinova, V., Drews, M., Heidersdorf, F., Krabbenhöft, A., Klaucke, I., Krastel, S., Leder, T., Polikarpov, I., Saburova, M.,

131

Schmale, O., Seifert, R., Volkonskaya, A. and Zillmer, M., 2003. Mud volcanoes and gas hydrates in the Black Sea: new data from Dvurechenskii and Odessa mud volcanoes. Geo-Marine Letters, 23(3): 239-249.

Bohrmann, G., Schenk, S., cruise participants, 2004. RV Sonne Cruise Report SO174, Geomar Report 117, Kiel, pp. 117.

Bohrmann, G. and Torres, M.E., 2006. Gas hydrates in marine sediments, Marine Geochemistry. Springer, Berlin Heidelberg New York, pp. 418–512.

Bohrmann, G., Pape, T. and cruise participants, 2007. Report and preliminary results of R/V METEOR Cruise M72/3, Istanbul-Trabzon-Istanbul, 17 March - 23 April, 2007. Marine gas hydrates of the Eastern Black Sea. 261, Berichte aus dem Fachbereich Geowissenschaften der Universität Bremen No. 261, Bremen.

Bohrmann, G. and cruise participants, 2008a. Report and preliminary results of R/V METEOR Cruise M74/3, Fujairah - Male, 30 October - 28 November 2007. Cold seeps of teh Makran subduction zone (continental margin of Pakistan). 266, Berichte aus dem Fachbereich Geowissenschaften der Universität Bremen No. 266, Bremen.

Bohrmann, G., Spiess, V., cruise participants, 2008b. Report and Preliminary Results of RV Meteor Cruise M67/2a and 2b, Balboa – Tampico – Bridgetown, 15 March– 24 April, 2006. Fluid seepage in the Gulf of Mexico. 263, Berichte Fachbereich Geowissenschaften, Universität Bremen, Bremen, pp. 161.

Boles, J.R., Clark, J.F., Leifer, I. and Washburn, L., 2001. Temporal variation in natural seep rate due to tides, Coal Oil Point, California. Journal of Geophysical Research, 106(C11): 27077-27086.

Borowski, W.S., Paull, C.K. and III, W.U., 1996. Marine pore-water sulfate profiles indicate in situ methane flux from underlying gas hydrate. Geology, 24(7): 655-658.

Boswell, R., 2009. Is gas hydrate energy within reach? Science, 325.

Bryant, W.R., Lugo, J., Córdova, C. and Salvador, A., 1991. Physiography and bathymetry. In: A. Salvador (Editor), The Gulf of Mexico Basin. Geological Society of America, Boulder, pp. 13-30.

Buffett, B. and Archer, D., 2004. Global inventory of methane clathrate: sensitivity to changes in the deep ocean. Earth and Planetary Science Letters, 227: 185-199.

C & C Technologies, 2010. C-Nav DGPS, http://www.cctechnol.com/site47.php.

Campbell, K.A., 2006. Hydrocarbon seep and hydrothermal vent paleoenvironments and paleontology: Past developments and future research directions. Palaeogeography, Palaeoclimatology, Palaeoecology, 232(2-4): 362-407.

Carson, B., Suess, E. and Strasser, J.C., 1990. Fluid flow and mass flux determination at vent sites on the Cascadia margin accretionary prism. Journal of Geophysical Research, 95(B6): 8891-8897.

Chamley, H., 1994. Clay Mineral Diagenesis, 2. Diagenesis with Depth of Burial. In: A. Parker and B.W. Sellwood (Editors), Quantitative diagenesis: recent developments and applications to reservoir geology. Kluwer Academic Publishers, Dordrecht.

Chanton, J.P., Burnett, W.C., Dulaiova, H., Corbett, D.R. and Taniguchi, M., 2003. Seepage rate variability in Florida Bay driven by Atlantic tidal height. Biogeochemistry, 66: 187-202.

Chapman, R., Pohlman, J., Coffin, R.B., Chanton, J. and Lapham, L., 2004. Thermogenic gas hydrates in the northern Cascadia Margin. EOS Transactions, 85(38).

Cita, M.B., Woodside, J.M., Ivanov, M.K., Kidd, R.B., Limonov, A.F. and stuff, S., 1995. Fluid venting from a mud volcano in the Mediterranean Ridge Diapiric Belt. Terra Nova, 7: 453-458.

Clarke, R.H. and Cleverly, R.W., 1991. Petroleum seepage and post-accumulation migration, Special Publications. Geological Society, London, pp. 265-271.

Collett, T.S., Riedel, M., Cochran, J.R., Boswell, R., Kumar, P., A.V. and Party, N.E.S., 2008. Indian continental margin gas hydrate prospects: Results of the Indian national Gas Hydrate Program (NGHP) expedition 1, 6th International Conference on Gas Hydrates, Vancouver, Canada.

Corliss, J.B., Dymond, J., Gordon, L.I., Edmond, J.M., Herzen, R.P.v., Ballard, R.D., Green, K., Williams, D., Bainbridge, A., Crane, K. and Andel, T.H.v., 1979. Submarine thermal springs on the Galápagos Rift. Science, 203(4385): 1073-1082.

Dallimore, S.R., Collett, T.S., Weber, M. and Uchida, T., 2002. Drilling Program investigates Permafrost Gas Hydrates. EOS Transactions, 83(18): 193,198.

Darcy, H.P.G., 1856. Les fontaines publices de la Ville de Dijon. Victor Dalmont, Paris.

De Beukelaer, S.M., MacDonald, I.R., Guinnasso, N.L. and Murray, J.A., 2003. Distinct side-scan sonar, RADARSAT SAR, and acoustic profiler signatures of gas and oil seeps on the Gulf of Mexico slope. Geo-Marine Letters, 23(3): 177-186.

Degens, E.T. and Ross, D.A. (Editors), 1974. The Black Sea-Geology, Chemistry, and Biology. AAPG Memoir, 20, Tulsa, Oklahoma, USA, 633 pp.

DeJong, K.A., 1982. Tectonics of the Persian Gulf, Gulf of Oman, and southern Pakistan region. In: A.E.M. Nain and F.G. Staehli (Editors), The Ocean Basins and Margins v6: The Indian Ocean, pp. 315-351.

Delisle, G., von Rad, U., Andruleit, H., von Daniels, C.H., Tabrez, A. and Inam, A., 2002. Active mud volcanoes on- and offshore eastern Makran, Pakistan. International Journal of Earth Sciences, 91(1): 93-110.

Delisle, G. and Berner, U., 2002. Gas hydrate acting as cap rock to fluid discharge in the Makran accretionary prism? In: P. Clift, D. Kroon, C. Gaedicke and J. Craig (Editors), The tectonic and climatic evolution of the Arabian Sea region. Special Publication. Geological Society, London, pp. 137-146.

Delisle, G., 2004. The mud volcanoes of Pakistan. Environmental Geology, 46: 1024-1029.

DeMets, C., Gordon, R.G., Argus, D.F. and Stein, S., 1990. Current plate motions. Geophysical Journal International, 101: 425-478.

Deuser, W.G., 1974. Evolution of anoxic conditions in Black Sea during holocene In: E.T.E. Degens and D.A. Ross (Editors), The Black Sea-geology, chemistry, and biology. The American Association of Petroleum Geologists Tulsa, Oklohoma, USA, pp. 133-136.

Díaz-del-Río, V., Somoza, L., Martínez-Frias, J., Mata, M.P., Delgado, A., Hernandez-Molina, F.J., Lunar, R., Martín-Rubí, J.A., Maestro, A., Fernández-Puga, M.C., León, R., Llave, E., Medialdea, T. and Vaázquez, J.T., 2003. Vast fields of hydrocarbon-derived carbonate chimneys related to the accretionary wedge/olistostrome of the Gulf of Cádiz. Marine Geology, 195: 177-200.

Dickens, G.R., O'Neil, J.R., Rea, D.K. and Owen, R.M., 1995. Dissociation of oceanic methane hydrate as a cause of the carbon isotope excursion at the end of the Paleocene. Paleoceanography, 10(6): 965-971.

Dickens, G.R., Paull, C.K. and Wallace, P., 1997. Direct measurements of in situ methane quantities in a large gas-hydrate reservoir. Nature, 385: 426-428.

Ding, F., Spieß, V., Brüning, M., Fekete, N., Keil, H. and Bohrmann, G., 2008a. A conceptual model for hydrocarbon accumulation and seepage processes around Chapopote asphalt site, Southern Gulf of Mexico: From high resolution seismic point of view. Journal of Geophysical Research, 113.

Ding, F., 2008b. Near-surface Sediment Structures at Cold Seeps and their Physical Control on Seepage: A Geophysical and Geological Study in the Southern Gulf of Mexico and at the frontal Makran Accretionary Prism/Pakistan, Universität Bremen, Bremen, 114 pp.

Ding, F., Spiess, V., Fekete, N., Murton, B.J., Brüning, M. and Bohrmann, G., 2010a. Interaction between accretionary thrust faulting and slope sedimentation at the frontal

Makran accretionary prism and its implications for hydrocarbon fluid seepage. Journal of Geophysical Research, 115(B08106): 16.

Ding, F., Spiess, V., McDonald, I.R., Brüning, M., Fekete, N. and Bohrmann, G., 2010b. Shallow sediment deformation styles in north-western Campeche Knolls, Gulf of Mexico and their controls on the occurrence of hydrocarbon seepage. Marine and Petroleum Geology, 27(4): 959-972.

Domenico, P.A. and Schwartz, F.W., 1998. Physical and Chemical Hydrogeology. Wiley & Sons, Inc., New York, 506 pp.

EdgeTech, 2010. 2400 Series, Deep towed side scan sonar & sub-bottom profiling system.

Egorov, V.N., Polikarpov, G.G., Gulin, S.B., Artemov, Y.G., Stokozov, N.A. and Kostova, S.K., 2003. Modern conception about forming-casting and ecological role of methane gas seeps from bottom of the Black Sea. Mar Ecol J, 2: 5-26.

Fiala-Médioni, A., Boulègue, J., Ohta, S., Felbeck, H. and Mariotti, A., 1993. Source of energy sustaining the *Calyptogena* populations from deep trenches in subduction zone off Japan. Deep-Sea Research I, 40(No. 6): 1241-1258.

Fink, J.H. and Fletcher, R.C., 1978. Ropy pahoehoe:Surface folding of a viscous fluid. Journal of Volcanology and Geothermal Research, 4: 151-170.

Fisher, C.R., 1990. Chemoautotrophic and methanotrophic symbioses in marine invertebrates. Reviews in Aquatic Sciences, 2(3/4): 399-436.

Flemings, P.B., Liu, X. and Winters, W.J., 2003. Critical pressure and multiphase flow in Blake Ridge gas hydrates. Geology, 31(12): 1057-1060.

Fowler, S.R., White, R.S. and Louden, K.E., 1985. Sediment dewatering in the Makran accretionary prism. Earth and Planetary Science Letters, 75: 427-438.

Fruehn, J., White, R.S. and Minshull, T.A., 1997. Internal deformation and compaction of the Makran accretionary wedge. Terra Nova, 9: 101-104.

Fryer, P., Ambos, E.L. and Hussong, D.M., 1985. Origin and emplacement of Mariana forearc seamounts. Geology, 13: 774-777.

Freytag, J.K., Girguis, P.R., Bergquist, D.C., Andras, J.P., Childress, J.J. and Fisher, C.R., 2001. A paradox resolved: Sulfide acquisition by roots of seep tubeworms sustains net chemoautotrophy. Proceedings of the National Academy of Sciences of the United States of America, 98(23): 13408-13413.

Garcia, O. and MacDonald, I.R., 2008. Synthetic aperture radar imaging processing using the supervised textural-neutral network classification algorithm, IEEE International Geoscience & Remote Sensing Symposium, Boston, Massachusetts, U.S.A.

Gay, A., Lopez, M., Ondreas, H., Charlou, J.-L., Sermondadaz, G. and Cochonat, P., 2006. Seafloor facies related to upward methane flux within a giant pockmark of the Lower Congo Basin. Marine Geology, 226: 81-95.

GEBCO Digital Atlas. British Oceanographic Data Centre on behalf of IOC and IHO, 2003. http://www.bodc.ac.uk/data/online_delivery/gebco/

Geo Community, 2010. Radarsat-1. http://imaging.geocomm.com/features/sensor/radarsat1/.

Geomar, 2010. SUGAR Project. http://www.ifm-geomar.de/index.php?id=3563&L=1

Ginsburg, G., Milkov, A.V., Soloviev, V.A., Egorov, A.V., Cherkashev, G.A., Vogt, P.R., Crane, K., Lorenson, T.D. and Khutorskoy, M.D., 1999. Gas hydrate accumulation at the Håkon Mosby Mud Volcano. Geo-Marine Letters, 19: 57-67.

Glover, R.E., 1964. The pattern of freshwater flowing in a coastal aquifer, Sea Water in Coastal Aquifers. U.S. Geological Survey Water Supply Paper. U.S. Geological Survey, pp. 32-35.

Gorman, A.R., Holbrook, W.S., Hornbach, M.J., Hackwith, K.L., Lizarralde, D. and Pecher, I., 2002. Migration of methane gas through the hydrate stability zone in a low-flux hydrate province. Geology, 30(4): 327-330.

Gregg, T.K.P., Fink, J.H. and Griffiths, R.W., 1998. Formation of multiple fold generations on lava flow surfaces: Influence of strain rate, cooling rate, and lava composition. Journal of Volcanology and Geothermal Research, 80: 281-292.

Grevemeyer, I., Rosenberger, A. and Villinger, H., 2000. Natural gas hydrates on the continental slope off Pakistan: constraints from seismic techniques. Geophysical Journal International, 140(2): 295-310.

Guzmán-Vega, M.A., Castro Ortíz, L., Román-Ramos, J.R., Medrano-Morales, L., Valdéz, L.C., Vázquez-Covarrubias, E. and Ziga-Rodríguez, G., 2001. Classification and origin of petroleum in the Mexican Gulf Coast Basin: An overview. In: C. Bartolini, R.T. Buffler and A. Cantú-Chapa (Editors), The Western Gulf of Mexico Basin. AAPG Memoir. AAPG, Tulsa, OK, USA, pp. 127-144.

Haeckel, M., Reitz, A. and Klaucke, I., 2008. Methane budget of a large gas hydrate province offshore Georgia, Black Sea, Proceedings of the 6th International Conference on Gas Hydrates (ICGH 2008), Vancouver, British Columbia, Canada.

Han, X., Suess, E., Sahling, H. and Wallmann, K., 2004. Fluid venting activity on the Costa Rica Margin: new results from authigenic carbonates. International Journal of Earth Sciences, 93: 596-611.

Head, I.M., Jones, D.M. and Larter, S.R., 2003. Biological activity in the deep subsurface and the origin of heavy oil. Nature, 426: 344-352.

Head, I.M., Jones, D.M. and Röling, W.F.M., 2006. Marine microorganisms make a meal of oil. Nature Reviews Microbiology, 4.

Heeschen, K.U., Haeckel, M., Klaucke, I., Ivanov, M.K. and Bohrmann, G., 2011. Quantifying in-situ gas hydrates at active seep sites in the eastern Black Sea using pressure coring technique. Biogeosciences, 8: 3555-3565.

Heggland, R., 1998. Gas seepage as an indicator of deeper prospective reservoirs. A study based on exploration 3D seismic data. Marine and Petroleum Geology, 15(1): 1-9.

Henry, P., Pichon, X.L., Lallemant, S., Lance, S., Martin, J., Foucher, J.-P., Fiala-Médioni, A., Rostek, F., Guilhaumou, N., Pranal, V. and Castrec, M., 1996. Fluid flow in and around a mud vulcano field seaward of the Barbados accretionary wedge: results from Manon cruise. Journal of Geophysical Research, 101(B9): 20297-20323.

Henry, P., Lallemant, S., Nakamura, K., Tsunogai, U., Mazzotti, S. and Kobayashi, K., 2002. Surface expression of fluid venting at the toe of the Nankai wedge and implications for flow path. Marine Geology, 187: 119-143.

Hester, K.C. and Brewer, P.G., 2009. Clathrate hydrates in nature. Annual Review of Marine Science, 1: 303-327.

Hill, A.E., 1937. The transition temperature of gypsum to anhydrite. Journal of the American Chemical Society, 59(11): 2242-2244.

Hill, T.M., Kennett, J.P., Valentine, D.L., Yang, Z., Reddy, C.M., Nelson, R.K., Behl, R.J., Robert, C. and Beaufort, L., 2006. Climatically driven emissions of hydrocarbons from marine sediments during deglaciation. Proceedings of the National Academy of Sciences, 103(37): 13570-13574.

Hinrichs, K.-U., Hayes, J.M., Sylva, S.P., Brewer, P.G. and DeLong, E.F., 1999. Methane-consuming archaebacteria in marine sediments. Nature, 398.

Holbrook, W.S., Hoskins, H., Wood, W.T., Stephen, R.A., Lizarralde, D. and Party, L.S., 1996. Methane Hydrate and Free Gas on the Blake Ridge from Vertical Seismic Profiling. Science, 273: 1840-1843.

Holbrook, W.S., Lizarralde, D., Pecher, I.A., Gorman, A.R., Hackwith, K.L., Hornbach, M. and Saffer, D., 2002. Escape of methane gas through sediment waves in a large methane hydrate province. Geology, 30(5): 467-470.

Hornbach, M.J., Saffer, D., Holbrook, W.S., Van Avendonk, H.J.A. and Gorman, A.R., 2008. Three-dimensional seismic imaging of the Blake Ridge methane hydrate province:

Evidence for large, concentrated zones of gas hydrate and morphologically driven advection. J. Geophys. Res., 113(B07101).

Houghton, J.T., Ding, Y., Griggs, D.J., Noguer, M., van der Linden, P.J., Dai, X., Maskell, K. and Johnson, C.A., 2001. Climate Change 2001: The Scientific Basis, Contribution of Working Group I to the Third Assessment Report of the Intergovernmental Panel on Climate Change. Cambridge University Press, Cambridge.

Hovland, H. and Judd, A.G., 1988. Seabed pockmarks and seepages. Graham & Trotman, Oxford. Hovland, M., Croker, P.F. and Martin, M., 1994. Fault-associated seabed mound (carbonate knolls?) off western Irland and north-west Australia. Marine and Petroleum Geology, 11(2): 232-246.

Hovland, M., 2002. On the self-sealing nature of marine seeps. Continental Shelf Research, 22(16): 2387-2394.

Hovland, M., MacDonald, I.R., Rueslåtten, H., Johnsen, H.K., Naehr, T. and Bohrmann, G., 2005. Chapopote asphalt volcano may have been generated by supercritical water. EOS, 86(42): 397, 402.

Hovland, M. and Svensen, H., 2006. Submarine pingoes: Indicators of shallow gas hydrates in a pockmark at Nyegga, Norwegian Sea. Marine Geology, 228: 15-23.

Hulme, G., 1974. The interpretation of lava flow morphology. Geophysical Journal of the Royal Astronomical Society, 39: 361-383.

Hyndman, R.D. and Spence, G.D., 1992. A seismic study of methane hydrate marine bottom simulating reflectors. Journal of Geophysical Research, 97(B5): 6683-6698.

Jerosch, K., Schlüter, M., Foucher, J.-P., Allais, A.-G., Klages, M. and Edy, C., 2007. Spatial distribution of mud flows, chemoautotrophic communities, and biogeochemical habitats at Håkon Mosby Mud Volcano. Marine Geology, 243: 1-17.

Johnson, J.E., Goldfinger, C. and Suess, E., 2003. Geophysical constraints on the surface distribution of authigenic carbonates across the Hydrate Ridge region, Cascadia margin. Marine Geology, 202: 79-120.

Judd, A.G. and Hovland, M., 2007. Seabed Fluid Flow. Cambridge University Press, New York, 475 pp. Klapp, S.A., Bohrmann, G., Kuhs, W.F., Murshed, M.M., Pape, T., Klein, H., Techmer, K.S., Heeschen, K.U. and Abegg, F., 2009. Microstructures of structure I and II gas hydrates from the Gulf of Mexico. Marine and Petroleum Geology, 27(1): 116-125.

Kearey, P. and Brooks, M., 1991. An Introduction to Geophysical Exploration. Blackwell Science Ltd., Oxford.

Kennett, J.P., Cannariato, K.G., Hendy, I.L. and Behl, R.J., 2003. Methane hydrates in Quaternary climate change: The clathrate gun hypothesis. AGU, Washington, D.C.

Kiel, S., 2009. Global hydrocarbon seep-carbonate precipitation correlates with deep-water temperatures and eustatic sea-level fluctuations since the Late Jurassic. Terra Nova, 21: 279-284.

Killops, S.D. and Killops, V.J., 2004. Introduction to Organic Geochemistry. Blackwell, 408 pp.

Kimura, G., Silver, E.A., Blum, P. and al., e., 1997. Initial Report. Proceedings of the Ocean Drilling Program, 170, Collage Station, TX, U.S.A.

Klapp, S.A., Hemes, S., Klein, H., Bohrmann, G., MacDonald, I.R. and Kuhs, W.F., 2010. Grain size measurements of natural gas hydrates. Marine Geology, 274: 85-94.

Klaucke, I., Sahling, H., Bürk, D., Weinrebe, W. and Bohrmann, G., 2005. Mapping deep-water gas emissions with sidescan sonar, EOS, pp. 341,346.

Klaucke, I., Sahling, H., Weinrebe, W., Blinova, V., Bürck, D., Lursmanashvili, N. and Bohrmann, G., 2006. Acoustic investigation of cold seeps offshore Georgia, eastern Black Sea. Marine Geology, 231: 51-67.

Klaucke, I., Masson, D.G., Petersen, C.J., Weinrebe, W. and Ranero, C.R., 2008. Multifrequency geoacoustic imaging of fluid escape structures offshore Costa Rica: Implications for the quantification of seep processes. Geochem. Geophys. Geosyst., 9.

Kongsberg Maritime AS, 2005a. EM 120, Multibeam echo sounder, Product description, Horton, pp. 44.

Kongsberg, M.A., 2005b. EM710 Multibeam echo sounder, Product description, Horton, pp. 40.

Kopf, A.J., 2002. Significance of mud volcanism. Review of Geophysics, 40(2). Kukowski, N., Schillhorn, T., Huhn, K., von Rad, U., Husen, S. and Flueh, E.R., 2001. Morphotectonics and mechanics of the central Makran accretionary wedge off Pakistan. Marine Geology, 173: 1-19.

Kopp, C., Fruehn, J., Flueh, E.R., Reichert, C., Kukowski, N., Bialas, J. and Klaeschen, D., 2000. Structure of the Makran subduction zone from wide-angle and reflection seismic data. Tectonophysics, 329(1-4): 171-191.

Krastel, S., Spiess, V., Ivanov, M.K., Weinrebe, W., Bohrmann, G., Shashkin, P. and Heidersdorf, F., 2003. Acoustic investigations of mud volcanoes in the Sorokin Trough, Black Sea. Geo-Marine Letters, 23: 230-238.

Krylova, E.M. and Sahling, H., 2006. Recent bivalve molluscs of the genus *Calyptogena* (Vesicomyidae). Journal of Molluscan Studies, 72: 359-395.

Kukowski, N., Schillhorn, T., Flueh, E.R. and Huhn, K., 2000. Newly identified strike-slip plate boundary in the northeastern Arabian Sea. Geology, 28(4): 355-358.

Kukowski, N., Schillhorn, T., Huhn, K., von Rad, U., Husen, S. and Flueh, E.R., 2001. Morphotectonics and mechanics of the central Makran accretionary wedge off Pakistan. Marine Geology, 173: 1-19.

Kulm, L.D., Suess, E., Moore, J.C., Carson, B., Lewis, B.T., Ritger, S.D., Kadko, D.C., Thornburg, T.M., Embley, R.W., Rugh, W.D., Massoth, G.J., Langseth, M.G., Cochrane, G.R. and Scamann, R.L., 1986. Oregon subduction zone: venting, fauna, and carbonates. Science, 231: 561-566.

Kvenvolden, K.A., 1998. A primer on the geological occurence of gas hydrate. In: J.P. Henriet and J. Mienert (Editors), Gas Hydrates: Relevance to World Margin Stability and Climate Change. Special Publications. Geological Society, London, pp. 9-30.

Kvenvolden, K.A. and Cooper, C.K., 2003. Natural seepage of crude oil into the marine environment. Geo-Marine Letters, 23: 140-146.

Le Bas, T.P., Douglas.C., M. and N.W., M., 1995. TOBI Image Processing - The State of the Art. IEEE Journal of Oceanic Engineering, 20(1): 85-93.

Le Bas, T.P. and Mason, D.C., 1997. Automatic registration of TOBI side-scan sonar and multi-beam bathymetry images for improved data fusion. Marine Geophysical Researches, 19: 163-176.

Le Bas, T., 2002. P.R.I.S.M., Processing of Remotely-sensed Imagery for Seafloor Mapping, version 4.0. Southampton Oceanography Centre, Southampton.

Leifer, I., Boles, J.R., Luyendyk, B.P. and Clark, J.F., 2004. Transient discharges from marine hydrocarbon seeps: spatial and temporal variability. Environmental Geology, 46: 1038-1052.

Leitstelle Meteor, IFM, Universität Hamburg, 2006. Werftbericht 8. http://www.ifm.zmaw.de/fileadmin/files/leitstelle/meteor/Werftzeit_Talchuano/Meteor_Werft_Bericht8.pdf

Linke, P., Pfannkuche, O., Torres, M.E., Collier, R.W., Witte, U., McManus, J., Hammond, D., Brown, K.M., Tyron, M.D. and Nakamura, K., 1999. Variability of benthic flux and discharge rates at vent sites determined by in situ instruments, Fall Meeting. AGU, San Francisco.

Luan, X., Jin, Y., Obzhirov, A. and Yue, B., 2008. Characteristics of shallow gas hydrate in Okhotsk Sea. Science in China, 51(3): 415-421.

Lurton, X., 2002. An Introductin to Underwater Acoustics, Priciples and Applications. Praxis Books in Geophysical Sciences. Springer, London, 341 pp.

Lykousis, V., Alexandri, S., Woodside, J.M., Nomikou, P., Perissoratis, C., Sakellariou, D., de Lange, G., Dahlmann, A., Casas, D., Rousakis, G., Ballas, D. and Ioakim, C., 2004. New evidence for extensive active mud volcanism in the Anaximander mountains (Eastern Mediterranean): The "ATHINA" mud volcano. Environmental Geology, 46: 1030-1037.

Lykousis, V., Alexandri, S., Woodside, J., de Lange, G., Dählmann, A., Perissoratis, C., Heeschen, K., Ioakim, C., Sakellariou, D., Nomikou, P., Rousakis, G., Casas, D., Ballas, D. and Ercilla, G., 2009. Mud volcanoes and gas hydrates in the Anaximander mountains (Eastern Mediterranean Sea). Marine and Petroleum Geology, 26: 854-872.

MacDonald, I.R., Guinasso Jr., N.L., Ackleson, S.G., Amos, J.F., Duckworth, R., Sassen, R. and Brooks, J.M., 1993. Natural oil slicks in the Gulf of Mexico visible from space. Journal of Geophysical Research, 98(C9): 16351–16364.

MacDonald, I.R., Buthman, D.B., Sager, W.W., Peccini, M.B. and Guinasso Jr., N.L., 2000. Pulsed oil discharge from a mud volcano. Geology, 28(10): 907-910.

MacDonald, I.R., Sager, W.W. and Peccini, M.B., 2003. Gas hydrate and chemosynthetic biota in mounded bathymetry at mid-slope hydrocarbon seeps: Northern Gulf of Mexico. Marine Geology, 198(1-2): 133-158.

MacDonald, I.R., Bohrmann, G., Escobar, E., Abegg, F., Blanchon, P., Blinova, V., Brückmann, W., Drews, M., Eisenhauer, A., Han, X., KHeeschen, K., Meier, F., Mortera, C., Naehr, T., Orcutt, B., Bernard, B., Brooks, M. and de Faragó, M., 2004. Asphalt volcanism and chemosynthetic life in the Campeche Knolls, Gulf of Mexico. Science, 304: 999-1002.

MacDonald, I.R., Kastner, M. and Leifer, I., 2005. Estimates of natural hydrocarbon flux in the Gulf of Mexico basin from remote sensing data. Geophysical Research Abstracts, 7(09970).

MacDonald, I.R., 2007. The Asphalt Ecosystem of the Gulf of Mexico: Results From the Chapopote III Cruise, AGU Fall Meeting, San Francisco.

Macgregor, D.S., 1993. Relationships between seepage, tectonics and subsurface petroleum reserves. Marine and Petroleum Geology, 10: 606-614.

Magoon, L.B., Hudson, T.L. and Cook, H.E., 2001. Pimienta-Tamabra(!) - A giant supercharged petroleum system in the Southern Gulf of Mexico, onshore and offshore Mexico. In: C. Bartolini, R.T. Buffler and A. Cantú-Chapa (Editors), The western Gulf of Mexico Basin: Tectonics, sedimentary basins, and petroleum systems. AAPG Memoir. Amercian Assosiation of Petroleum Geologists, Tulsa, Oklahoma, USA, pp. 83-125.

Mau, S., Sahling, H., Rehder, G., Suess, E., Linke, P. and Soeding, E., 2006. Estimates of methane output from mud extrusions at the erosive convergent margin off Costa Rica. Marine Geology, 225: 129-144.

Mazzini, A., Ivanov, M.K., Parnell, J., Stadnitskaia, A., Cronin, B.T., Poludetkina, E., Mazurenko, L. and van Weering, T.C.E., 2004. Methane-related authigenic carbonates from the Black Sea: geochemical characterisation and relation to seeping fluids. Marine Geology, 212(1-4): 153-181.

Mazurenko, L.L. and Soloviev, V.A., 2003. Worldwide distribution of deep-water fluid venting and potential occurrences of gas hydrate accumulations. Geo-Marine Letters, 23: 162-176.

McGinnis, D.F., Greinert, J., Artemov, Y., Beaubien, S.E. and Wüest, A., 2006. Fate of rising methane bubbles in stratified waters: How much methane reaches the atmosphere. J. Geophys. Res, 111: C09007.

Meiburg, P., 1995. Mexico. In: H. Kulke (Editor), Reginal Petroleum Geology of the world. Gebrüder Borntraeger, Berlin, pp. 421-454.

Michaelis, W., Seifert, R., Blumenberg, M., Pape, T., Lüdmann, T., Wong, H.K., Konerding, P., Zillmer, M., Petersen, J. and Reimer, A., 2006. Gas hydrates: Occurrence, Stability, Transformation, Dynamics, and Biology in the Black Sea, In: Stroink, L. (Editor), Geotechnologien Science Report, Gas Hydrates in the Geosystem, No. 7, Potsdam.

Mienert, J., Vanneste, M., Bünz, S., Andreassen, K., Haflidason, H. and Sejrup, H.P., 2005. Ocean warming and gas hydrate stability on the mid-Norwegian margin at the Storegga Slide. Marine and Petroleum Geology, 22: 233-244.

Milkov, A.V., 2004. Global estimates of hydrate-bound gas in marine sediments: how much is really out there? Earth-Science Reviews, 66: 183-197.

Minshull, T.A. and White, R., 1989. Sediment compaction and fluid migration in the Makran Accretionary Prism. Journal of Geophysical Research, 94(B6): 7387-7402.

Minshull, T.A., White, R.S., Barton, P.J. and Collier, J.S., 1992. Deformation at plate boundaries around the gulf of Oman. Marine Geology, 104(1-4): 265-277.

Mitchell, N.C., 1993. A model for attenuation of backscatter due to sediment accumulations and Its application to determine sediment thicknesses with GLORIA sidescan sonar. Journal of Geophysical Research, 98(B12): 22477-22493.

Murray, R.C., 1964. Origin and diagenesis of gypsum and anhydrite. Journal of Sedimentary Petrology, 34(3): 512-523.

Naehr, T.H., Birgel, D., Bohrmann, G., MacDonald, I.R. and Kasten, S., 2009. Biogeochemical controls on authigenic carbonate formation at Chapopote asphalt volcano, Bay of Campeche. Chemical Geology, 266: 399-411.

Naudts, L., Greinert, J., Artemov, Y., Staelens, P., Poort, J., Van Rensbergen, P. and De Batist, M., 2006. Geological and morphological setting of 2778 methane seeps in the Dnepr paleo-delta, northwestern Black Sea. Marine Geology, 227(3-4): 177-199.

Naudts, L., Greinert, J., Artemov, Y., Beaubien, S.E., Borowski, C. and Batist, M.D., 2008. Anomalous sea-floor backscatter patterns in methane venting areas, Dnepr paleo-delta, NW Black Sea. Marine Geology, 251(3-4): 253-267.

Niemann, H., Lösekann, T., de Beer, D., Elvert, M., Nadalig, T., Knittel, K., Amann, R., Sauter, E.J., Schlüter, M., Klages, M., Foucher, J.P. and Boetius, A., 2006. Novel microbial communities of the Haakon Mosby mud volcano and their role as a methane sink. Nature, 443: 854-858.

Nikishin, A.M., Korotaev, M.V., Ershov, A.V. and Brunet, M.-F., 2003. The Black Sea basin: tectonic history and Neogene-Quaternary rapid subsidence modelling. Sedimentary Geology, 156(1-4): 149-168.

Nikolovska, A., Sahling, H. and Bohrmann, G., 2008. Hydroacoustic methodology for detection, localization, and quantification of gas bubbles rising from the seafloor at gas seeps from the eastern Black Sea. Geochemistry Geophysics Geosystems G3, 9(10).

North, F.K., 1985. Petroleum Geology. Allen and Unwin Inc., Winchester, USA.

Orange, D.L., Yun, J., Maher, N., Barry, J. and Greene, G., 2002. Tracking California seafloor seeps with bathymetry, backscatter and ROVs. Continental Shelf Research, 22: 2273-2290.

Pape, T., Bahr, A., Rethemeyer, J., Kessler, J.D., Sahling, H., Hinrichs, K.-U., Klapp, S.A., Reeburgh, W.S. and Bohrmann, G., 2010. Molecular and isotopic partitioning of low-molecular-weight hydrocarbons during migration and gas hydrate precipitation in deposits of a high-flux seepage site. Chemical Geology, 269: 350-363.

Pape, T., Bahr, A., Klapp, S.A., Abegg, F. and Bohrmann, G., 2011. High-intensity gas seepage causes rafting of shallow gas hydrates in the southeastern Black Sea. Earth and Planetary Science Letters, 307: 35-46.

Paull, C.K., Hecker, B., Commeau, R., Freeman-Lynde, R.P., Neumann, C., Corso, W.P., Golubic, S., Hook, J.E., Sikes, E. and Curray, J., 1984. Biological Communities at the Florida Escarpment Resemble Hydrothermal Vent Taxa. Science, 226(4677): 965-967.

Paull, C.K., Ussler III, W. and Borowski, W.S., 1994. Sources of biogenic methane to form marine gas hydrates. New York Academy of Sciences Annals., 715: 392-409.

Paull, C. (Editor), 2001. Natural gas hydrates: Occurrence, distribution, and detection, 124. American Geophysical Union.

Paull, C.K., Brewer, P.G., Ussler III, W., Peltzer, E.T., Rehder, G. and Clague, D., 2003. An experiment demonstrating that marine slumping is a mechanism to transfer methane from seafloor gas-hydrate deposits into the upper ocean and atmosphere. Geo-Marine Letters, 22: 198-203.

Paull, C.K., Ussler, W., Greene, H.G., Barry, J. and Keaten, R., 2005. Bioerosion by chemosynthetic biological communities on Holocene submarine slide scars. Geo-Marine Letters, 25(1): 11-19.

Peacesoftware, www.peacesoftware.de/eigenwerte, 2009.

Peckmann, J., Reimer, A., Luth, U., Luth, C., Hansen, B.T., Heinicke, C., Hoefs, J. and Reitner, J., 2001. Methane-derived carbonates and authigenic pyrite from the northwestern Black Sea. Marine Geology, 177: 129-150.

Pequegnat, W.E. and Jeffrey, L.M., 1979. Petroleum in Deep Benthic Ecosystems of the Gulf of Mexico and Caribbean Sea. Contributions in Marine Science, 22: 63-75.

Platt, J.P., Leggett, J.K., Young, J. and Raza, H.S.A., 1985. Large-scale sediment underplating in the Makran accretionary prism, southwest Pakistan. Geology, 13: 507-511.

Ramaswamy, V., Boucher, O., Haigh, J., Hauglustaine, D., Haywood, J., Myhre, G., Nakajima, T., Shi, G., Solomon, S., Betts, R.E., Charlson, R., Chuang, C.C., Daniel, J.S., Del Genio, A.D., Feichter, J., Fuglestvedt, J., Forster, P.M., Ghan, S.J., Jones, A., Kiehl, J.T., Koch, D., Land, C., Lean, J., Lohmann, U., Minschwaner, K., Penner, J.E., Roberts, D.L., Rodhe, H., Roelofs, G.-J., Rotstayn, L.D., Schneider, T.L., Schumann, U., Schwartz, S.E., Schwartzkopf, M.D., Shine, K.P., Smith, S.J., Stevenson, D.S., Stordal, F., Tegen, I., van Dorland, R., Zhang, Y., Srinivasan, J. and Joos, F., 2001. Radiative forcing of climate change. In: J.T. Houghton and e. al. (Editors), The Scientific Basis. Contribution of Working Group I to the Third Assessment Report of the Intergovernmental Panel on Climate Change. Cambridge University Press, Cambridge, pp. 349-416.

Ranero, C. and von Huene, R., 2000. Subduction erosion along the Middle America convergent margin. Nature, 404: 748-752.

Ranero, C.R., Grevemeyer, I., Sahling, H., Barckhausen, U., Hensen, C., Wallmann, K., Weinrebe, W., Vannucchi, P., von Huene, R. and McIntosh, K., 2008. Hydrogeological system of erosional convergent margins and its influence on tectonics and interplate seismogenesis. Geochem. Geophys. Geosyst., 9.

Rice, D.D., 1992. Controls, Habitat, and Resource Potential of Ancient Bacterial Gas. In: R. Vially (Editor), Bacterial Gas. Editions Technip, Paris, pp. 91.

Ritger, S., Carson, B. and Suess, E., 1987. Methane-derived authigenic carbonates formed by subduction-induced pore-water expulsion along the Oregon/Washington margin. Geological Society of America Bulletin, 98: 147-156.

Roberts, H.H. and Aharon, P., 1994. Hydrocarbon-derived carbonate buildups of the northern Gulf of Mexico continental slope: A review of submersible investigations. Geo-Marine Letters, 14: 135-148.

Robinson, A.G., Rudat, J.H., Banks, C.J. and Wiles, R.L.F., 1996. Petroleum geology of the Black Sea. Marine and Petroleum Geology, 13(2): 195-223.

Robinson, A.G., Griffith, E.T., Gardiner, A.R. and Home, A.K., 1997. Petroleum geology of the Georgian Fold and thrust belts and foreland basins. In: A.G. Robinson (Editor), Regional and petroleum geology of the Black Sea and surrounding Region. The American Association of Petroleum Geologists, Tulsa, Oklahoma, USA, pp. 347-367.

Römer, M., Sahling, H., Pape, T., Spiess, V. and Bohrmann, G., subm. Gas bubble emission from submarine hydrocarbon seeps at the Makran continental margin, offshore Pakistan. Journal of Geophysical Research - Oceans.

Römer, M., 2011. Gas bubble emissions at continental margins - Detection, mapping and quantification Universität Bremen, Bremen, 153 pp.

Ross, D.A. and Degens, E.T., 1974. Recent sediments of Black Sea. In: E.T.E. Degens and D.A. Ross (Editors), The Black Sea-geology, chemistry, and biology. The American Association of Petroleum Geologists Tulsa, Oklohoma, USA, pp. 183-199.

Sahling, H., Rickert, D., Lee, R.W., Linke, P. and Suess, E., 2002. Macrofaunal community structure and sulfide flux at gas hydrate deposits from the Cascadia convergent margin, NE Pacific. Marine Ecology Progress Series, 231: 121-138.

Sahling, H., Galkin, S.V., Foerstel, H., Greinert, J., Piepenburg, D. and Suess, E., 2003. Depth-related structure and ecological significance of cold-seep communities - A case study from the Sea of Okhotsk. Deep-Sea Research I, 50: 1391-1409.

Sahling, H., Blinova, V., Bürk, D., Çifçi, G., Çorpur, S., Dondurur, D., Klaucke, I., Lursmanashvili, N., Okay, S., Renken, J. and Schott, T., 2004. Report and preliminary results of R/V Poseidon Cruise P317/4, Fachbereich Geowissenschaften der Universität Bremen, Bremen.

Sahling, H., Masson, D.G., Ranero, C.R., Hühnerbach, V., Weinrebe, W., Klaucke, I., Bürk, D., Brückmann, W. and Suess, E., 2008a. Fluid seepage at the continental margin offshore Costa Rica and southern Nicaragua. Geochemistry Geophysics Geosystems G3, 9(5): 22.

Sahling, H., Bohrmann, G., Spiess, V., Bialas, J., Breitzke, M., Ivanov, M., Kasten, S., Krastel, S. and Schneider, R., 2008b. Pockmarks in the Northern Congo Fan area, SW Africa: Complex seafloor features shaped by fluid flow. Marine Geology, 249(3-4): 206-225.

Sain, K., Minshull, T.A., Singh, S.C. and Hobbs, R.W., 2000. Evidence for a thick free gas layer beneath the bottom simulating reflector in the Makran accretionary prism. Marine Geology, 164: 3-12.

Salvador, A., 1991. Introduction. In: A. Salvador (Editor), The Gulf of Mexico Basin. Geological Society of America, Boulder, pp. 1-12.

Schmaljohann, R., Drews, M., Walter, S., Linke, P., von Rad, U. and Imhoff, J.F., 2001. Oxygen-minimum zone sediments in the northeastern Arabian Sea off Pakistan: a habitat for the bacterium Thioploca. Marine Ecology Progress Series, 211: 27-42.

Schmale, O., Greinert, J. and Rehder, G., 2005. Methane emission from high-intensity marine gas seeps in the Black Sea into the atmosphere. Geophys. Res. Lett, 32: L07609.

Scholten, R., 1974. Role of the Bosporus in Black Sea Chemistry and Sedimentation. In: E.T. Degens and D.A. Ross (Editors), The Black Sea - geology, chemistry, and biology. The American Association of Petroleum Geologists, Tulsa, Oklahoma, USA, pp. 115-126.

Schubotz, F., Wilhelm, T., Hohnberg, H.-J., Kasten, S., Zabel, M., Bohrmann, G. and Hinrichs, K.-U., 2007. Biogeochemical investigation of asphalt seepage at the Chapapote Knoll in the southern Gulf of Mexico, Goldschmidt Conference. Geochimica et Cosmochimica Acta, Cologne, Germany pp. A907.

Schubotz, F., Lipp, J.S., Elvert, M., Kasten, S., Prieto Mollar, X., Zabel, M., Bohrmann, G. and Hinrichs, K.-U., 2011. Petroleum degradation and associated microbial signatures at

the Chapopote asphalt volcano, Southern Gulf of Mexico. Geochimica et Cosmochimica Acta, 75: 4377-4398.

Schulz, H., Von Rad, U. and Erlenkeuser, H., 1998. Correlation between Arabian Sea and Greenland climate oscillations of the past 110000 years. Nature, 393: 54-57.

Shoji, H., Soloviev, V., Matveeva, T., Mazurenko, L.L., Minami, H., Hachikubo, A., Sakagami, H., Hyakutake, K., Kaulio, V., Gladysch, V., Logvina, E., Obzhirov, A., Baranov, B., Khlystov, O., Biebow, N., Poort, J., Jin, Y.K. and Kim, Y., 2005. Hydrate-bearing structures in the Sea of Okhotsk. EOS Transactions, 86(2).

Sibuet, M. and Olu, K., 1998. Biogeography, biodiversity and fluid dependence of deep-sea cold-seep communities at active and passive margins. Deep-Sea Research II, 45: 517-567.

Simmons, G.M., 1992. Importance of submarine groundwater discharge (SGWD) and seawater cycling to material flux across sediment/water interfaces in marine environments. Marine Ecology Progress Series, 84: 173-184.

Snead, R.E., 1964. Active mud volcanoes of Baluchistan. West Pakistan Geographical Review, 54(4): 546-560.

Sondhi, V.P., 1947. The Makran earthquake, 28th November 1945, the birth of new islands. Indian Minerals, 1(3): 146-154.

Spadini, G., Robinson, A. and Cloetingh, S., 1996. Western versus Eastern Black Sea tectonic evolution: pre-rift lithospheric controls on basin formation. Tectoniphysics, 266: 139-154.

Spahni, R., Chappellaz, J., Stocker, T.F., Loulergue, L., Hausammann, G., Kawamura, K., Fluckiger, J., Schwander, J., Raynaud, D. and Masson-Delmotte, V., 2005. Atmospheric Methane and Nitrous Oxide of the Late Pleistocene from Antarctic Ice Cores. Science, 310(5752): 1317-1321.

Spiess, V., Baumann, L., Brüning, M., Collins, G., Ding, F., Fekete, N., Förster, A., Gentz, T., Haider, S.W., Holtappels, M., Le Bas, T., Matthew, D., Max, L., Meyer, M., Murton, B., Preu, B., Rouse, I., Sahling, H., Schlüter, M., Schubert, K., Schwenk, T., Truscheit, T., Vieweg, I., Webb, A., Wittenberg, N. and Yoshinaga, M.Y., 2010. Nitrogen Cycle, Cold Seeps, Carbonate Platform, Development in the Northwestern Indian Ocean, Cruise No. 74, August 31 – December 22, 2007. Cold Seeps of the Makran Subduction Zone (Continental Margin of Pakistan), PART 2, Cruise No. 74, Leg 2, Leitstelle METEOR/MERIAN, Universität Hamburg, Institut für Meereskunde, Hamburg.

Stoll, R.A., 1985. Marine sediment acoustics. Journal of the Acoustical Society of America, 77(5): 1789-1799.

Suess, E., Carson, B., Ritger, S.D., Moore, J.C., Jones, M.L., Kulm, L.D. and Cochrane, G.R., 1985. Biological communities at vent sites along the subduction zone off Oregon. Bulletin of the Biological Society of Washington, 6: 475-484.

Suess, E. and Whiticar, M.J., 1989. Methane-derived CO_2 in pore fluids expelled from the Oregon subduction zone. Palaeogeography, Palaeoclimatology, Palaeoecology, 71: 119-136.

Suess, E., Bohrmann, G., Huene, R.v., Linke, P., Wallmann, K., Lammers, S., Sahling, H., Winckler, G., Lutz, R.A. and Orange, D., 1998. Fluid venting in the eastern Aleutian subduction zone. Journal of Geophysical Research, 103(B2): 2597-2614.

Suess, E., Torres, M.E., Bohrmann, G., Collier, R.W., Greinert, J., Linke, P., Rehder, G., Trehu, A., Wallmann, K., Winckler, G. and Zuleger, E., 1999. Gas hydrate destabilization: enhanced dewatering, benthic material turnover and large methane plumes at the Cascadia convergent margin. Earth and Planetary Science Letters, 170: 1-15.

Suess, E., Torres, M.E., Bohrmann, G., Collier, R.W., Rickert, D., Goldfinger, C., Linke, P., Heuser, A., Sahling, H., Heeschen, K., Jung, C., Nakamura, K., Greinert, J.,

Pfannkuche, O., Trehu, A., Klinkhammer, G., Whiticar, M.J., Eisenhauer, A., Teichert, B. and Elvert, M., 2001. Sea floor methane hydrates at Hydrate Ridge, Cascadia Margin. In: C. Paull (Editor), Natural gas hydrates: Occurrence, distribution, and detection. Geophysical Monograph 124. American Geophysical Union.

Suess, E. and Linke, P., 2006. Der Ozean unter dem Meeresboden. In: G. Wefer (Editor), expedition Erde. GeoUnion-Alfred-Wegener-Stiftung, Bremen, pp. 88-101.

SUGAR website, http://www.ifm-GEOMAR.de/index.php?id=3563&L=1, 2010.

Sumida, P.Y.G., Yoshinaga, M.Y., Madureira, L.A.S.-P. and Hovland, M., 2004. Seabed pockmarks associated with deepwater corals off SE Brazilian continental slope, Santos Basin. Marine Geology, 207: 159-167.

Sultan, N., Cochonat, P., Foucher, J.P. and Mienert, J., 2004. Effect of gas hydrates melting on seafloor slope instability. Marine Geology, 213: 379-401.

Teichert, B.M.A., Eisenhauer, A., Bohrmann, G., Haase-Schramm, A., Bock, B. and Linke, P., 2003. U/Th systematics and ages of authigenic carbonates from Hydrate Ridge, Cascadia Margin: Records of fluid flow variations. Geochimica et Cosmochimica Acta, 67(20): 3845-3857.

Teichert, B.M.A., Bohrmann, G. and Suess, E., 2005. Chemoherms on Hydrate Ridge: Unique microbially-mediated carboante build-ups growing into the water column. Palaeogeography, Palaeoclimatology, Palaeoecology, 227(1-3): 67-85.

Telford, W.M., Geldart, L.P. and Sheriff, R.E., 1990. Applied Geophysics. Cambridge University Press, Cambridge.

Tissot, B.P. and Welte, D.H., 1984. Petroleum, formation and occurrence. Springer Verlag, Berlin, 699 pp.

Torres, M.E., Wallman, K., Tréhu, A.M., Bohrmann, G., Borowski, W.S. and Tomaru, H., 2004. Gas hydrate growth, methane transport, and chloride enrichment at the southern summit of Hydrate Ridge, Cascadia margin off Oregon. Earth and Planetary Science Letters, 226: 225-241.

Tréhu, A.M., Long, P.E., Torres, M.E., Bohrmann, G., R., R.F., Collett, T.S., Goldberg, D.S., Milkov, A.V., Riedel, M., Schultheiss, P., Bangs, N.L., Barr, S.R., Borowski, W.S., Claypool, G.E., Delwiche, M.E., Dickens, G.R., Gracia, E., Guerin, G., Holland, M., Johnson, J.E., Lee, Y.-J., Liu, C.-S., Su, X., Teichert, B., Tomaru, H., Vanneste, M., Watanabe, M. and Weinberger, J.L., 2004. Three-dimensional distribution of gas hydrate beneath southern Hydrate Ridge: constraints from ODP Leg 204. Earth and Planetary Science Letters, 222: 845-862.

Tréhu, A.M., Bohrmann, G., Torres, M.E. and Colwell, F.S., 2006. 1. Leg 204 synthesis: gas hydrate distribution and dynamics in the central Cascadia accretionary complex.

Treude, T., Niemann, H., Orcutt, B., Joye, S., Witte, U., Joergensen, B.B. and Boetius, A., 2006. Microbial methane turnover at marine methane seeps (MUMM - SPI). In: Stroink, L. (Editor), Geotechnologien Science Report, Gas Hydrates in the Geosystem, No. 7, Potsdam.

Tugolesov, D.A., Gorshkov, A.S., Meisner, L.B. and Soloviev, V.V., 1985. Tectonics of the Mesozoic–Cenozoic Deposits of the Black Sea Basin. Nedra, Moscow, 215 pp.

Uchupi, E., Swift, S.A. and Ross, D.A., 2002. Morphology and Late Quaternary sedimentation in the Gulf of Oman Basin. Marine Geophysical Researches, 23(2): 185-208.

Urick, R.J., 1983. Principles of Underwater Sound, New York.

USGS website, www.usgs.gov, 2010.

Vannucchi, P., Scholl, D.W., Meschede, M. and McDougall-Reid, K., 2001. Tectonic erosion and consequent collapse of the Pacific margin of Costa Rica: Combined implications from ODP Leg 170, seismic offshore data, and regional gelogy of the Nicoya Peninsula. Tectonics, 20(5): 649-668.

Vernon, J.W. and Slater, R.A., 1963. Submarine tar mounds, Santa Barbara County, California. Bulletin of the American Association of Petroleum Geologists, 47(8): 1624-1627.

von Huene, R. and Scholl, D.W., 1991. Observations at convergent margins concerning sediment subduction, subduction erosion, and the growth of continental crust. Reviews of Geophysics, 29(3): 279-316.

von Huene, R., Ranero, C.R. and Vannucchi, P., 2004. Generic model of subduction erosion. Geology, 32(10): 913-916.

von Rad, U., 1979. SiO_2-Diagenese von Tiefseesideimenten. Geologische Rundschau, 68(3): 1025-1036.

von Rad, U., Schulz, H., Khan, A.A., Ansari, M., Berner, U., Cepek, P., Cowie, G., Dietrich, P., Erlenkeuser, H., Geyh, M., Jennerjahn, T., Lückge, A., Marchig, V., Riech, V., Rösch, H., Schäfer, P., Schulte, S., Sirocko, F., Tahir, M. and Weiss, W., 1995. Sampling the oxygen minimum zone off Pakistan: glacial-interglacial variations of anoxia and productivity (preliminary results, 90 cruise). Marine Geology, 125(1-2): 7-19.

von Rad, U., Rösch, H., Berner, U., Geyh, M., Marchig, V. and Schulz, H., 1996. Authigenic carbonates derived from oxidized methane vented from the Makran accretionary prism off Pakistan. Marine Geology, 136: 55-77.

von Rad, U., Berner, U., Delisle, G., Doose-Rolinski, H., Fechner, N., Linke, P., Lückge, A., Roeser, H.A., Schmaljohann, R. and Wiedicke, M., 2000. Gas and fluid venting at the Makran accretionary wedge off Pakistan. Geo-Marine Letters, 20: 10-19.

Wagner-Friedrichs, M., 2007. Seafloor seepage in the Black Sea: Mud volcanoes, seeps and diapiric structures imaged by acoustic methods. Dissertation Thesis, Universität Bremen, Bremen, 154 pp.

Wagner-Friedrichs, M., Krastel, S., Spiess, V., Ivanov, M., Bohrmann, G. and Meisner, L., 2008. Three-dimensional seismic investigations of the Sevastopol mud volcano in correlation to gas/fluid migration pathways and indications for gas hydrate occurrences in the Sorokin Trough (Black Sea). Geochem. Geophys. Geosyst., 9.

Walter, K.M., Zimov, S.A., Chanton, J.P., Verbyla, D. and Chapin III, F.S., 2006. Methane bubbling from Siberian thaw lakes as a positive feedback to climate warming. Nature, 443: 71-75.

Walter, K.M., Smith, L.C. and Chapin, F.S., 2007. Methane bubbling from northern lakes: present and future contributions to the global methane budget. Philosophical Transactions of the Royal Society of London. Series A, 365: 1657-1676.

Walsh, M.R., Hancock, S.H., Wilson, S.J., Patil, S.L., Moridis, G.J., Boswell, R., Collett, T.S., Koh, C.A. and Sloan, E.D., 2009. Preliminary report on the commercial viability of gas production from natural gas hydrates. Energy Economics.

Weber, M., K., B., Kulenkampff, J., Hennings, J., Huenges, E., Wiersberg, T., Erzinger, J. and Löwner, R., 2006. An in-situ laboratory to study terrestrial, permafrost related gas hydrates (Mallik 2002). In: Stroink, L. (Editor), Geotechnologien Science Report, Gas Hydrates in the Geosystem, No. 7, Potsdam.

Whelan, J., Eglinton, L., Cathles, L.I., Losh, S. and Roberts, H.H., 2005. Surface and subsurface manifestations of gas movement through a N - S transect of the Gulf of Mexico. Marine and Petroleum Geology, 22: 479-497.

White, R.S. and Klitgord, K., 1976. Sediment deformation and plate tectonics in the Gulf of Oman. Earth and Planetary Science Letters, 32(2): 199-209.

White, R.S., 1977. Seismic bright spots in the Gulf of Oman. Earth and Planetary Science Letters, 37(1): 29-37.

White, R.S., 1979. Gas hydrate layers trapping free gas in the Gulf of Oman. Earth and Planetary Science Letters, 42(1): 114-120.

White, R.S., 1982. Deformation of the Makran accretionary sediment prism in the Gulf of Oman (north-west Indian Ocean). In: J.K. Leggett (Editor), Trench-forearc geology: Sedimentation and tectonics on modern and ancient active margins. Geological Society, London, pp. 357-372.

White, R.S. and Louden, K.E., 1983. The Makran continental margin: structure of a thickly sedimented convergent plate boundary. Bulletin of the American Association of Petroleum Geologists, 34: 499-518.

Whiticar, M.J., Faber, E. and Schoell, M., 1986. Biogenic methane formation in marine and freshwater environments: CO2 reduction vs. Acetate fermentation - Isotope evidence. Geochimica et Cosmochimica Acta, 50: 693-709.

Whiticar, M.J., 1999. Carbon and hydrogen isotope systematics of bacterial formation and oxidation of methane. Chemical Geology, 161: 291-314.

Wiedicke, M., Neben, S. and Spieß, V., 2001. Mud volcanoes at the front of the Makran accretionary complex, Pakistan. Marine Geology, 172: 57-73.

Wiedicke, M., Sahling, H., Delisle, G., E, F., Neben, S., Beiersdorf, H., Marchig, V., Weiss, W., Mirbach, N.v. and Afiat, A., 2002. Characteristics of an active vent in the fore-arc basin of the Sunda arc, Indonesia. Marine Geology, 184: 121-141.

Wiese, K. and Kvenvolden, K.A., 1993. Introduction to microbial and thermal methane. In: D.G. Howell (Editor), The future of energy gases. United States Geological Survey, Professional Paper, US Geological Survey, Washington, pp. 13-20.

Worzel, L.J., Bryant, W.R., Beall jr., A.O., Capo, R., Dickinson, K., Foreman, H.P., Laury, R., McNeely, B.W. and Smith, L.A., 1973. Site 88. In: L.J. Worzel and W.R. Bryant (Editors), Initial Report of the Deep Sea Drilling Project. National Science Foundation, Washington, pp. 55-70.

Zitter, T.A.C., Huguen, C. and Woodside, J.M., 2005. Geology of mud volcanoes in the eastern Mediterranean from combined sidescan sonar and submersible surveys. Deep Sea Research I, 52: 457-475.

Zonenshayn, L.P., Murdmaa, I.O., Baranov, B.V., Kuznetsov, A.P., Kuzin, V.S., Kuz'min, M.I., Avdeyko, G.P., Stunzhas, P.A., Lukashin, V.N., Barash, M.S., Valyashko, G.M. and Demina, L.L., 1987. An underwater gas source in the Sea of Okhotsk west of Paramushir island. Oceanology, 27(5): 598-602.

Zühlsdorff, L. and Spiess, V., 2005. Three-dimensional seismic and acoustic imaging of gas migration and gas hydrate accumulation beneath pockmarks in hemipelagic sediments off Congo, south-west Africa, 5. International conference on gas hydrates, Trondheim, Norway.

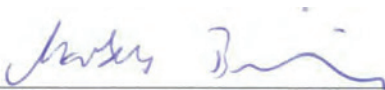N a m e: Markus Brüning   Datum: 01.01.2012

Anschrift: Reindorfer Landstr. 27, 21244 Buchholz i.d. N.

Erklärung

Hiermit versichere ich, dass ich

1. die Arbeit ohne unerlaubte fremde Hilfe angefertigt habe,

2. keine anderen als die von mir angegebenen Quellen und Hilfsmittel benutzt habe und

3. die den benutzten Werken wörtlich oder inhaltlich entnommenen Stellen als solche kenntlich gemacht habe.

Buchholz, den 01.01.2012

_____
(Unterschrift)

Acknowledgements

I would like to thank Prof. Dr. Gerhard Bohrmann for giving me the chance to study and progress the mapping of cold seeps in world-wide settings. I very much enjoyed the collaboration at sea and in the office. I am very grateful for his great and extensive support with inspiration, supervision as well as hardware during the thesis. Furthermore I wish to thank Dr. Heiko Sahling. He always had his door open for discussions. He critically reviewed texts and figures of this work, which largely improved from his comments. Prof. Dr. Volkhard Spieß was very supportive in geophysical questions. He many times contributed with independent objective suggestions and so fuelled my thinking. Very much I appreciated learning from and working with Dr. Ingo Klaucke on the side scan sonar survey of seeps. The four above, Prof. Dr. Gerhard Bohrmann, Dr. Heiko Sahling, Prof. Dr. Volkhard Spieß, and Dr. Ingo Klaucke advised me in regular biannual thesis committee meetings. Their professional guidance in the discussions was extremely helpful in the progress of the thesis.

Those meetings were one column of the 'Bremen International Graduate School for Marine Sciences Global Change in the Marine Realm', Glomar. I took part in the school from March 2007. Educational courses, meetings, and representative work largely improved my skills and abilities. I would like to thank Dr. Uta Brathauer, Prof. Dr. Dierk Hebbeln, Gabi Ratmeyer, and especially Dr. Verner B. Ernstsen. Verner did a great job to improve my knowledge of presentation skills and the theory of scientific research. Glomar funded my travel to an AGU conference in Mexico and partially a visit to Southampton.

Many thanks I would like to express to the Gulf of Mexico people: Adriana Gaytán-Caballero, Prof. Dr. Elva Escobar-Briones, and Prof. Dr. Ian MacDonald. Discussion about the deep Gulf and asphalt volcanism advanced my thoughts contributing to the manuscript on Chapopote.

About work in another part of the world I am grateful to the NOC TOBI team. Dr. Tim Le Bas and Dr. Bramley Murton generously allowed me to deepen my knowledge on side scan sonar surveying and processing. I would like to thank the NOC Geology and Geophysics group for their hospitality and frankness in discussion on the Makran project of cold seepage. Especially I would like to thank Veit Hühnerbach for not letting the social component down. My visit to Southampton was partly funded by the Deutsche Akademische Austauschdienst (DAAD).

I wish to highlight the company and friendship offered to me by my office and PhD mates Antonie Haas and Stephan Klapp, and later for a short period, Jan Hendrik Körber. I enjoyed working with you and would look forward to share facilities again. The same is valid for Katharina Jantzen. She also commented manuscripts from a fresh non-earth-scientific but economy-science point of view. This gave rise to challenging questions. Further PhD students always offered time and brain for discussions on the various research topics: Florence Schubotz, Gunter Wegener, Thorsten Wilhelm. In particular the great cooperation with Feng Ding was fertile for the understanding of sub-surface structures beyond my own datasets.

Sarah Althoff, Gregor von Halem, and Dr. Aneta Nikolovska earned my gratefulness for their work supporting this thesis regarding the Black Sea cruise. Sarah endlessly keen processed the bathymetry data. Gregor had a close look on many hours of seafloor videos from Batumi and supported the GIS work for Makran. Not specifying the thousand large and small things with which my other colleagues in the Marine Geology group supported this work, I wish to thank Dr. Thomas Pape, André Bahr, Fritz Abegg, Jürgen Hohnberg, Miriam Römer, David Fischer, Angelika Rinkel, and Greta Ohling. Accordingly I express my thanks to the geophysicists Dr. Tilmann Schenk, Dr. Noemi Fekete, and Dr. Hanno Keil. Julia

Schneider and Dr. Sebastian Krastel provided rare unreachable publications. Janis Thal and Nina Wittenberg helped in processing bathymetry datasets. Not named here, I am grateful to many people spending hours and days keeping an eye on the echo sounders recording the data this thesis is based upon. The same applies for RV METEOR captains, officers, and crews, doing great jobs in offering a reliable platform for this research. Dr. Volker Ratmeyer and the MARUM ROV team were great in running the vehicle without which this thesis would not have been as it became now. Them, and all other technicians not named here: Thank you!

This study was embedded and fully funded in the MARUM E1, later GB4, project. Hence I thank all keen proposal authors for their effort and the Deutsche Forschungsgemeinschaft (DFG) for their financial support. Besides the academia I wish to express my thanks to Patzold, Köbke & Partner Engineers, Dr. Ing. Volker Patzold, Dr. Wolfgang Thiessen, and Prof. Dr. G. Gruhn for prolonged motivation and support beyond university. Stefanie Pietschann supported me with motivation after long days in the VP-office, to stay up writing.

And, most important, I deeply wish to thank my parents for their continuing support, motivation, talks, not only since the start of my studies. Und am meisten und gründlichsten möchte ich meinen Eltern für ihre dauerhafte Unterstützung, Motivierung, Gespräche, nicht nur seit dem Beginn der Doktorarbeit, danken.

Appendix

A1

A conceptual model for hydrocarbon accumulation and seepage processes around Chapopote asphalt site, Southern Gulf of Mexico: From high resolution seismic point of view

Feng Ding [a], Volkhard Spiess [a], **Markus Brüning** [a], Noemi Fekete [a], Hanno Keil [a], Gerhard Bohrmann [a]

[a] MARUM, Center for Marine Environmental Sciences and Department of Geosciences, University of Bremen, GEO Building, PO 330440, 28334 Bremen, Germany

Due to copyright reasons this publications is not included here.
It can be accessed via the Library of the University of Bremen.

A2

Shallow sediment deformation styles in north-western Campeche Knolls, Gulf of Mexico and their controls on the occurrence of hydrocarbon seepage

Feng Ding [a], Volkhard Spiess [a], Ian R. MacDonald [b], **Markus Brüning** [a], Noemi Fekete [a], Gerhard Bohrmann [a]

[a] MARUM, Center for Marine Environmental Sciences and Department of Geosciences, University of Bremen, GEO Building, PO 330440, 28334 Bremen, Germany
[b] Texas A&M University, 6300 Ocean Drive, HRI-121, Corpus Christi, TX 78412-5869, USA

A3

Interaction between accretionary thrust faulting and slope sedimentation at the frontal Makran accretionary prism and its implications for hydrocarbon fluid seepage

Feng Ding [a], Volkhard Spiess [a], Noemi Fekete [a], Bramley J. Murton [b], **Markus Brüning** [a], Gerhard Bohrmann [a]

[a] MARUM, Center for Marine Environmental Sciences and Department of Geosciences, University of Bremen, GEO Building, PO 330440, 28334 Bremen, Germany
[b] National Oceanography Centre (NOC) Southampton, University of Southampton, Waterfront Campus, European Way, Southampton, SO14 3ZH, United Kingdom

A4

Vodyanitskii mud volcano, Sorokin trough, Black Sea: Geological characterization and quantification of gas bubble streams

Heiko Sahling [a], Gerhard Bohrmann [a], Yuriy G. Artemov [b], André Bahr [c], **Markus Brüning** [a], Stephan A. Klapp [a], Ingo Klaucke [c], Elena Kozlova [d], Aneta Nikolovska [a], Thomas Pape [a], Anja Reitz [c], Klaus Wallmann [c]

[a] MARUM – Center for Marine Environmental Sciences and Faculty of Geosciences, University of Bremen, Klagenfurter Strasse, 28359 Bremen, Germany
[b] IBSS – Institute of Biology of the Southern Seas, National Academy of Sciences of Ukraine, Nakhimov Prosp. 2, IBSS, UA-99011, Sevastopol, Ukraine
[c] IFM-GEOMAR – Leibniz-Institute of Marine Sciences, Wischhofstr. 1–3, 24148 Kiel, Germany
[d] UNESCO-MSU Center for Marine Geosciences, Geological Faculty, Moscow State University, Vorobjevy Gory, Moscow 119899, Russia